
Politecnico di Torino

Politecnico di Torino

Dipartimento di INGEGNERIA STRUTTURALE, EDILE E GEOTECNICA (DISEG)

A.Y. 2024/2025

Graduation period July 2025

# Analysis of a Mechanized Excavation Using an EPB TBM

## The Case of the Grottaminarda Tunnel

Supervisor:
Prof. PEILA Daniele

Candidate:
KESSERWAN Jad

Co-supervisors:
Eng. TODARO Carmine
Eng. CARIGI Andrea

# INDEX

# Acknowledgments

I would like to thank my advisor and Professor Daniele Peila for giving me the opportunity to explore, together with him, the topics related to tunneling and this thesis in particular.
I am grateful for the charisma and passion with which he shared his knowledge, which sparked in me a deep interest in this field of civil engineering.

I also wish to thank the company Webuild S.p.A. which, under the supervision of my company tutor, Eng. Marco Ricci, allowed me to take part in site activities that introduced me to the professional world.
I am especially grateful to the team who welcomed me and supported me with sincere friendship in collecting the data necessary for writing this thesis: Antonio, Flora, Tommaso, and Salvatore.

Finally, I want to thank my family: my mother, my father, and Lucia, thanks to whom I was able to achieve this important and long-awaited milestone in my life. I dedicate this entire journey to you and I am forever grateful for the sacrifices you made for me.

# Abstract

This thesis presents an analysis of the main excavation data regarding the Grottaminarda tunnel, excavated using an EPB-TBM, almost in closed mode and under hyperbaric conditions.

Chapter 2 will provide a brief introduction to the geological-geomechanical context of the area, in order to describe the main issues to be addressed throughout the section under investigation.

Chapter 3 and Chapter 4 will present the predictive models used by the designers to determine the necessary machine parameters for excavation, and the P.A.T. (TBM Advancement Protocol). The latter is the "guideline" for the various work teams on site, essential for achieving proper progress in terms of pressures, thrust, torque, excavation volumes, and other machine-soil parameters. Monitoring will then be a central part of Chapter 4, as it is the main feedback and control tool for all phases of the project. In this chapter, I will present the main monitoring tool used on site: the Tunnelling Process Control (TPC) software from Tunnelsoft (Tunnelsoft).

Chapter 5 will be focused on the main detailed analyses of the nine advancement sections examined. The entire analyzed path has been divided into nine time ranges, in accordance with what was established in the weekly excavation reports (Report, 2024). In each of these, the main tasks performed by the teams are presented, along with performance graphs regarding pressures and injection volumes, thrust, torque, and excavated material. Each graph will be followed by a brief comment and hypotheses.

Finally, Chapter 6 will provide a comprehensive view of the entire excavation with a comparison of the data collected, including those on soil conditioning and therefore on FER and FIR.

The consultation of the data was kindly provided by the Hirpinia AV Consortium, specifically authorized by the company Webuild S.p.A. (Webuild).

# List of Figures

# List of Tables

# Introduction

## context

The thesis is developed within the construction sites of the AV Hirpinia Consortium, specifically at the construction company Webuild S.p.a.

Webuild is one of the major global players in the construction of large, complex infrastructures for sustainable mobility (railways, metro systems, bridges, roads, ports), hydropower (hydroelectric dams, power plants), water (treatment plants, desalination plants, wastewater management, dams for drinking water and irrigation), and green buildings (civil and industrial buildings, airports, stadiums, and hospitals).

We are in the context of the construction of the HS/HC Naples-Bari high-speed rail line, which will allow trains to travel at a maximum speed of 250 km/h, significantly reducing travel times between Apulia and Campania, Lazio, and the rest of central-northern Italy, while also connecting the country on the East/West side. The construction of the Naples-Bari line has been divided into 7 sections.

Webuild is involved in the construction of four sections: Naples-Cancello, Apice-Hirpinia, Hirpinia-Orsara, and Orsara-Bovino, where over 74 km of new railway line are planned, along with 6 tunnels that will require the use of 8 TBMs, 10 viaducts, and 6 new stations and stops.

The Naples-Bari High-Speed / High-Capacity Rail Project, with a total of 145 km of track, is an important part of the European TEN-T program for sustainable transport. This program aims, by 2050, to shift 50% of freight traffic currently transported by road to rail, triple the high-speed railway network, and reduce transport-related emissions by 60%. Once completed, the Naples-Bari route will take 2 hours, compared to the current 4 hours, while the Rome-Bari connection will take 3 hours, saving about two hours.

The Apice-Hirpinia section includes the construction of a total of 18.7 km of High-Speed railway, approximately 13 km of which will be in tunnels, divided into 3 tunnels (Grottaminarda, Melito, and Rocchetta), along a route characterized by high structural and geomorphological complexity.

## Goal of the thesis

The objective of this thesis is to provide a detailed analysis of the excavation data related to the Grottaminarda tunnel, constructed using the EPB-TBM (Tunnel Boring Machine) named "Aurora" (EPB-TBM 978). The analysis will focus on various key parameters such as, thrust force, torque, injection pressure for backfilling, FIR (Foam Injection Ratio), FER (Foam Expansion Ratio) and other monitoring data. The aim is to examine how these parameters evolve throughout the

excavation progress, correlating the data with the geological and geomechanical characteristics of the area.

To achieve this goal, technical reports, calculation reports, and monitoring data collected through a monitoring system called TPC (Tunnel Processing Controller) will be analyzed, which allows the visualization of data in real-time and deferred. The analysis will focus on a specific time range, from March 19, 2024, to August 2, 2024, to ensure a sufficiently continuous set of data for a thorough analysis.

The aim is to provide an accurate interpretation of the excavation data to optimize the tunneling process's efficiency and contribute to understanding the parameters that influence the safety and performance of the TBM during the tunnel construction.

# 1. EPB-TBM technology

## 1.1. History of mechanized tunneling

Mechanized tunneling has a long and fascinating history, evolving with increasingly sophisticated technologies to address the challenges of building tunnels in difficult geological conditions and urban environments. The **TBM (Tunnel Boring Machine)**, particularly in its **EPB (Earth Pressure Balance)** version, represents one of the most advanced solutions for tunnel excavation.

The first forms of mechanized tunneling date back to the mid-19th century. The first tunnel boring machine was invented in 1840 by **Isambard Kingdom Brunel**, an English engineer, who created a rotating machine for building tunnels under the River Thames in London. However, these early machines were not capable of operating in all geological conditions and had limited capacity.

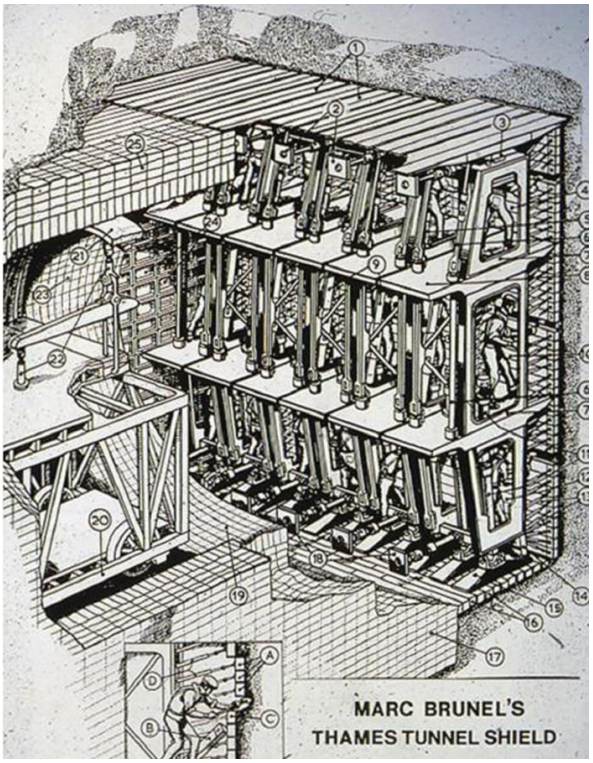


Figure 1.1 Marc Brunel's Thames Tunnel shield drawing

In the 1950s, the modern **Tunnel Boring Machine** began to take shape. In the 1960s and 1970s, mechanized tunneling machines became more sophisticated, thanks to technological advances in materials and control systems. The ability to dig tunnels more safely and efficiently led to the rapid adoption of these machines, especially for large-scale projects such as subways and highway tunnels.

## 1.2. The Evolution of the TBM EPB

The **TBM EPB** is one of the most recent and advanced versions of TBMs, developed mainly to address the challenges of cohesive soils, such as clay and sand. Its development is tied to the need to excavate tunnels in problematic ground where the stability of the excavation face is a primary concern.

The first EPB TBMs were developed in the 1970s and 1980s, when it became clear that balanced pressure machines were crucial for reducing the risks of soil collapse during excavation. The EPB technology is based on the use of **support pressure** at the excavation face, which keeps the surrounding soil stable, reducing the risk of subsidence or surface settlement, which can occur with traditional tunneling methods.

The **first successful use of an EPB TBM** took place in the early 1980s. One of the first projects to utilize this type of machine was the **Tokyo Bay Tunnel project in Japan** in 1980. This was a pioneering moment for EPB technology, as the machine successfully performed in difficult, water-saturated soils and overcame various engineering challenges. It was a turning point in tunneling, as it demonstrated the ability to manage the pressures of soft ground with the use of a pressure-controlled excavation system.

During the 1980s and 1990s, the EPB TBM technology continued to evolve with improvements in machine design, monitoring systems, and the incorporation of new materials. The machines were optimized to handle a wide range of geological conditions, from soft clays to mixed-face conditions, which had previously been difficult to manage with traditional tunnel excavation methods.

The late 20th century saw the development of increasingly sophisticated **EPB TBMs**, with enhanced features for controlling ground pressure, injecting backfill material, and ensuring stability throughout the excavation process. Some key innovations included:

1. **Real-time monitoring systems**: These systems were introduced to provide data on ground conditions, machine performance, and excavation progress. This helped operators to make immediate adjustments to the machine's operation, ensuring safety and efficiency.
2. **Enhanced face control**: EPB TBMs incorporated better control systems for managing the pressure at the excavation face, which reduced the risks associated with ground movements and ensured smooth tunneling in mixed and unstable soils.
3. **Advanced cutterhead designs**: The cutterhead was further refined to handle diverse ground types, from soft clays to harder rock layers, and improve excavation speed and efficiency.
4. **Backfilling and spoil removal systems**: New methods for managing backfill material and spoil removal were developed, allowing for cleaner operations and reducing the risk of settlement or damage to the surrounding area.

**Mechanized tunneling** and **TBM EPB** have revolutionized the way tunnels are built, allowing for the construction of complex infrastructures in a safer and more efficient manner. With the continuous improvement of technologies and monitoring capabilities, TBM EPBs represent an increasingly preferred solution for projects that require precise management and high safety, particularly in difficult terrains.

## 1.3. How a TBM EPB Works

The **TBM EPB** has a rotating cutting head that excavates the soil while the support system at the excavation face balances the pressure with that of the surrounding soil. As the material is removed, backfilling material is injected, which helps maintain stability and prevents the ground from collapsing. The machine is designed to operate under high pressure conditions, such as in clayey or sandy soils, where it is crucial to maintain the stability of the excavation face (Figure 1.2 and Figure 1.3).

The use of **earth pressure balance** is what sets TBM EPBs apart from other machines, such as **open-face TBMs** or **high-pressure TBMs**, which do not use this type of support system.

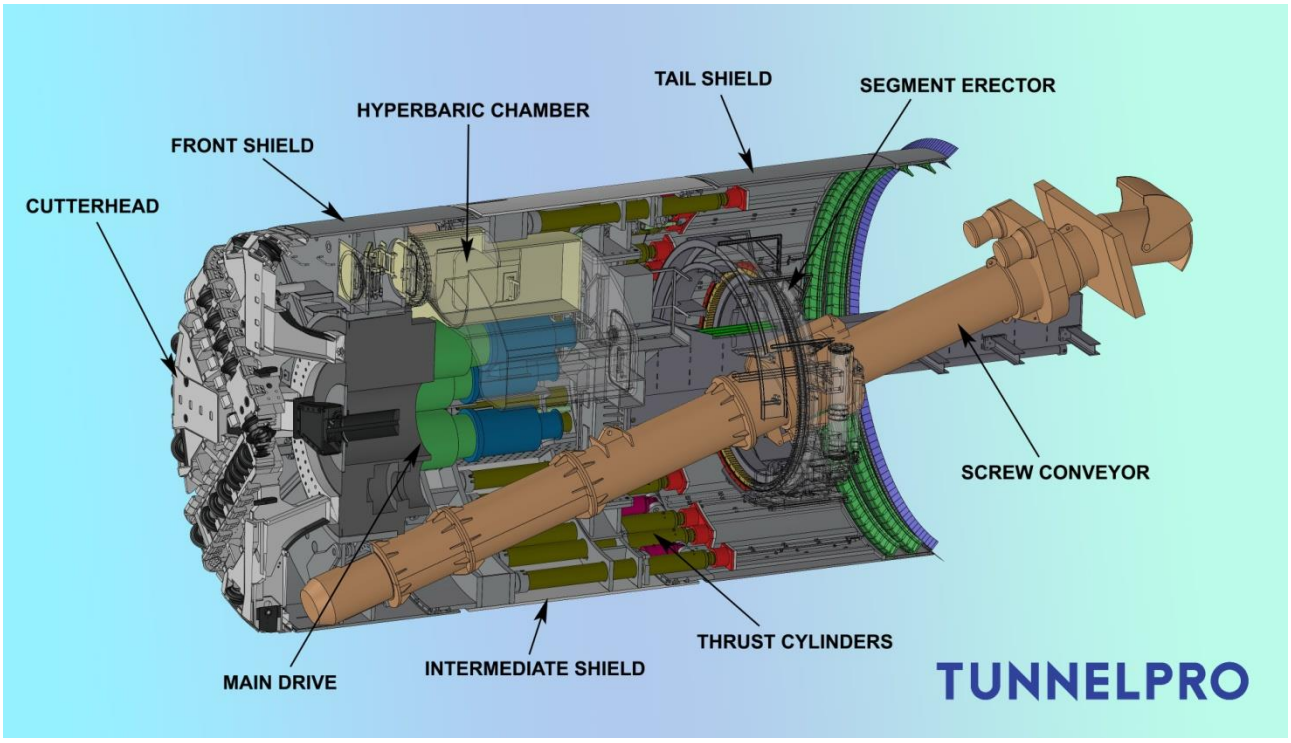


Figure 1.2 Common EPB-TBM configuration (TunnelPro)

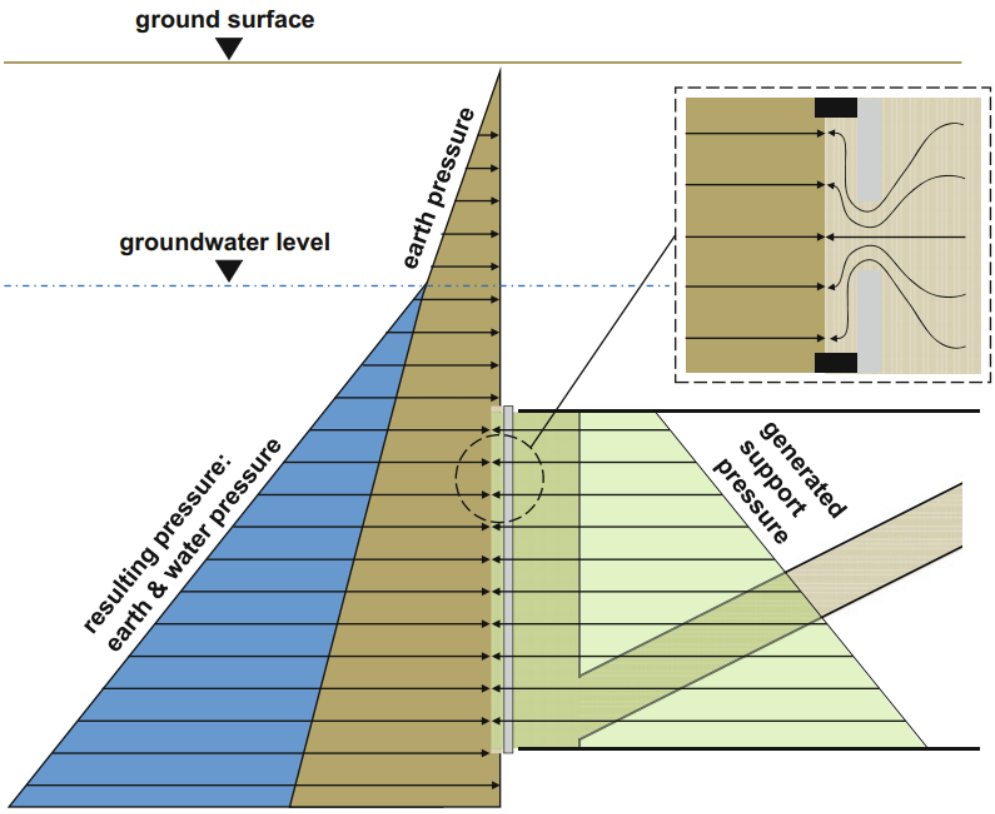


Figure 1.3 Face preassure control of an EPB-TBM (Britta Schößer, 2023)

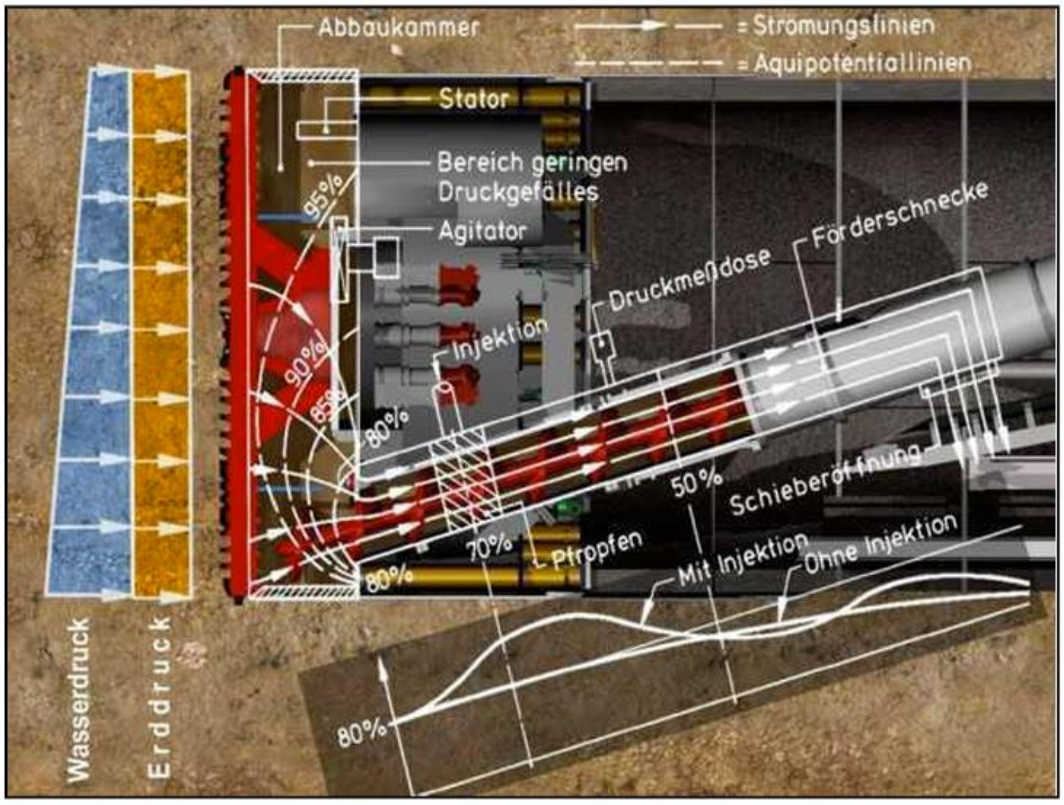


Figure 1.4 Conceptual scheme of both face and screw conveyor preassures (Peila, 2022-2023)

## 1.4. The Importance of the TBM EPB Today

Today, TBM EPBs are used worldwide for a wide range of projects, from rail and subway tunnels to highway tunnels and hydraulic infrastructure. Their ability to operate in complex environments and minimize surface disruption makes them ideal for excavating in densely populated urban areas. Additionally, these machines are safer compared to traditional tunneling methods, as they significantly reduce the risk of surface damage to buildings, monuments, or existing infrastructure.

Figure 1.5 EPB Front view (Herrenknecht, 2025)

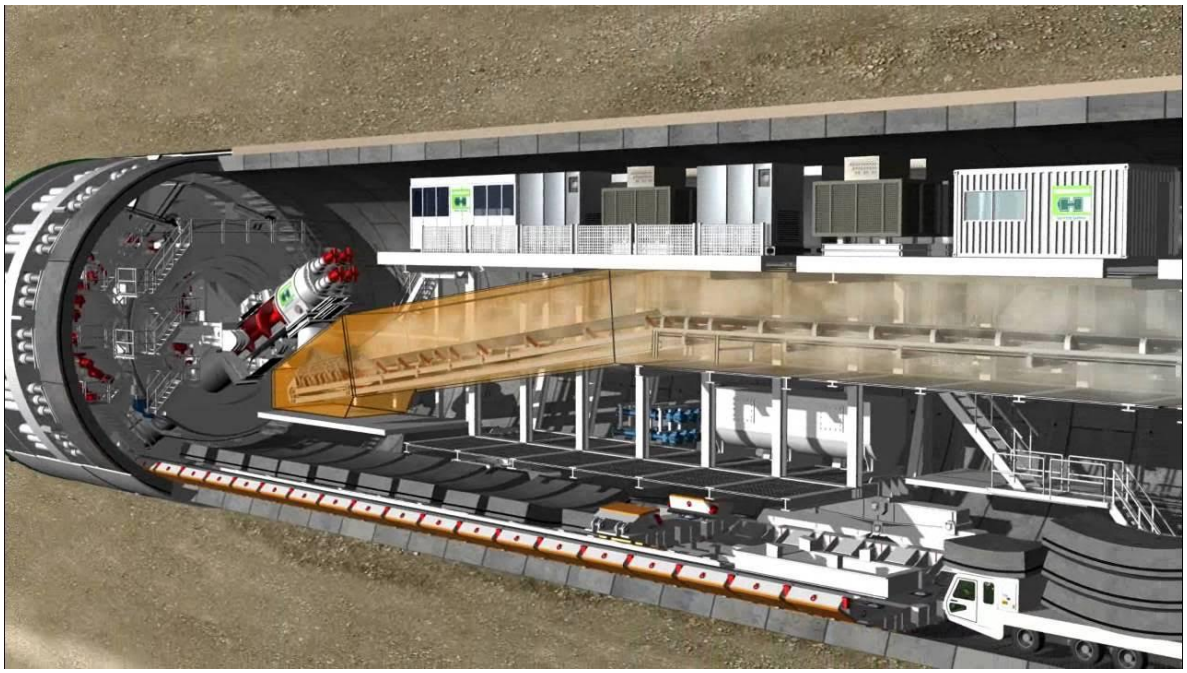

Figure 1.6 EPB Rear View, courtesy by Herrenknecht (TOTO, 2013)

## 1.5 Technical specifications and tool configuration for TBM 978 “Aurora”

The **TBM Aurora** measures 100 metres in length and has 18 engines providing 6.3 MW of power. Its cutting head has a diameter of approximately 12.5 metres. The TBM, along its journey, beside excavating the tunnel, also completed its lining with precast concrete segments.

The excavation of the Grottaminarda Tunnel will pass through heterogeneous lithological formations of the Red Flysch. Field surveys and boreholes have revealed the potential presence of calcareous inclusions, some of which may be of metric size, in the upper part of the Flysch, which predominantly exhibits a pelitic facies, particularly in the tectonized area affecting the approach section of the tunnel on the Naples side (Figure 1.8 and Figure 1.9, (Webuild)).


Figure 1.7 Assembly of conveyors for the Grottaminarda tunnel (Webuild)

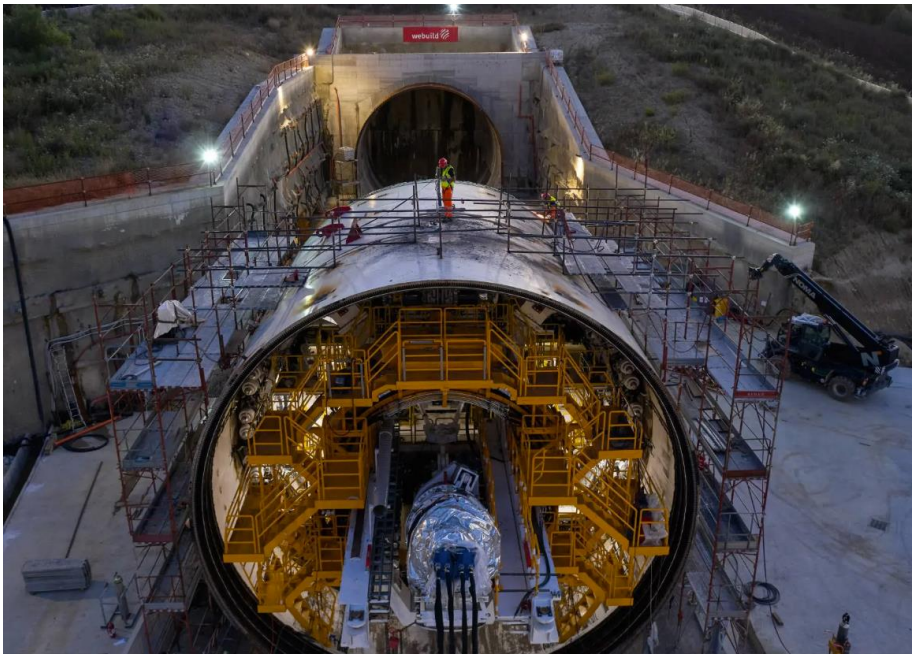


Figure 1.8 Assembly of conveyors for the Grottaminarda tunnel (Webuild)

Therefore, the excavation face must be designed to handle variable advancing conditions, including mixed fronts, where harder calcareous inclusions are embedded in the pelitic matrix. It will be necessary to provide appropriate systems for the rapid replacement of excavation tools (disc cutters/rippers), depending on the lithological variability of the material to be removed, specifically:

- fronts consisting of clayey material, locally of high plasticity, in the sections within the predominantly pelitic facies of the Red Flysch (FYR).
- The excavation fronts appear as mixed, characterized by an abundant presence of calcareous lithoid inclusions, which, in addition to showing a certain continuity with respect to the size of the front, possess medium to high mechanical resistance properties. These inclusions belong to the rudite facies with an argillaceous-marly matrix of the Red Flysch (FYRcc). Alternatively, there are fronts where a widespread distribution of calcareous benches is observed, interspersed with more marly levels, typical of the calcareous facies FYR2 of the Red Flysch.

To ensure the maintenance of excavation tools, such as scrapers and rippers, an initial machine stop is planned for interventions on the excavation face, to be carried out at the end of the passage beneath the Grottaminarda landslide. This intervention aims to appropriately configure the excavation face for the subsequent crossing of the final section of the tunnel, where a widespread presence of calcareous layers is expected.

The excavation face will be equipped with grizzly bars on the openings, with an expected opening ratio of around 40%, to prevent the entry of critical-sized lithoid fragments into the excavation chamber. The mucking screw will be designed to reduce potential abrasive effects and damage caused by the presence of calcareous material in the muck. Additionally, extra injection lines will be provided directly on the face for conditioning the material at the front and for optimal management of the excavation processes, particularly in sections where clayey passages are expected, with the associated risk of clogging.

The central sector of the excavation face will be designed with a larger opening ratio compared to standard EPB applications, in order to prevent the accumulation of fine material and the risk of clogging. The openings, as previously mentioned, will be equipped with grizzly bars to simultaneously manage the risk of rock inclusions that could be incompatible with extraction via the mucking screw from the excavation chamber to the conveyor belts (Webuild).

### 1.5.1 Conicity of the shield

To effectively manage the various conditions that may arise during excavation, including both scheduled and unforeseen stops, specific technical evaluations will be conducted regarding the provision of spherical bearings (main drive). These bearings will allow local variations in the excavation profile without the need for interventions on the excavation face, structure, or tools.

The geomechanical context and the characteristics of the overburden require the use of a shield with a radial taper of no less than 20 mm. This measure is necessary to reduce the pressure on the shield during advancement in more resistant sections and to facilitate restart after any machine stops.

### 1.5.2 Excavation Chamber pressures

The analyses conducted highlight the need to operate in "closed" mode throughout the development of the Grottaminarda tunnel. This approach involves maintaining earth pressure in the excavation chamber (with an average value at the centerline level of 4.5 bar) in order to limit the phenomena of plasticization of the material within the core-face.

### 1.5.3 Soil conditioning

As part of the previous geotechnical campaigns, the classification from literature regarding the risk of clogging was applied, analyzing the index properties and the consistency index of samples from the various lithologies making up the Red Flysch. The results revealed a scenario characterized by a high/medium-high risk of clogging (Figure 1.10). For this reason, a specific polymeric additive has been planned to reduce the risk of clogging, in combination with the injection of standard foaming agents into the excavation chamber.

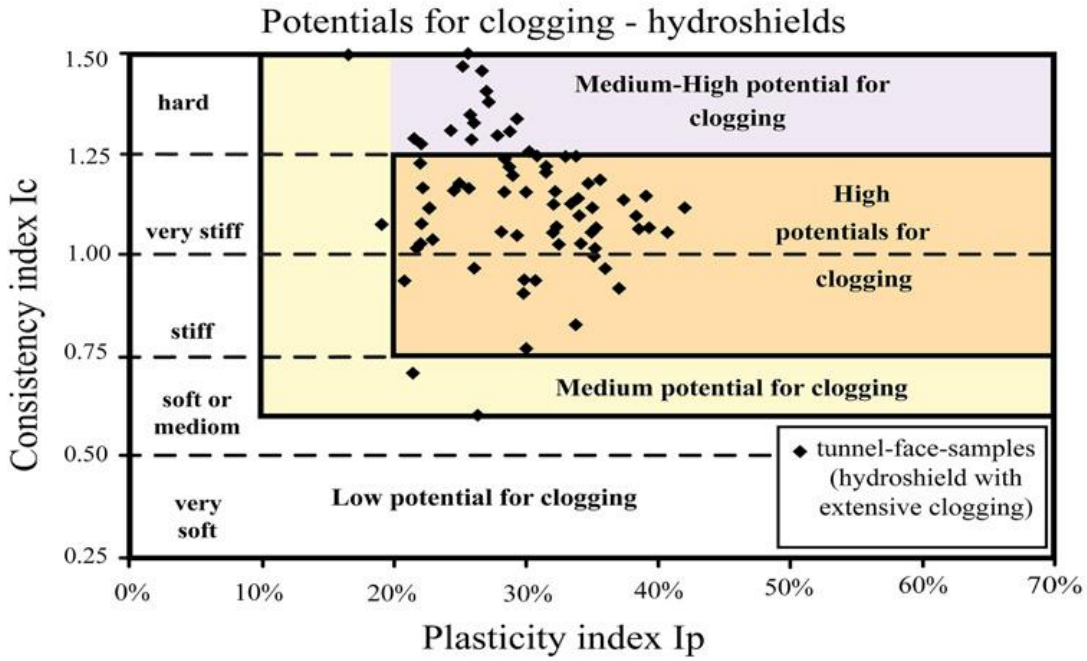


Figure 1.9 Modified clogging risk graphic representation for slurry TBM (Hollmann FS, 2013)

### 1.5.4 Special Equipment

- Drilling system for continuous core sampling ahead of the tunnel face;

- Drilling system for the creation of a consolidation injection umbrella around the tunnel perimeter and at the face, as well as drainage rods, advancing ahead of the excavation face;

- Pressure cells on the shield to detect the stress state induced by the release of stresses from the surrounding ground;

- Automated dimensional control system for the annular gap between the shield's outer surface and the excavation profile, based on the technical and technological solutions presented in the technical offer for the Grottaminarda Tunnel;

- Ability to inject lubricating agents from inside the shield to the interface between the shield and the surrounding ground.

### 1.5.5 Excavation management in the presence of gas

The presence of gas pockets within the flysch formation is possible. In this regard, it is highlighted that the Final Project identifies, for the galleries in question, a risk class of 1b (*NIR 28: Tunnels/sections for which structural geological analysis predicts the presence of gas flows, but there are no confirming elements derived from preliminary investigations (studies and research, historical analysis, boreholes) carried out during the design phase and from the portion of the work already completed. Ultimately, gas manifestations are possible but are expected to have modest flow rates or occur in a manner that is considered not to pose a risk*).

The investigation campaign of the Executive Project stipulated that, at each investigation station, continuous measurements and recordings of methane gas concentrations at the borehole were conducted during the drilling phase. The data collected through these recordings confirmed the risk classification as 1b, in accordance with NIR 28. Based on this classification, the use of a complete anti-deflagrant configuration for the Grottaminarda tunnel excavation machine is not considered necessary.

However, the TBM will be equipped with suitable systems to manage the potential risk associated with gas concentrations, through an advanced monitoring system. Specifically, the machine will be equipped with sensors placed both on the TBM head and on the muck removal system, via the screw conveyor and belt. These devices will allow for the detection of any gas concentrations and trigger the corresponding safety procedures.

Considering the 1b risk classification, no specific interventions for compartmentalization or the installation of an additional ventilation system are planned. However, it will be necessary to closely monitor the possibility that gas may be dissolved in water, paying particular attention to its potential presence in the drainage sumps (Relazione, 2021).

### 1.5.6 Precast segments lining

The lining ring will be made up of 8+1 prefabricated segments, each with a thickness of 55 cm and a length of 1.80 m. The remaining annular gap between the outer surface of the lining and the excavation profile will be filled by the tail of the shield with a fast-setting two-component mix.

The typical cross-section has the following characteristics:

- **Inner radius**: 5.40 m
- **Excavation diameter**: 12.30 m
- **Ring type**: Universal
- **Number of segments**: 8+1
- **Segment thickness**: 0.55 m
- **Segment length**: 1.80 m
- **Rck**: 45 MPa
- **Seal**: Single integrated EPDM gasket, coupled with hydrophilic cord/strip ensuring hydraulic seal for both longitudinal and radial joints.

- **Longitudinal connectors** for connection between segments of adjacent rings.

Particular attention will be given to the relative positioning of the segments to avoid the alignment of longitudinal joints between two consecutive rings (Elaborati, 2021).

Regarding the hydraulic sealing system, a single integrated EPDM gasket will be used, positioned on the outer surface and coupled with a hydrophilic cord. This solution replaces the originally planned double gasket system (outer and inner surfaces) in the Final Project. This proposal represents an improvement, as it ensures superior quality in the installation of the segments while providing hydraulic sealing performance that is equivalent to, if not better than, the double gasket system outlined in the initial design (Elaborati, 2021).

### 1.5.7 Backfilling

The injection of the annular gap behind the lining will be carried out using a two-component mortar or mixture, through the injection lines integrated into the tail shield. This will result in a configuration that is essentially impermeable, or at least with hydraulic conductivity significantly lower than that of the materials encountered during excavation. Each injection line will be equipped with an autonomous pumping device to ensure precise control over the volumes injected by each line.

The monitoring of the complete filling of the annular gap behind the segments will be automated, using equipment based on ultrasonic tomography technology, which will allow for accurate control of the process (Figure 1.11).

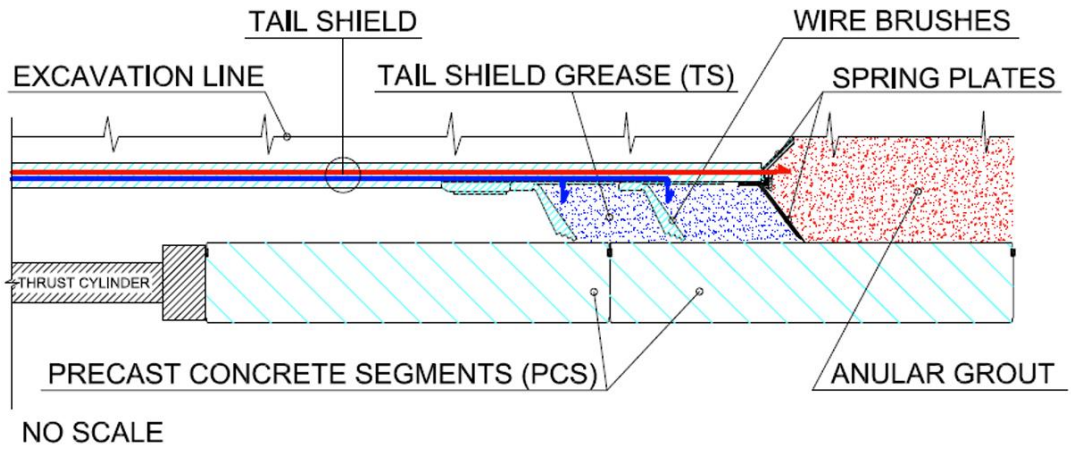


Figure 1.10 Detailed view of the backfilling system (R. Bono, G. Pini, B. Giurgola, 2018)

# 2. Geological-geomechanical context of the area

The Grottaminarda tunnel, a double-track tunnel, has a length of 1990 meters. The excavation of the natural section extends for about 1965 meters. The cover depths vary between 5 meters and 70 meters..

## 2.1 Regional overview

The route of the first functional lot Apice-Hirpinia falls within an area belonging to the orogenic system of the Southern Apennines. The current structural configuration of the Southern Apennines is the outcome of compressional, extensional, and strike-slip events, linked to the subduction and subsequent flexural retreat of the Apulian-Adriatic microplate.


Figure 2.1 Main physiographic elements of the area. The route is highlighted in yellow (Relazione, 2021)

The successions are almost exclusively composed of clastic terms deposited in environments ranging from proximal marine, coastal-lagoonal, and alluvial settings in wedge-top basins. These are bounded by erosional unconformity surfaces associated with tectonic phases that created angular unconformities. The Baronia system consists of a succession mainly made up of clastic materials, deposited during a complete sedimentary cycle.

Regarding the Flysch Rosso formation, it is composed of calcareous-clastic and pelitic ramp-basin successions, which rest in continuous sedimentation. Along the proposed route, in the area where the Flysch Rosso outcrops, the exposure percentage is very low, below 10%, and the only observable lithofacies are those dominated by limestone. Most of the information has been derived from data obtained from over 30 boreholes drilled during various project phases.

Despite the extreme tectonic-structural complexity of the area, the units found, from bottom to top, include: a calcareous-dominated unit, a unit mainly consisting of chaotic deposits, and a third unit with a clayey-marly dominance. The diagram in Figure 2.2 helps to understand the type of context in which the Flysch Rosso deposition and the different stratigraphic units that make it up occorre (Relazione, 2021).

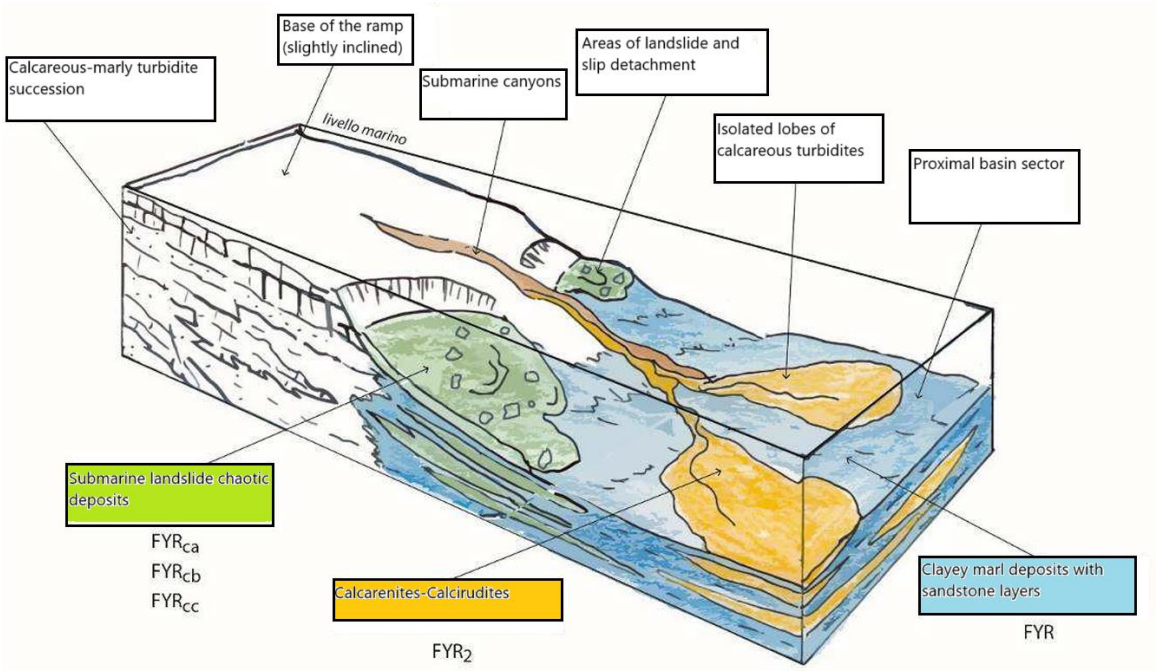


**Figure 2.2 An exemplary diagram of the depositional environments that led to the formation of the different lithologies recognized within the Red Flysch (Relazione, 2021)**

Figure 2.3 Samples with polygenic limestone breccias (left) and calcirudites (right) attributable to the FYR2 formation (Relazione, 2021)

A comparison was finally made between the identified faults and the active and capable faults reported in the literature. The results showed that existing data indicate two structures as active, which would be located at the margins of the studied area, specifically in the Grottaminarda basin (NE-SW direct fault) and in the open section of Iscalonga (NW-SE direct fault, parallel to the Calore River) (Relazione, 2021).

## 2.2 Grottaminarda tunnel

The Grottaminarda Tunnel crosses the left orographic side of the Ufita River. This side is characterized by numerous landslides of varying extent and activity levels (active, dormant, and stabilized). Additionally, the route runs through a tectonically complex area with fragile structures.

Starting from the Bari side tunnel entrance, the route is intersected by two presumed high-angle faults running in a NE-SW direction; the first is between chainages 2+975 and 3+000, and the second is at approximately chainage 3+325. Both faults were hypothesized based on geomorphological considerations derived from LIDAR data analysis and ground surveys (Figure 2.4 and Figure 2.5).

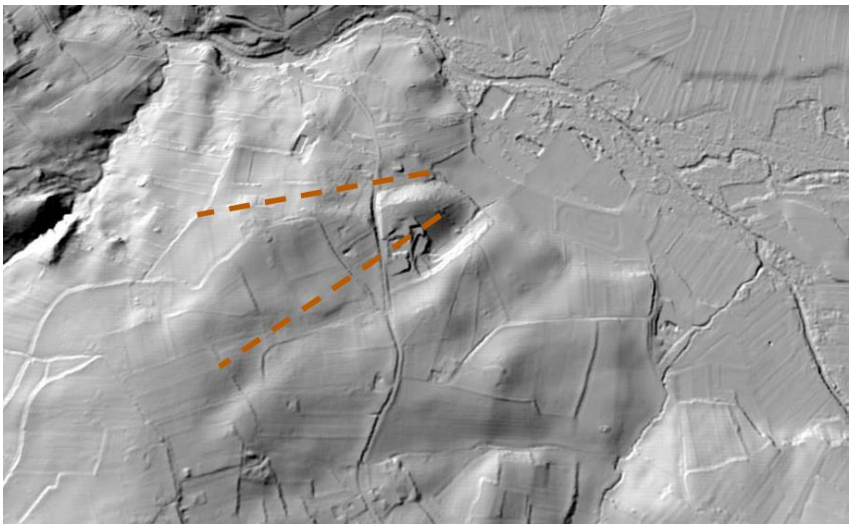

Figure 2.4 Non-to-scale excerpt of the digital terrain model obtained from LiDAR, showing the trace of the presumed fault surfaces (Relazione, 2021)

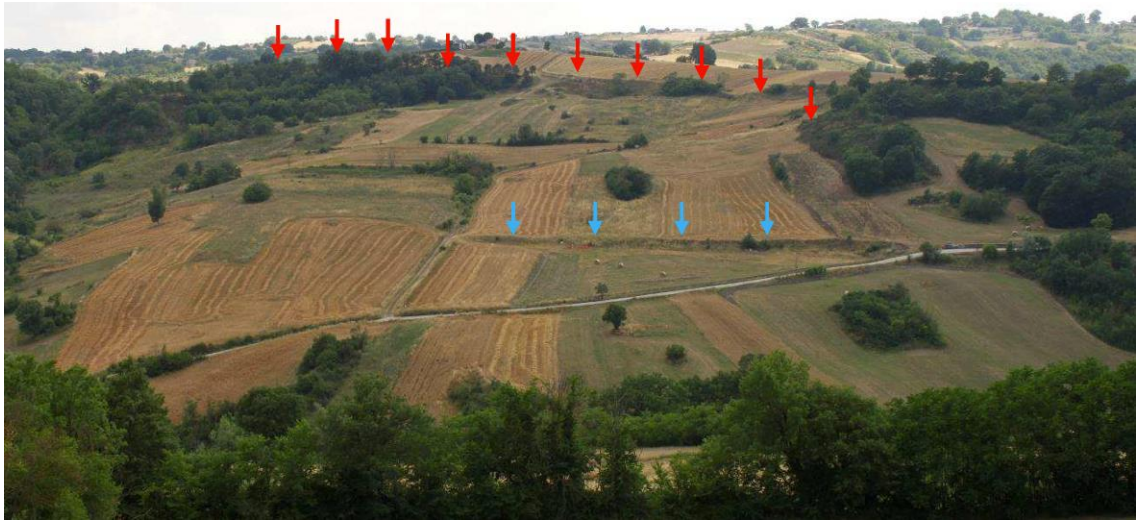

Figure 2.5 Photo with a frontal view of the Grottaminarda landslide. The red arrows indicate the position of the main scarp, while the blue arrows point to an internal scarp within the landslide body (Relazione, 2021)

There are also several hydrogeological complexes with varying permeability levels, distinguishing areas within the rock masses and soils crossed by the works that exhibit homogeneous hydrogeological behavior. The classification of these complexes is based on a critical analysis of permeability tests conducted during the borehole surveys.

For the Geotechnical/Geomechanical profile of the Grottaminarda Tunnel, please refer to the attachments (Annex 1).

# 3. Prediction models

Prediction is a crucial element in engineering projects, particularly in the design and construction of tunnels, where uncertainties and risks are particularly high due to geological complexity and environmental variables. The prediction methods used in these projects are essential for accurately planning construction phases, estimating completion times, costs, and managing risks associated with phenomena such as ground settlement, groundwater interaction, and unforeseen conditions that may arise during the work.

Some of the main factors that influence the performance of the TBM can be divided into:

- rock mass factors;
- machine factors.

## 3.1 Diagnosis phase

In the diagnostic phase, the tensile-deformative response of the surrounding material during excavation is predicted, in the absence of stabilization interventions. For low covers (up to 40 m), the Tamez method was used to assess tunnel stability, while for higher covers, characteristic lines were employed.

Tamez & Cornejo's Method (1984)

The limit equilibrium method proposed by Tamez (1984) (Tamez) is based on the assumption that the response of the excavation face occurs under drained conditions; therefore, the calculation is carried out using effective stresses. It is assumed that a failure mechanism develops at the face, which can be represented by prismatic solids, as shown in Figure 3.1. Subsequently, the safety factor (FSF) is calculated for this collapse condition by obtaining the ratio between the moments of the resisting forces and the moments of the acting forces. (Elaborati, 2021)

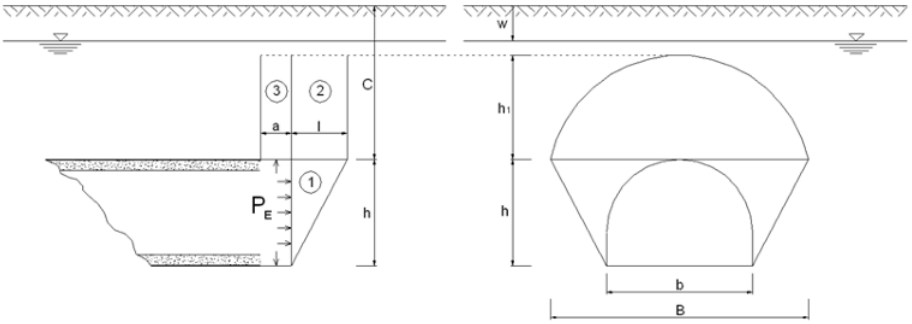


Figure 3.6 Stability of the front according to Tamez's Method (1984) (Elaborati, 2021)

In some cases, the stability of just prism 3, which affects the portion of the tunnel that is not yet supported by the lining, may be more critical than the combined stability of all three prisms. Therefore, a second safety factor, FS3, is defined, and the stability of the face is assumed to be governed by the minimum safety factor between the two.

The excavation face is considered stable when FSF is greater than 1.5, and support for the face can be considered unnecessary when FSF exceeds a value of 2.

In the case of the analysis performed using Tamez's method, the designers classified the ground as belonging to the "core-unstable face" category, which implies that once the ground's resistance is exceeded, deformative phenomena develop quickly in the plastic field, leading to the progressive instability of the excavation face and the expansion of the decompressed and plastified zone surrounding the cavity, resulting in the rapid deterioration of the material's mechanical properties. (Elaborati, 2021)

## 3.2 Theraphy phase

The therapy phase involves defining the necessary interventions to ensure the stability of the excavation face, in line with the findings from the exploratory phase and the analysis of the ground behavior during excavation without any interventions.

For mechanized excavation with EPB technology, the determination of pressures in the excavation chamber follows a logical-operational approach: depending on the tunnel classification (decided by the designer), pressures are calculated.

A counterpressure is applied to the excavation face to maintain deformational control at the face and around the cavity until the final lining is installed. Since this is a verification for an ultimate limit state of the GEO type, for the most critical condition, Approach 1 - Combination 2 (A2+M2+R2) was used, with R2 = 1, applying partial coefficients to the material's resistance parameters and evaluating the verification result according to the adopted calculation method (Tamez's method, (Tamez)). (Elaborati, 2021)

## 3.3 Evaluation of Maximum Operating Thrusts of the TBM and Stress State Release Factors

The formulation adopted by the designer for the evaluation of the overall thrust for the dimensioning of a TBM is provided (reference is made to what is proposed in "Mechanised Shield Tunneling" by B. Miadl, M. Herrenknecht, L. Anheuser) (M. Herrenknecht, 1996). Specifically, the overall thrust must take into account four individual terms::

$$\Sigma W = W_{sh}+W_{sk}+W_{exc}+W_{sup} \qquad (3.1)$$

- Force due to machine-terrain friction $W_{sk}$;
- Pressure force to be applied to the face $W_{sup}$;
- Force required for excavation $W_{exc}$;
- Force due to the presence of the brushes and the cutting edge $W_{sh}$.

The analyses conducted show that the maximum thrust expected for the advancement of the TBM shield is always lower than $N_{max}$ = 110,000 kN (110 MN).

## 3.4 Release percentages

The release factor defines the reduction of excavation forces compared to the initial condition. This factor has been determined based on the lost volume expected at the time of the installation of the final segmental lining, in relation to the characteristics of the analysis section. Specifically, two conditions of lost volume were considered, calculated based on the average convergence measured around the tunnel contour, amounting to about 0.3% and 0.6% at the shield's end (Figure 3.2). During the excavation phase, no lowering of the original piezometric level is expected, as this condition is compatible with both the earth pressure balance advancement and the relationship between the cutter head's advancement speed and the permeability of the material at the face, excluding the possibility of technically significant filtration phenomena toward the excavation chamber (Elaborati, 2021).

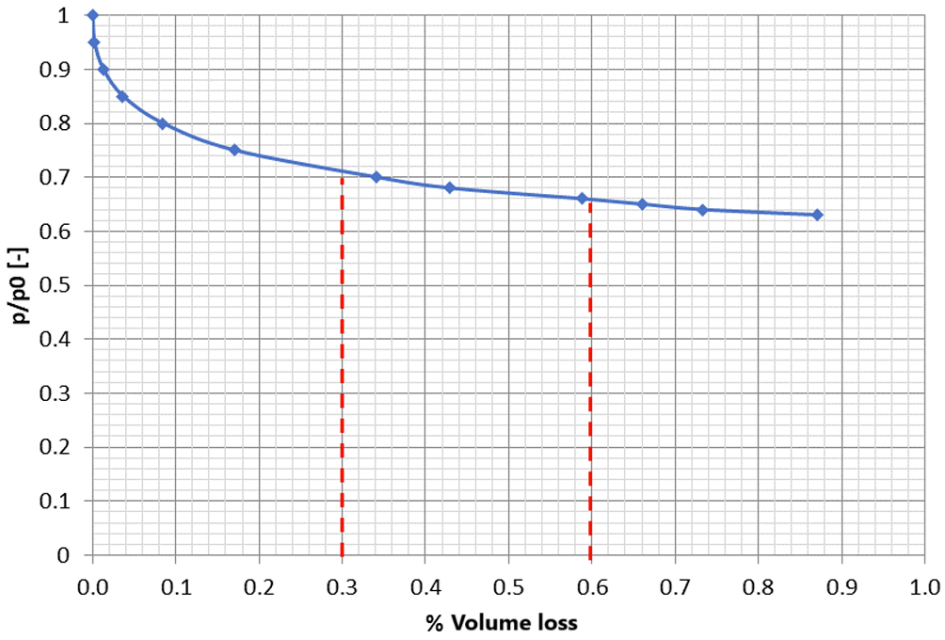


Figure 3.7 Volume lost as a function of the cable relaxation curve (Elaborati, 2021)

The aforementioned reduction is a function of the ratio between the isotropic and deviatoric stresses acting on-site at the tunnel perimeter.

## 3.5 Segment gasket

The final lining must ensure, during the operational phase, a hydraulic seal of 8 bar, corresponding to a hydraulic head of 80 meters, with seal misalignments of up to 15 mm and joint openings of up to 6 mm. The chosen gasket is the UG037A by Fama, made of EPDM (Ethylene-Propylene Diene Monomer) with a hardness of 70 Shore A, fixed in the concrete pour to prevent its displacement during the segment installation. Additionally, the gasket features a bentonite cord placed at the center of the contact surface to ensure sealing even in the case of misalignment between the

contacting gaskets (Figure 3.3). The calculation coefficient to determine the test pressure in relation to the operating pressure, proposed by ITA and approved by Stuva, is 2 (Elaborati, 2021).

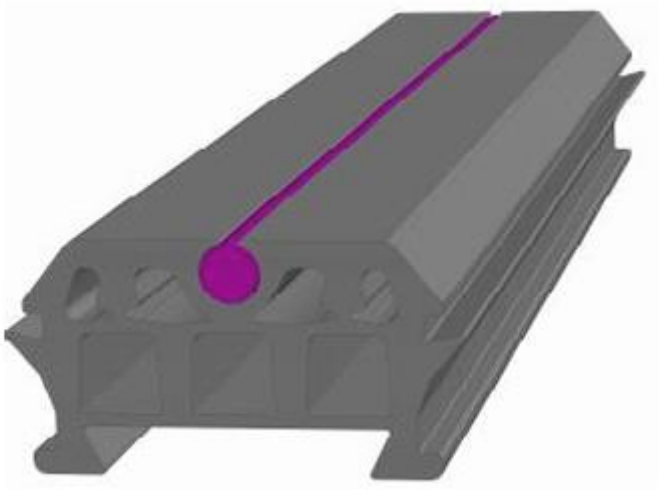

Figure 3.8 Gasket with hydrophilic cord installed (Elaborati, 2021)

## 3.6 Milling study

Milling ability refers to the evaluation of the TBM's performance in relation to the machine parameters and the geological characteristics of the ground, focusing on two main aspects: the prediction of advancement and the estimation of tool wear.

The most well-known methods for this type of analysis are the CSM method from the Colorado School of Mines (Rostami and Ozdemir, 1993; Rostami, 1997) (Rostami J., 1996) and the NTNU or "Norwegian" method (Bruland, 1998). In this case, only the CSM method was used to estimate the TBM's advancement.

For the characterization of the Flysch Rosso, the uniaxial compressive strength of the rock material is estimated to be in the range of $\sigma_c$ = 25-50 MPa, while the rock's elastic modulus has not been specified. However, the deformability modulus of the mass, derived from correlations with the RMR obtained from boreholes, is $E_d$ = 10 GPa.

The second lithotype considered is the Apollosa Member (BNA3), which has a uniaxial compressive strength between $\sigma_c$ = 40-60 MPa and an elastic modulus E = 9 GPa.

One of the necessary parameters for applying the CSM method is the tensile strength σt of the rock material, which, in the absence of direct tests, can be assumed to be between 1/8 and 1/10 of the compressive strength.

For the abrasiveness analysis, it is essential to know the mineralogical composition of the rocks or the values of the CAI and CLI indices, which allow the quantification of tool wear through empirical correlations. The evaluation of these parameters was based on correlations with the

predicted mineralogy for each type of rock. Mineralogical composition is crucial because it helps identify the content of quartz and other minerals, which affect abrasiveness. Although quartz content is a key factor in abrasiveness, it is not the only one; the presence, shape, and size of other minerals can also influence the rock's wear rate.

It is possible to consider the presence of other minerals by introducing the equivalent quartz content, which relates the abrasiveness of many common minerals to that of quartz (some typical values are listed in Table 1).

| | | | |
|---|---|---|---|
| **Quartz** | 100% | **Pyroxenes** | 50-53% |
| **Feldspars** | 70-80% | **Amphiboles** | 47-53% |
| **Olivine** | 57-60% | **Carbonates** | 17-34% |

Table 1 Quartz equivalent of some minerals (Tj., 1982)

In the case under consideration, this equivalence means that the FYR2 limestones, composed of 100% carbonates, will be as abrasive as a rock composed of 17-34% quartz, while the quartzo-feldspathic sandstones will behave as if they were composed of approximately 90% quartz (Plinninger R.J., 2004).

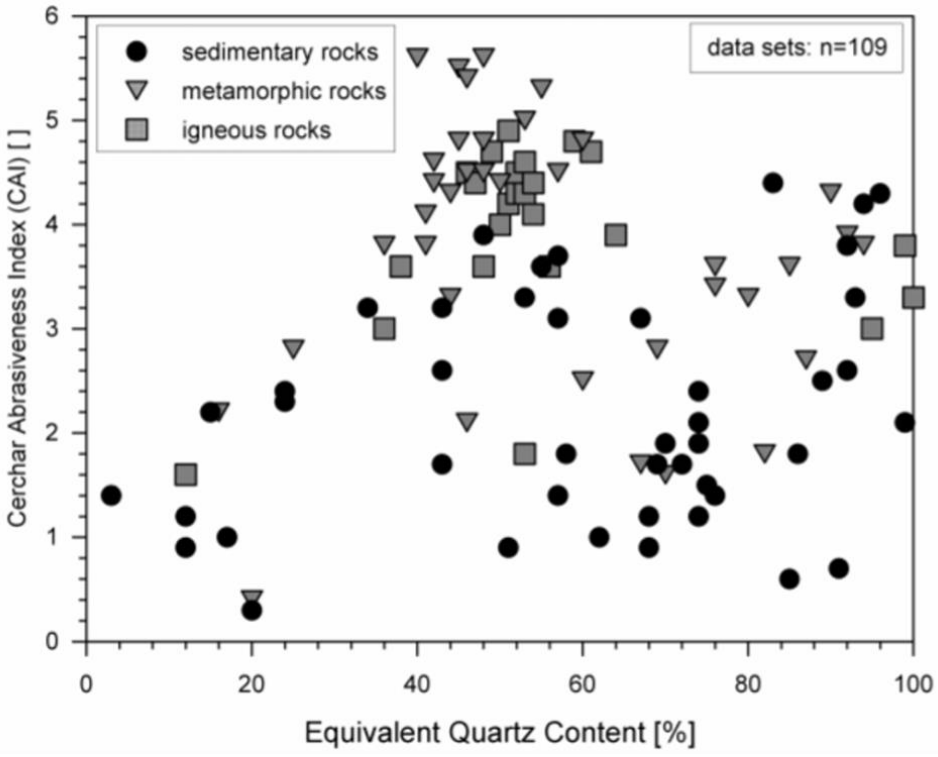


Figure 3.9 Measurements of the CAI index as a function of quartz content and rock origin (Plinninger R.J., 2004)

Based on Figure 3.4 and literature sources (Tj., 1982), it was possible to conclude that the FYR2 lithotype is either slightly or very slightly abrasive, with a CAI index close to 1, whereas the BNA3 lithotype is highly abrasive, with a CAI of approximately 4.

### 3.6.1 Analysis of TBM Performance with the CSM Model

The CSM method was developed in 1977 by Ozdemir (Ozdemir, 1977) at the Colorado School of Mines and later modified by Rostami in 1993 (Rostami, 1993). This approach is widely used to

study the performance of TBMs during excavation operations (Rostami J., 1996). The model aims to calculate the advance and penetration rates by analyzing the normal and tangential forces acting on the excavation tool as it interacts with the rock during the advancement of the cutter head. The theory is based on the analytical description of the physical phenomenon occurring during the excavation process. According to the model, the mechanism consists of the propagation of fractures that develop from a zone of fractured rock formed beneath each cutter, caused by the concentration of stresses (Figure 3.5).

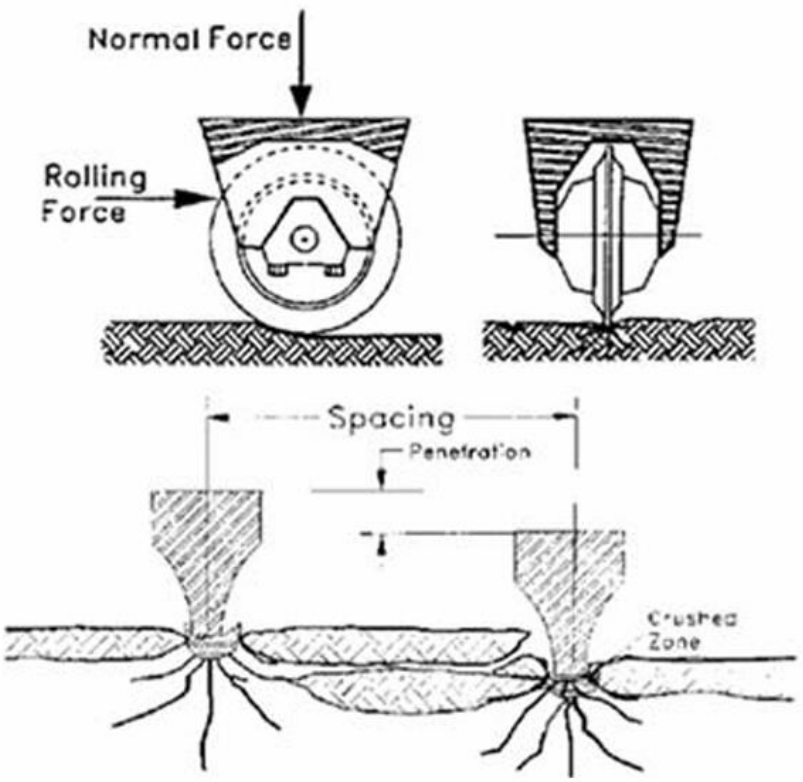


Figure 3.10 Chip's formation (Cigla, M., & Ozdemir, L., 2000)

The efficiency of excavation depends not only on the power of the machine but also on the energy that the tools are able to transfer to the face, based on their geometric characteristics, such as diameter and spacing, as well as the strength of the rock.

By considering the penetration **p** [mm/rev] and the radius of the disc cutter **R**, it is possible to determine a contact angle $\boldsymbol{\varphi}$, which defines the area of rock involved in the tool's action. Knowing the uniaxial compressive strength $\boldsymbol{\sigma_c}$, the tensile strength $\boldsymbol{\sigma_t}$ of the rock, and the thickness of the cutter T, the thrust per tool $\mathbf{F_t}$ can be calculated using the following relation:

$$F_t = 2.12TR\varphi\sqrt[3]{\frac{\sigma_c^2\sigma_t S}{\varphi\sqrt{RT}}} \qquad (3.2)$$

$$\varphi = cos^{-1}\left(\frac{R-p}{R}\right) \qquad (3.3)$$

which can be decomposed into its normal and tangential components $F_N$ and $F_R$ (Figure 3.6).

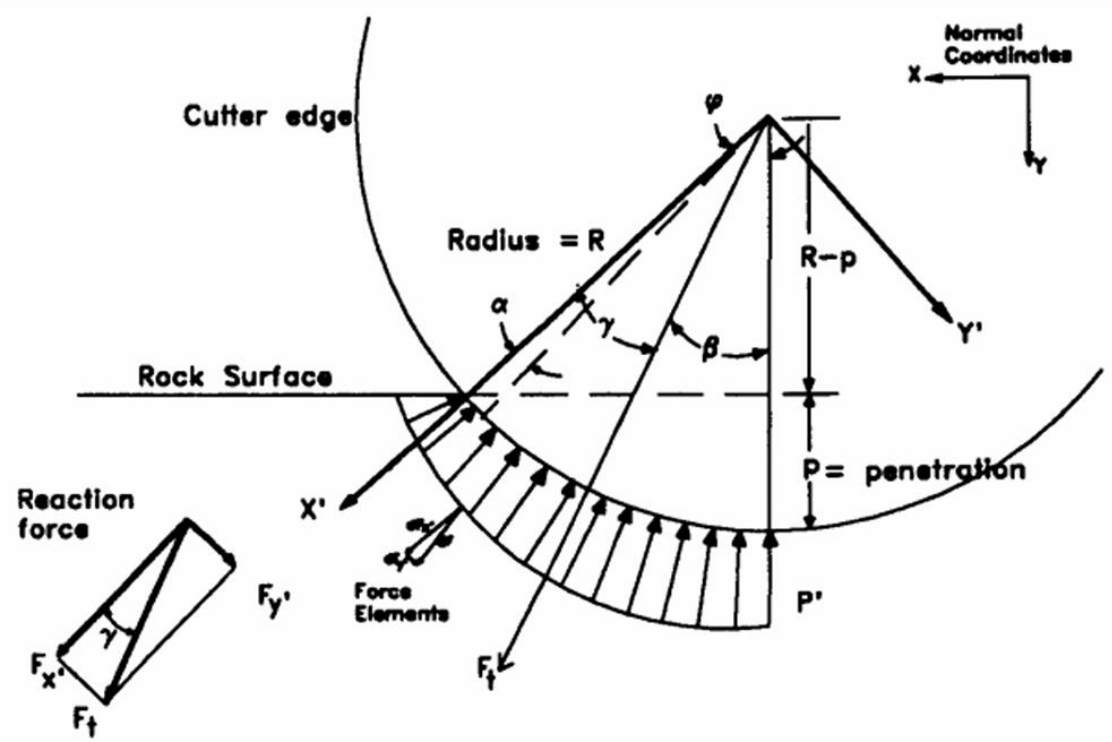


Figure 3.11 General shape of distribution between rock surface and disc cutter (Rostami, 1993)

Knowing the diameter of the TBM, $D_{TBM}$, and the number of discs $n$, it is possible to calculate the total thrust $T_H$, the torque $T_Q$ and the power HP as follows:

$$T_H = n\, F_N \qquad (3.4a)$$

$$T_Q = 0.3\, n\, F_R\, D_{TBM} \qquad (3.4b)$$

$$HP = RPM\, T_Q\, \frac{\pi}{30} \qquad (3.4c)$$

### 3.6.2 Parameters and Estimation of Penetration

The construction details and characteristics of the TBM were provided by the Hirpinia consortium and are listed in Table 2, while the preliminary evaluation was conducted by consultants (GEEG, 2020).

The maximum torque used in the analysis was derived from the following relation, considering the maximum installed power HP.

$$T_{Qmax} = \frac{30 * HP}{\pi * RPM_{max}} \qquad (3.5)$$

| Tunnel | **Grottaminarda** |
|---|---|
| Head Diameter | 12.5 m |
| Cutters | 64 discs of 17'' + 16 gauge disc |
| Average cutters spacing | 90 mm |
| Maximum load per cutter | 250 kN |
| Maximum thrust at the head | 20 MN |

| | |
|---|---|
| Maximum power at the head | 6300 kW |
| Rotational speed | 0 – 3 RPM |
| Maximum torque at the head | 20.1 MNm |
| Nominal/maximum total thrust | 132.1/158.5 MN |
| Nominal/maximum total torque | 48.8/53.7 MN m |

Table 2 Main characteristics of the TBM

The values of maximum penetration in mm/rev for each lithotype resulting from the analyses carried out with the CSM model are listed in Table 3. For each lithotype, the extremes of the compressive strength range were considered.

| Tunnel | **Grottaminarda** | |
|---|---|---|
| Lithotype | FYR2 | |
| $\sigma_c$ [MPa] | 25.0 | 50.0 |
| $\sigma_t$ [MPa] | 3.1 | 6.3 |
| Applied thrust [MN] | 8.8 | 14.5 |
| RPM [rev/min] | 2.0 | 2.0 |
| $\varphi$ | 1.09 | 0.71 |
| Torque [MNm] | 20.1 | 20.1 |
| $i_0$ [mm/rev] | 115.7 | 51.6 |
| S/p | 0.8 | 1.7 |
| CC [%] | 60 | 36 |

Table 3 Maximum theoretical penetrations estimated according to the CSM method

Although these values derive from a theoretical calculation, they are well beyond the ideal range of the S/p ratio between the spacing of the discs and penetration, which should be between 10 and 20 for different lithotypes. Significantly higher values result in insufficient rock fragmentation under the disc, preventing chip formation as expected by the CSM method. On the other hand, values that are too low (like in our case, 1-2, as shown in Table 3) lead to excessive fragmentation. For this reason, it was decided to determine the S/p value that optimizes the energy required to excavate a unit volume of rock.

It is concluded that optimal penetrations can be achieved using the designed TBMs, but at capacities lower than maximum. Table 4 presents an evaluation of the operational parameters required to achieve optimal penetration, taking into account an average compressive strength within the indicated range and with S/p values of 5 and 7.5, lower than the value of 10 predicted for the indicated $\sigma_c$ values.

| Tunnel | **Grottaminarda** | |
|---|---|---|
| Lithotype | FYR2 | |
| $\sigma_c$ [MPa] | 37.5 | |
| $\sigma_t$ [MPa] | 4.7 | |
| S/p | 5.0 | 7.5 |
| $i_0$ [mm/rev] | 18.0 | 12.0 |
| $\varphi$ | 0.41 | 0.33 |
| RPM [rev/min] | 2.0 | 2.0 |
| Applied thrust [MN] | 7.9 | 7.0 |
| Torque [MNm] | 6.2 | 4.4 |
| $i_0$ [mm/min] | 36.0 | 24.0 |

| | | |
|---|---|---|
| $i_0$ [m/h] | 2.2 | 1.4 |
| CC | 21 | 17 |

Table 4 Performance evaluated according to the CSM method

It follows that with the characteristics of the TBM designed for the Grottaminarda tunnel, it is possible to achieve penetration values between 12 and 18 mm/rev in FYR2 limestones with a thrust of about 7-8 MN and a torque of 4.4-6 MNm, corresponding to about 35-40% and 20-30% of the maximum available values, respectively.

### 3.6.3 Cutters wear

The average lifespan of the cutters for each lithotype in terms of volume excavated per cutter has been estimated to obtain values as plausible as possible based on the available characterization.

A widely used method for estimating the lifespan of excavation tools was proposed by NTNU and is based on empirical correlations between on-site consumption data and laboratory test results performed on the same rocks. The parameter to estimate is the useful life of the discs, expressed in hours per cutter (cutter ring life), and denoted by $\mathbf{H_h}$, obtained from the following relationship::

$$H_h = \frac{(H_0 k_D k_Q k_{RPM} k_n)}{N_{TBM}} \quad (3.6)$$

where $H_0$ is the basic cutter ring life [h/c] and is obtained from a specific chart as a function of the CLI index and the disc diameter, while $k_D$ , $k_Q$ , $k_{RPM}$, $k_N$ are correction coefficients that account for the TBM diameter, quartz content, rotation speed, and the number of cutters, respectively (Bruland, 1998).
In the model, the distance traveled by a cutter on a given lithotype is constant, regardless of the rotation speed (RPM). Therefore, the consumption in terms of hours is inversely proportional to the rotation speed, with the corresponding correction coefficient $k_{RPM}$. The coefficient $k_Q$ onsiders the effect of the presence of quartz or other abrasive minerals in the rock, while the other coefficients stem from geometric considerations regarding the arrangement and number of discs on the cutterhead. Starting from $H_h$, cutter consumption can be estimated in terms of distance traveled $H_m$, by multiplying by the advance rate $i_0$ [m/h] and in terms of volume excavated per cutter $H_m^3$, by multiplying $H_m$ by the excavation cross-sectional area.

Table 5 presents the estimated consumption values, considering the abrasivity parameters already examined, the machine parameters, and the advance rates indicated in Table 4.

| Tunnel | **Grottaminarda** | |
|---|---|---|
| Lithotype | FYR2 | |
| $\sigma_c$ [MPa] | 37.5 | |
| Quarts content | 25.0 | |
| CLI | 78.0 | |
| $H_h$ [h/cutter] | 5.9 | |
| $H_m$ [m/cutter] | 13 | 8 |
| $H_m^3$ [m$^3$/cutter] | 1552 | 1035 |

Table 5 Cutters consumption estimated using the NTNU method

In summary, the performance analysis carried out using the CSM model has shown that optimal penetrations can be achieved in the expected rock sections, with values around 20 mm/rev, using operational parameters lower than the maximum available. For the Grottaminarda tunnel, thrust values equal to 40% of the maximum thrust at the cutterhead and torque equal to 30% of the maximum torque at the cutterhead are sufficient.
For the prediction of cutter consumption, the $H_m^3$ values calculated in this way range from 1000 to 1500 m³/cutter. The evaluation only refers to wear consumption and does not take into account other causes of cutter failure (such as clogging) that may occur in other sections of the alignment.

# 4. Monitoring

Mechanized tunneling is one of the most advanced and widely used techniques in civil and mining engineering, particularly for the construction of tunnels for infrastructures such as railways, subways, highways, and underground conduits. The complexity of these excavations requires continuous and accurate monitoring to ensure that the work progresses without compromising the stability of the surrounding structures, the safety of the workers, and the efficiency of the process.

The monitoring system has been designed to provide, in the most complete and rapid way possible, all the elements necessary to perform an analysis of the interaction between the ongoing work and the surrounding volumes of soil. The aim is to define any corrective actions (intensification of measures, installation of additional equipment, changes to the execution phases, etc.) aimed at preventing the occurrence of hazardous situations.

Its organization involves the use of equipment arranged to form monitoring sections distributed along the entire tunnel route. This distribution is defined based on the surrounding conditions along the alignment, such as the geomechanical characteristics of the soil, the position relative to the tunnel itself, the presence of anthropic interference, and so on, while the reading frequency is mainly related to the sequence of working phases.

Monitored aspects include the thrust and torque applied, cutter penetration, energy consumption, changes in ground pressure, and the integrity of existing structures. The analysis of data collected through advanced technologies such as sensors, GPS, real-time monitoring systems, and geotechnical modeling allows for optimizing progress, preventing operational issues, and making timely decisions in case of anomalies. In this context, the monitoring approach develops based on both theoretical and practical methods that, combined with the use of specialized software, allow for the analysis and interpretation of data for effective control and safe project management.

## 4.1 Monitoring system

In addition to recording the operational parameters of the TBM and the investigations that can be conducted during excavation from inside the TBM, the designers have planned the installation of an instrumental monitoring system capable of evaluating the behavior of the lining rings made of precast segments.

The instrumentation provided is for monitoring the following parameters:

- Deformations of the in-situ lining, made of precast segments, assessing any phenomena of convergence or ovalization of the laid rings;
- The stress state of the in-situ linings.

For this purpose, the following equipment has been planned:

- Convergence stations in the tunnel, consisting of 5 optical targets (Figure 4.1);
- Stress measurement stations, by installing 8 pairs of strain gauges welded to the reinforcements and 2 load cells positioned at the longitudinal joint of the segments (Figure 4.2).

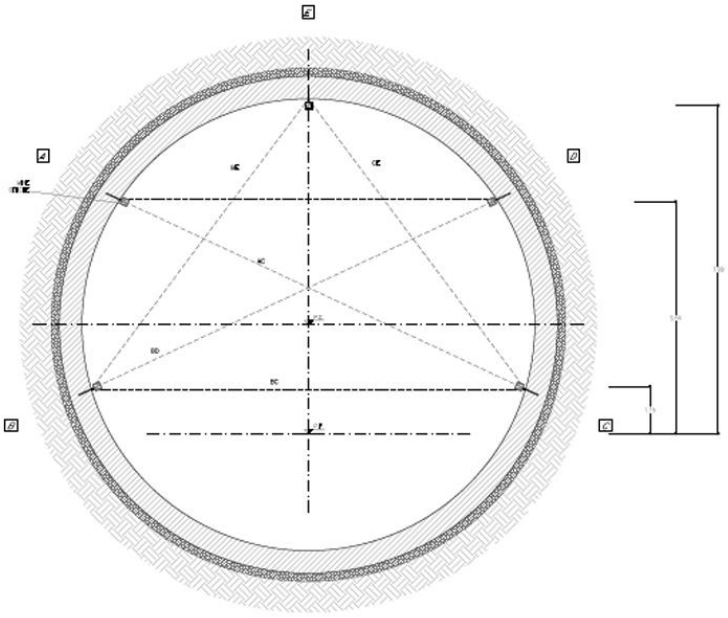

Figure 4.1 Example of a convergence measurement station (Monitoraggio, 2020)

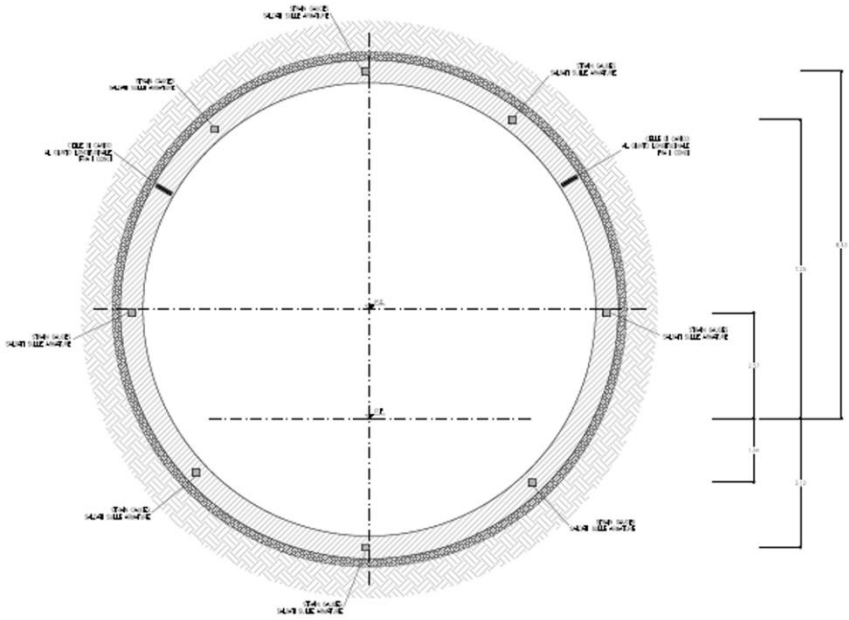

Figure 4.2 Example of a stress state measurement station (Monitoraggio, 2020)

It is considered that the instrumentation can still be useful even if not installed directly at the tunnel face, in order to assess any ovalizations of the reference system, particularly in the sections of pushing ground.

It is planned to install convergence measurement stations every approximately 150 meters, except in the section corresponding to the landslide phenomenon. For the measurement of the stress state, 8 monitoring stations for the lining are planned (Monitoraggio, 2020).

## 4.2 Monitoring instrumentation

The key characteristics of some of the main instruments are described below, specifying that the reading frequency will be subject to adjustments due to the backup equipment available in the tunnel.

### 4.2.1 Optical survey targets

The displacement measurement stations will be equipped with topographic displacement meters in order to compare site deformations and expected displacements (Figure 4.3).

Optical base measurement stations will be installed (with equipment placed on the crown and on the sidewalls, protruding by about 10 cm), with the frequency specified in the previous paragraph.

The execution and reporting of the convergence measurements will require the involvement of an experienced surveyor and an assistant. For the measurement of convergences, optical targets and total stations will be used.

The instruments will be selected to ensure accuracy consistent with the thresholds for attention and alarm.

Figure 4.3 Example of an optical survey target (Sisgeo)

The data collected in this way will be transferred via an interface to a computer on which software will be installed, capable of performing analysis, processing, and displaying the data through a graphical visualization.

### 4.2.2 Strain gauges

Deformation is measured along the maximum length direction of the instrument, through the frequency variations induced in the vibrating wire sensor (Figure 4.4). The instruments will be chosen to ensure accuracy consistent with any attention and alarm thresholds.

Starting from the measured deformation, it will then be possible to indirectly determine the stress state. Specifically, the stress state can be derived with reference to Hooke's Law $\sigma = E \cdot \varepsilon$, where:

- $\sigma$ : stress state in [MPa] in the concrete or steel fiber;
- E : elastic modulus of concrete (se $\varepsilon < 0$) or steel (se $\varepsilon > 0$) in [MPa] ;
- $\varepsilon$ : deformation of the strain gauge.

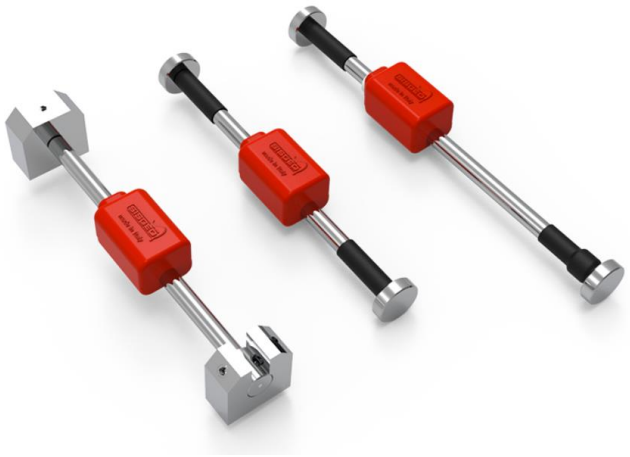

Figure 4.4 Example of a vibrating wire strain gauges (Sisgeo)

The measured data will then be presented in the form of tables and diagrams showing the variation of deformation with respect to time and temperature..

### 4.2.3 Load cells

The typical load cell consists of a stainless steel body sensitized by a series of strain gauges applied to the internal surface of the body and isolated. A steel plate allows for the uniform distribution of the load across the entire body of the cell (Figure 4.5).
The deformation induced by the load on the cell is detected by the strain gauges and converted into an electrical signal proportional to the applied load. The instruments will be selected to ensure accuracy consistent with any attention and alarm thresholds.

Figure 4.5 Example of a load cell (Sisgeo)

The data will then be presented in tabular form and in diagrams showing the variation of the load with respect to time and temperature.

### 4.2.4 Casagrande piezometer “PZ”

Piezometric monitoring will be carried out using Casagrande-type piezometers, which allow for the measurement of the piezometric surface depth using a special electric probe (phreatimeter) equipped with a graduated cable. This is done by inserting the piezometer, consisting of a cylindrical filter connected to two rigid PVC tubes for connection to the surface, into a borehole (Figure 4.6).

The phreatimeter is a device consisting of a cable mounted on a reel housing the signaling circuit and the battery, making it easily portable. The probe tip, mounted at the lower end of the cable, closes a circuit when it contacts the water, activating both a sound and visual signal. The position at which these alarm signals are triggered corresponds to the water level, which can be directly read on the graduated cable (Monitoraggio, 2020).

Figure 4.6 Casagrande piezometers (Sisgeo)


Figure 4.7 Open tube piezometers (Sisgeo)

The data will be presented in tabular form and diagrams referring to the variation of the water table with respect to time.

### 4.2.5 TPC (Tunneling Process Control) Software

For the fleet of TBMs used by the company (Webuild), the choice was made to use the Tunnelling Process Control (TPC) software by Tunnelsoft (Tunnelsoft), an advanced solution designed to support the tunneling industry in managing and visualizing data. It offers a wide range of features to monitor and optimize mechanized tunneling processes, ensuring complete and real-time control of operations.

The main features of the TPC are:

- Real-time monitoring: TPC provides a detailed overview of tunneling operations, including data on the position of the TBM (Tunnel Boring Machine), key performance indicators (KPIs), alert messages, and geotechnical information. This information is accessible at any time and from any location, enabling timely and informed decision-making. (Tunnelsoft)

- Advanced analysis and reporting: The software enables the creation of customized reports, statistical analyses, and tool consumption monitoring, contributing to efficient cost and resource management. The special report feature allows the generation of tailored reports based on data from various sources, facilitating documentation and information sharing. (Tunnelsoft)

- Integration with mobile devices: With the TPC Mobile application, users can access project data directly from their mobile devices, improving flexibility and responsiveness on the field. The app offers features such as real-time overview visualization, shift reporting, and sensor monitoring, ensuring a continuous and uninterrupted workflow. (Tunnelsoft)

- Segment lifecycle management: TPC Segment Tracker allows for easy tracking of segments throughout their lifecycle, from production to installation, ensuring effective quality management and complete documentation. This tool facilitates tunnel inspection, recording of damages and repairs, and management of tool inventories, contributing to preventive maintenance and reducing operational costs. (Tunnelsoft)

Below are some screenshots captured from the software.

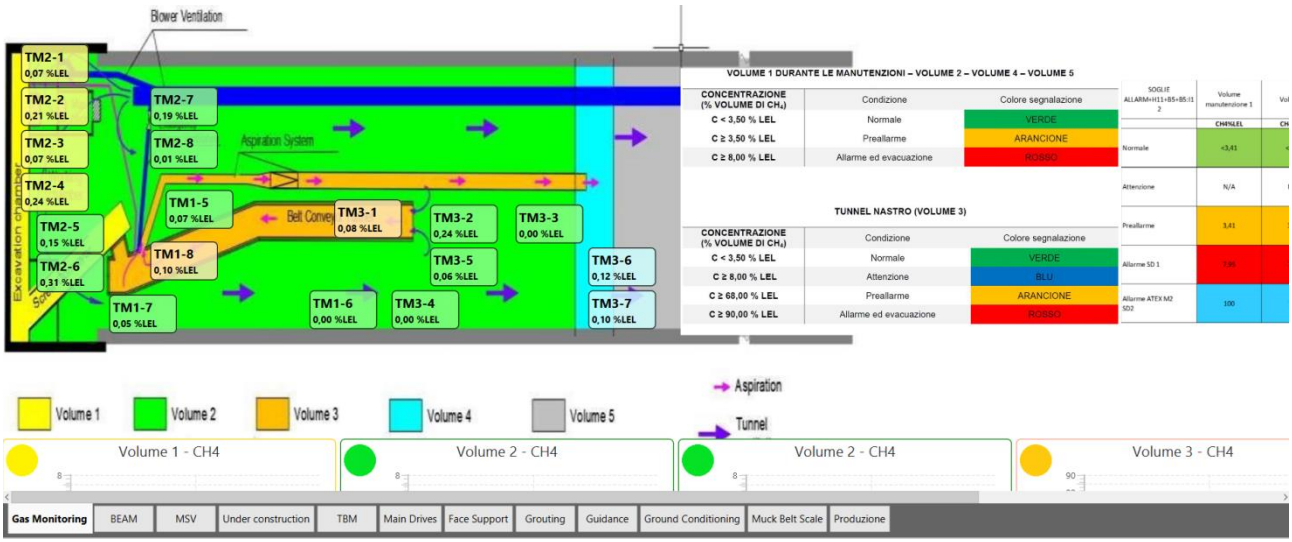


Figure 4.8 Example of TPC's Gas Monitoring layout (Tunnelsoft)

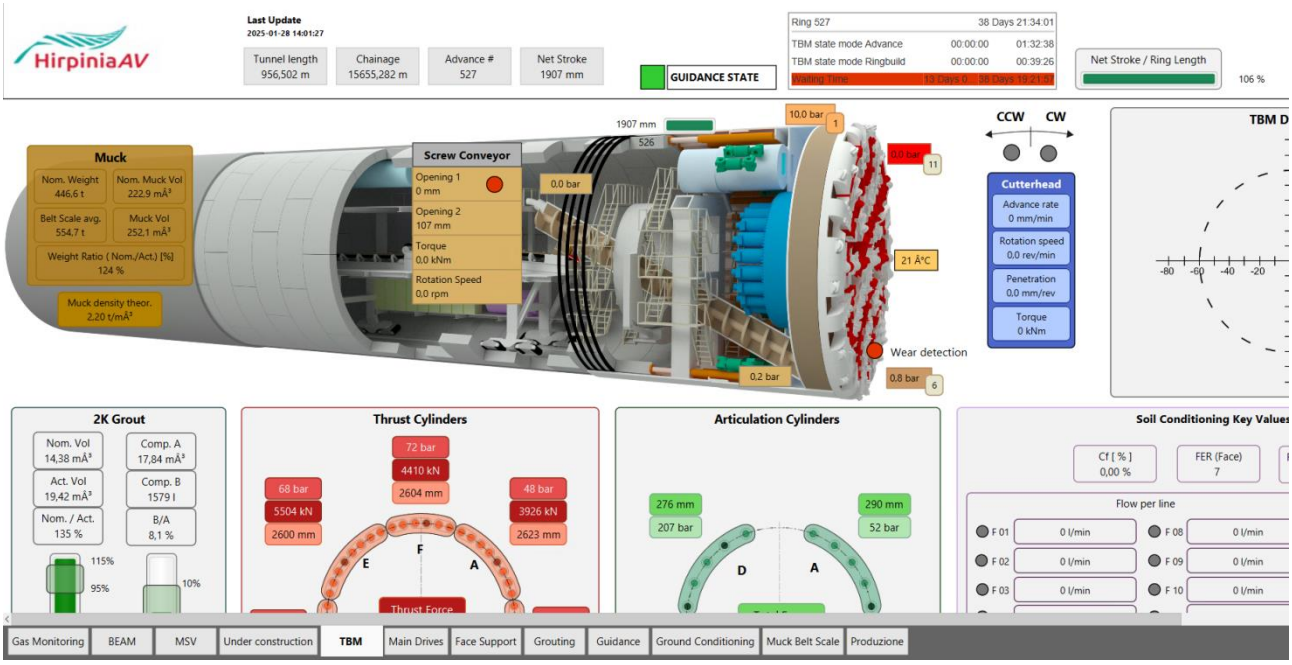


Figure 4.9 Example of TPC's TBM General view layout (Tunnelsoft)

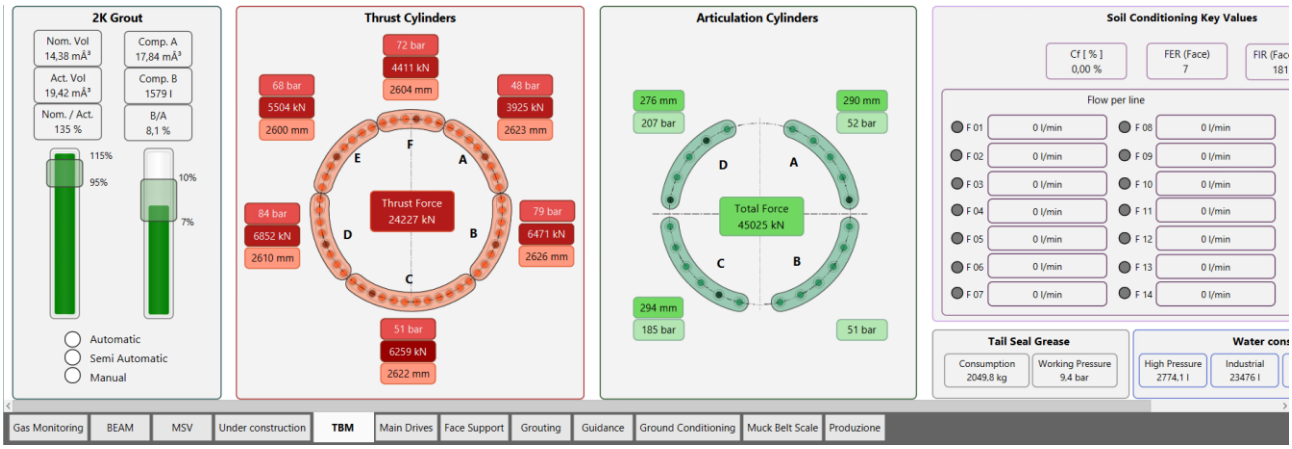


Figure 4.10 Example of TPC's TBM Grout, Thrust and Articulation Cylinder layout (Tunnelsoft)

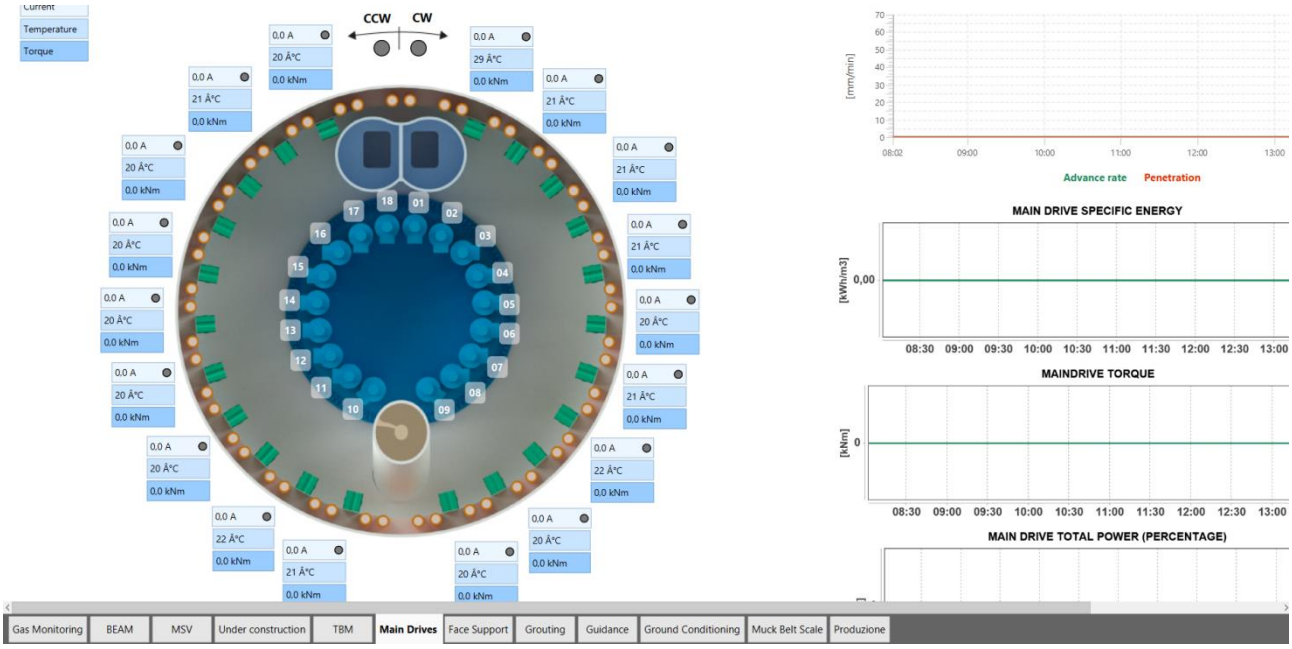


Figure 4.11 Example of TPC's TBM Main Drive layout (Tunnelsoft)

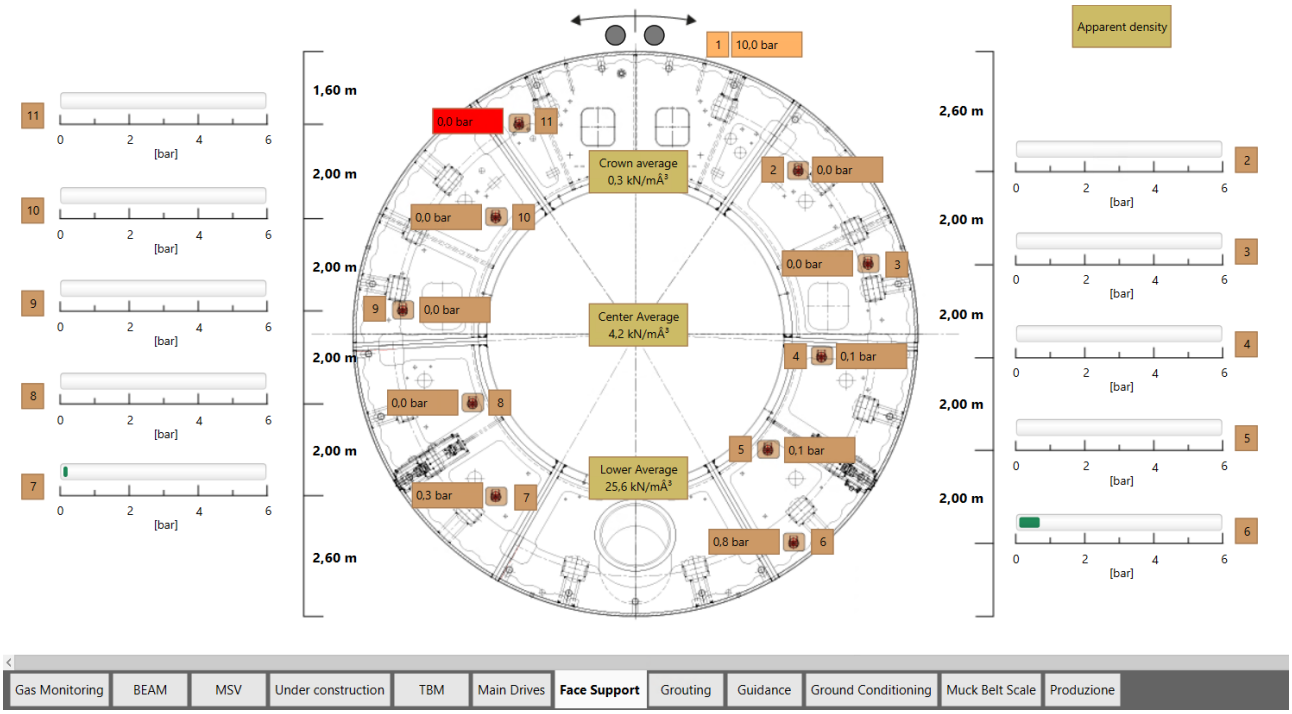


Figure 4.12 Example of TPC's TBM Face Support layout (Tunnelsoft)

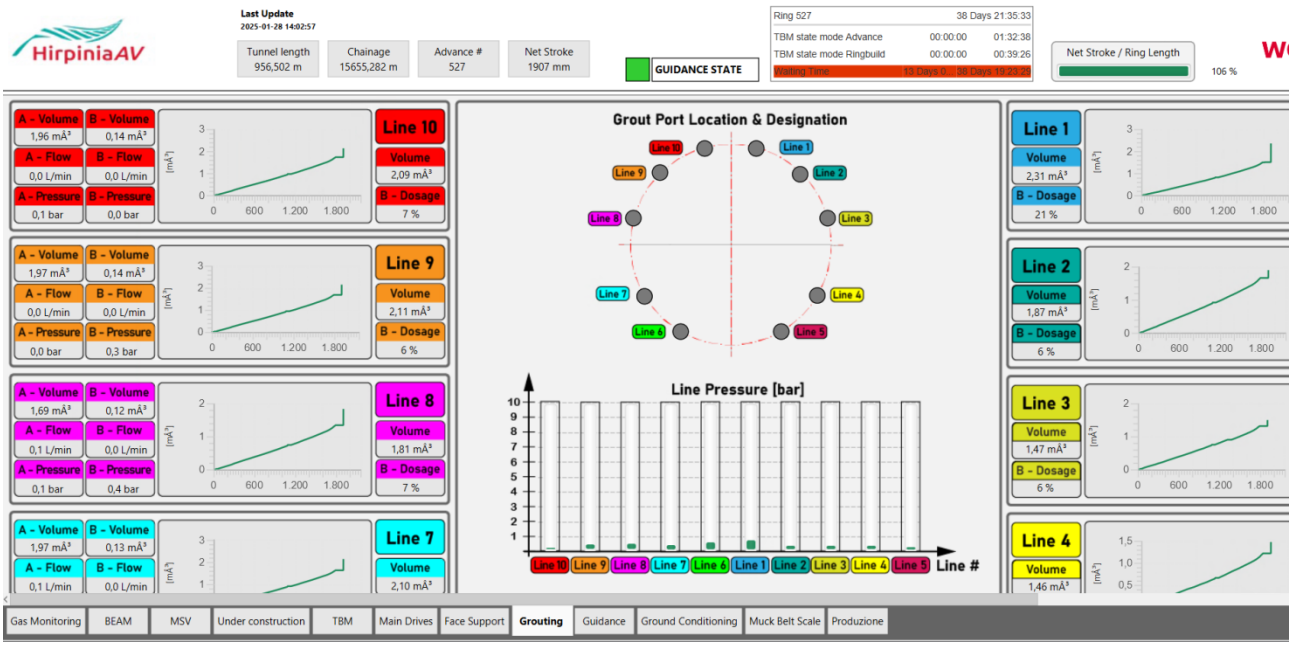


Figure 4.13 Example of TPC's TBM Grouting injection lines layout (Tunnelsoft)

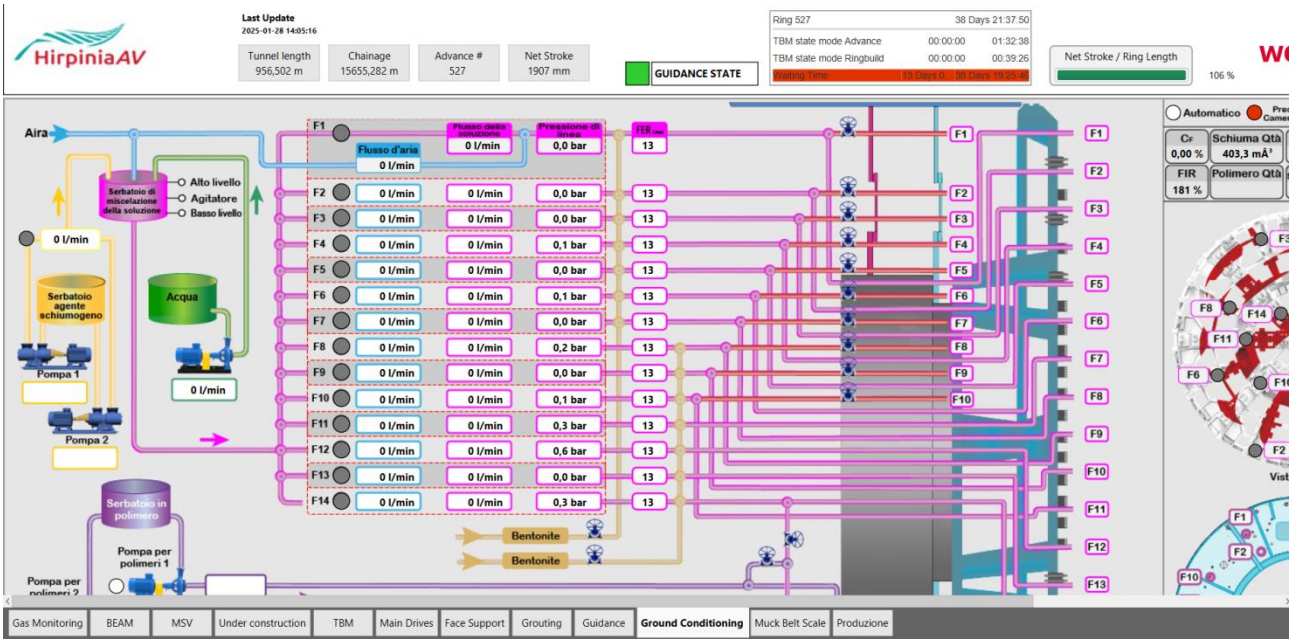


Figure 4.14 Example of TPC's Soil Conditioning layout (Tunnelsoft)

Particular mention should be made of the BEAM-Scan system (Bore-tunnelling Electrical Ahead Monitoring), a geophysical prediction technology that allows real-time monitoring of ground conditions and the presence of water ahead of the tunnel face, simultaneously with the excavation. Is a non-intrusive focused-electrical induced polarisation ground prediction technique especially designed for the underground construction industry.
The TBM based BEAM system allows a permanent driving accompanying exploration of ground conditions about 3 times the tunnel diameter ahead of the face. Data acquisition and evaluation is performed automatically and prediction results are displayed in real time enabling fast on-site decisions (Figure 4.15).

An advantageous feature of the system is the utilization of excavation tools and safety constructional components as electrodes, which are automatically electrical coupled to the ground by the TBM itself.
Because of using voltages lower a continuous operation is possible without any danger for staff and machine.


Figure 4.15 Example of customized matrix for ground classification, water-inflow indication and risk assesment (Tunnelsoft)

In summary, Tunnelsoft's TPC is a comprehensive and flexible solution for managing tunneling projects, offering advanced tools for monitoring, analysis, and documentation of operations, with the aim of increasing efficiency, reducing costs, and ensuring quality at every stage of the project.

## 4.3 Definition of threshold values

For the threshold value of tension in the prefabricated segments, a value of 15 MPa has been set (control value for the compression rate, as per current regulations), considering that concrete of class C35/45 is used.
The expected convergence values are negligible; however, a threshold of attention is set at the achievement of radial displacement values of 5 mm, with an alarm threshold of 10 mm (Monitoraggio, 2020).

### 4.3.1 P.A.T. (TBM Advancement Protocol)

The threshold values described so far (Sections 3.6 and 4.3) define the P.A.T. (TBM Advancement Protocol), which is a crucial tool in the management and planning of tunnel construction, used to monitor and optimize the progress of work throughout all phases of the project.

The progress program establishes the work plan for the tunnel, defining the timelines, the amount of work to be completed, the required resources, and the operational procedures. It plans the advance rate of excavation operations, taking into account the geotechnical characteristics of the ground and any potential challenges that may arise along the route. The P.A.T. consists of various phases, including site preparation, the construction of temporary works, actual excavation, installation of the final lining, and tunnel completion.

A fundamental aspect of the P.A.T. is the continuous monitoring of tunnel progress. Thanks to advanced measurement tools, such as piezometers and inclinometers, it is possible to monitor the ground conditions in real time, such as any subsidence or water infiltration, and adjust ongoing operations to avoid delays or risks. The program also includes risk management related to unforeseen situations, such as ground settlement or water infiltration, providing emergency protocols to ensure the safety of the construction site and the integrity of the structure.

In addition to ensuring safety, the P.A.T. focuses on optimizing resources, such as machinery, materials, and personnel. The choice of the most suitable technologies and equipment for the type of terrain, such as the use of TBMs (Tunnel Boring Machines), is essential to improve efficiency and reduce costs. The plan must also monitor the time and costs of operations, ensuring that the project meets delivery deadlines and the budget.

The P.A.T. often relies on specific software for project management (such as TPC, Section 4.2.5), which allows for real-time planning and updates, taking into account any unforeseen events. These management tools help optimize scheduling and ensure that all phases are properly followed. The ability to integrate different disciplines, such as geology, geotechnical engineering, and safety, is crucial for the success of the P.A.T., as every aspect of the project must be monitored and coordinated to avoid misunderstandings and inefficiencies.

The benefits of the P.A.T. are evident in terms of predictability, safety, and cost control. A well-structured program helps reduce the risks of delays and optimize resource usage, while maintaining a high level of safety. Constantly monitoring ground conditions and potential issues that may arise enables timely intervention, preventing damage and difficulties. Furthermore, controlling the advance times and costs ensures that the project stays within the planned limits, increasing efficiency and reducing waste.

# 5. Excavation analysis

In this chapter, I list a series of data and information extracted from the TPC monitoring software (presented in the previous chapter), which is directly connected to the TBM 978 during its various advancement phases. The data analysis focuses on a time frame from March 19, 2024, to August 2, 2024 (from the installation of ring 552 to ring 1052), as it is more fruitful in terms of continuous tunneling and, therefore, data.

Each graph was generated by the software and used to compile a daily excavation report. The various daily reports for the analyzed time period are divided into nine periods, which are:

| Time period | Associated P.A.T. | N° of rings installed |
|---|---|---|
| From March 19th to May 10th | 3 | 552-613 |
| From May 10th to May 17th | 3 | 614-669 |
| From May 17th to May 31st | 3-4 | 670-730 |
| From May 31st to June 9th | 4 | 731-798 |
| From June 9th to June 20th | 4 | 799-44 |
| From June 21st to July 4th | 4-5 | 845-923 |
| From July 5th to July 15th | 5 | 924-972 |
| From July 15th to July 24th | 5 | 973-1009 |
| From July 24th to August 2nd | 5 | 1010-1052 |

Table 6 Nine time ranges analyzed

Each value and threshold of the P.A.T. will be listed later; in the meantime, it is important to clarify that:

- Il P.A.T. 3 From pk 3+716.097 to 3+949.06;
- Il P.A.T. 4 From pk 3+716.097 to 3+949.06;
- Il P.A.T. 5 From pk 3+716.097 to 3+949.06.

Below is a simplified diagram showing the position of the 11 pressure sensors present in the TBM's excavation chamber, from which it can be inferred whether the thrust applied by the machine complies with the protocol set by the P.A.T.

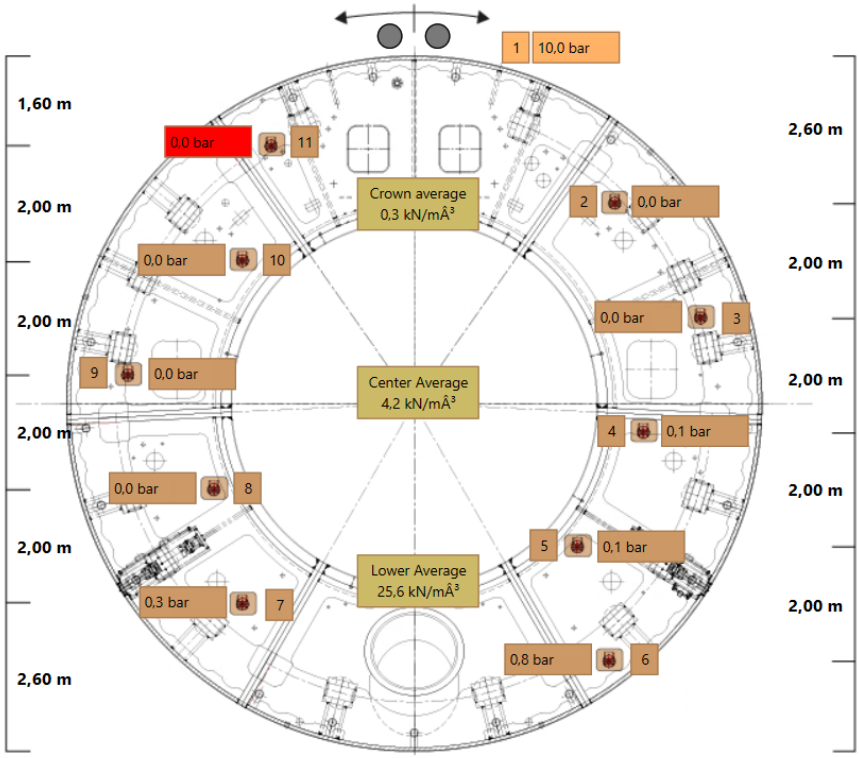


Figure 5.1 Position of ground pressure sensors in the excavation chamber (Tunnelsoft)

The following will specifically refer to sensor 11 (TY11).

## 5.1 From March 19th to May 10th (rings installed 552-613)

The excavation progress reports fall within the section covered by P.A.T. No. 3 (the design pressures are listed in Table 7). Excavation stopped on March 19 at pk 3+718.73 to inspect the cutter head conditions and restore its functionality. Excavation then resumed on May 1.

| Omog. Segments Geom. | segment number | starting pk (m) | final pk (m) | Lenght L (m) | L total (m) | $p_f$ (bar) | $p_{f,c}$ (bar) | ATTENTION (bar) | | ALARM (bar) | |
|---|---|---|---|---|---|---|---|---|---|---|---|
| | | | | | | | | MIN | MAX | MIN | MAX |
| FYRavc | 6 | 3413.2 | 3450 | 36.80 | 535.86 | 3 | 2.3 | 2.1 | 2.8 | 1.8 | 3.0 |
| | | 3450 | 3475 | 25 | | 3.3 | 2.6 | 2.3 | 3.1 | 2.1 | 3.4 |
| | | 3475 | 3600 | 125 | | 3.5 | 2.8 | 2.5 | 3.4 | 2.2 | 3.6 |
| | | 3600 | 3625 | 25 | | 3.3 | 2.6 | 2.3 | 3.1 | 2.1 | 3.4 |
| | | 3625 | 3700 | 75 | | 3 | 2.3 | 2.1 | 2.8 | 1.8 | 3.0 |
| | | 3700 | 3725 | 25 | | 2.8 | 2.1 | 1.9 | 2.5 | 1.7 | 2.7 |
| | | 3725 | 3867.37 | 142.37 | | 2.5 | 1.8 | 1.6 | 2.2 | 1.4 | 2.3 |
| FYRagms | 7 | 3867.37 | 3935.93 | 68.56 | | 2.2 | 1.5 | 1.4 | 1.8 | 1.2 | 2.0 |
| FYRmar+FYRar | 8 | 3935.93 | 3949.06 | 13.13 | | 2.2 | 1.5 | 1.4 | 1.8 | 1.2 | 2.0 |

Table 7 P.A.T. n°3

Where $\mathbf{p_f}$ refers to the average pressure at the excavation face, while $\mathbf{p_{f,c}}$ refers to the average pressure at the crown of the excavation face (sensor TY11, Figure 5.2).

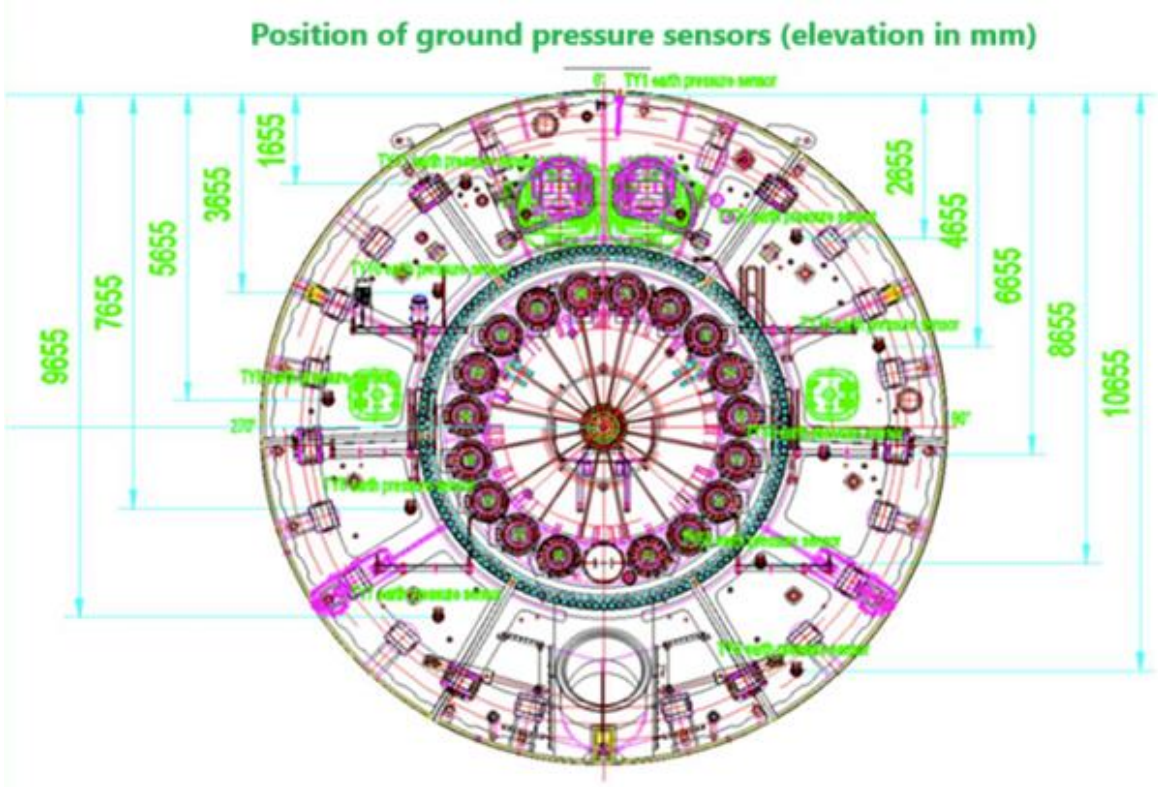


Figure 5.2 Position of ground pressure sensors in the excavation chamber (TY11 sensor at 1655 mm from the crown of the excavation chamber) (Report, 2024)

The graph in Figure 5.3 shows the pressure $\mathbf{p_{f,c}}$ as a function of the ring number, while Table 8 presents the average value of $\mathbf{p_{f,c}}$ for each section, based on the progress. The blue and green dashed lines indicate that the decompression of the face during ring installation is minimal.

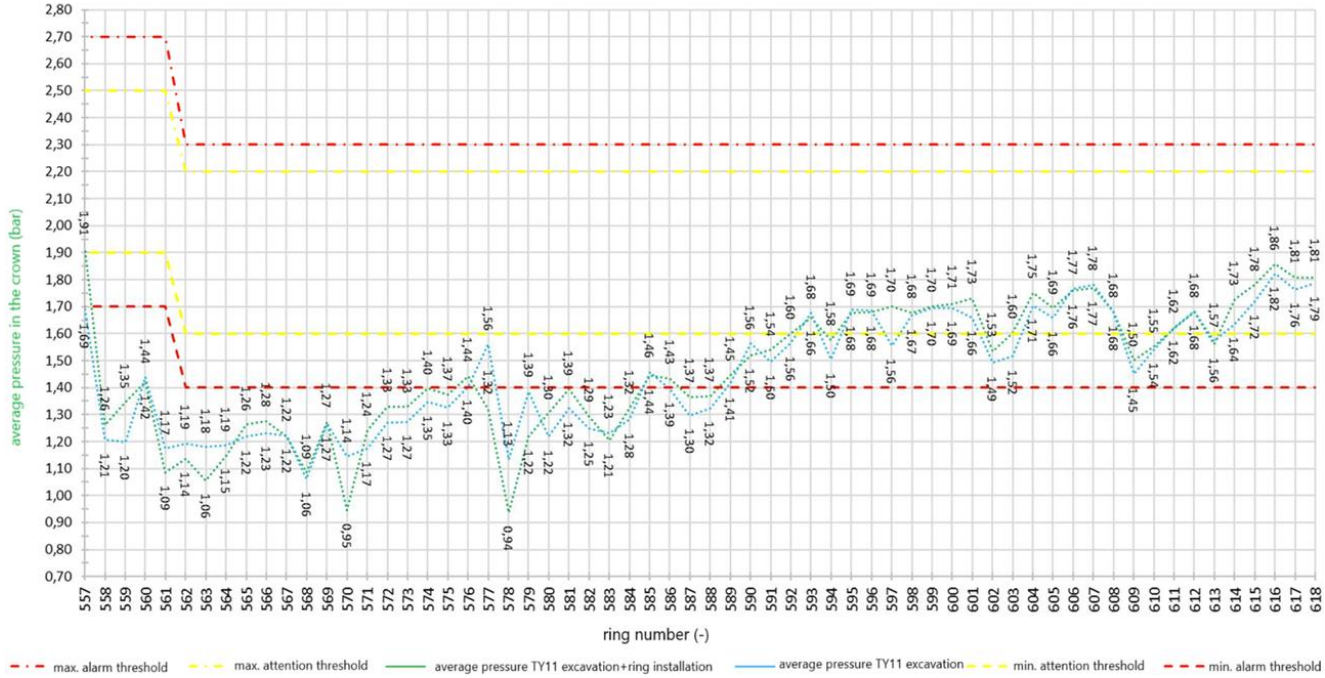


Figure 5.3 Average pressure in the crown during excavation and at the completion of the ring installation (TY11 sensor) (Report, 2024)

| Omog. Segments Geom. | segment number | starting pk (m) | final pk (m) | Lenght L (m) | L total (m) | $p_f$ (bar) | $p_{f,c}$ (bar) | ATTENTION (bar) | | ALARM (bar) | | average pressure of $p_{f,c}$ per segment (bar) | |
|---|---|---|---|---|---|---|---|---|---|---|---|---|---|
| | | | | | | | | MIN | MAX | MIN | MAX | excavation | excavation + ring installation |
| FYRavc | 6 | 3716 | 3725 | 9 | 112 | 2.8 | 2.1 | 1.9 | 2.5 | 1.7 | 2.7 | 1.34 | 1.41 |
| | | 3725 | 3828 | 103 | | 2.5 | 1.8 | 1.6 | 2.2 | 1.4 | 2.3 | 1.46 | 1.47 |

Table 8 Average pressure in the crown during excavation and at the completion of the ring installation (TY11 sensor) (Report, 2024)

The aforementioned $\mathbf{p_{f,c}}$ values, although below the minimum alarm threshold of 1.7 bar, did not have any negative impact on the stability of the face and the tunnel. This should indicate a generally more stable excavation face than initially anticipated.

### 5.1.1 Injection volume and pressure

The TBM 978 has 10 injection lines, arranged as shown in Figure 5.4.

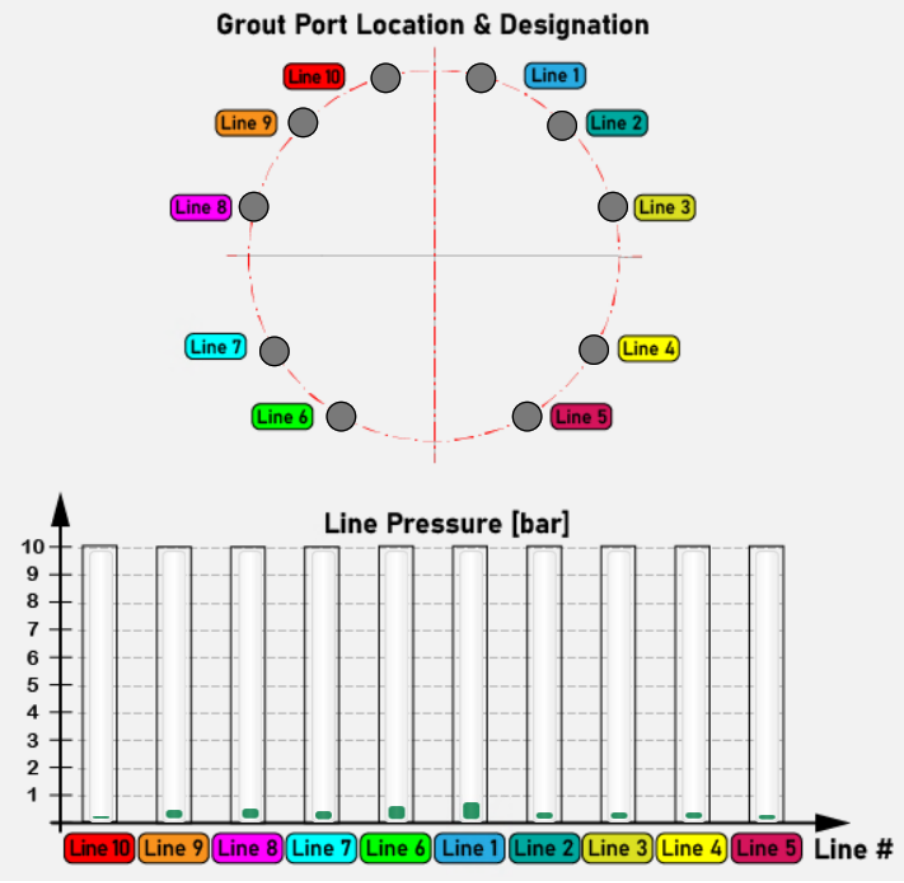


Figure 5.4 Position of the two-component injection lines (Tunnelsoft)

For the calculation of the volumes of two-component grout to be injected from each individual line, the following proportion was used, valid for lines at the same elevation (as an example, the one for lines 1 and 10 is provided):

$$V_{\#1,\#10} = \frac{arch_{\#1,\#10}}{2\pi R_{shield}} \cdot V_{ring} \qquad (5.1)$$

$$V = \sum_{\#1}^{\#10} V_{\#i} \qquad (5.2)$$

The same proportions were used to calculate the minimum volume of 10.74 m³ in the case of contact between the ground and the tail shield.

For the alert and alarm thresholds of the volume corresponding to line #i, to be filled with the two-component grout, the procedure followed was the same as for the total mix volume per ring:

$$V_{\#i,min.alert} = 0{,}9 \cdot V_{\#i;} \qquad (5.3a)$$

$$V_{\#i,max.alert} = 1{,}1 \cdot V_{\#i;} \qquad (5.3b)$$

$$V_{\#i,min.alarm} = 0{,}8 \cdot V_{\#i;} \qquad (5.3c)$$

$$V_{\#i,max.alarm} = 1{,}2 \cdot V_{\#i;} \qquad (5.3d)$$

The graph in Figure 5.5 shows the injection volume of the two-component grout, while Table 9 presents the average volume value **V** for each section.

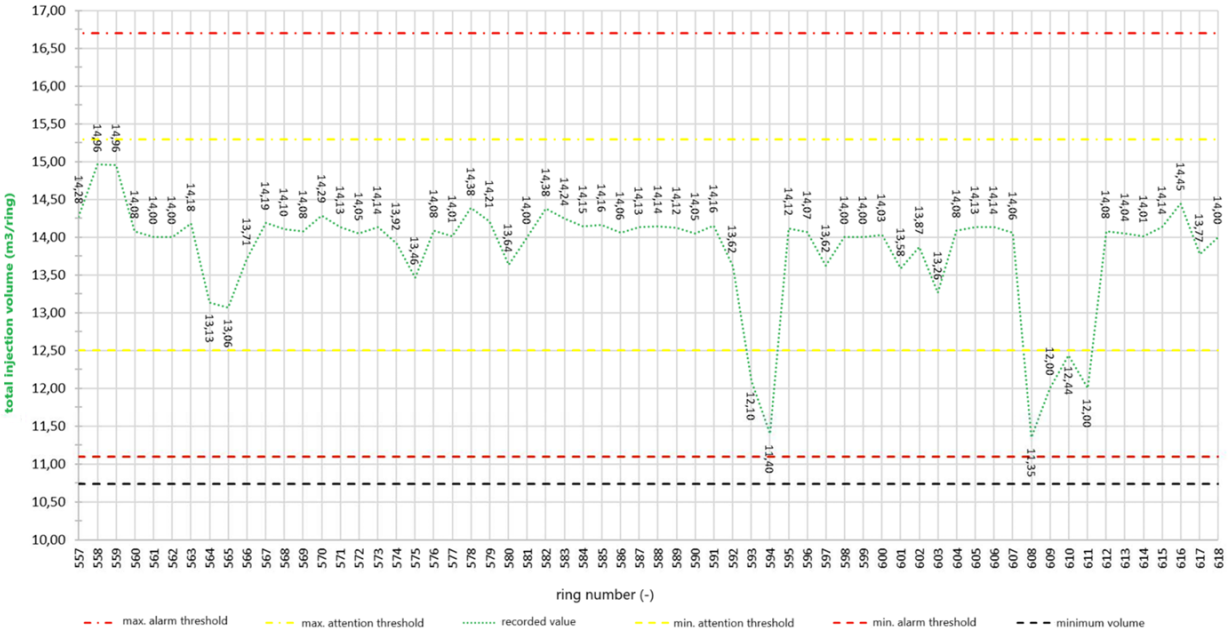


Figure 5.5 Total injection volume of the two-component mixture in m³/ring (Report, 2024)

| Omog. Segments Geom. | segment number | starting pk (m) | final pk (m) | Lenght L (m) | L total (m) | V ($m^3$/ring) | ATTENTION ($m^3$/ring) | | ALARM ($m^3$/ring) | | average V per segment ($m^3$/ring) |
|---|---|---|---|---|---|---|---|---|---|---|---|
| | | | | | | | MIN | MAX | MIN | MAX | |
| FYRavc | 6 | 3716 | 3725 | 9 | 112 | 13.91 | 12.5 | 15.3 | 11.1 | 16.7 | 14.45 |
| | | 3725 | 3828 | 103 | | 13.91 | 12.5 | 15.3 | 11.1 | 16.7 | 13.77 |

Table 9 Average injection volume of the two-component mixture in $m^3$/ring per section (Report, 2024)

The pressure of each injection line for component A was calculated using the following formula:

$$p_{\#i} = p_m - (R_{shield} - z_{\#i})\gamma_{app} \quad for \quad i = 1, \dots 10 \qquad (5.4)$$

- $p_m = p_f + 0{,}5$ bar;
- $R_{shield} = 6135$ mm;
- $\gamma_{app} = 15$ kN/m3, the apparent density in the excavation chamber.

Where $\mathbf{p_f}$ is the pressure at the excavation face, $\mathbf{p_m}$ is the average injection pressure of the two-component grout, $\mathbf{p_{\#i}}$ is the injection pressure of line **#i**, and $\mathbf{z_{\#i}}$ is the elevation of that line. The alert and alarm thresholds were defined as for the face pressure and the crown pressure:

$$p_{\#i,min.alert} = 0{,}9 \cdot p_{\#i;} \qquad (5.5a)$$

$$p_{\#i,max.alert} = 1{,}2 \cdot p_{\#i;} \qquad (5.5b)$$

$$p_{\#i,min.alarm} = 0{,}8 \cdot p_{\#i;} \qquad (5.5c)$$

$$p_{\#i,max.alarm} = 1{,}3 \cdot p_{\#i;} \qquad (5.5d)$$

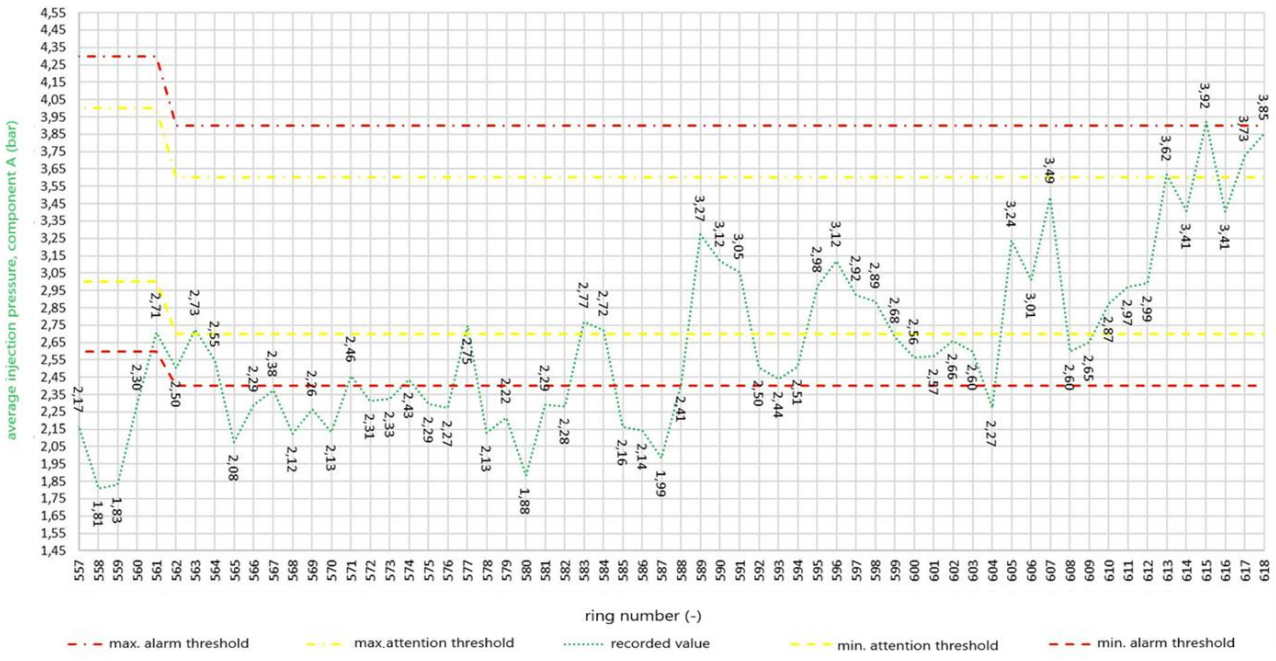


Figure 5.6 Average injection pressure of component A per section (Report, 2024)

| Omog. Segments Geom. | segment number | starting pk (m) | final pk (m) | Lenght L (m) | L total (m) | $p_m$ (bar) | ATTENTION (bar) | | ALARM (bar) | | average $p_m$ per segment (bar) |
|---|---|---|---|---|---|---|---|---|---|---|---|
| | | | | | | | MIN | MAX | MIN | MAX | |
| FYRavc | 6 | 3716 | 3725 | 9 | 112 | 3.3 | 3.0 | 4.0 | 2.6 | 4.3 | 2.16 |
| | | 3725 | 3828 | 103 | | 3.0 | 2.7 | 3.6 | 2.4 | 3.9 | 2.68 |

Table 10 Average injection pressure of component A per section (Report, 2024)

The injection pressure values recorded from the installation of ring 557 to 588, although below the minimum alarm threshold of 2.4 bar, did not have any negative impact on the stability of the face and the tunnel. The reduction is justified by the fact that, as mentioned with reference to Figure 5.3, a more stable excavation face is assumed (thus, since the injection pressure for backfilling is always higher than the pressure at the face, this confirms the assumption).

### 5.1.2 Thrust and torque

The TBM 978 has 6 thrust groups (A, B, C, D, E, F), arranged as shown in Figure 5.7.

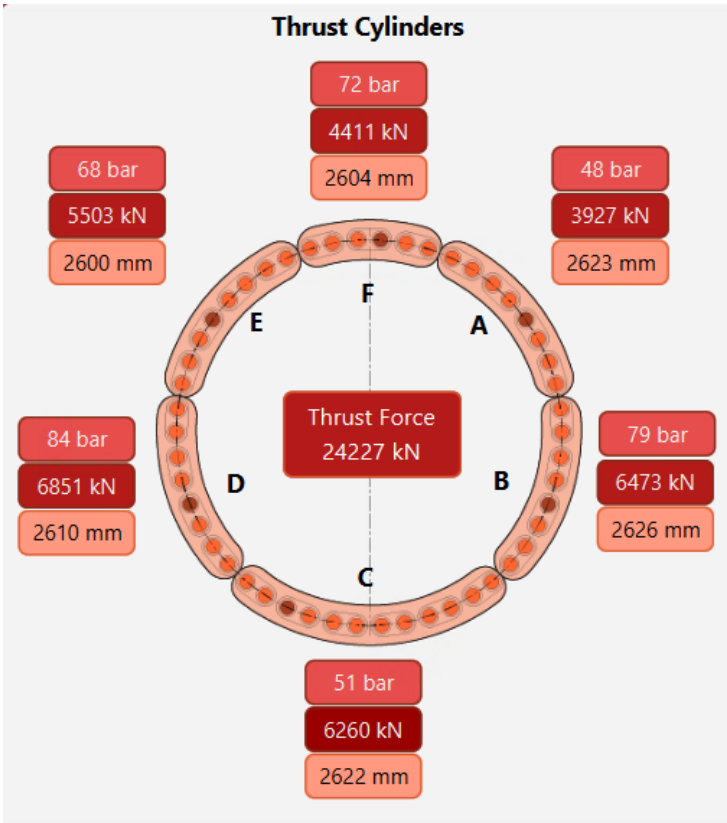


Figure 5.7 Position of the thrust cylinders (Tunnelsoft)

The thrusts in the individual thrust groups A, B, C, D, E, and F, generated by the expected minimum and maximum thrust values, 67 and 103 MN, between pk 3+681.904 and 3+699.61, and 64 and 97 MN between pk 3+699.61 and 3+716.097, were determined considering that the center of gravity of the pistons is located on the tunnel axis. The eccentricity between the thrust axis and the center of gravity of the pistons $\mathbf{e_{app}}$ was calculated by assuming a trapezoidal pressure distribution on the excavation face.

Each thrust is considered on Type 2 segments, i.e., segments reinforced with a denser reinforcement starting from 300 m from the tunnel entrance. The maximum excavation thrusts in groups A, B, C, D, E, and F meet the SLE, and consequently, the maximum thrust during excavation was always lower than the "maximum thrust for Type 2 segments" (as indicated by the red line and point in the diagram).

The thrust exerted by the generic piston i is obtained as follows:

$$S_i = S_f + \bar{S}_{app} \cdot z_i \qquad (5.6)$$

$$S_f = \frac{S}{50} \qquad (5.7)$$

$$\bar{S}_{app} = \frac{S \cdot e_{app}}{\sum_{i=1}^{50} z_i^2} \qquad (5.8)$$

With $\mathbf{S_i}$ and $\mathbf{z_i}$, we respectively indicate the total thrust exerted by the pistons on the tunnel lining and the distance from the horizontal axis to the center of gravity of the generic piston **i**, while **S** represents the total thrust exerted by the pistons.

Below are the average and maximum thrusts for groups F and C only (Figure 5.8 and Figure 5.9):

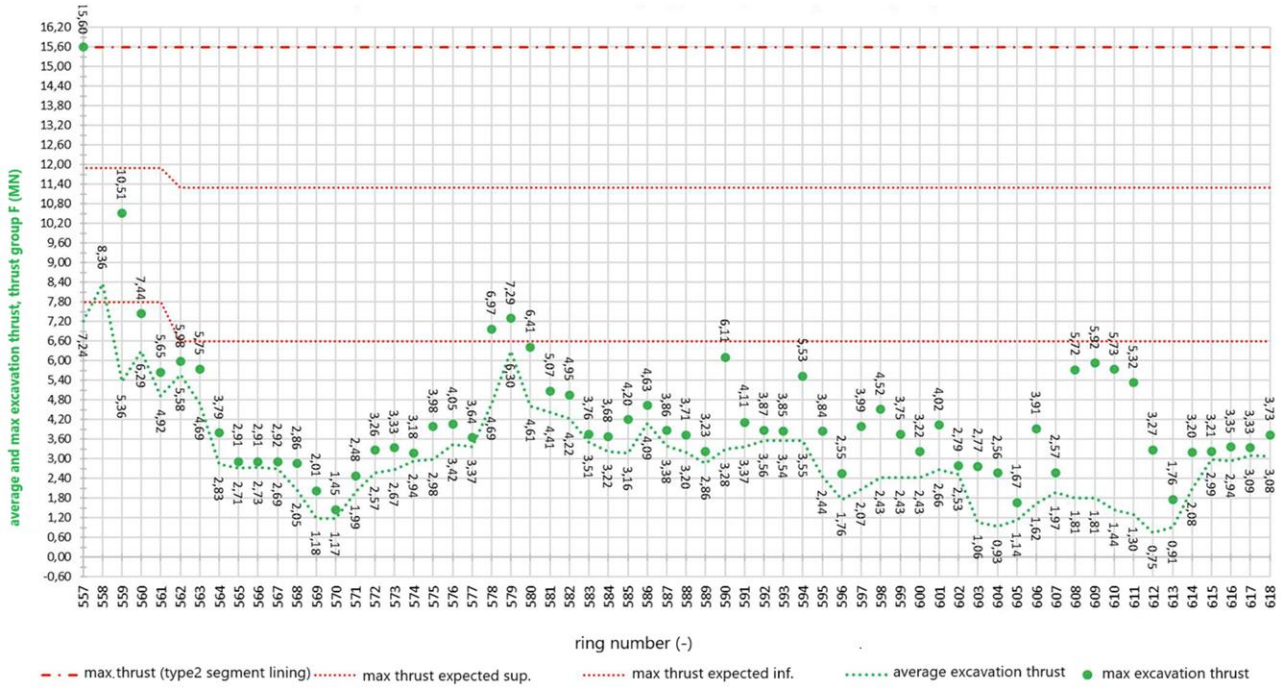


Figure 5.8 Average thrust and maximum thrust during the excavation phase exerted by the thrust group F (Report, 2024)

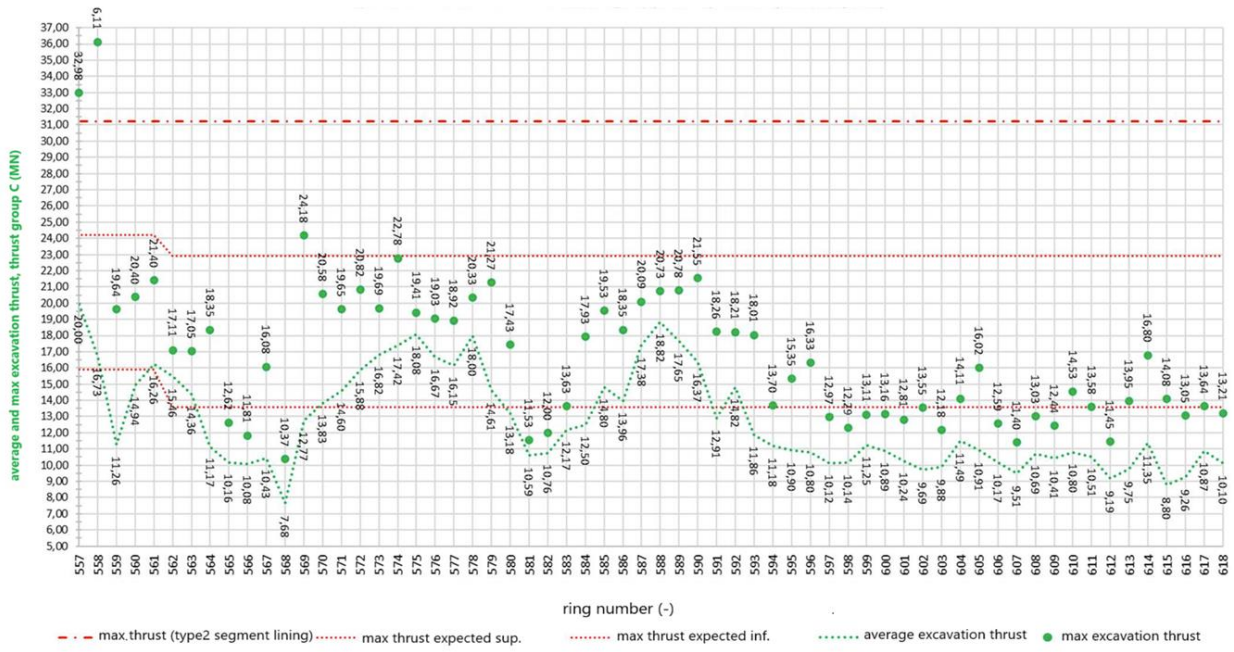


Figure 5.9 Average thrust and maximum thrust during the excavation phase exerted by the thrust group C (Report, 2024)

As expected from the trapezoidal pressure distribution on the excavation face, the thrust pistons of group C show higher values compared to those of group F, as the former are positioned lower than the latter.

In general, values below the minimum threshold indicate a face that is softer than expected, thus requiring less thrust to be applied. This could also be associated with a more stable face, which needs less thrust. This choice did not lead to any negative repercussions on the ongoing excavation.

Regarding the torque, the maximum torque values are also shown in the graph in Figure 5.10. The highest torque values were recorded during the excavation of rings 557 and 558, similarly to what was recorded for the thrust. It is important to note that the torque on the cutterhead due to friction is closely connected to the thrust force and the penetration.

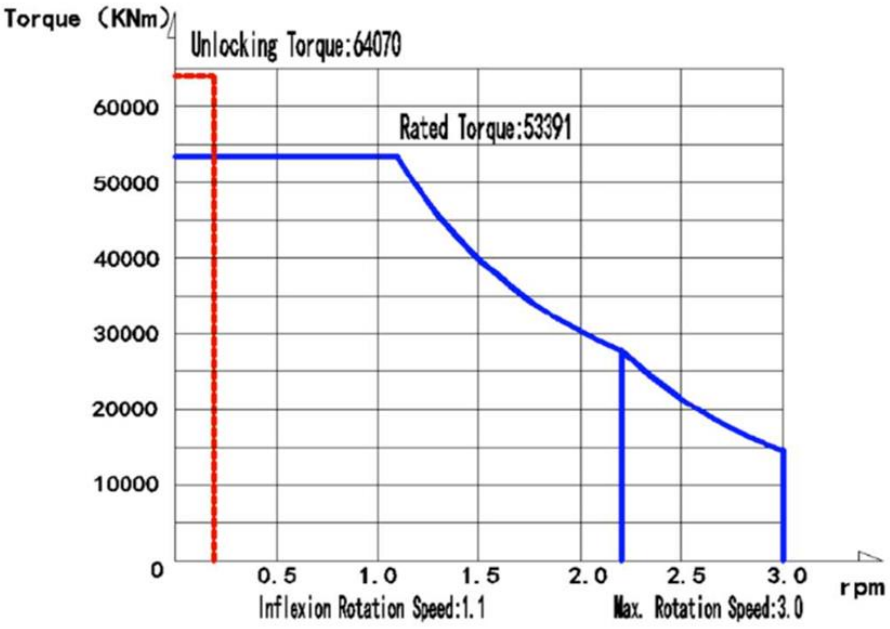


Figure 5.10 Characteristic of the cutterhead torque (Report, 2024)

The graph in Figure 5.11 shows the average torque as a function of the ring number, while Table 11 presents the average values per section based on the progress.

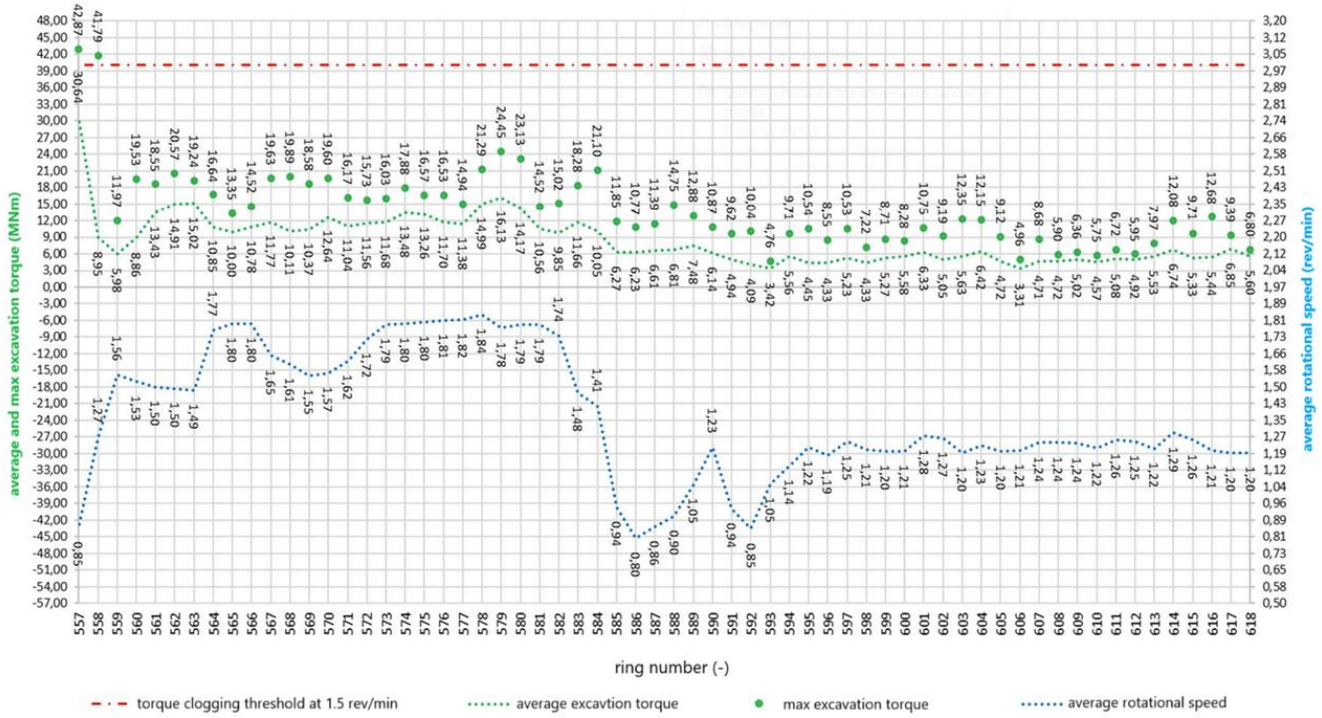


Figure 5.11 Average torque and maximum torque during excavation and average rotational speed (Report, 2024)

In the above graph, a roughly constant trend of the torque can be observed, while the trend of the average rotational speed is rather fluctuating. This can be justified by the fact that a section of harder ground increases the friction between the excavation face and the cutterhead, thereby requiring a reduction in the average rotational speed (and vice versa). Another explanation is that when encountering softer ground, the penetration per revolution **p** increases. Therefore, to maintain the same advance speed **v**, the rotational speed of the cutterhead **ω** can be lowered.

The following relationship exists between the kinematic quantities **v**, **p**, and **ω**:

$$\boldsymbol{v}\left[\frac{mm}{min}\right] = \boldsymbol{p}\left[\frac{mm}{giri}\right] \cdot \boldsymbol{\omega}\left[\frac{giri}{min}\right] \qquad (5.9)$$

| Omog. Segments Geom. | segment number | starting pk (m) | final pk (m) | Lenght L (m) | L total (m) | AVERAGE TORQUE (MNm) | MAX. TORQUE (MNm) | TORQUE FOR A CLOGGING THRESHOLD OF 1.5 rev/min (MNm) | average rotation speed ω (rev/min) |
|---|---|---|---|---|---|---|---|---|---|
| FYRavc | 6 | 3716 | 3725 | 9 | 112 | 13.57 | 26.94 | 40 | 1.34 |
| | | 3725 | 3828 | 103 | | 8.08 | 12.82 | 40 | 1.37 |

Table 11 Average torque and maximum torque during excavation and average rotational speed (Report, 2024)

As can be observed from the graph, each value falls within the limits.

### 5.1.3 Excavated material

The coverage on the crown of the tunnel's final lining, in the section covered by this weekly report, ranges from 31 to 40 m, as per the Geomechanical/Geotechnical profile. In this section, the FYRavc is planned, and for this formation, a unit weight of 20.0 kN/m³ has been estimated.

The diagram of the average weight of the excavated soil for each installed ring, net of conditioning (see Chapter 6 for more details on soil conditioning), is compared with its gross average weight in Figure 5.12. In Table 12 following the graph, the average net values per section are presented.

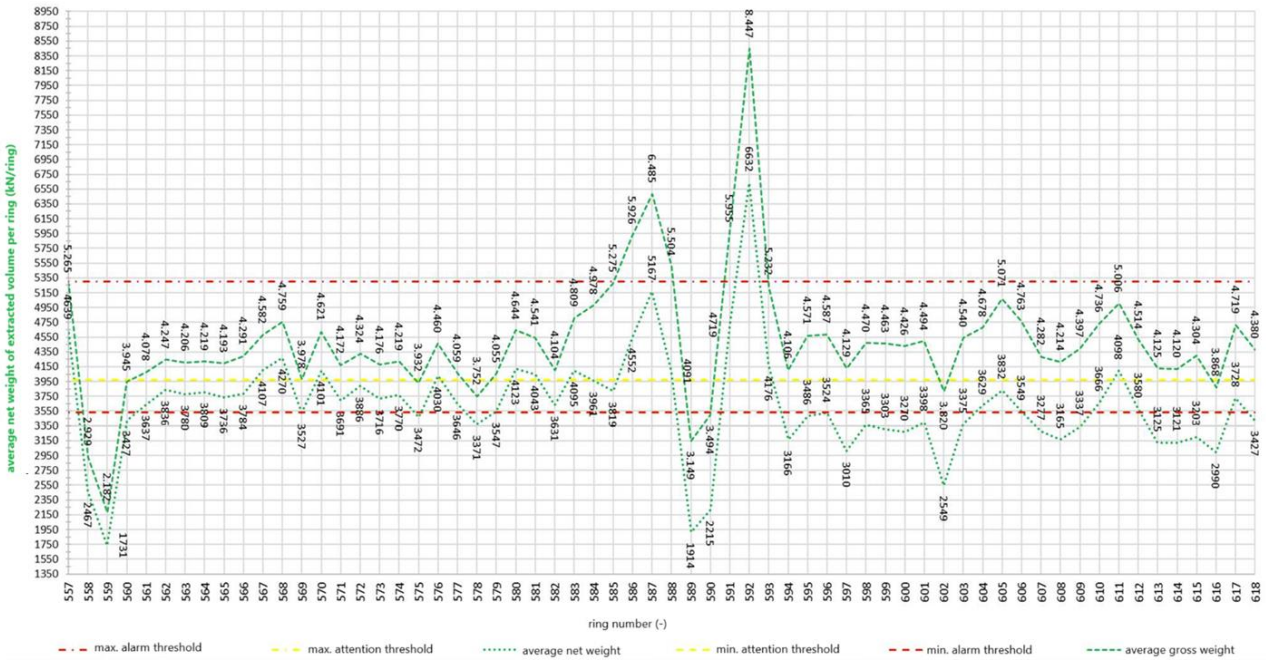


Figure 5.12 Comparison between the net weight and the gross weight of the material extracted per ring (Report, 2024)

| Omog. Segments Geom. | segment number | starting pk (m) | final pk (m) | Lenght L (m) | L total (m) | segment lining weight (kN) | ATTENTION (kN) | | ALARM (kN) | | average $P_t$ per segment (kN/ring) |
|---|---|---|---|---|---|---|---|---|---|---|---|
| | | | | | | | MIN | MAX | MIN | MAX | |
| FYRavc | 6 | 3716 | 3725 | 9 | 112 | 4418 | 3976 | 4860 | 3534 | 5302 | 3180 |
| | | 3725 | 3828 | 103 | | 4418 | 3976 | 4860 | 3534 | 5302 | 3674 |

Table 12 The weight of the net excavated material extracted per ring (Report, 2024)

In Figure 5.12, we can observe peaks in the gross average weight of the excavated soil at rings 587 and 592, and a significant minimum at ring 589. An increase in the gross average weight indicates optimal conditioning, while a minimum value could indicate either excessively compact or too loose ground. Although these values exceed the alarm threshold, they did not cause any issues

during the extraction from the screw conveyor, as the conditioning was sufficient to keep the machine operating at optimal levels.

In the diagram in Figure 5.13, the average pressures on sensors TY11 and TY07 are shown (for their positions, refer to Figure 5.1). The average values are calculated during the shield's advance phase or considering this phase plus the installation of the ring with prefabricated segments.

Sensor TY11 is located above TY07, which justifies the fact that the pressures of the second are higher than those of the first, due to the trapezoidal distribution of thrusts in the excavation chamber.

Figure 5.14 shows the average apparent density calculated using the pressures reported in Figure 5.13, taking into account that the elevation difference between the two sensors is 8 m.
Knowing the average apparent density in the excavation chamber allows us to adjust the TBM for more efficient screw conveyor extraction, reducing the risk of clogging. Density affects the pressure required to support the excavation face: if too high, it could indicate compact ground that may require more force or a special support system; a low density could suggest less stable ground. Specifically, for low-density ground, water infiltration could become a problem, so monitoring density helps predict and mitigate this risk. Furthermore, it is emphasized that higher apparent density values in the excavation chamber correspond to lower $\mathbf{p_{f,c}}$ values at the crown than expected. This indicates that the excavation is proceeding correctly, with average $\mathbf{p_f}$ pressures at the face even exceeding those necessary for the stability of the face and tunnel based on the ADECO-RS method (Analysis of Controlled Deformations in Rocks and Soils).

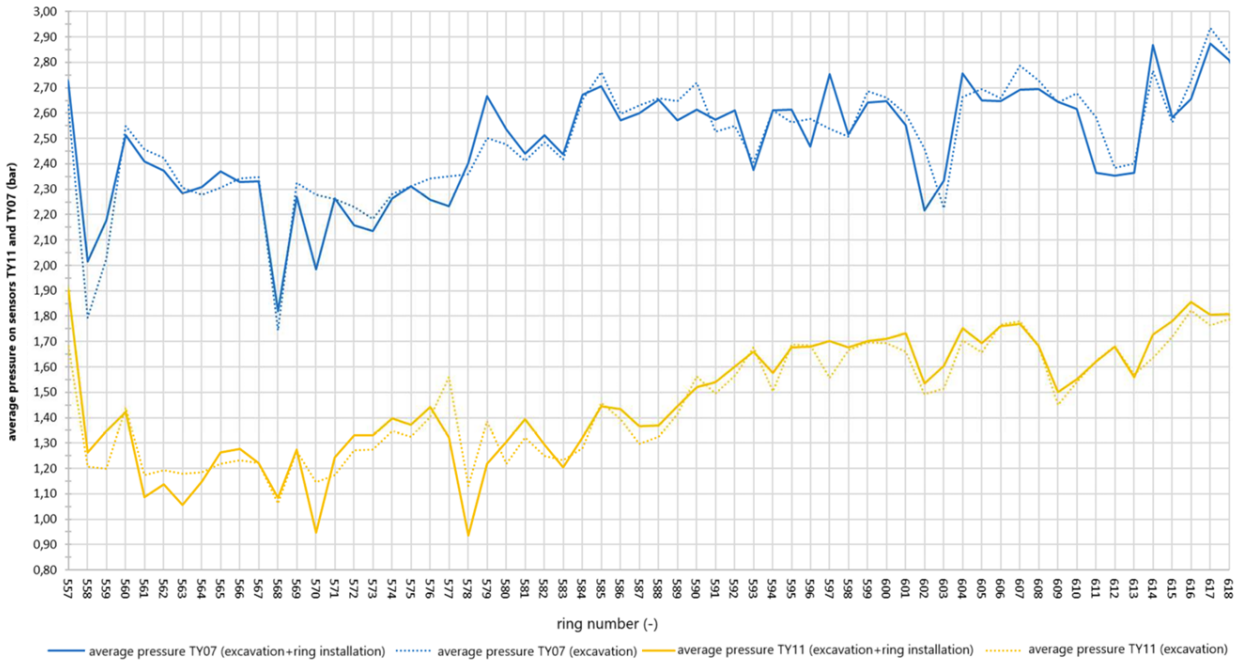


Figure 5.13 Face pressure: comparison between TY06 and TY11 sensors (Report, 2024)

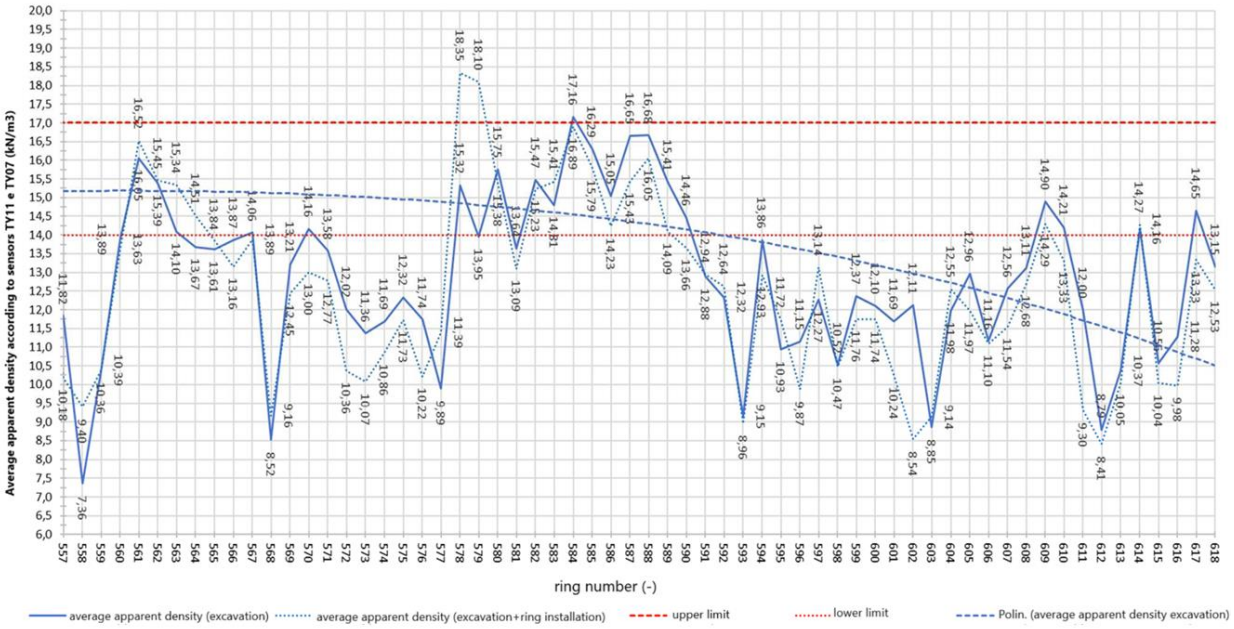


Figure 5.14 Average apparent density in the excavation chamber, TY06 and TY11 sensors (Report, 2024)

| Omog. Segments Geom. | segment number | starting pk (m) | final pk (m) | Lenght L (m) | L total (m) | pressure sensors TY11-TY07 | | | | |
|---|---|---|---|---|---|---|---|---|---|---|
| | | | | | | $\gamma_{app,\ exc.}$ (kN/m$^3$) | lower limit | upper limit | average $\gamma_{app}$ value per segment | |
| | | | | | | | | | $\gamma_{app,\ excavation}$ (kN/m$^3$) | $\gamma_{app,\ excavation+ring\ installation}$ (kN/m$^3$) |
| FYRavc | 6 | 3716 | 3725 | 9 | 112 | 15 | 14 | 17 | 11.9 | 12.02 |
| | | 3725 | 3828 | 103 | | 15 | 14 | 17 | 12.57 | 12.26 |

Table 13 Average apparent density in the excavation chamber, TY06 and TY11 sensors (Report, 2024)

## 5.2 From May 10th to May 17th (rings installed 614-669)

The excavation progress reports fall within the section covered by P.A.T. No. 3 (Table 7). Excavation stopped on May 17 at pk 3+932.293 for the maintenance of the conveyor belt, and at the same time, the temporary muck storage tanks were emptied.

In the graph in Figure 5.15, the pressure $\mathbf{p_{f,c}}$ is shown as a function of the ring number, while Table 14 presents the average value of $\mathbf{p_{f,c}}$ for each section, based on the progress.

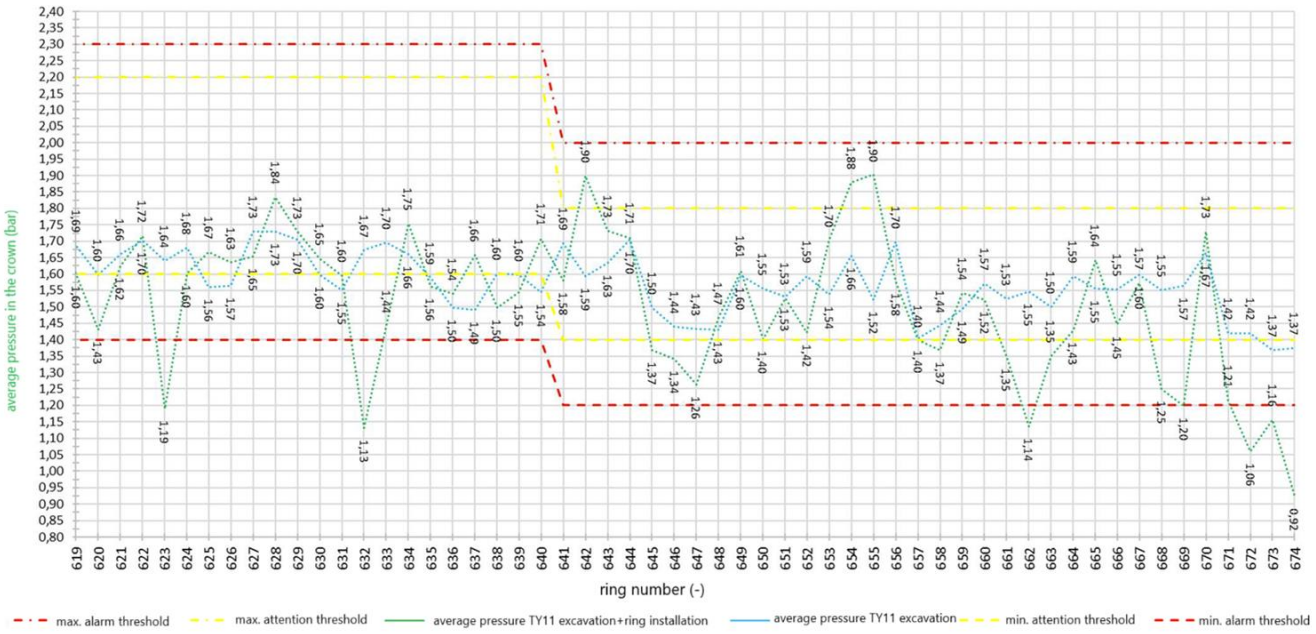


Figure 5.15 pressure in the crown during excavation and at the completion of the ring installation (TY11 sensor) (Report, 2024)

| Omog. Segments Geom. | segment number | day | n° of ring installed | Lenght L (m) | starting pk (m) | final pk (m) | L total (m) | $p_f$ (bar) | $p_{f,c}$ (bar) | ATTENTION (bar) | | ALARM (bar) | | average $p_{f,c}$ value (bar) | |
|---|---|---|---|---|---|---|---|---|---|---|---|---|---|---|---|
| | | | | | | | | | | MIN | MAX | MIN | MAX | excavation | excavation + ring installation |
| FYRavc | 6 | 10/05/2024 | 11 | 19.8 | 3827.8 | 3847.6 | 100.8 | 2.5 | 1.8 | 1.6 | 2.2 | 1.4 | 2.3 | 1.7 | 1.6 |
| | | 12/05/2024 | 12 | 21.5 | 3847.6 | 3867.3 | | 2.5 | 1.8 | 1.6 | 2.2 | 1.4 | 2.3 | 1.5 | 1.6 |
| FYRagms | 7 | | | | 3867.3 | 3869.1 | | 2.2 | 1.5 | 1.4 | 1.8 | 1.2 | 2 | | |
| | | 13/05/2024 | 11 | 19.8 | 3869.1 | 3888.9 | | 2.2 | 1.5 | 1.4 | 1.8 | 1.2 | 2 | 1.5 | 1.5 |
| | | 14/04/2024 | 11 | 19.8 | 3888.9 | 3908.7 | | 2.2 | 1.5 | 1.4 | 1.8 | 1.2 | 2 | 1.5 | 1.5 |
| | | 15/05/2024 | 1 | 1.9 | 3908.7 | 3910.6 | | 2.2 | 1.5 | 1.4 | 1.8 | 1.2 | 2 | 1.6 | 1.4 |
| | | 16/05/2024 | 10 | 18.0 | 3910.6 | 3928.6 | | 2.2 | 1.5 | 1.4 | 1.8 | 1.2 | 2 | 1.5 | 1.3 |

Table 14 pressure in the crown during excavation and at the completion of the ring installation (TY11 sensor) (Report, 2024)

Some $\mathbf{p_{f,c}}$ values (rings 623, 632, 662, etc.), although below the minimum alarm threshold of 1.2-1.4 bar, did not have any negative impact on the stability of the face and tunnel. This should indicate a generally more stable excavation face than initially anticipated.

### 5.2.1 Injection volume and pressure

For the position of the injection lines, refer to Figure 5.4, while for the calculation of the volumes of two-component grout to be injected from each individual line, equations (5.1) and (5.2) from paragraph 5.1.1 have been used.

The same proportions were applied to calculate the minimum volume of 10.74 m³ in the case of contact between the shield and the ground at the rear.For the alert and alarm thresholds of the volume corresponding to line #i, to be filled with two-component grout, the procedure followed is the same as for the total volume of mixture per ring, using formulas (5.3a)–(5.3.d) already discussed in paragraph 5.1.1.

In the graph in Figure 5.16, the injection volume of the two-component grout is shown, while Table 16 presents the average volume value **V** per section.

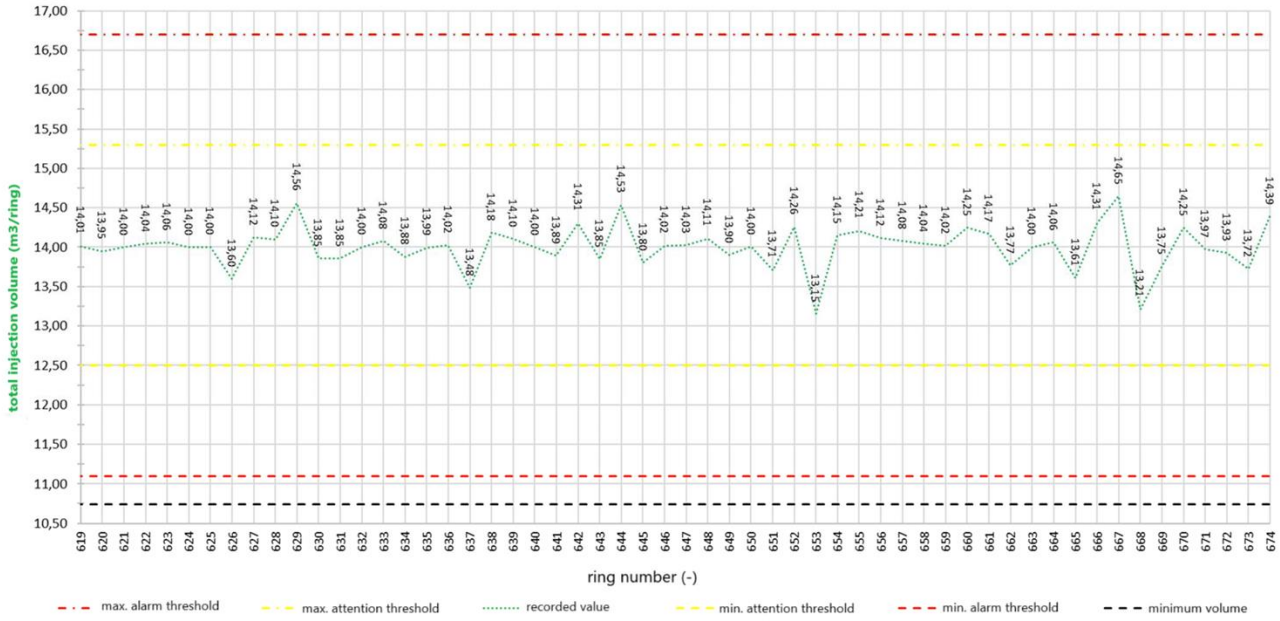


Figure 5.16 Total injection volume of the two-component mixture in m³/ring (Report, 2024)

| Omog. Segments Geom. | segment number | day | n° of ring installed | Lenght L (m) | starting pk (m) | final pk (m) | L total (m) | V (m³/ring) | ATTENTION (m³/ring) | | ALARM (m³/ring) | | average V (m³/ring) |
|---|---|---|---|---|---|---|---|---|---|---|---|---|---|
| | | | | | | | | | MIN | MAX | MIN | MAX | |
| FYRavc | 6 | 10/05/2024 | 11 | 19.8 | 3827.8 | 3847.6 | 100.8 | 13.91 | 12.5 | 15.3 | 11.1 | 16.7 | 14.0 |
| | | 12/05/2024 | 12 | 21.5 | 3847.6 | 3867.3 | | 13.91 | 12.5 | 15.3 | 11.1 | 16.7 | 14.0 |
| FYRagms | 7 | | | | 3867.3 | 3869.1 | | | | | | | |
| | | 13/05/2024 | 11 | 19.8 | 3869.1 | 3888.9 | | 13.91 | 12.5 | 15.3 | 11.1 | 16.7 | 14.0 |
| | | 14/04/2024 | 11 | 19.8 | 3888.9 | 3908.7 | | 13.91 | 12.5 | 15.3 | 11.1 | 16.7 | 14.0 |
| | | 15/05/2024 | 1 | 1.9 | 3908.7 | 3910.6 | | 13.91 | 12.5 | 15.3 | 11.1 | 16.7 | 14.1 |
| | | 16/05/2024 | 10 | 18.0 | 3910.6 | 3928.6 | | 13.91 | 12.5 | 15.3 | 11.1 | 16.7 | 14.0 |

Table 15 Average injection volume of the two-component mixture in m³/ring per section (Report, 2024)

The pressure of the individual injection lines for component A has been calculated using formula (5.4) (paragraph 5.1.1).

The alert and alarm thresholds have been defined in the same way as for the face pressure and crown pressure (equations (5.5a)-(5.5d), paragraph 5.1.1).

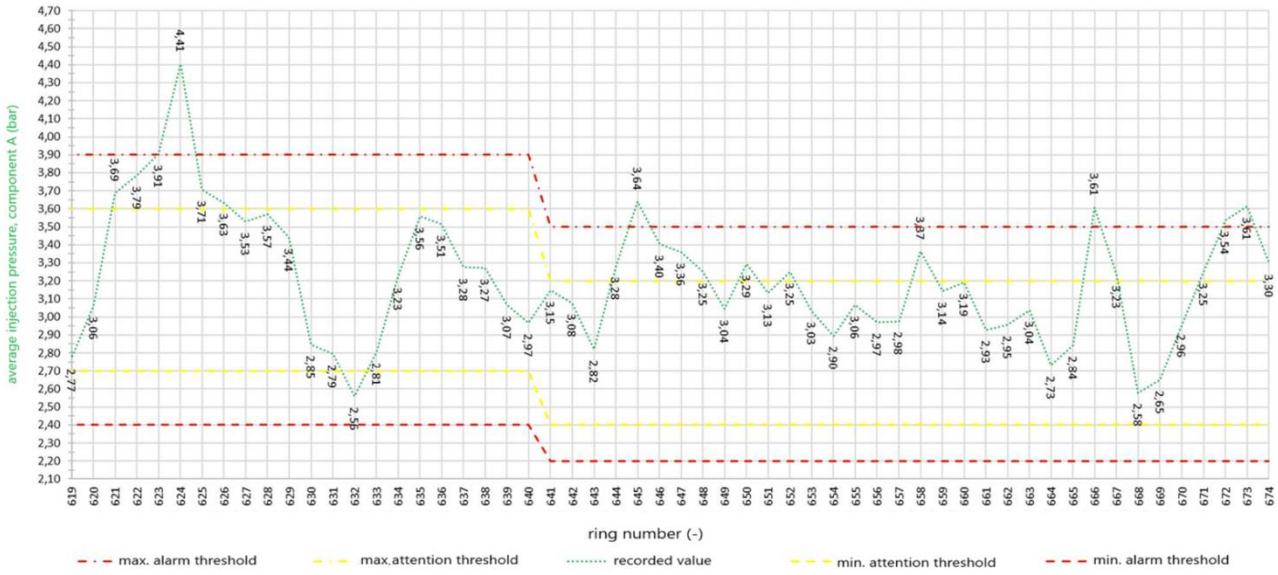


Figure 5.17 Average injection pressure of component A per section (Report, 2024)

| Omog. Segments Geom. | segment number | day | n° of ring installed | Lenght L (m) | starting pk (m) | final pk (m) | L total (m) | $p_m$ (bar) | ATTENTION (bar) | | ALARM (bar) | | average $p_m$ (bar) |
|---|---|---|---|---|---|---|---|---|---|---|---|---|---|
| | | | | | | | | | MIN | MAX | MIN | MAX | |
| FYRavc | 6 | 10/05/2024 | 11 | 19.8 | 3827.8 | 3847.6 | 100.8 | 3 | 2.7 | 3.6 | 2.4 | 3.9 | 3.6 |
| FYRagms | 7 | 12/05/2024 | 12 | 21.5 | 3847.6 | 3867.3 | | 3 | 2.7 | 3.6 | 2.4 | 3.9 | 3.1 |
| | | | | | 3867.3 | 3869.1 | | 2.7 | 2.4 | 3.2 | 2.2 | 3.5 | |
| | | 13/05/2024 | 11 | 19.8 | 3869.1 | 3888.9 | | 2.7 | 2.4 | 3.2 | 2.2 | 3.5 | 3.2 |
| | | 14/04/2024 | 11 | 19.8 | 3888.9 | 3908.7 | | 2.7 | 2.4 | 3.2 | 2.2 | 3.5 | 3.1 |
| | | 15/05/2024 | 1 | 1.9 | 3908.7 | 3910.6 | | 2.7 | 2.4 | 3.2 | 2.2 | 3.5 | 2.7 |
| | | 16/05/2024 | 10 | 18.0 | 3910.6 | 3928.6 | | 2.7 | 2.4 | 3.2 | 2.2 | 3.5 | 3.2 |

Table 16 Average injection pressure of component A per section (Report, 2024)

The injection pressure values recorded are mostly within the alarm thresholds, with the only exception being during the installation of ring 624. This ring shows a peak beyond the maximum alarm threshold of 3.90 bar. The increase is justified by the fact that, as mentioned in reference to Figure 5.17, a less stable excavation face is assumed between rings 623 and 625. Despite this, no issues have arisen during the advancing face.

### 5.2.2 Thrust and torque

For the position of the 6 thrust groups (A, B, C, D, E, F), refer to Figure 5.7 in paragraph 5.1.2.

The thrusts in the individual groups (A, B, C, D, E, and F), generated by the expected maximum thrusts, both lower and upper (54 and 92 MN between pk 3+827.8 and 3+867.3, and 42 and 63 MN between pk 3+867.3 and 3+928.6), have been determined considering that the center of gravity of the pistons is located along the axis of the tunnel. The eccentricity between the thrust axis and the center of gravity of the pistons $\mathbf{e_{app}}$ was calculated by assuming a trapezoidal pressure distribution on the excavation face.

Each thrust is considered on type 2 segments, which are reinforced segments with denser reinforcement starting from 300 meters from the tunnel entrance. The maximum thrusts during excavation in groups A, B, C, D, E, and F meet the SLE (Service Limit State); therefore, the maximum thrust during excavation has always been lower than the "maximum thrust of type 2 segments" (line and point marked in red).
The thrust exerted by each individual piston **i** is calculated as shown in paragraph 5.1.2 (equations (5.6)-(5.8)). Here, $\mathbf{S_i}$ and $\mathbf{z_i}$ represent the total thrust exerted by the pistons on the lining ring and the distance from the horizontal axis to the center of gravity of piston **i**, respectively, while **S** is the total thrust exerted by the pistons.

Below, the average and maximum thrust values for only groups F and C are provided (Figures 5.18 and 5.19).

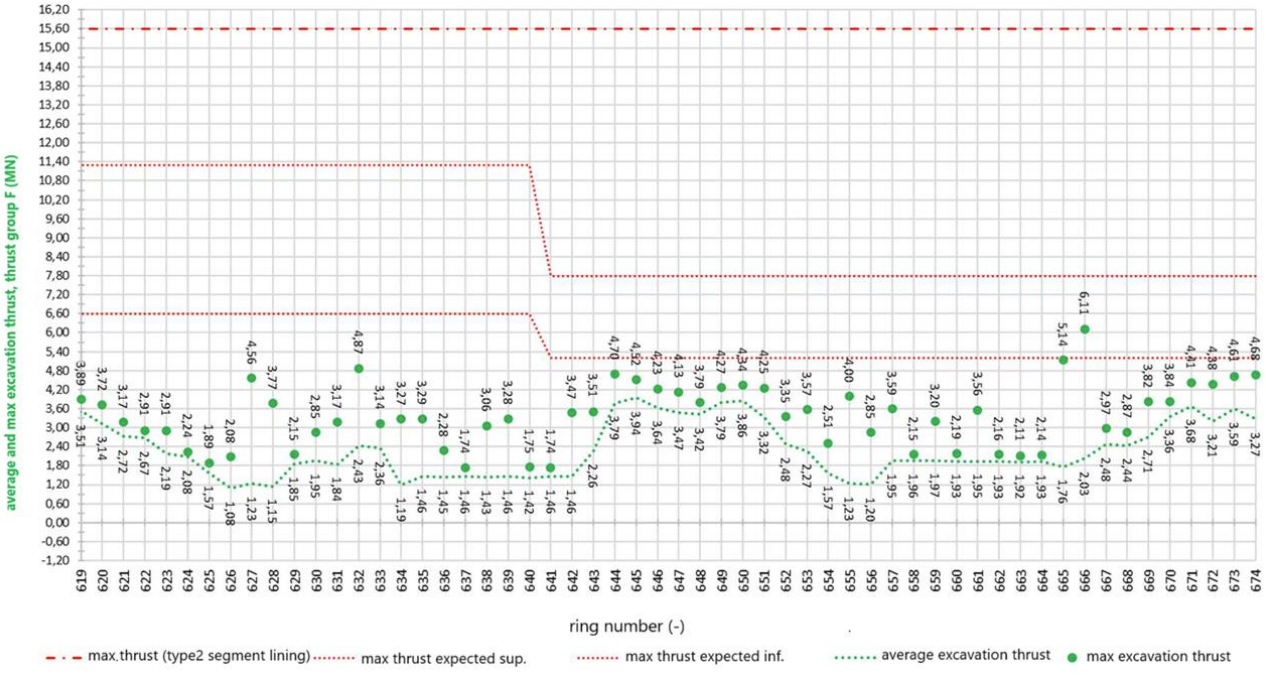


Figure 5.18 Average thrust and maximum thrust during the excavation phase exerted by the thrust group F (Report, 2024)

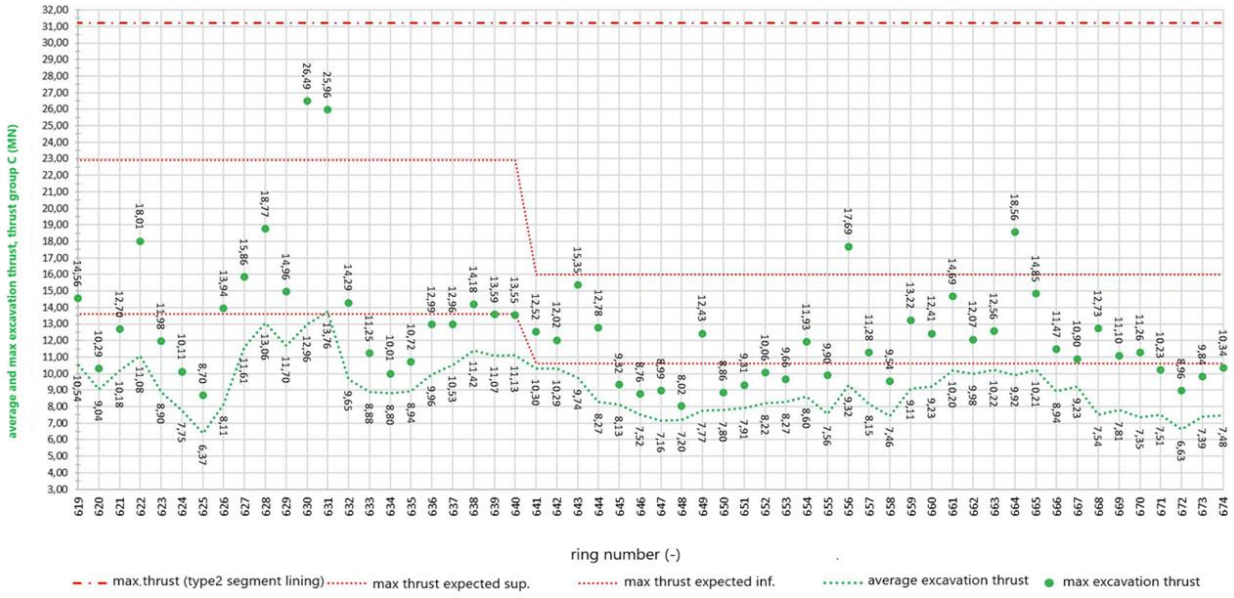


Figure 5.19 Average thrust and maximum thrust during the excavation phase exerted by the thrust group C (Report, 2024)

As expected from the trapezoidal pressure distribution on the excavation face, the thrust pistons in group C exhibit higher values compared to those in group F, as the former are located lower than the latter.
In general, values below the minimum threshold indicate a softer face than expected, requiring less thrust to be applied. This may also be linked to a more stable face, which requires less thrust. This situation did not lead to any negative consequences for the advancing excavation.

Regarding the torque, Figure 5.10 (paragraph 5.1.2) also shows the maximum torque values. It is important to note that the torque on the cutterhead, due to friction, is strictly related to the thrust force and penetration.

In the graph in Figure 5.20, the average torque is shown as a function of the ring number, while Table 18 presents the average values for each section according to the progressive.

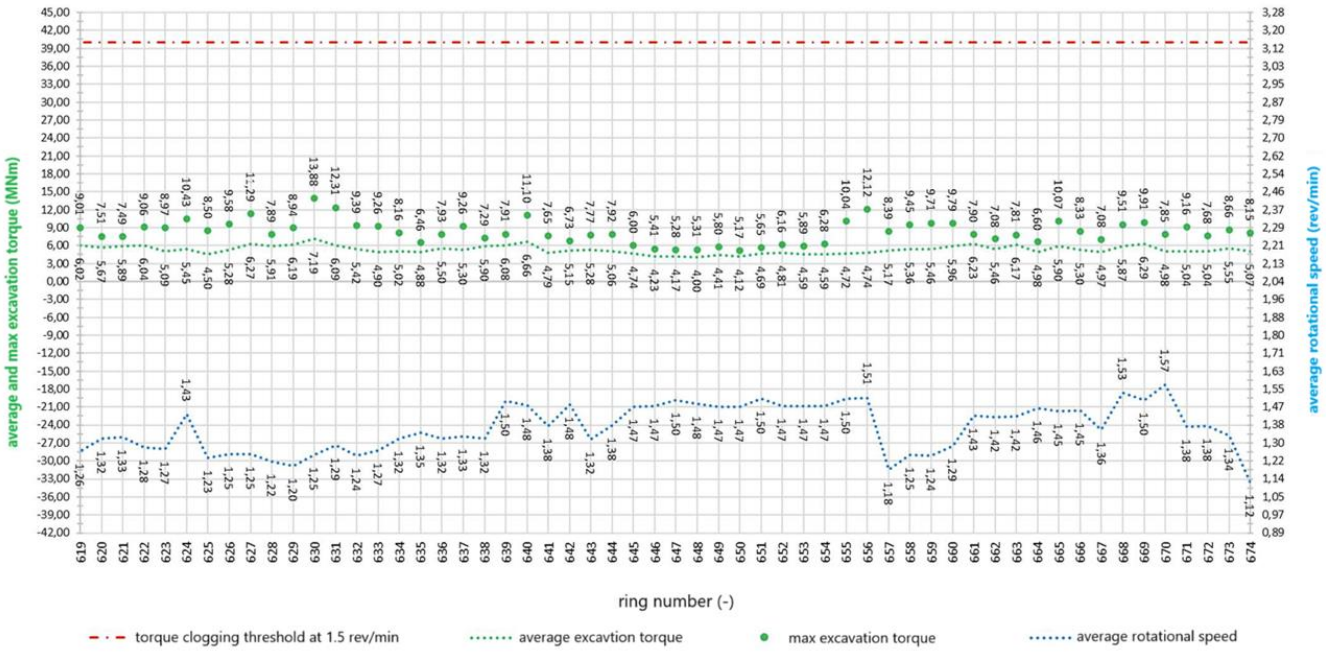


Figure 5.20 Average torque and maximum torque during excavation and average rotational speed (Report, 2024)

In the above graph, we can observe an approximately constant trend in the torque, as well as in the average rotational speed. The latter fluctuates more significantly between rings 657 and 660, which can be explained by the fact that a harder stretch of ground increases the friction between the excavation face and the cutterhead, thus requiring a reduction in the average rotational speed (and vice versa, as seen with ring 624). This is because harder ground increases the friction between the excavation face and the cutterhead, which in turn demands a decrease in the average rotational speed (and vice versa).

| Omog. Segments Geom. | segment number | day | n° of ring installed | Lenght L (m) | starting pk (m) | final pk (m) | L total (m) | AVERAGE TORQUE (MNm) | MAX. TORQUE (MNm) | TORQUE FOR A CLOGGING THRESHOLD OF 1.5 rev/min (MNm) | average rotation speed ω (rev/min) |
|---|---|---|---|---|---|---|---|---|---|---|---|
| FYRavc | 6 | 10/05/2024 | 11 | 19.8 | 3827.8 | 3847.6 | 100.8 | 6 | 9 | 40 | 1.3 |
| | | 12/05/2024 | 12 | 21.5 | 3847.6 | 3867.3 | | 6 | 9 | 40 | 1.3 |
| FYRagms | 7 | | | | 3867.3 | 3869.1 | | | | | |
| | | 13/05/2024 | 11 | 19.8 | 3869.1 | 3888.9 | | 5 | 6 | 40 | 1.5 |
| | | 14/04/2024 | 11 | 19.8 | 3888.9 | 3908.7 | | 5 | 9 | 40 | 1.4 |
| | | 15/05/2024 | 1 | 1.9 | 3908.7 | 3910.6 | | 5 | 7 | 40 | 1.5 |
| | | 16/05/2024 | 10 | 18.0 | 3910.6 | 3928.6 | | 5 | 9 | 40 | 1.4 |

Table 17 Average torque and maximum torque during excavation and average rotational speed (Report, 2024)

As can be seen from the graph, each value falls within the established limits.

### 5.2.3 Excavated material

The coverages on the crown of the tunnel's final lining, in the section covered by this weekly report, range from 8.3 to 31.4 meters, as per the Geomechanical/Geotechnical profile. In this section, the FYRavc is specified, and for this formation, an estimated weight per unit volume of 20.0 kN/m³ has been assigned.

The diagram of the average weight of the extracted soil for each installed ring, net of conditioning (see Chapter 6 for more details on soil conditioning), is compared with its gross average weight in

Figure 5.21. In Table 19, which follows the graph, the net average values for the section are reported.

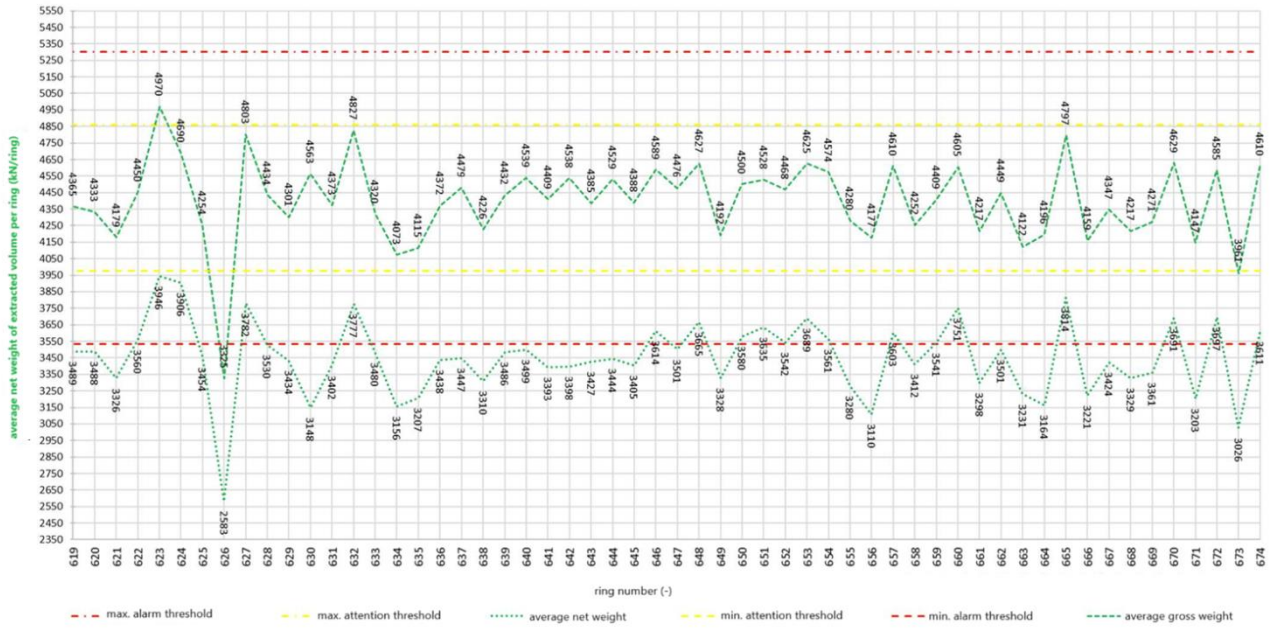


Figure 5.21 Comparison between the net weight and the gross weight of the material extracted per ring (Report, 2024)

| Omog. Segments Geom. | segment number | day | n° of ring installed | Lenght L (m) | starting pk (m) | final pk (m) | L total (m) | REFERENCE WEIGHT $P_t$ (kN) | ATTENTION MIN. (kN) | ATTENTION MAX. (kN) | ALARM MIN. (kN) | ALARM MAX. (kN) | AVERAGE NET WEIGHT (kN) | AVERAGE GROSS WEIGHT (kN) |
|---|---|---|---|---|---|---|---|---|---|---|---|---|---|---|
| FYRavc | 6 | 10/05/2024 | 11 | 19.8 | 3827.8 | 3847.6 | 100.8 | 4418 | 3976 | 4860 | 3534 | 5302 | 3500 | 4373 |
| | | 12/05/2024 | 12 | 21.5 | 3847.6 | 3867.3 | | 4418 | 3976 | 4860 | 3534 | 5302 | 3395 | 4394 |
| FYRagms | 7 | | | | 3867.3 | 3869.1 | | | | | | | | |
| | | 13/05/2024 | 11 | 19.8 | 3869.1 | 3888.9 | | 4418 | 3976 | 4860 | 3534 | 5302 | 3504 | 4475 |
| | | 14/04/2024 | 11 | 19.8 | 3888.9 | 3908.7 | | 4418 | 3976 | 4860 | 3534 | 5302 | 3452 | 4393 |
| | | 15/05/2024 | 1 | 1.9 | 3908.7 | 3910.6 | | 4418 | 3976 | 4860 | 3534 | 5302 | 3164 | 4196 |
| | | 16/05/2024 | 10 | 18.0 | 3910.6 | 3928.6 | | 4418 | 3976 | 4860 | 3534 | 5302 | 3438 | 4372 |

Table 18 The weight of the net excavated material extracted per ring (Report, 2024)

In Figure 5.21, we observe a significant minimum value on ring 626. Generally, an increase in the average extracted soil weight indicates optimal conditioning, while a minimum value could suggest either overly compacted or excessively loose soil. Although these values exceed the alarm threshold, they did not cause issues during the excavation, as the conditioning was sufficient to maintain the machine's operation at optimal levels.

In Figure 5.22, the average pressures recorded on sensors TY11 and TY07 are shown. The average values are calculated during the shield advancement phase or considering the shield advancement plus the installation of the precast ring. Since sensor TY11 is located above TY07, it is expected that the pressures measured by TY11 are higher than those at TY07, in line with the trapezoidal pressure distribution at the excavation face. A significant minimum is also observed at ring 626, which aligns with the previous observation and suggests that the face is relatively stable.

In Figure 5.23, the average apparent density is calculated based on the pressures reported in Figure 5.22, taking into account the 8-meter difference in elevation between the two sensors.

The knowledge of the average apparent density in the excavation chamber helps us adjust the TBM for more efficient extraction of the spoil, reducing the risk of clogging. The density influences the pressure needed to support the excavation face: if the density is too high, it could indicate compacted ground, which may require more force or special support systems. On the other hand, low density could suggest less stable ground. Particularly for low-density ground, water infiltration could become a problem, so monitoring the density helps predict and mitigate this risk.

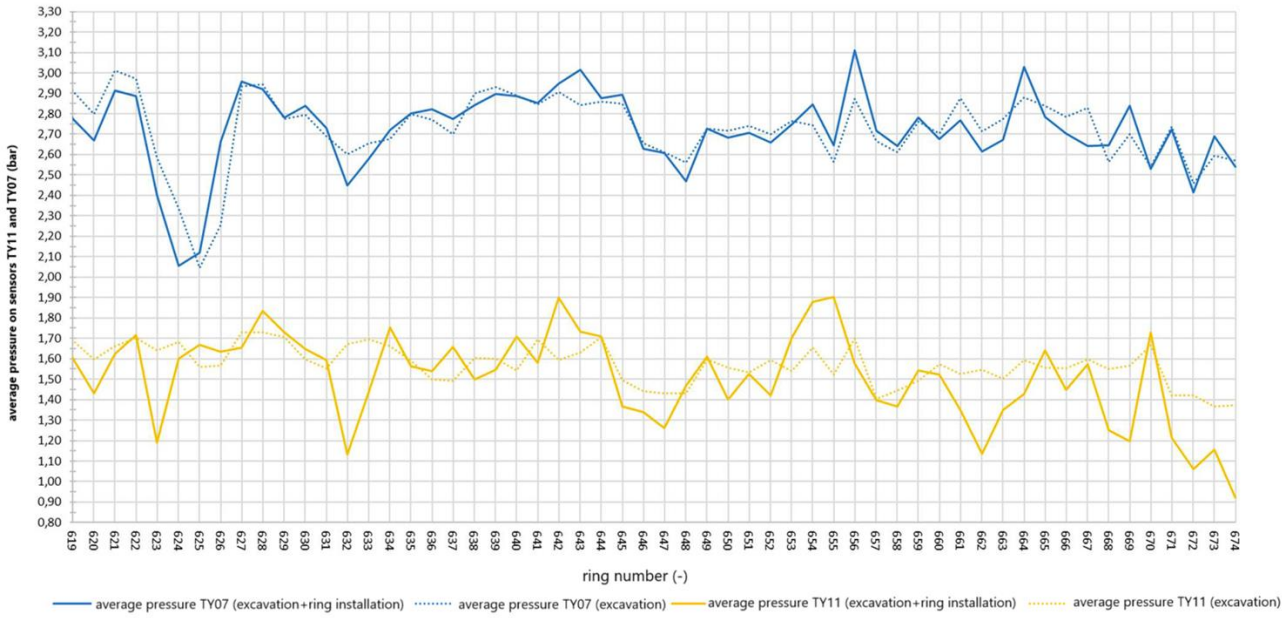


Figure 5.22 Face pressure: comparison between TY06 and TY11 sensors (Report, 2024)

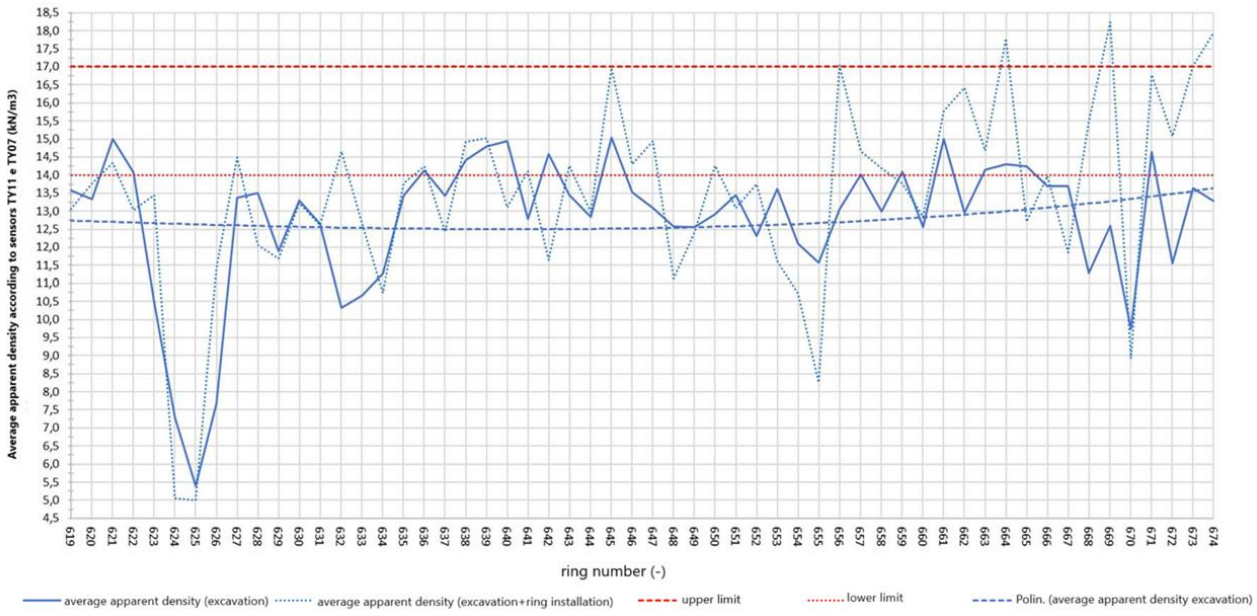


Figure 5.23 Average apparent density in the excavation chamber, TY06 and TY11 sensors (Report, 2024)

| Omog. Segments Geom. | segment number | day | n° of ring installed | Lenght L (m) | starting pk (m) | final pk (m) | L total (m) | pressure sensors TY11-TY07 | | | | |
|---|---|---|---|---|---|---|---|---|---|---|---|---|
| | | | | | | | | $\gamma_{app,\ exc.}$ (kN/m$^3$) | lower limit | upper limit | average $\gamma_{app}$ over 24h | |
| | | | | | | | | | | | $\gamma_{app,\ excavation}$ (kN/m$^3$) | $\gamma_{app,\ excavation+ring\ installation}$ (kN/m$^3$) |
| FYRavc | 6 | 10/05/2024 | 11 | 19.8 | 3827.8 | 3847.6 | 100.8 | 15 | 14 | 17 | 11.4 | 11.6 |
| | | 12/05/2024 | 12 | 21.5 | 3847.6 | 3867.3 | | 15 | 14 | 17 | 13.0 | 13.5 |
| FYRagms | 7 | | | | 3867.3 | 3869.1 | | | | | | |
| | | 13/05/2024 | 11 | 19.8 | 3869.1 | 3888.9 | | 15 | 14 | 17 | 13.3 | 13.6 |
| | | 14/04/2024 | 11 | 19.8 | 3888.9 | 3908.7 | | 15 | 14 | 17 | 13.3 | 13.6 |
| | | 15/05/2024 | 1 | 1.9 | 3908.7 | 3910.6 | | 15 | 14 | 17 | 14.3 | 17.8 |
| | | 16/05/2024 | 10 | 18.0 | 3910.6 | 3928.6 | | 15 | 14 | 17 | 12.8 | 14.8 |

Table 19 Average apparent density in the excavation chamber, TY06 and TY11 sensors (Report, 2024)

## 5.3 From May 17th to May 31st (rings installed 670-730)

The excavation progress reports fall within the sections covered by P.A.T. n°3 and n°4 (Table 7). As mentioned in the previous paragraph, excavation was halted on May 17 at pk 3+932.293 for conveyor maintenance, and at the same time, the temporary spoil storage tanks were emptied; excavation then resumed on May 23.

In the graph in Figure 5.24, the pressure $\mathbf{p_{f,c}}$ is shown as a function of the ring number, while Table 21 presents the average value of $\mathbf{p_{f,c}}$ for each section, based on the progress.

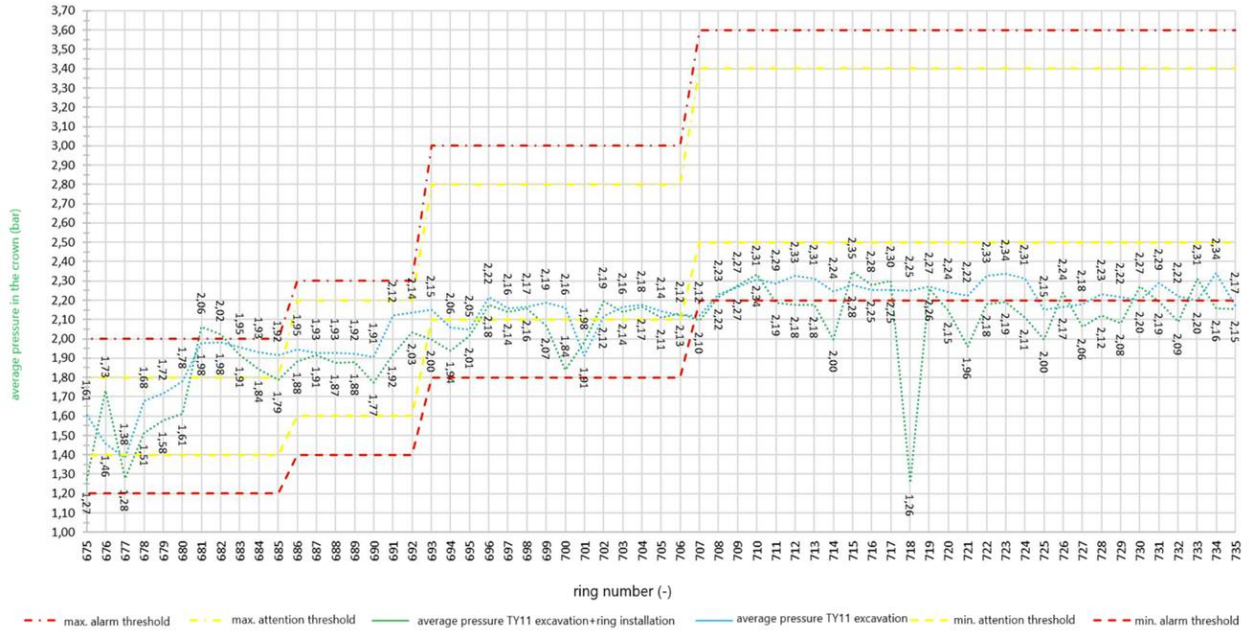


Figure 5.24 Average pressure in the crown during excavation and at the completion of the ring installation (TY11 sensor) (Report, 2024)

| Omog. Segments Geom. | segment number | day | n° of ring installed | Lenght L (m) | starting pk (m) | final pk (m) | L total (m) | $p_f$ (bar) | $p_{f,c}$ (bar) | ATTENTION (bar) | | ALARM (bar) | | average $p_{f,c}$ value (bar) | |
|---|---|---|---|---|---|---|---|---|---|---|---|---|---|---|---|
| | | | | | | | | | | MIN | MAX | MIN | MAX | excavation | excavation + ring installation |
| FYRavc | 7 | 17/052024 | 1 | 1.723 | 3928.56 | 3930.29 | 109.7 | 2.2 | 1.5 | 1.4 | 1.8 | 1.2 | 2.0 | 1.61 | 1.27 |
| FYRmar+FYRar | | 23/05/2024 | 4 | 5.644 | 3930.29 | 3935.93 | | 2.2 | 1.5 | 1.4 | 1.8 | 1.2 | 2.0 | 1.56 | 1.53 |
| | 8 | | | 1.722 | 3935.93 | 3937.65 | | | | | | | | | |
| | | 24/05/2024 | 10 | 11.408 | 3937.65 | 3949.06 | | 2.2 | 1.5 | 1.4 | 1.8 | 1.2 | 2.0 | 1.93 | 1.88 |
| | 9 | | | 6.465 | 3949.06 | 3955.53 | | 2.5 | 1.8 | 1.6 | 2.2 | 1.4 | 2.3 | | |
| | | 25/05/2024 | 12 | 6.975 | 3955.53 | 3962.50 | | 2.5 | 1.8 | 1.6 | 2.2 | 1.4 | 2.3 | 2.10 | 2.00 |
| | | | | 14.621 | 3962.50 | 3977.12 | | 3 | 2.3 | 2.1 | 2.8 | 1.8 | 3.0 | | |
| | | 26/05/2024 | 12 | 10.379 | 3977.12 | 3987.50 | | 3 | 2.3 | 2.1 | 2.8 | 1.8 | 3.0 | 2.21 | 2.18 |
| | | | | 11.266 | 3987.50 | 3998.77 | | 3.5 | 2.8 | 2.5 | 3.4 | 2.2 | 3.6 | | |
| | | 27/05/2024 | 12 | 21.558 | 3998.77 | 4020.32 | | 3.5 | 2.8 | 2.5 | 3.4 | 2.2 | 3.6 | 2.26 | 2.09 |
| | | 28/05/2024 | 4 | 7.181 | 4020.32 | 4027.51 | | 3.5 | 2.8 | 2.5 | 3.4 | 2.2 | 3.6 | 2.20 | 2.16 |
| | | 30/05/2024 | 6 | 10.710 | 4027.51 | 4038.22 | | 3.5 | 2.8 | 2.5 | 3.4 | 2.2 | 3.6 | 2.24 | 2.18 |

Table 20 Average pressure in the crown during excavation and at the completion of the ring installation (TY11 sensor) (Report, 2024)

Only from ring 718 onwards, the $\mathbf{p_{f,c}}$ is below the minimum alarm threshold of 2.20 bar during the installation phase. Despite this, there were no negative impacts on the stability of the face and the cable. This should indicate a face of excavation that is generally more stable than expected.

### 5.3.1 Injection volume and pressure

The location of the injection lines is referenced in Figure 5.4, while for the calculation of the volumes of two-component grout to be injected from each individual line, equations (5.1) and (5.2) from section 5.1.1 were used.

The same proportions were applied to calculate the minimum volume of 10.74 m³ in the case of shield tail ground contact.

For the alert and alarm thresholds of the volume corresponding to line #i, to be filled with two-component grout, the procedure followed was the same as for the total mix volume per ring, using the formulas (5.3a)-(5.3.d) already presented in section 5.1.1.

The graph in Figure 5.25 shows the injection volume of the two-component grout, while Table 22 provides the average volume value **V** per section.

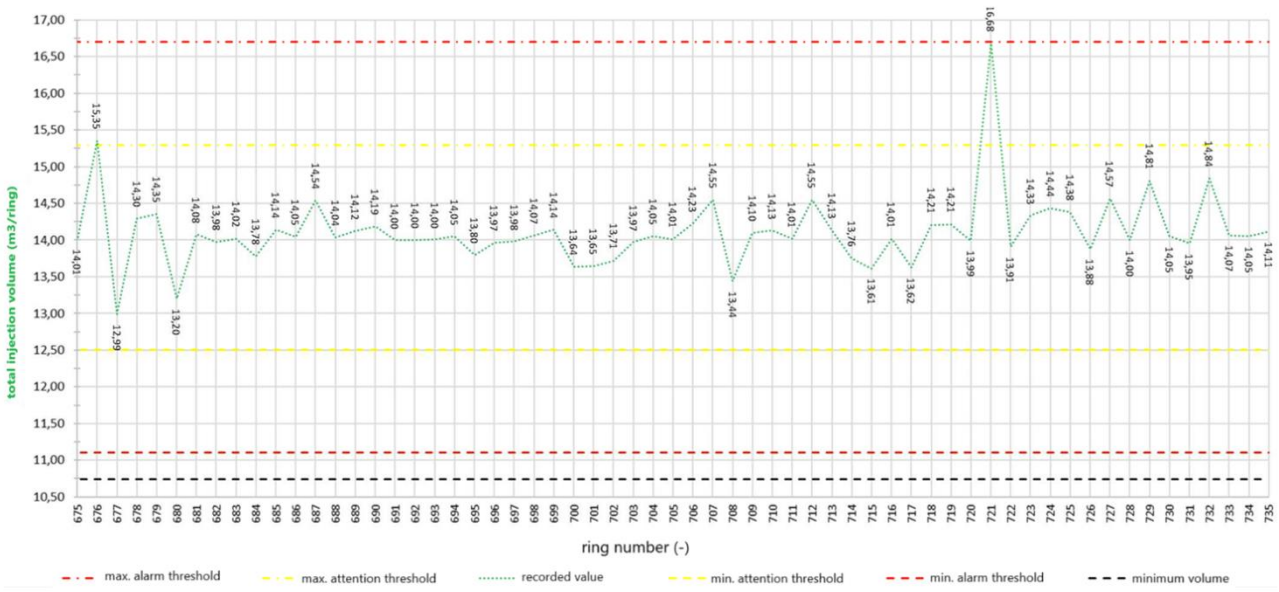


Figure 5.25 Total injection volume of the two-component mixture in m³/ring (Report, 2024)

| Omog. Segments Geom. | segment number | day | n° of ring installed | Lenght L (m) | starting pk (m) | final pk (m) | L total (m) | V (m³/ring) | ATTENTION (m³/ring) | | ALARM (m³/ring) | | average V (m³/ring) |
|---|---|---|---|---|---|---|---|---|---|---|---|---|---|
| | | | | | | | | | MIN | MAX | MIN | MAX | |
| FYRavc | 7 | 17/052024 | 1 | 1.723 | 3928.56 | 3930.29 | 109.7 | 13.91 | 12.5 | 15.3 | 11.1 | 16.7 | 14.01 |
| FYRmar+FYRar | | 23/05/2024 | 4 | 5.644 | 3930.29 | 3935.93 | | 13.91 | 12.5 | 15.3 | 11.1 | 16.7 | 14.25 |
| | 8 | | | 1.722 | 3935.93 | 3937.65 | | 13.91 | 12.5 | 15.3 | 11.1 | 16.7 | |
| | | 24/05/2024 | 10 | 11.408 | 3937.65 | 3949.06 | | 13.91 | 12.5 | 15.3 | 11.1 | 16.7 | 13.99 |
| | 9 | | | 6.465 | 3949.06 | 3955.53 | | 13.91 | 12.5 | 15.3 | 11.1 | 16.7 | |
| | | 25/05/2024 | 12 | 6.975 | 3955.53 | 3962.50 | | 13.91 | 12.5 | 15.3 | 11.1 | 16.7 | 13.96 |
| | | | | 14.621 | 3962.50 | 3977.12 | | 13.91 | 12.5 | 15.3 | 11.1 | 16.7 | |
| | | 26/05/2024 | 12 | 10.379 | 3977.12 | 3987.50 | | 13.91 | 12.5 | 15.3 | 11.1 | 16.7 | 14.07 |
| | | | | 11.266 | 3987.50 | 3998.77 | | 13.91 | 12.5 | 15.3 | 11.1 | 16.7 | |
| | | 27/05/2024 | 12 | 21.558 | 3998.77 | 4020.32 | | 13.91 | 12.5 | 15.3 | 11.1 | 16.7 | 14.26 |
| | | 28/05/2024 | 4 | 7.181 | 4020.32 | 4027.51 | | 13.91 | 12.5 | 15.3 | 11.1 | 16.7 | 14.31 |
| | | 30/05/2024 | 6 | 10.710 | 4027.51 | 4038.22 | | 13.91 | 12.5 | 15.3 | 11.1 | 16.7 | 14.18 |

Table 21 Average injection volume of the two-component mixture in m³/ring per section (Report, 2024)

The pressure of the individual injection lines for component A was calculated using formula (5.4) (section 5.1.1).

The alert and alarm thresholds were defined as for the face pressure and the pressure in the crown (equations (5.5a)-(5.5d), section 5.1.1).

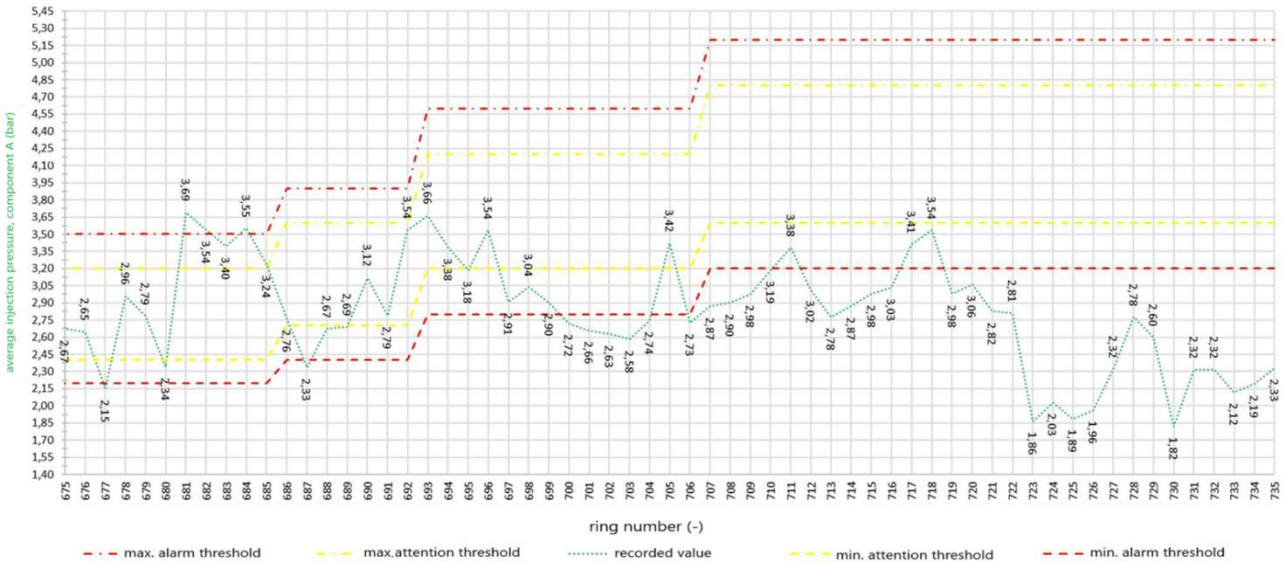


Figure 5.26 Average injection pressure of component A per section (Report, 2024)

| Omog. Segments Geom. | segment number | day | n° of ring installed | Lenght L (m) | starting pk (m) | final pk (m) | L total (m) | $p_m$ (bar) | ATTENTION (bar) | | ALARM (bar) | | average $p_m$ (bar) |
|---|---|---|---|---|---|---|---|---|---|---|---|---|---|
| | | | | | | | | | MIN | MAX | MIN | MAX | |
| FYRavc | 7 | 17/052024 | 1 | 1.723 | 3928.56 | 3930.29 | 109.7 | 2.7 | 2.4 | 3.2 | 2.2 | 3.5 | 2.67 |
| FYRmar+FYRar | 8 | 23/05/2024 | 4 | 5.644 | 3930.29 | 3935.93 | | 2.7 | 2.4 | 3.2 | 2.2 | 3.5 | 2.64 |
| | | | | 1.722 | 3935.93 | 3937.65 | | | | | | | |
| | | 24/05/2024 | 10 | 11.408 | 3937.65 | 3949.06 | | 2.7 | 2.4 | 3.2 | 2.2 | 3.5 | 3.02 |
| | 9 | | | 6.465 | 3949.06 | 3955.53 | | 3.0 | 2.7 | 3.6 | 2.4 | 3.9 | |
| | | 25/05/2024 | 12 | 6.975 | 3955.53 | 3962.50 | | 3.0 | 2.7 | 3.6 | 2.4 | 3.9 | 3.12 |
| | | | | 14.621 | 3962.50 | 3977.12 | | 3.5 | 3.2 | 4.2 | 2.8 | 4.6 | |
| | | 26/05/2024 | 12 | 10.379 | 3977.12 | 3987.50 | | 3.5 | 3.2 | 4.2 | 2.8 | 4.6 | 2.93 |
| | | | | 11.266 | 3987.50 | 3998.77 | | 4.0 | 3.6 | 4.8 | 3.2 | 5.2 | |
| | | 27/05/2024 | 12 | 21.558 | 3998.77 | 4020.32 | | 4.0 | 3.6 | 4.8 | 3.2 | 5.2 | 2.77 |
| | | 28/05/2024 | 4 | 7.181 | 4020.32 | 4027.51 | | 4.0 | 3.6 | 4.8 | 3.2 | 5.2 | 2.41 |
| | | 30/05/2024 | 6 | 10.710 | 4027.51 | 4038.22 | | 4.0 | 3.6 | 4.8 | 3.2 | 5.2 | 2.18 |

Table 22 Average injection pressure of component A per section (Report, 2024)

The injection pressure values recorded from the installation of ring 700 onwards show a decreasing trend, staying below the minimum alarm threshold, which fluctuates between 2.80 and 3.20 bar. However, there were no negative impacts on the stability of the face and the cable. This reduction is justified by the fact that, as explained with reference to Figure 5.26, a more stable excavation face is assumed (thus, since the injection pressure for backfilling is always higher than the face pressure, it confirms the assumption).

### 5.3.2 Thrust and torque

For the position of the 6 thrust groups (A, B, C, D, E, F), refer to Figure 5.7 in paragraph 5.1.2.

The thrusts in the individual thrust groups A, B, C, D, E, and F, generated by the lower and upper expected maximum thrust, respectively

a) 42 and 63 MN between pk 3+928.56 and 3+949.06;
b) 45 and 68 MN between pk 3+949.06 and 3+962.50;
c) 50 and 75 MN between pk 3+962.50 and 3+987.50;
d) 55 and 82 MN between pk 3+987.50 and 4+038.22;

They were determined taking into account that the center of gravity of the pistons is located on the axis of the tunnel.
The eccentricity between the thrust axis and the center of gravity of the pistons $\mathbf{e_{app}}$ was calculated by assuming a trapezoidal pressure distribution on the excavation face.
Each thrust is considered on type 2 segments, i.e., segments reinforced with a denser reinforcement starting from 300 m from the tunnel entrance. The maximum excavation thrusts in groups A, B, C, D, E, and F satisfy the SLE, so the maximum thrust during excavation was always lower than the "maximum thrust for type 2 segments" (red line, section, and point).
The thrust exerted by the generic piston i is obtained as seen in section 5.1.2 (equations (5.6)-(5.8)). $\mathbf{S_i}$ and $\mathbf{z_i}$ represent the total thrust exerted by the pistons on the lining ring and the distance from the horizontal axis to the center of gravity of the generic piston **i**, respectively, while **S** is the total thrust exerted by the pistons.

The average and maximum thrusts of only the thrust groups F and C are reported below (Figures 5.27 and Figures 5.28):

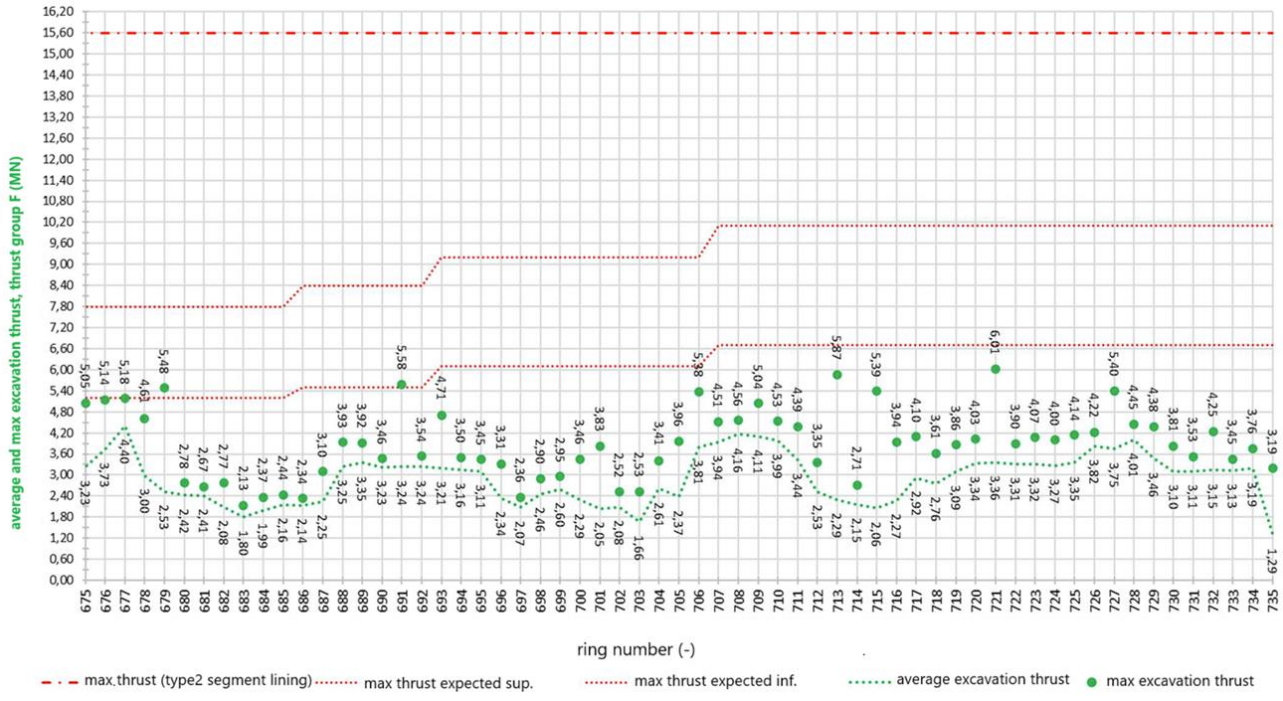


Figure 5.27 Average thrust and maximum thrust during the excavation phase exerted by the thrust group F (Report, 2024)

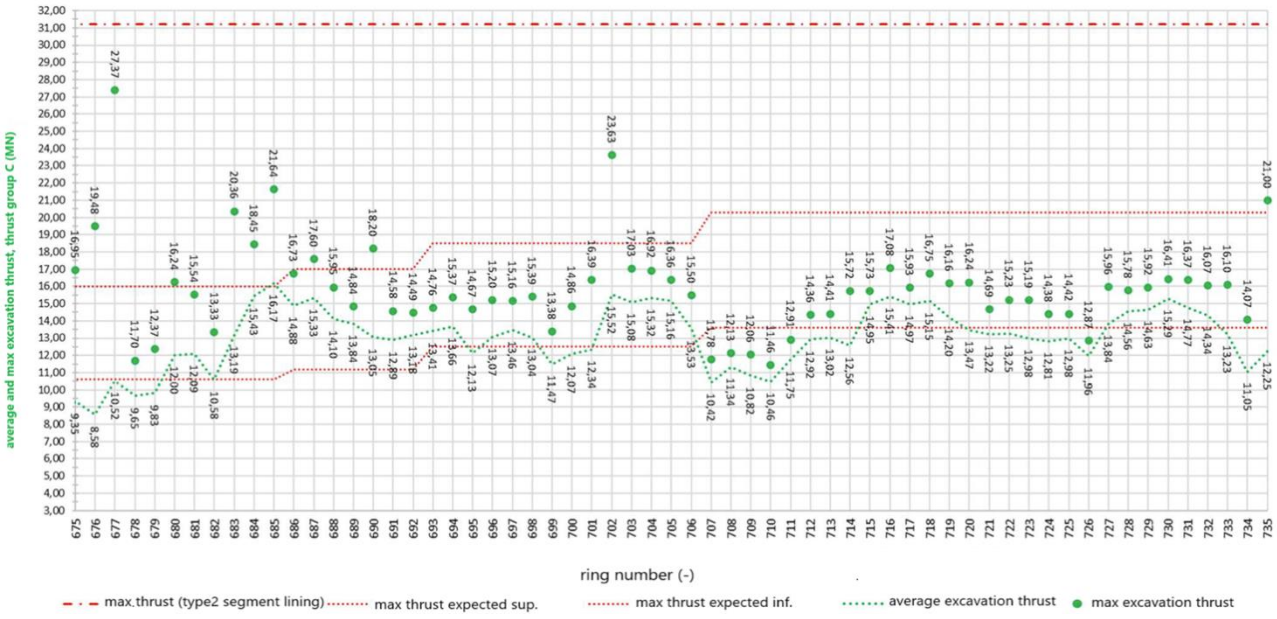


Figure 5.28 Average thrust and maximum thrust during the excavation phase exerted by the thrust group C (Report, 2024)

As expected from the trapezoidal pressure distribution on the excavation face, the thrust pistons of group C show higher values compared to those of group F, as the former are positioned lower than the latter.

In general, values below the minimum threshold indicate a softer face than expected, which therefore requires less thrust to be exerted. This could also be related to a more stable face, which requires less thrust, and vice versa. This choice did not lead to any negative impacts on the ongoing excavation.

Regarding the torque in the graph of Figure 5.10 (section 5.1.2), the maximum torque values are also shown. It is reminded that the torque on the cutterhead due to friction is strictly connected to the thrust force and the penetration.

In the graph in Figure 5.29, the average torque is shown as a function of the ring number, while in Table 24, the average values per section are listed as a function of the progress.

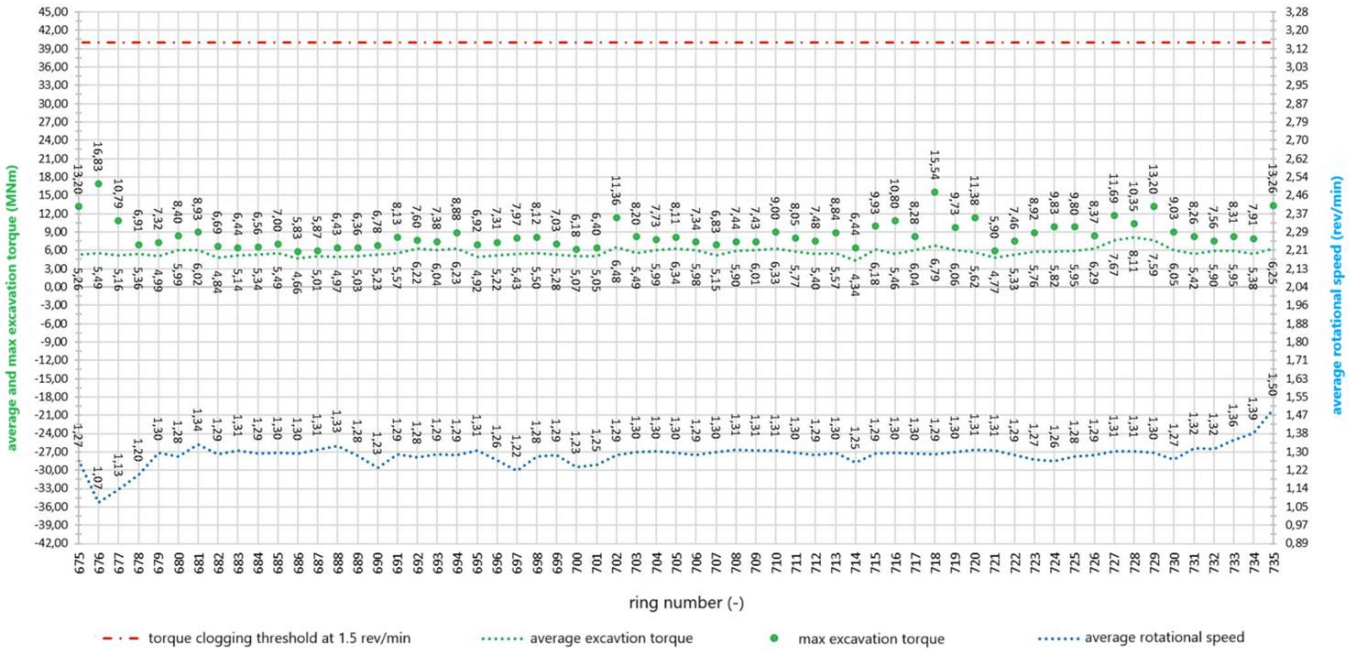


Figure 5.29 Average torque and maximum torque during excavation and average rotational speed (Report, 2024)

In the graph above, a roughly constant trend of the torque can be observed, similar to the average rotational speed.

| Omog. Segments Geom. | segment number | day | n° of ring installed | Lenght L (m) | starting pk (m) | final pk (m) | L total (m) | AVERAGE TORQUE (MNm) | MAX. TORQUE (MNm) | TORQUE FOR A CLOGGING THRESHOLD OF 1.5 rev/min (MNm) | average rotation speed ω (rev/min) |
|---|---|---|---|---|---|---|---|---|---|---|---|
| FYRavc | 7 | 17/052024 | 1 | 1.723 | 3928.56 | 3930.29 | 109.7 | 5.3 | 13.2 | 40 | 1.3 |
| | | 23/05/2024 | 4 | 5.644 | 3930.29 | 3935.93 | | 5.3 | 10.5 | 40 | 1.2 |
| FYRmar+FYRar | 8 | | | 1.722 | 3935.93 | 3937.65 | | | | | |
| | | 24/05/2024 | 10 | 11.408 | 3937.65 | 3949.06 | | 5.2 | 6.8 | 40 | 1.3 |
| | 9 | | | 6.465 | 3949.06 | 3955.53 | | | | | |
| | | 25/05/2024 | 12 | 6.975 | 3955.53 | 3962.50 | | 5.5 | 7.4 | 40 | 1.3 |
| | | | | 14.621 | 3962.50 | 3977.12 | | | | | |
| | | 26/05/2024 | 12 | 10.379 | 3977.12 | 3987.50 | | 5.9 | 8.2 | 40 | 1.3 |
| | | | | 11.266 | 3987.50 | 3998.77 | | | | | |
| | | 27/05/2024 | 12 | 21.558 | 3998.77 | 4020.32 | | 5.7 | 9.5 | 40 | 1.3 |
| | | 28/05/2024 | 4 | 7.181 | 4020.32 | 4027.51 | | 7.4 | 10.9 | 40 | 1.3 |
| | | 30/05/2024 | 6 | 10.710 | 4027.51 | 4038.22 | | 5.8 | 9.1 | 40 | 1.4 |

Table 23 Average torque and maximum torque during excavation and average rotational speed (Report, 2024)

As can be seen from the graph, each value falls within the limits.

### 5.3.3 Excavated material

The cover on the crown of the final tunnel lining, in the section covered by this weekly report, ranges from 8.3 to 31.4 meters, as per the Geomechanical/Geotechnical profile. In the section in question, the primary material used was FYRmar+FYRar, for which a weight per unit volume of 21.5 kN/m³ was estimated

The diagram of the average weight of the excavated soil for each installed ring, excluding the conditioning (see Chapter 6 for more details on soil conditioning), is compared with its gross average weight in Figure 5.30. In Table 25, following the graph, the net average values per section are provided.

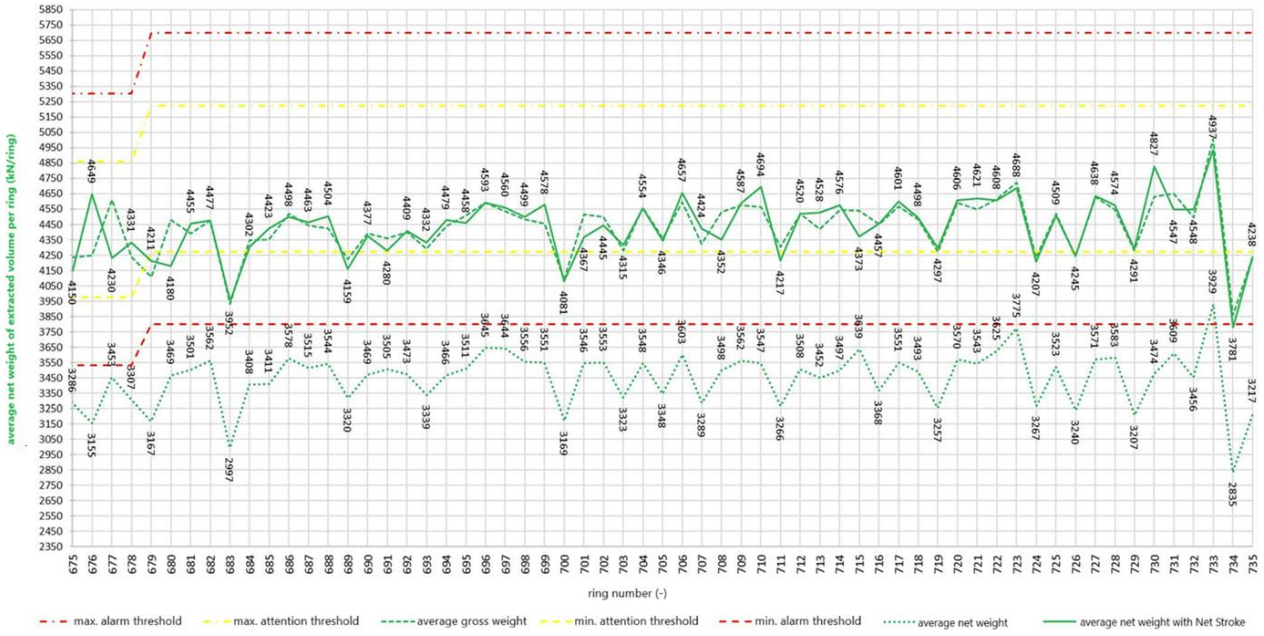


Figure 5.30 Comparison between the net weight and the gross weight of the material extracted per ring (Report, 2024)

| Omog. Segments Geom. | segment number | day | n° of ring installed | Lenght L (m) | starting pk (m) | final pk (m) | L total (m) | REFERENCE WEIGHT $P_t$ (kN) | ATTENTION MIN. (kN) | ATTENTION MAX. (kN) | ALARM MIN. (kN) | ALARM MAX. (kN) | AVERAGE NET WEIGHT (kN) | AVERAGE GROSS WEIGHT (kN) |
|---|---|---|---|---|---|---|---|---|---|---|---|---|---|---|
| FYRavc | 7 | 17/052024 | 1 | 1.723 | 3928.56 | 3930.29 | 109.7 | 4418 | 3976 | 4860 | 3534 | 5302 | 3286 | 4237 |
| | | 23/05/2024 | 4 | 5.644 | 3930.29 | 3935.93 | | | | | | | | |
| FYRmar+FYRar | 8 | | | 1.722 | 3935.93 | 3937.65 | | 4749 | 4274 | 5224 | 3799 | 5699 | 3270 | 4302 |
| | | 24/05/2024 | 10 | 11.408 | 3937.65 | 3949.06 | | 4749 | 4274 | 5224 | 3799 | 5699 | 3430 | 4359 |
| | 9 | | | 6.465 | 3949.06 | 3955.53 | | | | | | | | |
| | | 25/05/2024 | 12 | 6.975 | 3955.53 | 3962.50 | | 4749 | 4274 | 5224 | 3799 | 5699 | 3490 | 4422 |
| | | | | 14.621 | 3962.50 | 3977.12 | | | | | | | | |
| | | 26/05/2024 | 12 | 10.379 | 3977.12 | 3987.50 | | 4749 | 4274 | 5224 | 3799 | 5699 | 3458 | 4462 |
| | | | | 11.266 | 3987.50 | 3998.77 | | | | | | | | |
| | | 27/05/2024 | 12 | 21.558 | 3998.77 | 4020.32 | | 4749 | 4274 | 5224 | 3799 | 5699 | 3509 | 4508 |
| | | 28/05/2024 | 4 | 7.181 | 4020.32 | 4027.51 | | 4749 | 4274 | 5224 | 3799 | 5699 | 3400 | 4424 |
| | | 30/05/2024 | 6 | 10.710 | 4027.51 | 4038.22 | | 4749 | 4274 | 5224 | 3799 | 5699 | 3420 | 4480 |

Table 24 The weight of the net excavated material extracted per ring (Report, 2024)

In Figure 5.30, we can observe that the gross average weight remains within the limits set by the P.A.T.

In the diagram in Figure 5.31, the average pressures on sensors TY11 and TY07 are shown (for their positions, refer to Figure 5.1). The average values are calculated during the advancement phase of the shield or considering both the shield advancement and the installation of the precast ring.The TY11 sensor is located at the top compared to TY07, which justifies the fact that the pressures from the former are higher than those from the latter, given the trapezoidal distribution of thrusts in the excavation chamber.
At ring 718, we observe a significant minimum, which is consistent with what was seen in the previous figure, allowing us to hypothesize a rather stable face.

In Figure 5.32, the average apparent density is shown, calculated using the pressures reported in Figure 5.31, taking into account that the elevation difference between the two sensors is 8 m. Knowing the average apparent density in the excavation chamber allows us to adjust the TBM for more efficient auger extraction, reducing the risk of clogging. Density affects the pressure needed to support the excavation face: if it is too high, it could indicate compact soils, which may require more force or a special support system; a low density might suggest less stable soils. In particular, for soils with low density, water infiltration could become a problem, so monitoring the density helps predict and mitigate this risk.


Figure 5.31 Face pressure: comparison between TY06 and TY11 sensors (Report, 2024)

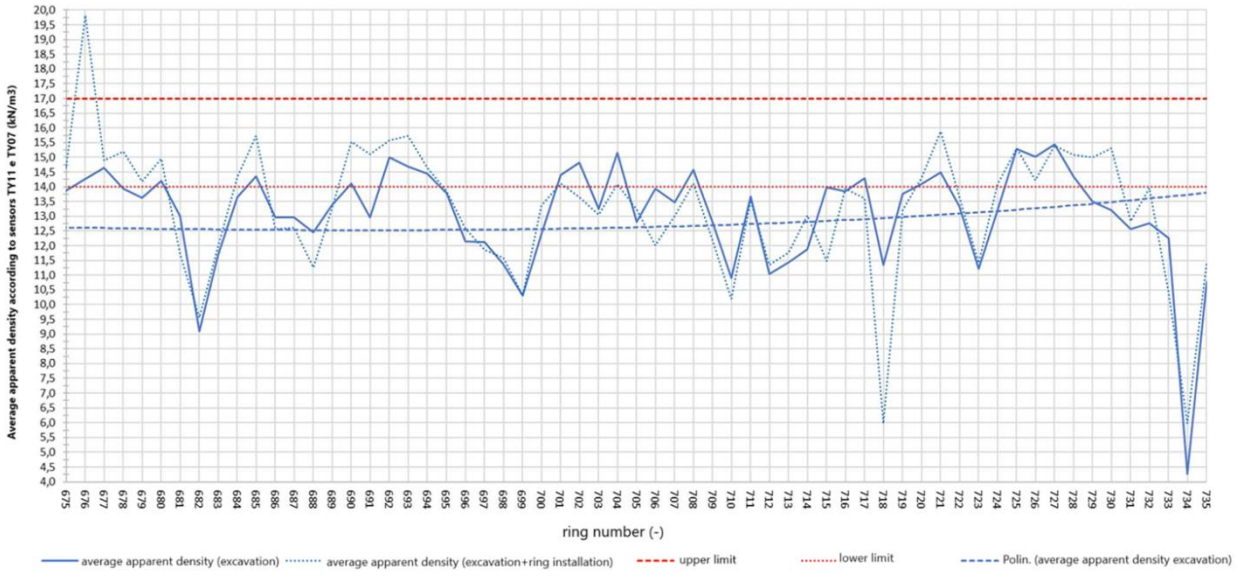


Figure 5.32 Average apparent density in the excavation chamber, TY06 and TY11 sensors (Report, 2024)

| Omog. Segments Geom. | segment number | day | n° of ring installed | Lenght L (m) | starting pk (m) | final pk (m) | L total (m) | pressure sensors TY11-TY07 | | | | |
|---|---|---|---|---|---|---|---|---|---|---|---|---|
| | | | | | | | | $\gamma_{app,\ exc.}$ (kN/m$^3$) | lower limit | upper limit | average $\gamma_{app}$ over 24h | |
| | | | | | | | | | | | $\gamma_{app,\ excavation}$ (kN/m$^3$) | $\gamma_{app,\ excavation+ring\ installation}$ (kN/m$^3$) |
| FYRavc | 7 | 17/052024 | 1 | 1.723 | 3928.56 | 3930.29 | 109.7 | 15 | 14 | 17 | 13.9 | 14.6 |
| | | 23/05/2024 | 4 | 5.644 | 3930.29 | 3935.93 | | 15 | 14 | 17 | 14.1 | 16.0 |
| FYRmar+ FYRar | 8 | | | 1.722 | 3935.93 | 3937.65 | | | | | | |
| | | 24/05/2024 | 10 | 11.408 | 3937.65 | 3949.06 | | 15 | 14 | 17 | 12.8 | 12.8 |
| | 9 | | | 6.465 | 3949.06 | 3955.53 | | | | | | |
| | | 25/05/2024 | 12 | 6.975 | 3955.53 | 3962.50 | | 15 | 14 | 17 | 13.1 | 13.7 |
| | | | | 14.621 | 3962.50 | 3977.12 | | | | | | |
| | | 26/05/2024 | 12 | 10.379 | 3977.12 | 3987.50 | | 15 | 14 | 17 | 13.2 | 12.7 |
| | | | | 11.266 | 3987.50 | 3998.77 | | | | | | |
| | | 27/05/2024 | 12 | 21.558 | 3998.77 | 4020.32 | | 15 | 14 | 17 | 13.4 | 13.0 |
| | | 28/05/2024 | 4 | 7.181 | 4020.32 | 4027.51 | | 15 | 14 | 17 | 14.6 | 14.9 |
| | | 30/05/2024 | 6 | 10.710 | 4027.51 | 4038.22 | | 15 | 14 | 17 | 11.0 | 11.7 |

Table 25 Average apparent density in the excavation chamber, TY06 and TY11 sensors (Report, 2024)

## 5.4 From May 31st to June 9th (rings installed 731-798 )

The excavation progress reports fall within the section covered by P.A.T. n°4 (Table 7). Excavation was halted on June 9 at pk 4+161.488 to allow for the emptying of the temporary spoil storage tanks.

In the graph in Figure 5.33, the pressure $\mathbf{p_{f,c}}$ is shown as a function of the ring number, while Table 27 presents the average value of $\mathbf{p_{f,c}}$ for each section, based on the progress.

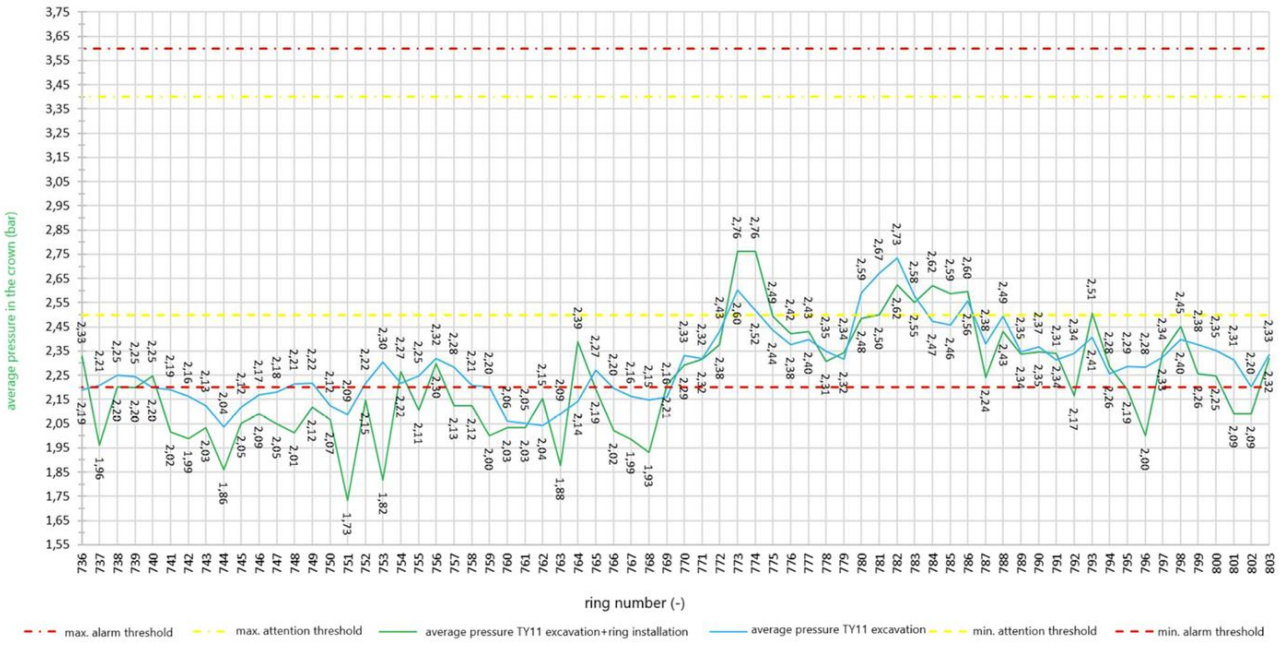


Figure 5.33 Average pressure in the crown during excavation and at the completion of the ring installation (TY11 sensor) (Report, 2024)

| Omog. Segments Geom. | segment number | day | n° of ring installed | Lenght L (m) | starting pk (m) | final pk (m) | L total (m) | $p_f$ (bar) | $p_{f,c}$ (bar) | ATTENTION (bar) | | ALARM (bar) | | average $p_{f,c}$ value (bar) | |
|---|---|---|---|---|---|---|---|---|---|---|---|---|---|---|---|
| | | | | | | | | | | MIN | MAX | MIN | MAX | excavation | excavation + ring installation |
| FYRmar+FYRar | 9 | 01/06/2024 | 2 | 3.607 | 4038.22 | 4041.82 | 122.5 | 3.5 | 2.8 | 2.5 | 3.4 | 2.2 | 3.6 | 2.20 | 2.15 |
| | | 02/06/2024 | 13 | 23.383 | 4041.82 | 4065.21 | | 3.5 | 2.8 | 2.5 | 3.4 | 2.2 | 3.6 | 2.17 | 2.07 |
| FYRagms | 10 | 03/06/2024 | 14 | 25.198 | 4065.21 | 4090.40 | | 3.5 | 2.8 | 2.5 | 3.4 | 2.2 | 3.6 | 2.18 | 2.08 |
| | | 04/06/2024 | 8 | 14.394 | 4090.40 | 4104.80 | | 3.5 | 2.8 | 2.5 | 3.4 | 2.2 | 3.6 | 2.25 | 2.17 |
| | | 06/06/2024 | 9 | 16.189 | 4104.80 | 4120.99 | | 3.5 | 2.8 | 2.5 | 3.4 | 2.2 | 3.6 | 2.47 | 2.50 |
| | | 07/06/2024 | 6 | 10.856 | 4120.99 | 4131.84 | | 3.5 | 2.8 | 2.5 | 3.4 | 2.2 | 3.6 | 2.53 | 2.54 |
| | | 08/06/2024 | 9 | 16.238 | 4131.84 | 4148.08 | | 3.5 | 2.8 | 2.5 | 3.4 | 2.2 | 3.6 | 2.34 | 2.29 |
| | | 09/06/2024 | 7 | 12.637 | 4148.08 | 4160.72 | | 3.5 | 2.8 | 2.5 | 3.4 | 2.2 | 3.6 | 2.33 | 2.26 |

Table 26 Average pressure in the crown during excavation and at the completion of the ring installation (TY11 sensor) (Report, 2024)

Ciò dovrebbe indicare un fronte di scavo tendenzialmente più stabile di quanto previsto. For almost the entire section, the $\mathbf{p_{f,c}}$ values are below the minimum alarm threshold of 2.20 bar during the installation phase. Despite this, there were no negative impacts on the stability of the face and the cable. This should indicate a face of excavation that is generally more stable than expected.

### 5.4.1 Injection volume and pressure

The location of the injection lines is referenced in Figure 5.4, while for the calculation of the volumes of two-component grout to be injected from each individual line, equations (5.1) and (5.2) from section 5.1.1 were used.

The same proportions were applied to calculate the minimum volume of 10.74 m³ in the case of shield tail ground contact.

For the alert and alarm thresholds of the volume corresponding to line #i, to be filled with two-component grout, the procedure followed was the same as for the total mix volume per ring, using the formulas (5.3a)-(5.3.d) already presented in section 5.1.1.

The graph in Figure 5.34 shows the injection volume of the two-component grout, while Table 28 provides the average volume value **V** per section.

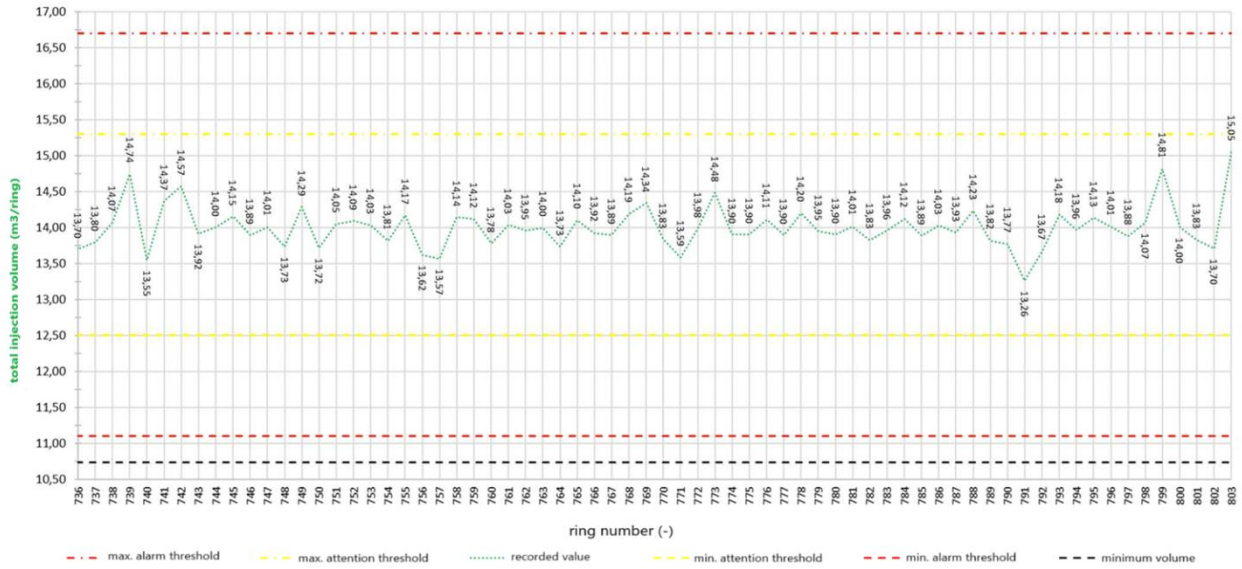


Figure 5.34 Total injection volume of the two-component mixture in m³/ring (Report, 2024)

| Omog. Segments Geom. | segment number | day | n° of ring installed | Lenght L (m) | starting pk (m) | final pk (m) | L total (m) | V ($m^3$/ring) | ATTENTION ($m^3$/ring) | | ALARM ($m^3$/ring) | | minimum V ($m^3$/ring) | average V ($m^3$/ring) |
|---|---|---|---|---|---|---|---|---|---|---|---|---|---|---|
| | | | | | | | | | MIN | MAX | MIN | MAX | | |
| FYRmar+FYRar | 9 | 01/06/2024 | 2 | 3.607 | 4038.22 | 4041.82 | 122.5 | 13.91 | 12.52 | 15.30 | 11.13 | 16.69 | 10.74 | 13.75 |
| | | 02/06/2024 | 13 | 23.383 | 4041.82 | 4065.21 | | 13.91 | 12.52 | 15.30 | 11.13 | 16.69 | 10.74 | 14.08 |
| FYRagms | 10 | 03/06/2024 | 14 | 25.198 | 4065.21 | 4090.40 | | 13.91 | 12.52 | 15.30 | 11.13 | 16.69 | 10.74 | 13.94 |
| | | 04/06/2024 | 8 | 14.394 | 4090.40 | 4104.80 | | 13.91 | 12.52 | 15.30 | 11.13 | 16.69 | 10.74 | 13.98 |
| | | 06/06/2024 | 9 | 16.189 | 4104.80 | 4120.99 | | 13.91 | 12.52 | 15.30 | 11.13 | 16.69 | 10.74 | 14.04 |
| | | 07/06/2024 | 6 | 10.856 | 4120.99 | 4131.84 | | 13.91 | 12.52 | 15.30 | 11.13 | 16.69 | 10.74 | 13.96 |
| | | 08/06/2024 | 9 | 16.238 | 4131.84 | 4148.08 | | 13.91 | 12.52 | 15.30 | 11.13 | 16.69 | 10.74 | 13.89 |
| | | 09/06/2024 | 7 | 12.637 | 4148.08 | 4160.72 | | 13.91 | 12.52 | 15.30 | 11.13 | 16.69 | 10.74 | 14.19 |

Table 27 Average injection volume of the two-component mixture in $m^3$/ring per section (Report, 2024)

La The pressure of the individual injection lines for component A was calculated using formula (5.4) (section 5.1.1).

The alert and alarm thresholds were defined as for the face pressure and the pressure in the crown (equations (5.5a)-(5.5d), section 5.1.1).

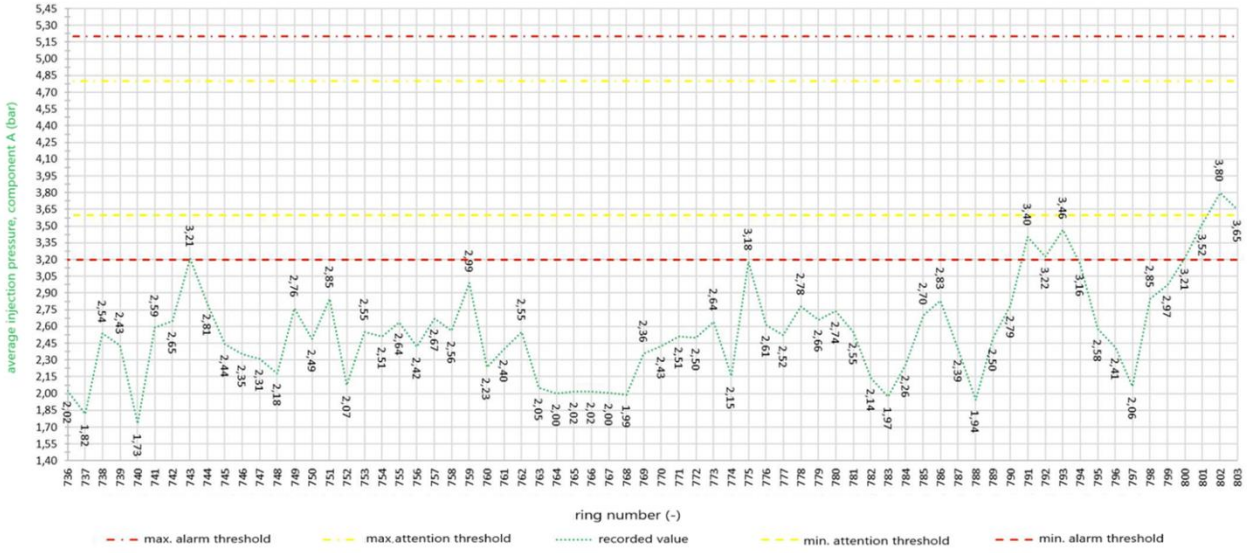


Figure 5.35 Average injection pressure of component A per section (Report, 2024)

| Omog. Segments Geom. | segment number | day | n° of ring installed | Lenght L (m) | starting pk (m) | final pk (m) | L total (m) | $p_m$ (bar) | ATTENTION (bar) | | ALARM (bar) | | average $p_m$ (bar) |
|---|---|---|---|---|---|---|---|---|---|---|---|---|---|
| | | | | | | | | | MIN | MAX | MIN | MAX | |
| FYRmar+FYRar | 9 | 01/06/2024 | 2 | 3.607 | 4038.22 | 4041.82 | 122.5 | 4.0 | 3.6 | 4.8 | 3.2 | 5.2 | 1.92 |
| | | 02/06/2024 | 13 | 23.383 | 4041.82 | 4065.21 | | 4.0 | 3.6 | 4.8 | 3.2 | 5.2 | 2.50 |
| FYRagms | 10 | 03/06/2024 | 14 | 25.198 | 4065.21 | 4090.40 | | 4.0 | 3.6 | 4.8 | 3.2 | 5.2 | 2.46 |
| | | 04/06/2024 | 8 | 14.394 | 4090.40 | 4104.80 | | 4.0 | 3.6 | 4.8 | 3.2 | 5.2 | 2.23 |
| | | 06/06/2024 | 9 | 16.189 | 4104.80 | 4120.99 | | 4.0 | 3.6 | 4.8 | 3.2 | 5.2 | 2.65 |
| | | 07/06/2024 | 6 | 10.856 | 4120.99 | 4131.84 | | 4.0 | 3.6 | 4.8 | 3.2 | 5.2 | 2.38 |
| | | 08/06/2024 | 9 | 16.238 | 4131.84 | 4148.08 | | 4.0 | 3.6 | 4.8 | 3.2 | 5.2 | 2.83 |
| | | 09/06/2024 | 7 | 12.637 | 4148.08 | 4160.72 | | 4.0 | 3.6 | 4.8 | 3.2 | 5.2 | 3.15 |

Table 28 Average injection pressure of component A per section (Report, 2024)

The injection pressure values recorded along the section are all below the minimum alarm threshold of 3.2 bar. Despite this, there were no negative impacts on the stability of the face and the cable. The reduction is justified by the fact that, as explained with reference to Figure 5.35, a more stable

excavation face is assumed (thus, since the injection pressure for backfilling is always higher than the face pressure, this confirms the assumption).

### 5.4.2 Thrust and torque

For the position of the 6 thrust groups (A, B, C, D, E, F), refer to Figure 5.7 in paragraph 5.1.2.

The thrusts in the individual thrust groups A, B, C, D, E, and F, generated by the lower and upper expected maximum thrusts, respectively 55 and 82 MN, between pk 4+038.22 and 4+170.72, they were determined taking into account that the center of gravity of the pistons is located on the axis of the tunnel. The eccentricity between the thrust axis and the center of gravity of the pistons $\mathbf{e_{app}}$ was calculated by assuming a trapezoidal pressure distribution on the excavation face.
Each thrust is considered on type 2 segments, i.e., segments reinforced with a denser reinforcement starting from 300 m from the tunnel entrance. The maximum excavation thrusts in groups A, B, C, D, E, and F satisfy the SLE, so the maximum thrust during excavation was always lower than the "maximum thrust for type 2 segments" (red line, section, and point).
The thrust exerted by the generic piston i is obtained as seen in section 5.1.2 (equations (5.6)-(5.8)). $\mathbf{S_i}$ and $\mathbf{z_i}$ represent the total thrust exerted by the pistons on the lining ring and the distance from the horizontal axis to the center of gravity of the generic piston **i**, respectively, while **S** is the total thrust exerted by the pistons.

The average and maximum thrusts of only the thrust groups F and C are reported below (Figures 5.36 and Figures 5.37):

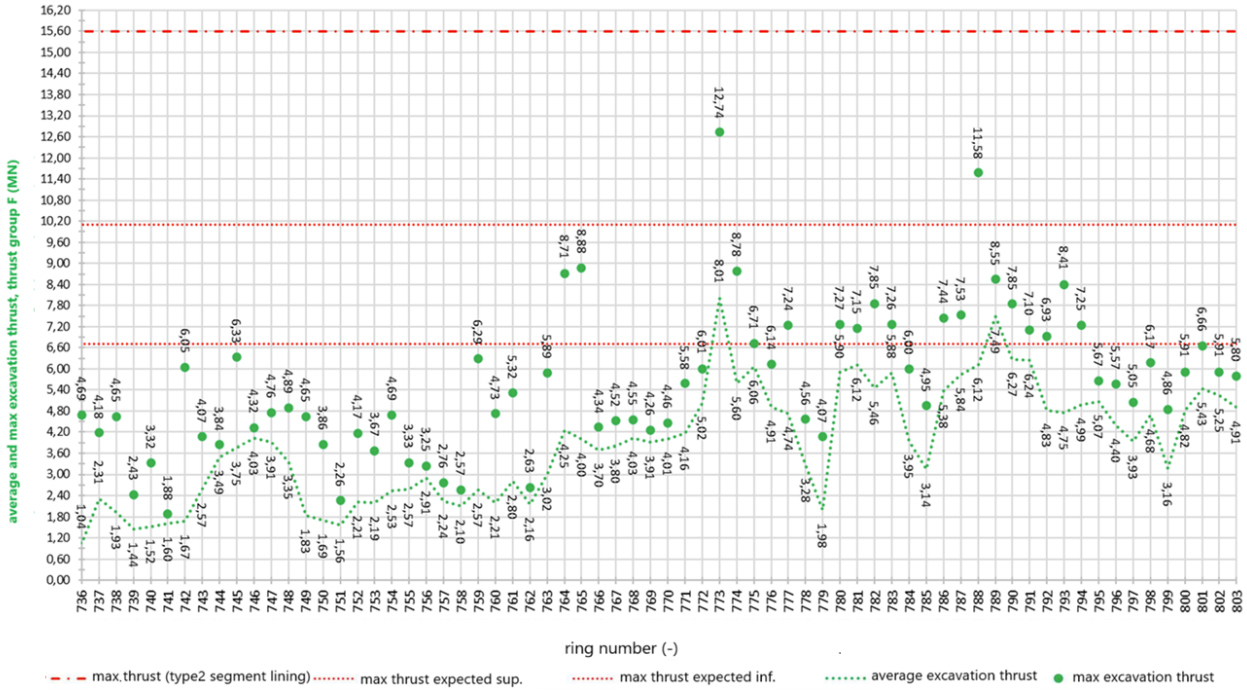


Figure 5.36 Average thrust and maximum thrust during the excavation phase exerted by the thrust group F (Report, 2024)

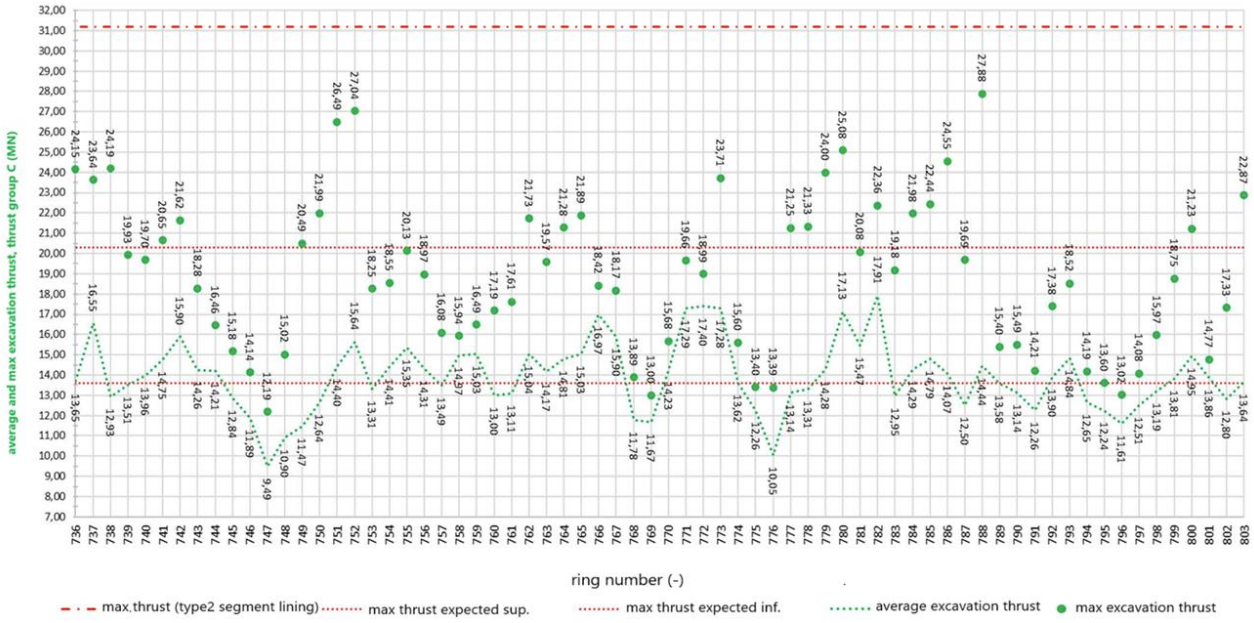


Figure 5.37 Average thrust and maximum thrust during the excavation phase exerted by the thrust group C (Report, 2024)

As expected from the trapezoidal pressure distribution on the excavation face, the thrust pistons of group C show higher values compared to those of group F, as the former are positioned lower than the latter.
In general, values below the minimum threshold indicate a softer face than expected, which therefore requires less thrust to be exerted. This could also be linked to a more stable face, which requires less thrust (and vice versa). The most noticeable peak occurs at the installation of ring 788. This choice did not lead to any negative impacts on the ongoing excavation.

Regarding the torque, Figure 5.10 (paragraph 5.1.2) also shows the maximum torque values. It is important to note that the torque on the cutterhead, due to friction, is strictly related to the thrust force and penetration.

In the graph in Figure 5.38, the average torque is shown as a function of the ring number, while Table 30 presents the average values for each section according to the progressive.

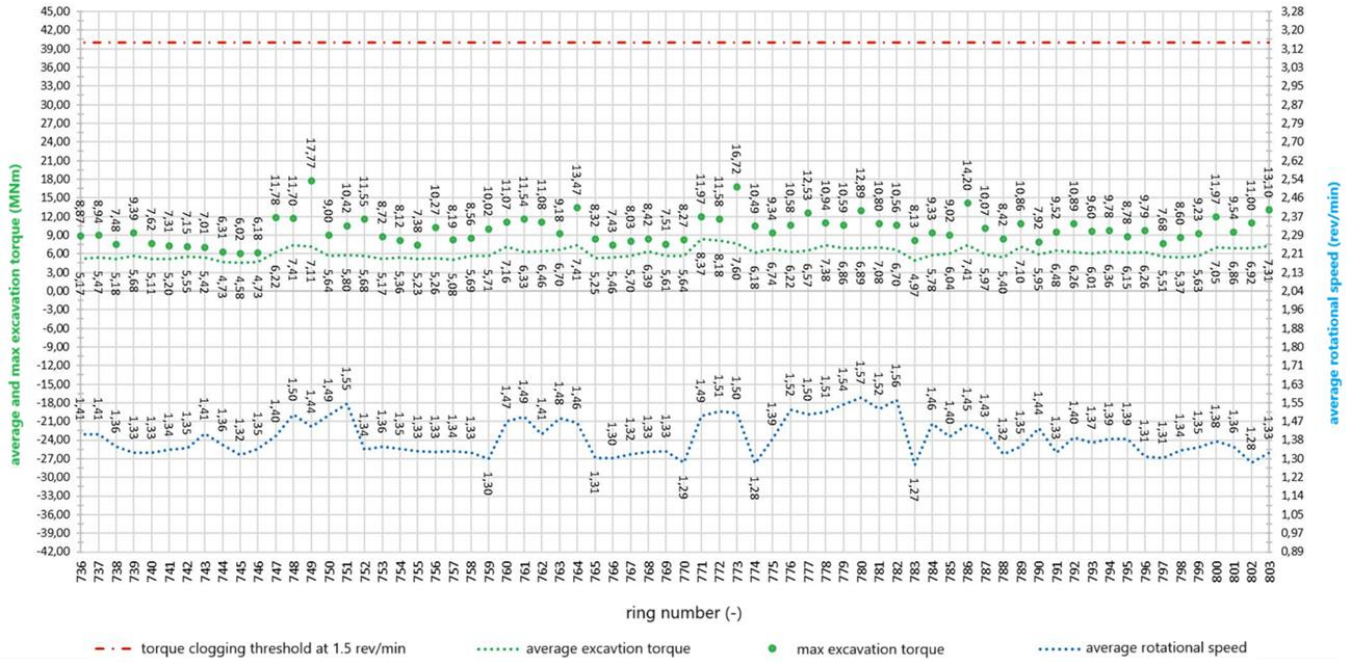


Figure 5.38 Average torque and maximum torque during excavation and average rotational speed (Report, 2024)

In the graph above, a roughly constant trend of the torque can be observed, while the average rotational speed is slightly more fluctuating. This can be justified by the fact that a section of harder ground increases the friction between the excavation face and the cutterhead, thus requiring a reduction in the average rotational speed (and vice versa).

| Omog. Segments Geom. | segment number | day | n° of ring installed | Lenght L (m) | starting pk (m) | final pk (m) | L total (m) | AVERAGE TORQUE (MNm) | MAX. TORQUE (MNm) | TORQUE FOR A CLOGGING THRESHOLD OF 1.5 rev/min (MNm) | average rotation speed ω (rev/min) |
|---|---|---|---|---|---|---|---|---|---|---|---|
| FYRmar+FYRar | 9 | 01/06/2024 | 2 | 3.607 | 4038.22 | 4041.82 | 122.5 | 5.32 | 8.91 | 40 | 1.41 |
| | | 02/06/2024 | 13 | 23.383 | 4041.82 | 4065.21 | | 5.58 | 8.83 | 40 | 1.38 |
| FYRagms | 10 | 03/06/2024 | 14 | 25.198 | 4065.21 | 4090.40 | | 5.93 | 9.97 | 40 | 1.39 |
| | | 04/06/2024 | 8 | 14.394 | 4090.40 | 4104.80 | | 6.32 | 8.94 | 40 | 1.36 |
| | | 06/06/2024 | 9 | 16.189 | 4104.80 | 4120.99 | | 6.84 | 11.65 | 40 | 1.48 |
| | | 07/06/2024 | 6 | 10.856 | 4120.99 | 4131.84 | | 6.14 | 10.22 | 40 | 1.43 |
| | | 08/06/2024 | 9 | 16.238 | 4131.84 | 4148.08 | | 6.22 | 9.51 | 40 | 1.37 |
| | | 09/06/2024 | 7 | 12.637 | 4148.08 | 4160.72 | | 6.38 | 10.16 | 40 | 1.34 |

Table 29 Average torque and maximum torque during excavation and average rotational speed (Report, 2024)

As can be seen from the graph, each value falls within the limits.

### 5.4.3 Excavated material

The cover on the crown of the final tunnel lining, in the section covered by this weekly report, ranges between 31.5 and 32 meters, as per the Geomechanical/Geotechnical profile. In the section in question, FYRmar+FYRar is specified between pk 4+038.22 and 4+065.21, and FYRagms is specified between pk 4+065.21 and 4+160.72; the design weight per unit volume for the two geotechnical units is 21.5 and 20.0 kN/m³, respectively.

The diagram of the average weight of the excavated soil for each installed ring, excluding the conditioning (see Chapter 6 for more details on soil conditioning), is compared with its gross average weight in Figure 5.39. In Table 31, following the graph, the net average values per section are provided.

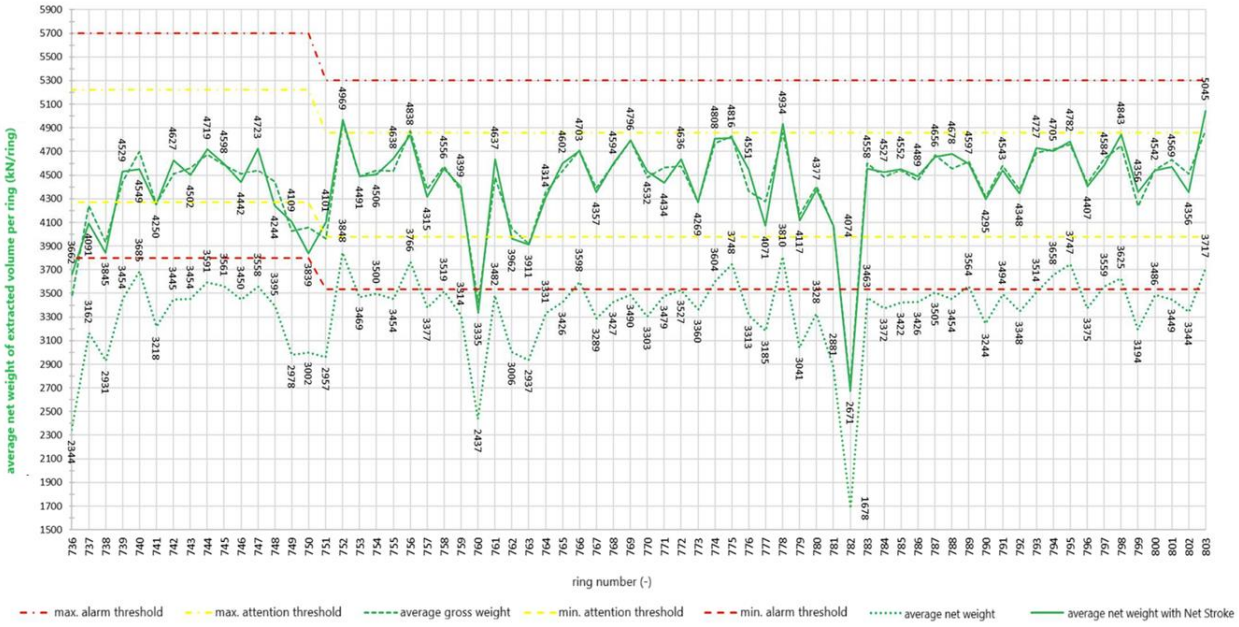


Figure 5.39 Comparison between the net weight and the gross weight of the material extracted per ring (Report, 2024)

| Omog. Segments Geom. | segment number | day | n° of ring installed | Lenght L (m) | starting pk (m) | final pk (m) | L total (m) | REFERENCE WEIGHT $P_t$ (kN) | ATTENTION MIN. (kN) | ATTENTION MAX. (kN) | ALARM MIN. (kN) | ALARM MAX. (kN) | AVERAGE NET WEIGHT (kN) | AVERAGE GROSS WEIGHT (kN) |
|---|---|---|---|---|---|---|---|---|---|---|---|---|---|---|
| FYRmar+FYRar | 9 | 01/06/2024 | 2 | 3.607 | 4038.22 | 4041.82 | | 4749 | 4274 | 5224 | 3799 | 5699 | 2753 | 3854 |
| | | 02/06/2024 | 13 | 23.383 | 4041.82 | 4065.21 | | 4749 | 4274 | 5224 | 3799 | 5699 | 3363 | 4404 |
| FYRagms | 10 | 03/06/2024 | 14 | 25.198 | 4065.21 | 4090.40 | | 4418 | 3976 | 4860 | 3534 | 5302 | 3314 | 4350 |
| | | 04/06/2024 | 8 | 14.394 | 4090.40 | 4104.80 | | 4418 | 3976 | 4860 | 3534 | 5302 | 3442 | 4580 |
| | | 06/06/2024 | 9 | 16.189 | 4104.80 | 4120.99 | 122.5 | 4418 | 3976 | 4860 | 3534 | 5302 | 3363 | 4446 |
| | | 07/06/2024 | 6 | 10.856 | 4120.99 | 4131.84 | | 4418 | 3976 | 4860 | 3534 | 5302 | 3145 | 4245 |
| | | 08/06/2024 | 9 | 16.238 | 4131.84 | 4148.08 | | 4418 | 3976 | 4860 | 3534 | 5302 | 3489 | 4560 |
| | | 09/06/2024 | 7 | 12.637 | 4148.08 | 4160.72 | | 4418 | 3976 | 4860 | 3534 | 5302 | 3482 | 4599 |

Table 30 The weight of the net excavated material extracted per ring (Report, 2024)

In Figure 5.39, we can observe a significant minimum at rings 760 and 782. In general, an increase in the average extracted weight value indicates optimal conditioning, while a minimum value may indicate either overly compact or excessively loose ground. Although these values exceed the alarm threshold, they did not cause issues during the auger extraction, as the conditioning was sufficient to keep the machine operating at optimal levels.

In the diagram in Figure 5.40, the average pressures on sensors TY11 and TY07 are shown (for their positions, refer to Figure 5.1). The average values are calculated during the advancement phase of the shield or considering both the shield advancement and the installation of the precast ring.The TY11 sensor is located at the top compared to TY07, which justifies the fact that the

pressures from the former are higher than those from the latter, given the trapezoidal distribution of thrusts in the excavation chambre.

In Figure 5.41, the average apparent density is shown, calculated using the pressures reported in Figure 5.40, taking into account that the elevation difference between the two sensors is 8 m. Knowing the average apparent density in the excavation chamber allows us to adjust the TBM for more efficient auger extraction, reducing the risk of clogging. Density affects the pressure needed to support the excavation face: if it is too high, it could indicate compact soils, which may require more force or a special support system; a low density might suggest less stable soils. In particular, for soils with low density, water infiltration could become a problem, so monitoring the density helps predict and mitigate this risk.

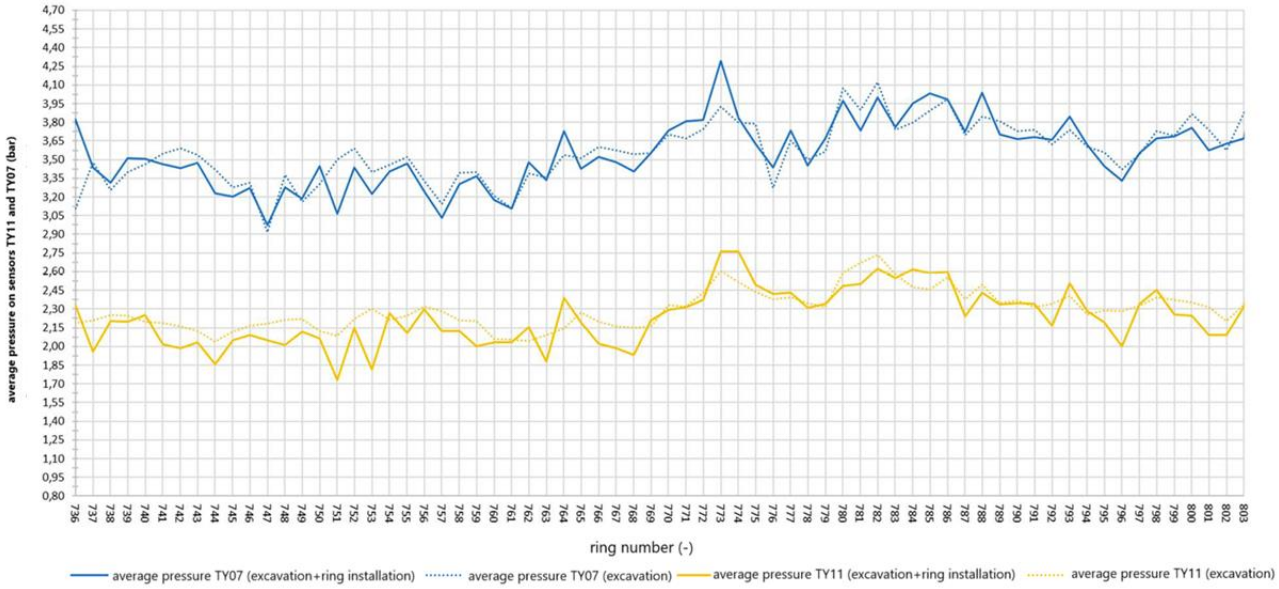


Figure 5.40 Face pressure: comparison between TY06 and TY11 sensors (Report, 2024)

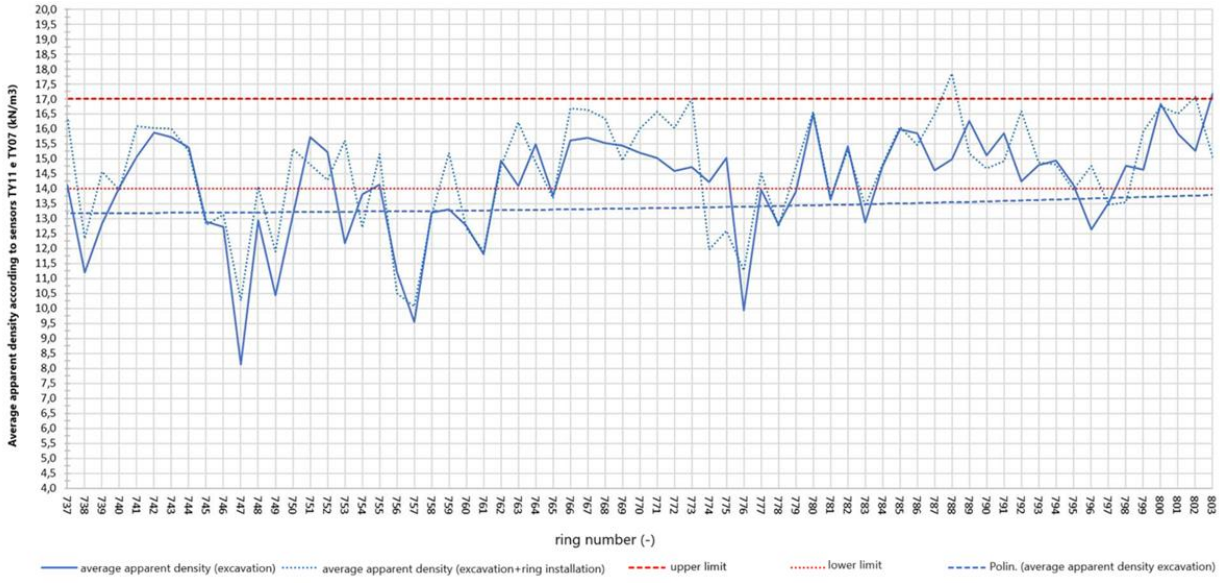


Figure 5.41 Average apparent density in the excavation chamber, TY06 and TY11 sensors (Report, 2024)

| Omog. Segments Geom. | segment number | day | n° of ring installed | Lenght L (m) | starting pk (m) | final pk (m) | L total (m) | pressure sensors TY11-TY07 | | | | |
|---|---|---|---|---|---|---|---|---|---|---|---|---|
| | | | | | | | | $\gamma_{app,\ exc.}$ (kN/m$^3$) | lower limit | upper limit | average $\gamma_{app}$ over 24h | |
| | | | | | | | | | | | $\gamma_{app,\ excavation}$ (kN/m$^3$) | $\gamma_{app,\ excavation+ring\ installation}$ (kN/m$^3$) |
| FYRmar+ FYRar | 9 | 01/06/2024 | 2 | 3.607 | 4038.22 | 4041.82 | 122.5 | 15 | 14 | 17 | 12.14 | 16.51 |
| | | 02/06/2024 | 13 | 23.383 | 4041.82 | 4065.21 | | 15 | 14 | 17 | 13.11 | 13.98 |
| FYRagms | 10 | 03/06/2024 | 14 | 25.198 | 4065.21 | 4090.40 | | 15 | 14 | 17 | 13.39 | 13.71 |
| | | 04/06/2024 | 8 | 14.394 | 4090.40 | 4104.80 | | 15 | 14 | 17 | 15.11 | 15.87 |
| | | 06/06/2024 | 9 | 16.189 | 4104.80 | 4120.99 | | 15 | 14 | 17 | 13.86 | 13.90 |
| | | 07/06/2024 | 6 | 10.856 | 4120.99 | 4131.84 | | 15 | 14 | 17 | 14.92 | 15.26 |
| | | 08/06/2024 | 9 | 16.238 | 4131.84 | 4148.08 | | 15 | 14 | 17 | 14.78 | 15.30 |
| | | 09/06/2024 | 7 | 12.637 | 4148.08 | 4160.72 | | 15 | 14 | 17 | 15.44 | 15.47 |

Table 31 Average apparent density in the excavation chamber, TY06 and TY11 sensors (Report, 2024)

## 5.5 From June 9th to June 20th (rings installed 799-844 )

The excavation progress reports fall within the section covered by P.A.T. n°4 (Table 7). From June 9 to June 17, excavation operations were paused due to the saturation of the temporary spoil storage tanks; excavation then resumed regularly on June 17.

In the graph in Figure 5.42, the pressure $\mathbf{p_{f,c}}$ is shown as a function of the ring number, while Table 33 presents the average value of $\mathbf{p_{f,c}}$ for each section, based on the progress.

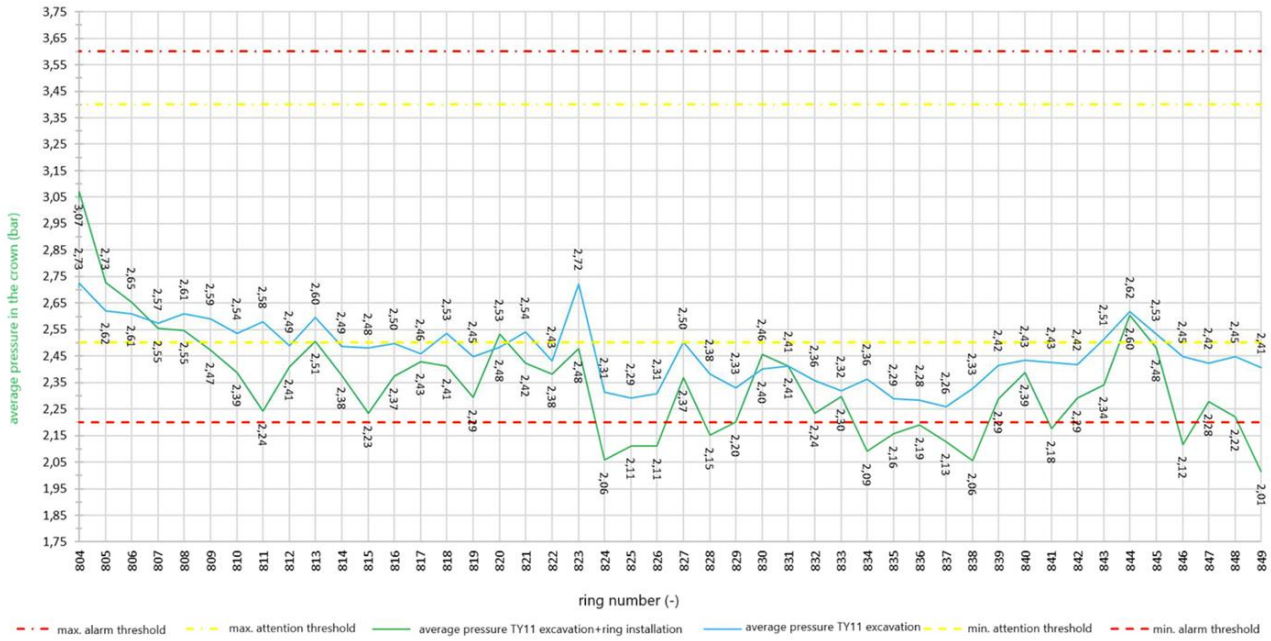


Figure 5.42 Average pressure in the crown during excavation and at the completion of the ring installation (TY11 sensor) (Report, 2024)

| Omog. Segments Geom. | segment number | day | n° of ring installed | Lenght L (m) | starting pk (m) | final pk (m) | L total (m) | $p_f$ (bar) | $p_{f,c}$ (bar) | ATTENTION (bar) | | ALARM (bar) | | average $p_{f,c}$ value (bar) | |
|---|---|---|---|---|---|---|---|---|---|---|---|---|---|---|---|
| | | | | | | | | | | MIN | MAX | MIN | MAX | excavation | excavation + ring installation |
| FYRagms | 10 | 09/06/2024 | 1 | 1.676 | 4160.71 | 4162.39 | 82.8 | 3.5 | 2.8 | 2.5 | 3.4 | 2.2 | 3.6 | 2.73 | 3.07 |
| | | 17/06/2024 | 10 | 17.986 | 4162.39 | 4180.38 | | 3.5 | 2.8 | 2.5 | 3.4 | 2.2 | 3.6 | 2.57 | 2.49 |
| | | 18/06/2024 | 12 | 6.971 | 4180.38 | 4187.35 | | 3.5 | 2.8 | 2.5 | 3.4 | 2.2 | 3.6 | 2.47 | 2.34 |
| FYRmar+FYRar | 11 | | | 12.996 | 4187.35 | 4200.35 | | 3.5 | 2.8 | 2.5 | 3.4 | 2.2 | 3.6 | | |
| | | 19/06/2024 | 12 | 21.570 | 4200.35 | 4221.92 | | 3.5 | 2.8 | 2.5 | 3.4 | 2.2 | 3.6 | 2.35 | 2.23 |
| | | 20/06/2024 | 12 | 21.565 | 4221.92 | 4243.48 | | 3.5 | 2.8 | 2.5 | 3.4 | 2.2 | 3.6 | 2.45 | 2.27 |

Table 32 Average pressure in the crown during excavation and at the completion of the ring installation (TY11 sensor) (Report, 2024)

The $\mathbf{p_{f,c}}$ values remain within the threshold values up until the installation of ring 824, after which a trend below the minimum alarm threshold of 2.20 bar is observed. This did not have any negative impacts on the stability of the face and the cable, indicating an excavation face that is generally more stable than expected.

### 5.5.1 Injection volume and pressure

The location of the injection lines is referenced in Figure 5.4, while for the calculation of the volumes of two-component grout to be injected from each individual line, equations (5.1) and (5.2) from section 5.1.1 were used.

The same proportions were applied to calculate the minimum volume of 10.74 m³ in the case of shield tail ground contact.

For the alert and alarm thresholds of the volume corresponding to line #i, to be filled with two-component grout, the procedure followed was the same as for the total mix volume per ring, using the formulas (5.3a)-(5.3.d) already presented in section 5.1.1.

The graph in Figure 5.43 shows the injection volume of the two-component grout, while Table 34 provides the average volume value **V** per section.

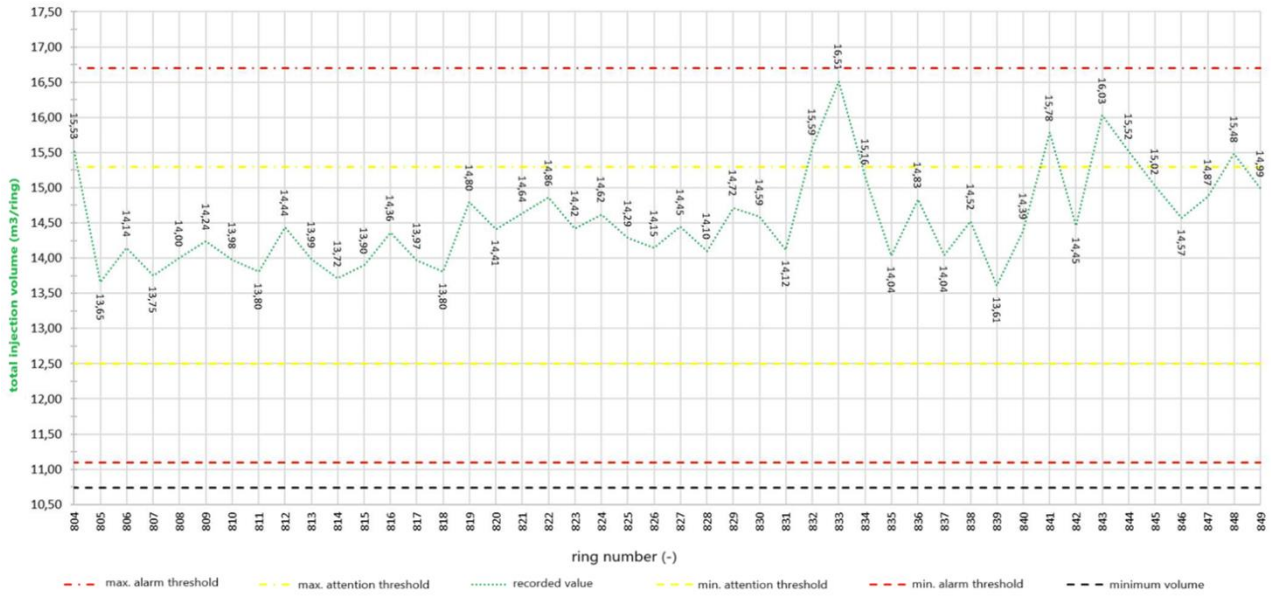


Figure 5.43 Total injection volume of the two-component mixture in m³/ring (Report, 2024)

| Omog. Segments Geom. | segment number | day | n° of ring installed | Lenght L (m) | starting pk (m) | final pk (m) | L total (m) | V ($m^3$/ring) | ATTENTION ($m^3$/ring) | | ALARM ($m^3$/ring) | | minimum V ($m^3$/ring) | average V ($m^3$/ring) |
|---|---|---|---|---|---|---|---|---|---|---|---|---|---|---|
| | | | | | | | | | MIN | MAX | MIN | MAX | | |
| FYRagms | 10 | 09/06/2024 | 1 | 1.676 | 4160.71 | 4162.39 | 82.8 | 13.91 | 12.52 | 15.30 | 11.13 | 16.69 | 10.74 | 15.53 |
| | | 17/06/2024 | 10 | 17.986 | 4162.39 | 4180.38 | | 13.91 | 12.52 | 15.30 | 11.13 | 16.69 | 10.74 | 13.97 |
| | | 18/06/2024 | 12 | 6.971 | 4180.38 | 4187.35 | | 13.91 | 12.52 | 15.30 | 11.13 | 16.69 | 10.74 | 14.37 |
| FYRmar+FYRar | 11 | | | 12.996 | 4187.35 | 4200.35 | | 13.91 | 12.52 | 15.30 | 11.13 | 16.69 | | |
| | | 19/06/2024 | 12 | 21.570 | 4200.35 | 4221.92 | | 13.91 | 12.52 | 15.30 | 11.13 | 16.69 | 10.74 | 14.69 |
| | | 20/06/2024 | 12 | 21.565 | 4221.92 | 4243.48 | | 13.91 | 12.52 | 15.30 | 11.13 | 16.69 | 10.74 | 14.94 |

Table 33 Average injection volume of the two-component mixture in $m^3$/ring per section (Report, 2024)

The pressure of the individual injection lines for component A was calculated using formula (5.4) (section 5.1.1).

The alert and alarm thresholds were defined as for the face pressure and the pressure in the crown (equations (5.5a)-(5.5d), section 5.1.1).

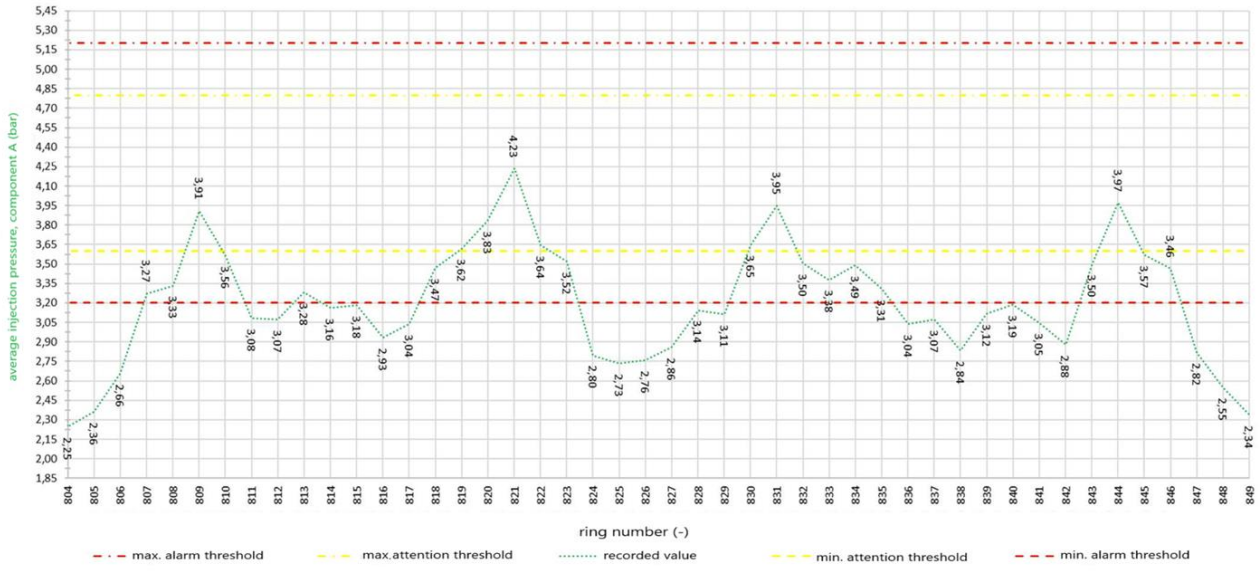


Figure 5.44 Average injection pressure of component A per section (Report, 2024)

| Omog. Segments Geom. | segment number | day | n° of ring installed | Lenght L (m) | starting pk (m) | final pk (m) | L total (m) | $p_m$ (bar) | ATTENTION (bar) | | ALARM (bar) | | average $p_m$ (bar) |
|---|---|---|---|---|---|---|---|---|---|---|---|---|---|
| | | | | | | | | | MIN | MAX | MIN | MAX | |
| FYRagms | 10 | 09/06/2024 | 1 | 1.676 | 4160.71 | 4162.39 | 82.8 | 4.0 | 3.6 | 4.8 | 3.2 | 5.2 | 2.25 |
| | | 17/06/2024 | 10 | 17.986 | 4162.39 | 4180.38 | | 4.0 | 3.6 | 4.8 | 3.2 | 5.2 | 3.17 |
| | | 18/06/2024 | 12 | 6.971 | 4180.38 | 4187.35 | | 4.0 | 3.6 | 4.8 | 3.2 | 5.2 | 3.36 |
| FYRmar+FYRar | 11 | | | 12.996 | 4187.35 | 4200.35 | | 4.0 | 3.6 | 4.8 | 3.2 | 5.2 | |
| | | 19/06/2024 | 12 | 21.570 | 4200.35 | 4221.92 | | 4.0 | 3.6 | 4.8 | 3.2 | 5.2 | 3.27 |
| | | 20/06/2024 | 12 | 21.565 | 4221.92 | 4243.48 | | 4.0 | 3.6 | 4.8 | 3.2 | 5.2 | 3.11 |

Table 34 Average injection pressure of component A per section (Report, 2024)

The injection pressure values recorded throughout the section are below the minimum alarm threshold of 3.2 bar, without compromising the stability of the face and the cable. The reduction is justified by the fact that, as explained with reference to Figure 5.44, a more stable excavation face is assumed (thus, since the injection pressure for backfilling is always higher than the face pressure, this confirms the assumption).

### 5.5.2 Thrust and torque

For the position of the 6 thrust groups (A, B, C, D, E, F), refer to Figure 5.7 in paragraph 5.1.2.

The thrusts in the individual thrust groups A, B, C, D, E, and F, generated by the lower and upper expected maximum thrusts, respectively 55 and 82 MN, between pk 4+160.717 and 4+243.481, they were determined taking into account that the center of gravity of the pistons is located on the axis of the tunnel.The eccentricity between the thrust axis and the center of gravity of the pistons $\mathbf{e_{app}}$ was calculated by assuming a trapezoidal pressure distribution on the excavation face.
Each thrust is considered on type 2 segments, i.e., segments reinforced with a denser reinforcement starting from 300 m from the tunnel entrance. The maximum excavation thrusts in groups A, B, C, D, E, and F satisfy the SLE, so the maximum thrust during excavation was always lower than the "maximum thrust for type 2 segments" (red line, section, and point).
The thrust exerted by the generic piston i is obtained as seen in section 5.1.2 (equations (5.6)-(5.8)). $\mathbf{S_i}$ and $\mathbf{z_i}$ represent the total thrust exerted by the pistons on the lining ring and the distance from the horizontal axis to the center of gravity of the generic piston **i**, respectively, while **S** is the total thrust exerted by the pistons.

The average and maximum thrusts of only the thrust groups F and C are reported below (Figures 5.45 and Figures 5.46):

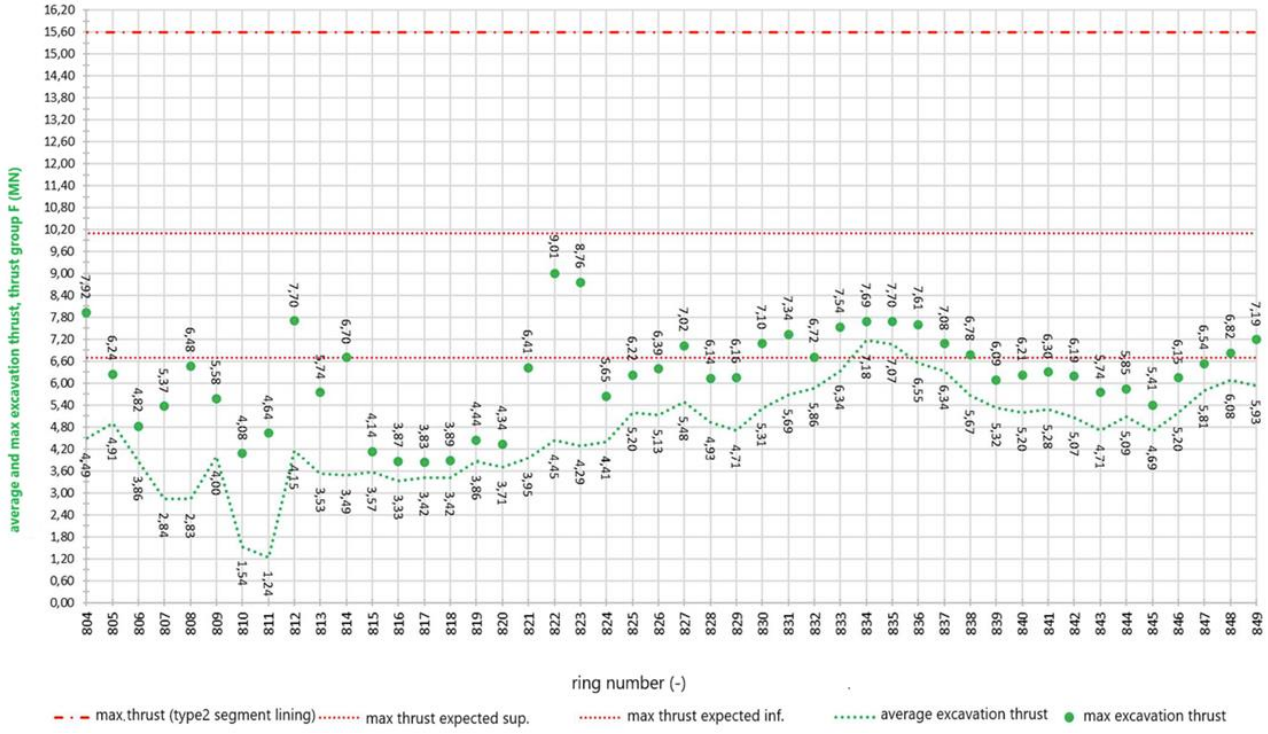


Figure 5.45 Average thrust and maximum thrust during the excavation phase exerted by the thrust group F (Report, 2024)

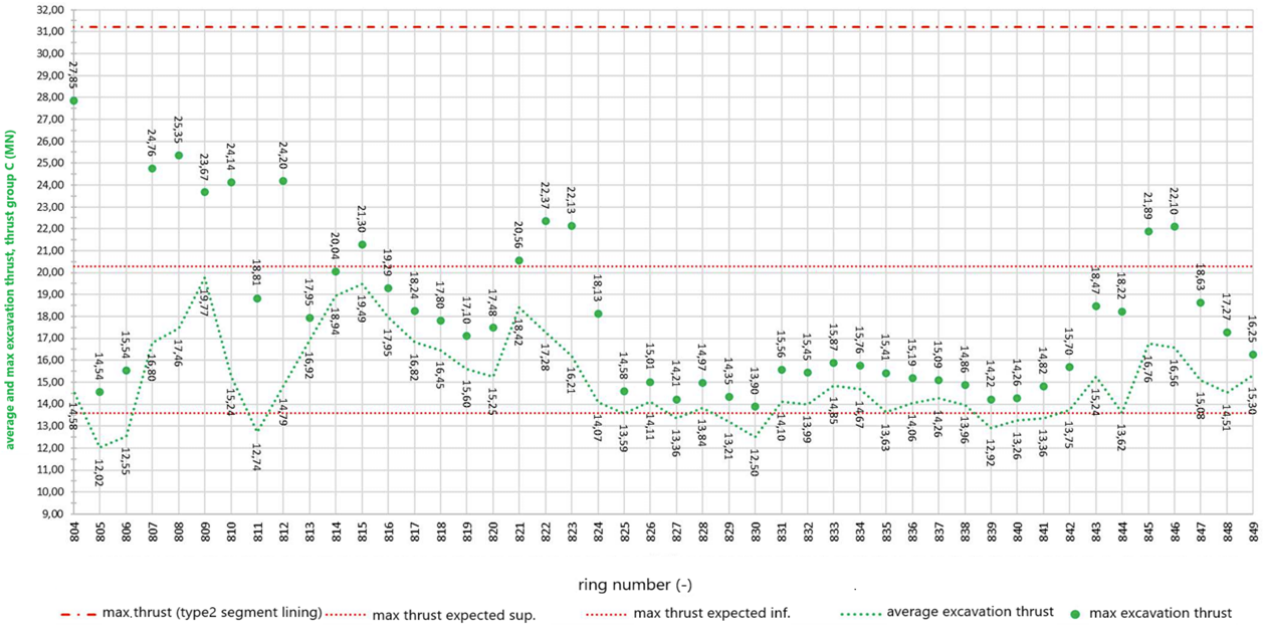


Figure 5.46 Average thrust and maximum thrust during the excavation phase exerted by the thrust group C (Report, 2024)

As expected from the trapezoidal pressure distribution on the excavation face, the thrust pistons of group C show higher values compared to those of group F, as the former are positioned lower than the latter.
In general, values below the minimum threshold indicate a softer face than expected, which therefore requires less thrust to be exerted. This could also be related to a more stable face, which requires less thrust. This choice did not lead to any negative impacts on the ongoing excavation.

Regarding the torque, Figure 5.10 (paragraph 5.1.2) also shows the maximum torque values. It is important to note that the torque on the cutterhead, due to friction, is strictly related to the thrust force and penetration.

In the graph in Figure 5.47, the average torque is shown as a function of the ring number, while Table 36 presents the average values for each section according to the progressive.

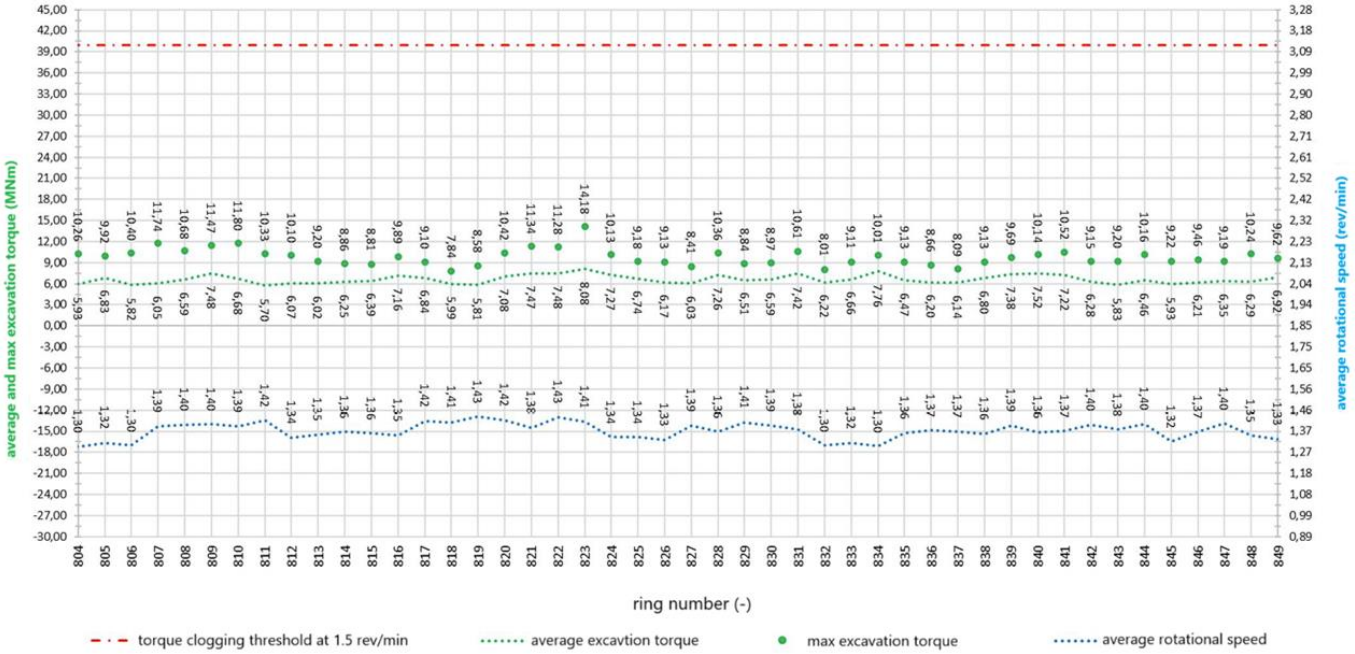


Figure 5.47 Average torque and maximum torque during excavation and average rotational speed (Report, 2024)

In the graph above, a roughly constant trend of the torque can be observed, as well as for the average rotational speed.

| Omog. Segments Geom. | segment number | day | n° of ring installed | Lenght L (m) | starting pk (m) | final pk (m) | L total (m) | AVERAGE TORQUE (MNm) | MAX. TORQUE (MNm) | TORQUE FOR A CLOGGING THRESHOLD OF 1.5 rev/min (MNm) | average rotation speed ω (rev/min) |
|---|---|---|---|---|---|---|---|---|---|---|---|
| FYRagms | 10 | 09/06/2024 | 1 | 1.676 | 4160.71 | 4162.39 | 82.8 | 5.93 | 10.26 | 40 | 1.30 |
| | | 17/06/2024 | 10 | 17.986 | 4162.39 | 4180.38 | | 6.35 | 10.45 | 40 | 1.37 |
| | | 18/06/2024 | 12 | 6.971 | 4180.38 | 4187.35 | | 6.94 | 10.07 | 40 | 1.39 |
| FYRmar+FYRar | 11 | | | 12.996 | 4187.35 | 4200.35 | | | | 40 | |
| | | 19/06/2024 | 12 | 21.570 | 4200.35 | 4221.92 | | 6.62 | 9.11 | 40 | 1.36 |
| | | 20/06/2024 | 12 | 21.565 | 4221.92 | 4243.48 | | 6.60 | 9.64 | 40 | 1.37 |

Table 35 Average torque and maximum torque during excavation and average rotational speed (Report, 2024)

As can be seen from the graph, each value falls within the limits.

### 5.5.3 Excavated material

The cover on the crown of the final tunnel lining in the section covered by the report ranges from approximately 31.5 to 32.0 meters, as shown in the Geomechanical/Geotechnical profile. In the FYRagms, between pk 4+160.717 and 4+187.350, the design weight per unit volume of the material is 20 kN/m³, while in the FYRmar+FYRar, between pk 4+187.350 and 4+243.481, it is 21.5 kN/m³.

The diagram of the average weight of the excavated soil for each installed ring, excluding the conditioning (see Chapter 6 for more details on soil conditioning), is compared with its gross average weight in Figure 5.48. In Table 37, following the graph, the net average values per section are provided.

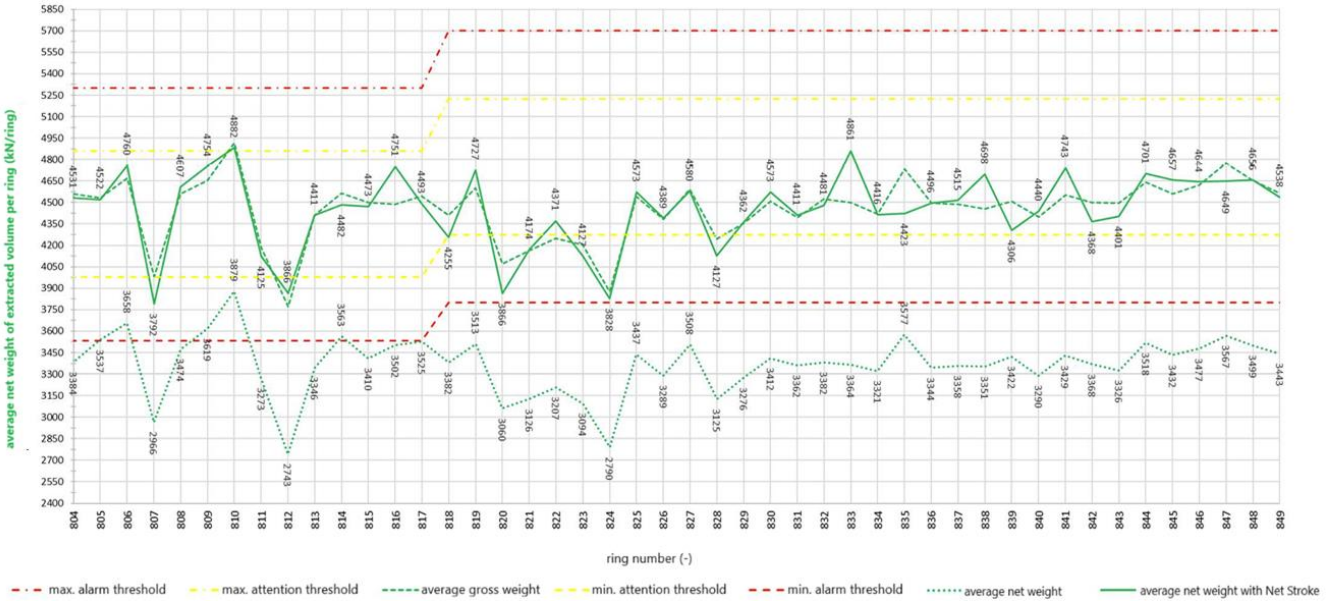


Figure 5.48 Comparison between the net weight and the gross weight of the material extracted per ring (Report, 2024)

| Omog. Segments Geom. | segment number | day | n° of ring installed | Lenght L (m) | starting pk (m) | final pk (m) | L total (m) | REFERENCE WEIGHT $P_t$ (kN) | ATTENTION MIN. (kN) | ATTENTION MAX. (kN) | ALARM MIN. (kN) | ALARM MAX. (kN) | AVERAGE NET WEIGHT (kN) | AVERAGE GROSS WEIGHT (kN) |
|---|---|---|---|---|---|---|---|---|---|---|---|---|---|---|
| FYRagms | 10 | 09/06/2024 | 1 | 1.676 | 4160.71 | 4162.39 | 82.8 | 4418 | 3976 | 4860 | 3534 | 5302 | 3384 | 4560 |
| | | 17/06/2024 | 10 | 17.986 | 4162.39 | 4180.38 | | 4418 | 3976 | 4860 | 3534 | 5302 | 3406 | 4424 |
| | | 18/06/2024 | 12 | 6.971 | 4180.38 | 4187.35 | | 4418 | 3976 | 4860 | 3534 | 5302 | 3277 | 4331 |
| FYRmar+FYRar | 11 | | | 12.996 | 4187.35 | 4200.35 | | 4749 | 4274 | 5224 | 3799 | 5699 | | |
| | | 19/06/2024 | 12 | 21.570 | 4200.35 | 4221.92 | | 4749 | 4274 | 5224 | 3799 | 5699 | 3360 | 4470 |
| | | 20/06/2024 | 12 | 21.565 | 4221.92 | 4243.48 | | 4749 | 4274 | 5224 | 3799 | 5699 | 3427 | 4560 |

Table 36 The weight of the net excavated material extracted per ring (Report, 2024)

In Figure 5.48, we can observe that the gross average extracted weight remains within the limits defined by the P.A.T.

In the diagram in Figure 5.49, the average pressures on sensors TY11 and TY07 are shown (for their positions, refer to Figure 5.1). The average values are calculated during the advancement phase of the shield or considering both the shield advancement and the installation of the precast ring.The TY11 sensor is located at the top compared to TY07, which justifies the fact that the pressures from the former are higher than those from the latter, given the trapezoidal distribution of thrusts in the excavation chambre.

In Figure 5.50, the average apparent density is shown, calculated using the pressures reported in Figure 5.49, taking into account that the elevation difference between the two sensors is 8 m. Knowing the average apparent density in the excavation chamber allows us to adjust the TBM for more efficient auger extraction, reducing the risk of clogging. Density affects the pressure needed to support the excavation face: if it is too high, it could indicate compact soils, which may require more force or a special support system; a low density might suggest less stable soils. In particular, for soils with low density, water infiltration could become a problem, so monitoring the density helps predict and mitigate this risk.

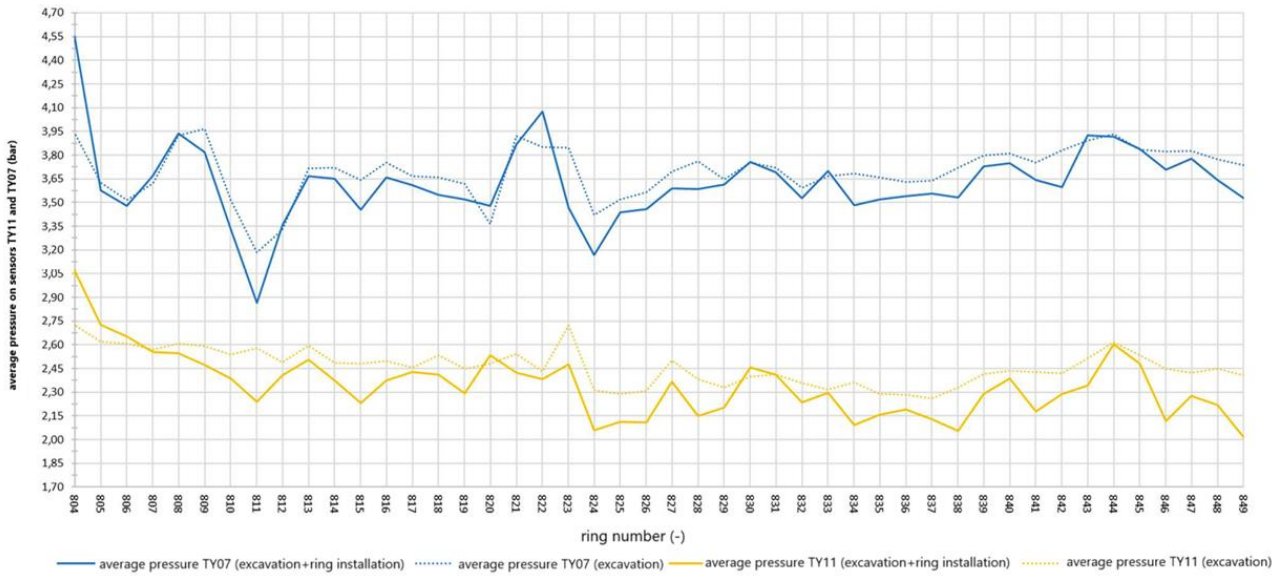


Figure 5.49 Face pressure: comparison between TY06 and TY11 sensors (Report, 2024)

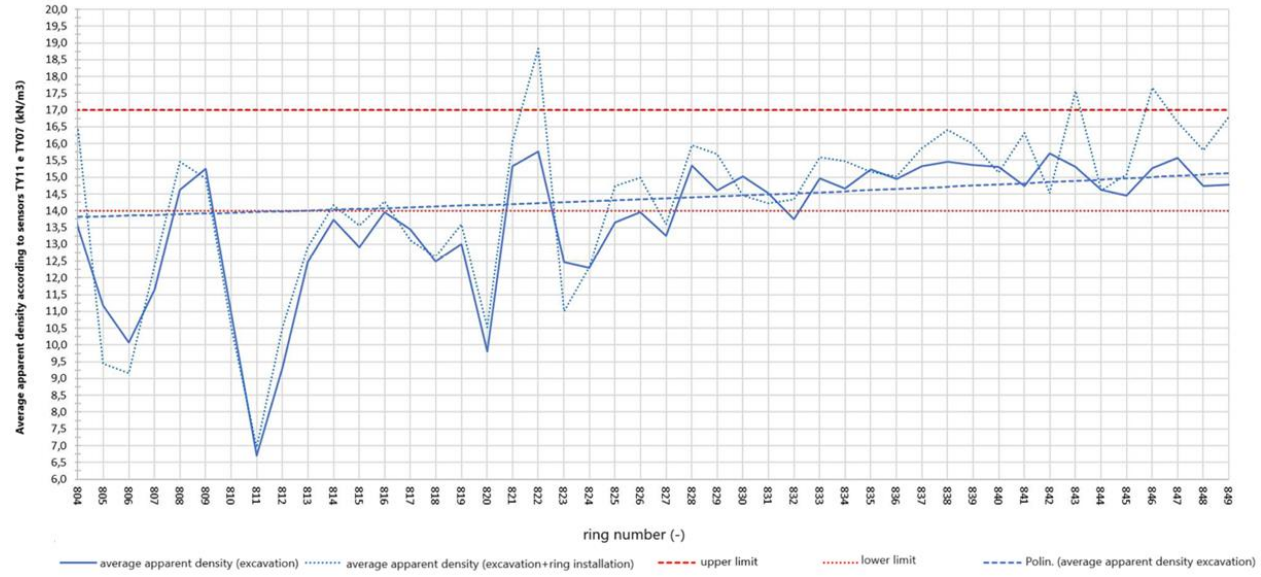


Figure 5.50 Average apparent density in the excavation chamber, TY06 and TY11 sensors (Report, 2024)

| Omog. Segments Geom. | segment number | day | n° of ring installed | Lenght L (m) | starting pk (m) | final pk (m) | L total (m) | pressure sensors TY11-TY07 | | | | |
|---|---|---|---|---|---|---|---|---|---|---|---|---|
| | | | | | | | | $\gamma_{app,\ exc.}$ (kN/m$^3$) | lower limit | upper limit | average $\gamma_{app}$ over 24h | |
| | | | | | | | | | | | $\gamma_{app,\ excavation}$ (kN/m$^3$) | $\gamma_{app,\ excavation+ring\ installation}$ (kN/m$^3$) |
| FYRagms | 10 | 09/06/2024 | 1 | 1.676 | 4160.71 | 4162.39 | 82.8 | 15 | 14 | 17 | 13.52 | 16.46 |
| | | 17/06/2024 | 10 | 17.986 | 4162.39 | 4180.38 | | 15 | 14 | 17 | 11.59 | 11.65 |
| | | 18/06/2024 | 12 | 6.971 | 4180.38 | 4187.35 | | 15 | 14 | 17 | 13.19 | 13.70 |
| FYRmar+FYRar | 11 | | | 12.996 | 4187.35 | 4200.35 | | 15 | 14 | 17 | | |
| | | 19/06/2024 | 12 | 21.570 | 4200.35 | 4221.92 | | 15 | 14 | 17 | 14.63 | 15.03 |
| | | 20/06/2024 | 12 | 21.565 | 4221.92 | 4243.48 | | 15 | 14 | 17 | 15.11 | 16.05 |

Table 37 Average apparent density in the excavation chamber, TY06 and TY11 sensors (Report, 2024)

## 5.6 From June 21st to July 4th (rings installed 845-923 )

The excavation progress reports fall within the sections covered by P.A.T. n°4 and P.A.T. n°5 (Table 7). From June 25 until the morning of July 1, excavation operations were interrupted for maintenance on the tail shield brushes; excavation then resumed regularly on July 1.

In the graph in Figure 5.51, the pressure $\mathbf{p_{f,c}}$ is shown as a function of the ring number, while Table 39 presents the average value of $\mathbf{p_{f,c}}$ for each section, based on the progress.

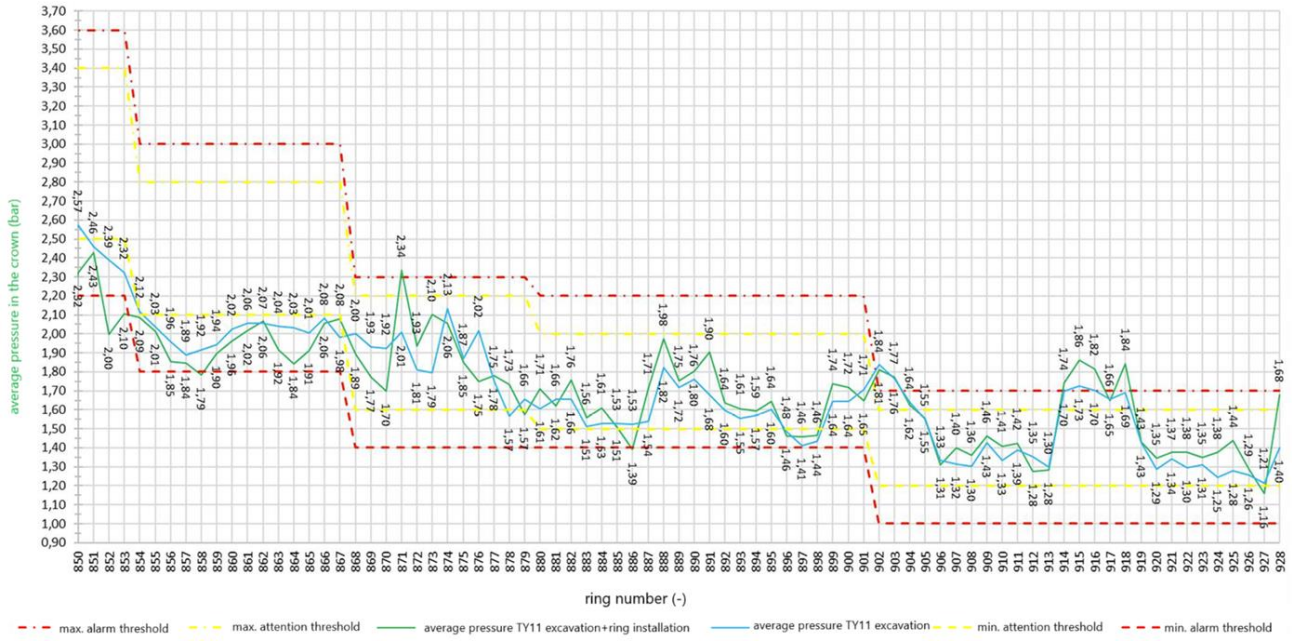


Figure 5.51 Average pressure in the crown during excavation and at the completion of the ring installation (TY11 sensor) (Report, 2024)

| Omog. Segments Geom. | segment number | day | n° of ring installed | Lenght L (m) | starting pk (m) | final pk (m) | L total (m) | $p_f$ (bar) | $p_{f,c}$ (bar) | ATTENTION (bar) | | ALARM (bar) | | average $p_{f,c}$ value (bar) | |
|---|---|---|---|---|---|---|---|---|---|---|---|---|---|---|---|
| | | | | | | | | | | MIN | MAX | MIN | MAX | excavation | excavation + ring installation |
| FYRmar+FYRar | 11 | 21/06/2024 | 10 | 6.52 | 4243.48 | 4250.00 | 104.0 | 3.5 | 2.8 | 2.5 | 3.4 | 2.2 | 3.6 | 2.16 | 2.03 |
| | | | | 11.54 | 4250.00 | 4261.54 | | 3 | 2.3 | 2.1 | 2.8 | 1.8 | 3.0 | | |
| | | 22/06/2024 | 11 | 13.46 | 4261.54 | 4275.00 | | 3 | 2.3 | 2.1 | 2.8 | 1.8 | 3.0 | 2.01 | 1.93 |
| | | | | 6.26 | 4275.00 | 4281.26 | | 2.5 | 1.8 | 1.6 | 2.2 | 1.4 | 2.3 | | |
| | | 24/06/2024 | 10 | 15.68 | 4281.26 | 4296.94 | | 2.5 | 1.8 | 1.6 | 2.2 | 1.4 | 2.3 | 1.82 | 1.88 |
| | | | | 2.33 | 4296.94 | 4299.27 | | 2.4 | 1.7 | 1.5 | 2.0 | 1.4 | 2.2 | | |
| | | 25/06/2024 | 1 | 1.79 | 4299.27 | 4301.07 | | 2.4 | 1.7 | 1.5 | 2.0 | 1.4 | 2.2 | 1.66 | 1.62 |
| | | 01/07/2024 | 10 | 17.96 | 4301.07 | 4319.03 | | 2.4 | 1.7 | 1.5 | 2.0 | 1.4 | 2.2 | 1.63 | 1.70 |
| | | 02/07/2024 | 12 | 17.91 | 4319.03 | 4336.94 | | 2.4 | 1.7 | 1.5 | 2.0 | 1.4 | 2.2 | 1.60 | 1.63 |
| | 12 | | | 3.65 | 4336.94 | 4340.59 | | 2.0 | 1.3 | 1.2 | 1.6 | 1.0 | 1.7 | | |
| | | 03/07/2024 | 15 | 26.99 | 4340.59 | 4367.58 | | 2.0 | 1.3 | 1.2 | 1.6 | 1.0 | 1.7 | 1.49 | 1.53 |
| | | 04/07/2024 | 10 | 17.99 | 4367.58 | 4385.57 | | 2.0 | 1.3 | 1.2 | 1.6 | 1.0 | 1.7 | 1.31 | 1.38 |

Table 38 Average pressure in the crown during excavation and at the completion of the ring installation (TY11 sensor) (Report, 2024)

The $\mathbf{p_{f,c}}$ values remain within the alarm threshold values. It is observed that only during the installation of rings 915 and 918 did the pressure exceed the maximum alarm threshold of 1.7 bar, suggesting a less stable excavation face than expected. Nevertheless, no problems occurred during the advancement process.

### 5.6.1 Injection volume and pressure

The location of the injection lines is referenced in Figure 5.4, while for the calculation of the volumes of two-component grout to be injected from each individual line, equations (5.1) and (5.2) from section 5.1.1 were used.

The same proportions were applied to calculate the minimum volume of 10.74 m³ in the case of shield tail ground contact.

For the alert and alarm thresholds of the volume corresponding to line #i, to be filled with two-component grout, the procedure followed was the same as for the total mix volume per ring, using the formulas (5.3a)-(5.3.d) already presented in section 5.1.1.

The graph in Figure 5.52 shows the injection volume of the two-component grout, while Table 40 provides the average volume value **V** per section.

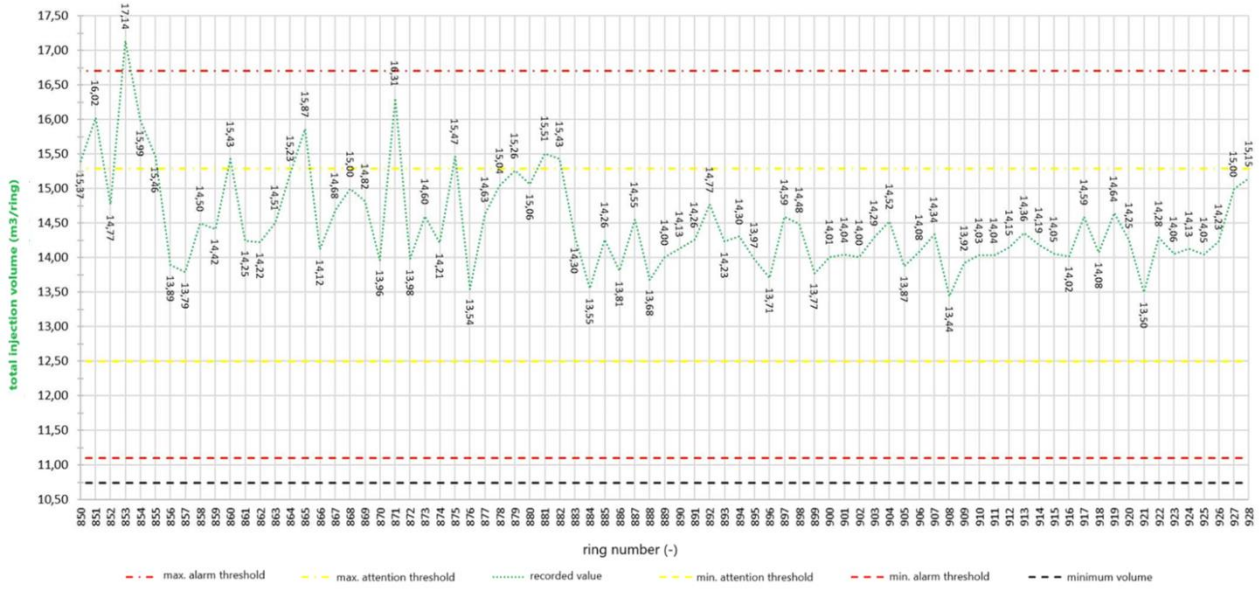


Figure 5.52 Total injection volume of the two-component mixture in m³/ring (Report, 2024)

| Omog. Segments Geom. | segment number | day | n° of ring installed | Lenght L (m) | starting pk (m) | final pk (m) | L total (m) | V (m³/ring) | ATTENTION (m³/ring) | | ALARM (m³/ring) | | minimum V (m³/ring) | average V (m³/ring) |
|---|---|---|---|---|---|---|---|---|---|---|---|---|---|---|
| | | | | | | | | | MIN | MAX | MIN | MAX | | |
| FYRmar+FYRar | 11 | 21/06/2024 | 10 | 6.52 | 4243.48 | 4250.00 | 104.0 | 13.91 | 12.52 | 15.30 | 11.13 | 16.69 | 10.74 | 15.13 |
| | | | | 11.54 | 4250.00 | 4261.54 | | | | | | | | |
| | | 22/06/2024 | 11 | 13.46 | 4261.54 | 4275.00 | | 13.91 | 12.52 | 15.30 | 11.13 | 16.69 | 10.74 | 14.73 |
| | | | | 6.26 | 4275.00 | 4281.26 | | | | | | | | |
| | | 24/06/2024 | 10 | 15.68 | 4281.26 | 4296.94 | | 13.92 | 12.53 | 15.31 | 11.14 | 16.70 | 10.75 | 14.81 |
| | | | | 2.33 | 4296.94 | 4299.27 | | | | | | | | |
| | | 25/06/2024 | 1 | 1.79 | 4299.27 | 4301.07 | | 13.91 | 12.52 | 15.30 | 11.13 | 16.69 | 10.74 | 15.51 |
| | | 01/07/2024 | 10 | 17.96 | 4301.07 | 4319.03 | | 13.91 | 12.52 | 15.30 | 11.13 | 16.69 | 10.74 | 14.20 |
| | | 02/07/2024 | 12 | 17.91 | 4319.03 | 4336.94 | | 13.91 | 12.52 | 15.30 | 11.13 | 16.69 | 10.74 | 14.17 |
| | | | | 3.65 | 4336.94 | 4340.59 | | | | | | | | |
| | 12 | 03/07/2024 | 15 | 26.99 | 4340.59 | 4367.58 | | 13.91 | 12.52 | 15.30 | 11.13 | 16.69 | 10.74 | 14.11 |
| | | 04/07/2024 | 10 | 17.99 | 4367.58 | 4385.57 | | 13.91 | 12.52 | 15.30 | 11.13 | 16.69 | 10.74 | 14.33 |

Table 39 Average injection volume of the two-component mixture in m³/ring per section (Report, 2024)

The pressure of the individual injection lines for component A was calculated using formula (5.4) (section 5.1.1).

The alert and alarm thresholds were defined as for the face pressure and the pressure in the crown (equations (5.5a)-(5.5d), section 5.1.1).

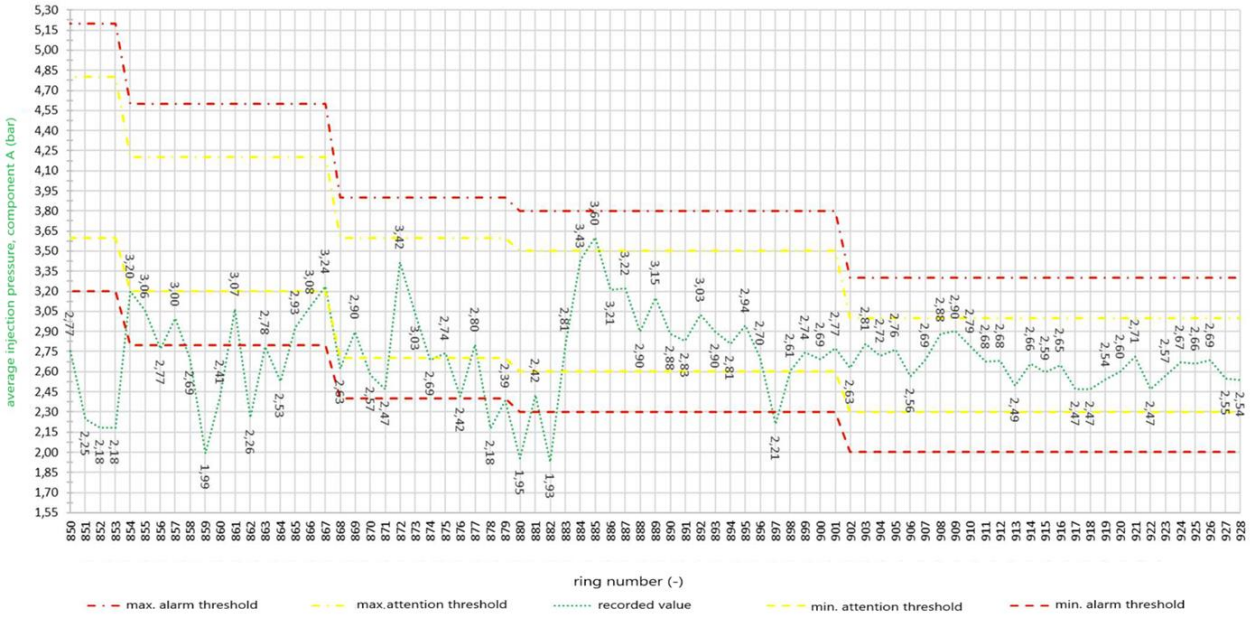


Figure 5.53 Average injection pressure of component A per section (Report, 2024)

| Omog. Segments Geom. | segment number | day | n° of ring installed | Lenght L (m) | starting pk (m) | final pk (m) | L total (m) | $p_m$ (bar) | ATTENTION (bar) | | ALARM (bar) | | average $p_m$ (bar) |
|---|---|---|---|---|---|---|---|---|---|---|---|---|---|
| | | | | | | | | | MIN | MAX | MIN | MAX | |
| FYRmar+FYRar | 11 | 21/06/2024 | 10 | 6.52 | 4243.48 | 4250.00 | 104.0 | 4 | 3.6 | 4.8 | 3.2 | 5.2 | 2.61 |
| | | | | 11.54 | 4250.00 | 4261.54 | | 3.5 | 3.2 | 4.2 | 2.8 | 4.6 | |
| | | 22/06/2024 | 11 | 13.46 | 4261.54 | 4275.00 | | 3.5 | 3.2 | 4.2 | 2.8 | 4.6 | 2.76 |
| | | | | 6.26 | 4275.00 | 4281.26 | | 3 | 2.7 | 3.6 | 2.4 | 3.9 | |
| | | 24/06/2024 | 10 | 15.68 | 4281.26 | 4296.94 | | 3 | 2.7 | 3.6 | 2.4 | 3.9 | 2.61 |
| | | | | 2.33 | 4296.94 | 4299.27 | | 2.9 | 2.6 | 3.5 | 2.3 | 3.8 | |
| | | 25/06/2024 | 1 | 1.79 | 4299.27 | 4301.07 | | 2.9 | 2.6 | 3.5 | 2.3 | 3.8 | 2.42 |
| | | 01/07/2024 | 10 | 17.96 | 4301.07 | 4319.03 | | 2.9 | 2.6 | 3.5 | 2.3 | 3.8 | 3.00 |
| | | 02/07/2024 | 12 | 17.91 | 4319.03 | 4336.94 | | 2.9 | 2.6 | 3.5 | 2.3 | 3.8 | 2.74 |
| | 12 | | | 3.65 | 4336.94 | 4340.59 | | 2.5 | 2.3 | 3.0 | 2.0 | 3.3 | |
| | | 03/07/2024 | 15 | 26.99 | 4340.59 | 4367.58 | | 2.5 | 2.3 | 3.0 | 2.0 | 3.3 | 2.67 |
| | | 04/07/2024 | 10 | 17.99 | 4367.58 | 4385.57 | | 2.5 | 2.3 | 3.0 | 2.0 | 3.3 | 2.60 |

Table 40 Average injection pressure of component A per section (Report, 2024)

The injection pressure values recorded from the installation of rings 850 to 882, while below the minimum alarm threshold of 2.8 bar, did not have negative impacts on the stability of the face and the cable. The reduction is justified by the fact that, as explained with reference to Figure 5.53, a more stable excavation face is assumed (thus, since the injection pressure for backfilling is always higher than the face pressure, this confirms the assumption).

### 5.6.2 Thrust and torque

For the position of the 6 thrust groups (A, B, C, D, E, F), refer to Figure 5.7 in paragraph 5.1.2.

Le spinte nei singoli gruppi di spinta A, B, C, D, E ed F generate dalla spinta attesa massima inferiore e superiore,

respectively:

a) 55 and 82MN between pk 4+243.481 and 4+250;
b) 50 and 75MN between pk 4+250 and 4+275;
c) 45 and 68MN between pk 4+275 and 4+296.94;
d) 44 and 66MN between pk 4+296.94 and 4+336.94;
e) 40 and 60MN between 4+336.94 and 4+385.573;

they were determined taking into account that the center of gravity of the pistons is located on the axis of the tunnel. The eccentricity between the thrust axis and the center of gravity of the pistons $\mathbf{e_{app}}$ was calculated by assuming a trapezoidal pressure distribution on the excavation face.
Each thrust is considered on type 2 segments, i.e., segments reinforced with a denser reinforcement starting from 300 m from the tunnel entrance. The maximum excavation thrusts in groups A, B, C, D, E, and F satisfy the SLE, so the maximum thrust during excavation was always lower than the "maximum thrust for type 2 segments" (red line, section, and point).
The thrust exerted by the generic piston i is obtained as seen in section 5.1.2 (equations (5.6)-(5.8)). $\mathbf{S_i}$ and $\mathbf{z_i}$ represent the total thrust exerted by the pistons on the lining ring and the distance from the horizontal axis to the center of gravity of the generic piston **i**, respectively, while **S** is the total thrust exerted by the pistons.

The average and maximum thrusts of only the thrust groups F and C are reported below (Figures 5.54 and Figures 5.55):

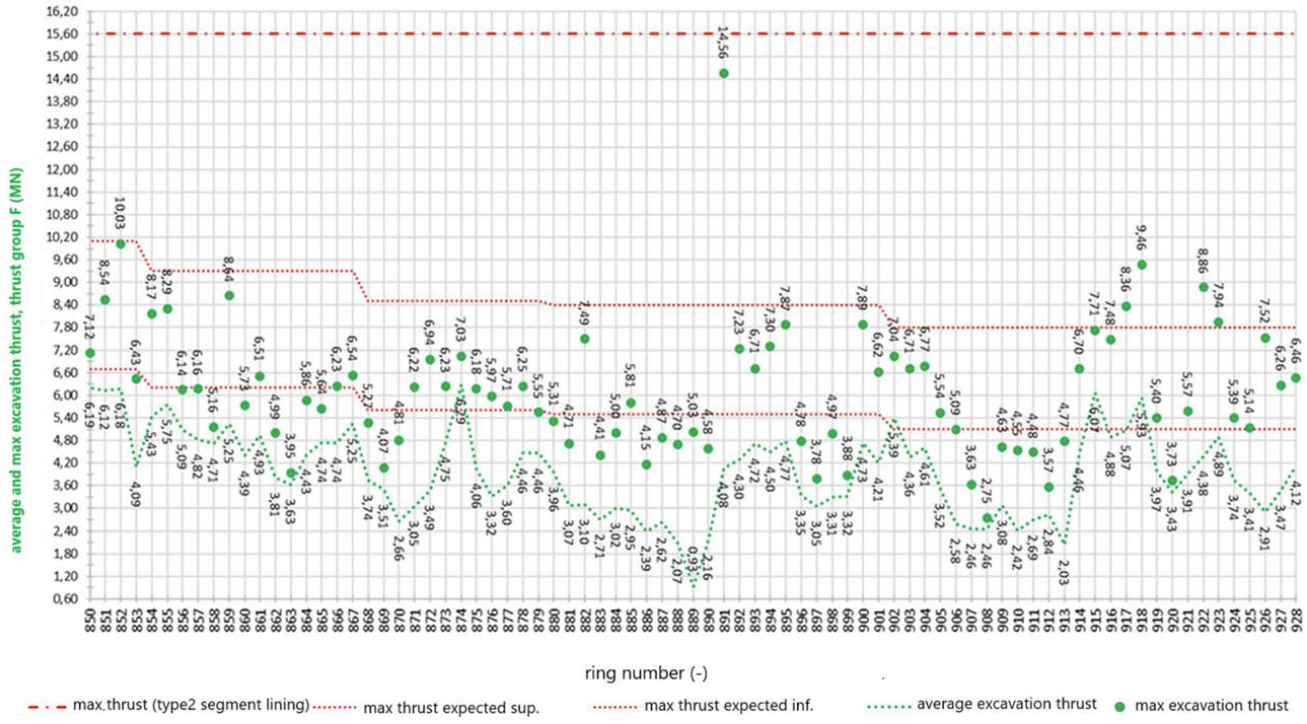


Figure 5.54 Average thrust and maximum thrust during the excavation phase exerted by the thrust group F (Report, 2024)

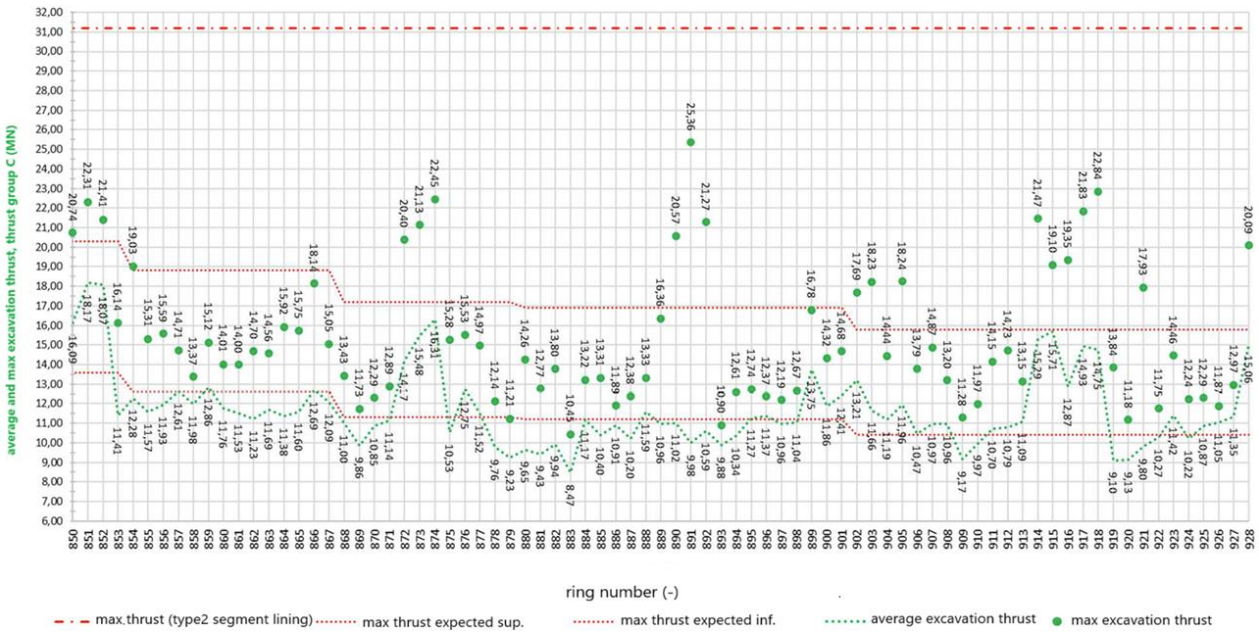


Figure 5.55 Average thrust and maximum thrust during the excavation phase exerted by the thrust group C (Report, 2024)

As expected from the trapezoidal pressure distribution on the excavation face, the thrust pistons of group C show higher values compared to those of group F, as the former are positioned lower than the latter.
In general, values below the minimum threshold indicate a softer face than expected, which therefore requires less thrust to be exerted. This could also be related to a more stable face, which requires less thrust. This choice did not lead to any negative impacts on the ongoing excavation.

Regarding the torque, Figure 5.10 (paragraph 5.1.2) also shows the maximum torque values. It is important to note that the torque on the cutterhead, due to friction, is strictly related to the thrust force and penetration.

In the graph in Figure 5.56, the average torque is shown as a function of the ring number, while Table 42 presents the average values for each section according to the progressive.

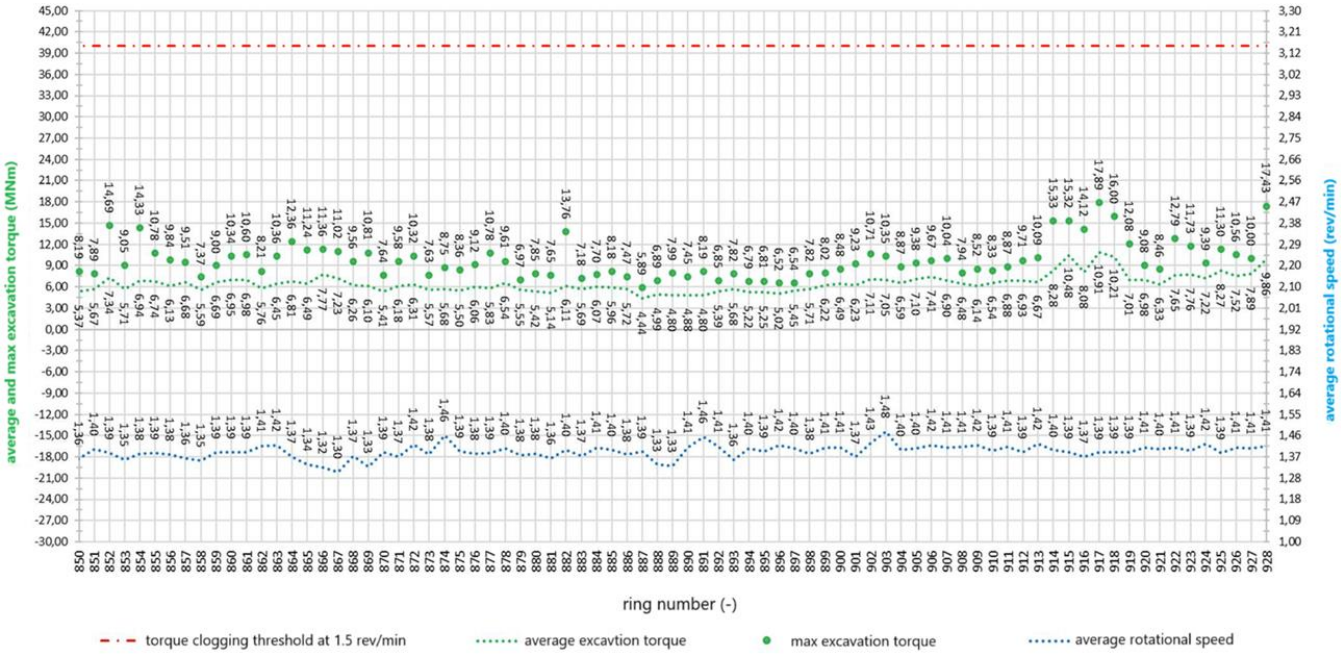


Figure 5.56 Average torque and maximum torque during excavation and average rotational speed (Report, 2024)

In the graph above, a roughly constant trend of the pair can be observed, as well as for the average rotational speed.

| Omog. Segments Geom. | segment number | day | n° of ring installed | Lenght L (m) | starting pk (m) | final pk (m) | L total (m) | AVERAGE TORQUE (MNm) | MAX. TORQUE (MNm) | TORQUE FOR A CLOGGING THRESHOLD OF 1.5 rev/min (MNm) | average rotation speed ω (rev/min) |
|---|---|---|---|---|---|---|---|---|---|---|---|
| FYRmar+FYRar | 11 | 21/06/2024 | 10 | 6.52 | 4243.48 | 4250.00 | 104.0 | 6.28 | 10.07 | 40 | 1.38 |
| | | | | 11.54 | 4250.00 | 4261.54 | | | | 40 | |
| | | 22/06/2024 | 11 | 13.46 | 4261.54 | 4275.00 | | 6.56 | 10.32 | 40 | 1.37 |
| | | | | 6.26 | 4275.00 | 4281.26 | | | | 40 | |
| | | 24/06/2024 | 10 | 15.68 | 4281.26 | 4296.94 | | 5.86 | 8.90 | 40 | 1.40 |
| | | | | 2.33 | 4296.94 | 4299.27 | | | | 40 | |
| | | 25/06/2024 | 1 | 1.79 | 4299.27 | 4301.07 | | 5.14 | 7.65 | 40 | 1.36 |
| | | 01/07/2024 | 10 | 17.96 | 4301.07 | 4319.03 | | 5.34 | 8.07 | 40 | 1.39 |
| | | 02/07/2024 | 12 | 17.91 | 4319.03 | 4336.94 | | 5.90 | 7.78 | 40 | 1.40 |
| | 12 | | | 3.65 | 4336.94 | 4340.59 | | | | 40 | |
| | | 03/07/2024 | 15 | 26.99 | 4340.59 | 4367.58 | | 7.71 | 11.34 | 40 | 1.40 |
| | | 04/07/2024 | 10 | 17.99 | 4367.58 | 4385.57 | | 7.65 | 11.28 | 40 | 1.40 |

Table 41 Average torque and maximum torque during excavation and average rotational speed (Report, 2024)

As can be seen from the graph, each value falls within the limits.

### 5.6.3 Excavated material

The coverings on the dome of the final lining of the tunnel in the section covered by the report are approximately between 33.5m and 40.3m, as shown in the Geomechanical profile; the unit weight of the FYRmar+FYRar between pk 4+243.481 and 4+385.573 is 21.5 kN/m³.

The diagram of the average weight of the excavated soil for each installed ring, excluding the conditioning (see Chapter 6 for more details on soil conditioning), is compared with its gross average weight in Figure 5.57. In Table 43, following the graph, the net average values per section are provided.

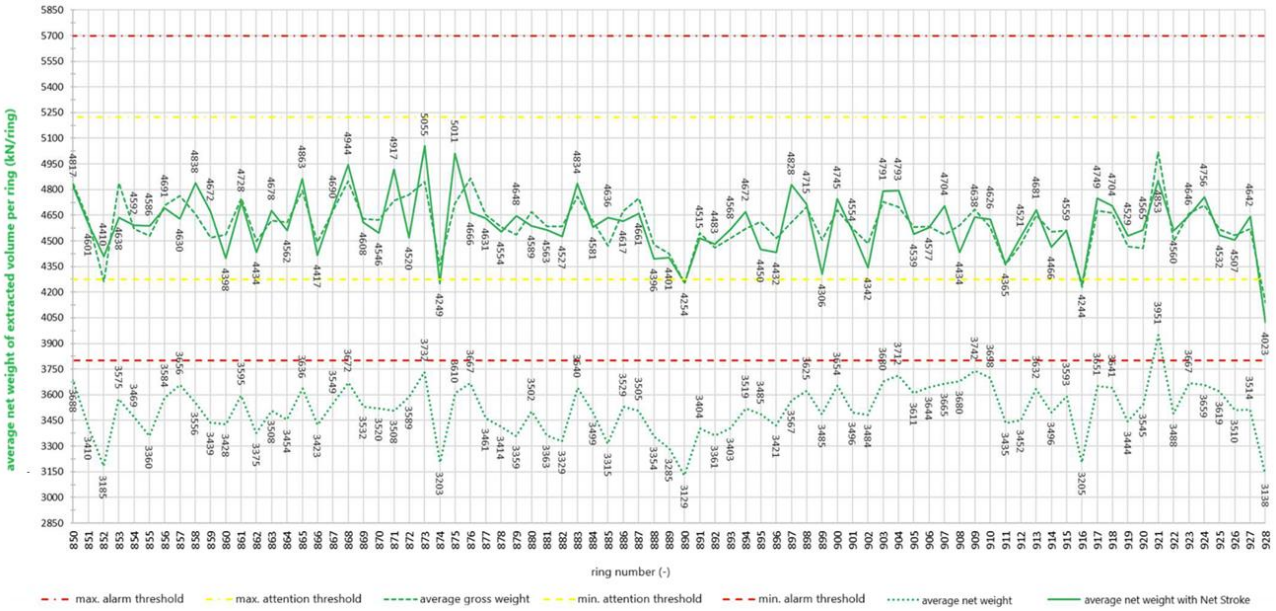


Figure 5.57 Comparison between the net weight and the gross weight of the material extracted per ring (Report, 2024)

| Omog. Segments Geom. | segment number | day | n° of ring installed | Lenght L (m) | starting pk (m) | final pk (m) | L total (m) | REFERENCE WEIGHT $P_t$ (kN) | ATTENTION MIN. (kN) | ATTENTION MAX. (kN) | ALARM MIN. (kN) | ALARM MAX. (kN) | AVERAGE NET WEIGHT (kN) | AVERAGE GROSS WEIGHT (kN) |
|---|---|---|---|---|---|---|---|---|---|---|---|---|---|---|
| FYRmar+FYRar | 11 | 21/06/2024 | 10 | 6.52 | 4243.48 | 4250.00 | 104.0 | 4749 | 4274 | 5224 | 3799 | 5699 | 3492 | 4631 |
| | | | | 11.54 | 4250.00 | 4261.54 | | 4749 | 4274 | 5224 | 3799 | 5699 | | |
| | | 22/06/2024 | 11 | 13.46 | 4261.54 | 4275.00 | | 4749 | 4274 | 5224 | 3799 | 5699 | 3517 | 4643 |
| | | | | 6.26 | 4275.00 | 4281.26 | | 4749 | 4274 | 5224 | 3799 | 5699 | | |
| | | 24/06/2024 | 10 | 15.68 | 4281.26 | 4296.94 | | 4749 | 4274 | 5224 | 3799 | 5699 | 3504 | 4674 |
| | | | | 2.33 | 4296.94 | 4299.27 | | 4749 | 4274 | 5224 | 3799 | 5699 | | |
| | | 25/06/2024 | 1 | 1.79 | 4299.27 | 4301.07 | | 4749 | 4274 | 5224 | 3799 | 5699 | 3363 | 4586 |
| | | 01/07/2024 | 10 | 17.96 | 4301.07 | 4319.03 | | 4749 | 4274 | 5224 | 3799 | 5699 | 3399 | 4556 |
| | | 02/07/2024 | 12 | 17.91 | 4319.03 | 4336.94 | | 4749 | 4274 | 5224 | 3799 | 5699 | 3515 | 4579 |
| | 12 | | | 3.65 | 4336.94 | 4340.59 | | 4749 | 4274 | 5224 | 3799 | 5699 | | |
| | | 03/07/2024 | 15 | 26.99 | 4340.59 | 4367.58 | | 4749 | 4274 | 5224 | 3799 | 5699 | 3590 | 4562 |
| | | 04/07/2024 | 10 | 17.99 | 4367.58 | 4385.57 | | 4749 | 4274 | 5224 | 3799 | 5699 | 3561 | 4562 |

Table 42 The weight of the net excavated material extracted per ring (Report, 2024)

In Figure 5.57, we can observe that the gross average weight extracted falls within the limits set by the P.A.T.

In the diagram in Figure 5.58, the average pressures on sensors TY11 and TY07 are shown (for their positions, refer to Figure 5.1). The average values are calculated during the advancement phase of the shield or considering both the shield advancement and the installation of the precast ring.The TY11 sensor is located at the top compared to TY07, which justifies the fact that the pressures from the former are higher than those from the latter, given the trapezoidal distribution of thrusts in the excavation chambre.
At the ring 871, we observe a significant maximum, consistent with what was seen in the previous figure, and we can therefore hypothesize a less stable face.

In Figure 5.59, the average apparent density is shown, calculated using the pressures reported in Figure 5.58, taking into account that the elevation difference between the two sensors is 8 m.

Knowing the average apparent density in the excavation chamber allows us to adjust the TBM for more efficient auger extraction, reducing the risk of clogging. Density affects the pressure needed to support the excavation face: if it is too high, it could indicate compact soils, which may require more force or a special support system; a low density might suggest less stable soils. In particular, for soils with low density, water infiltration could become a problem, so monitoring the density helps predict and mitigate this risk.

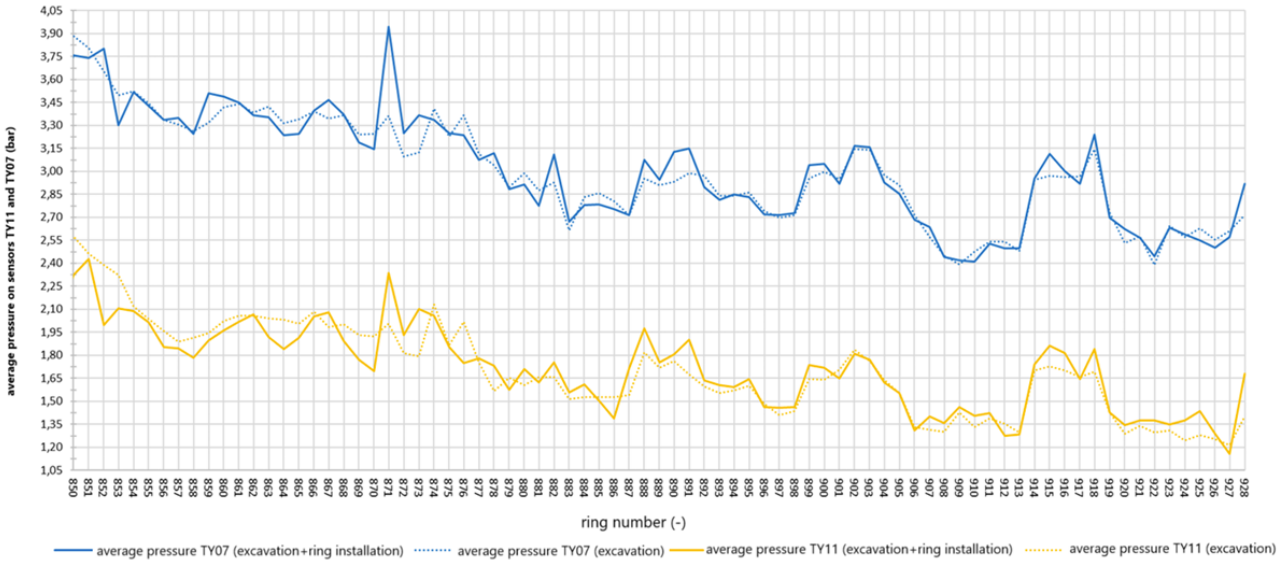


Figure 5.58 Face pressure: comparison between TY06 and TY11 sensors (Report, 2024)

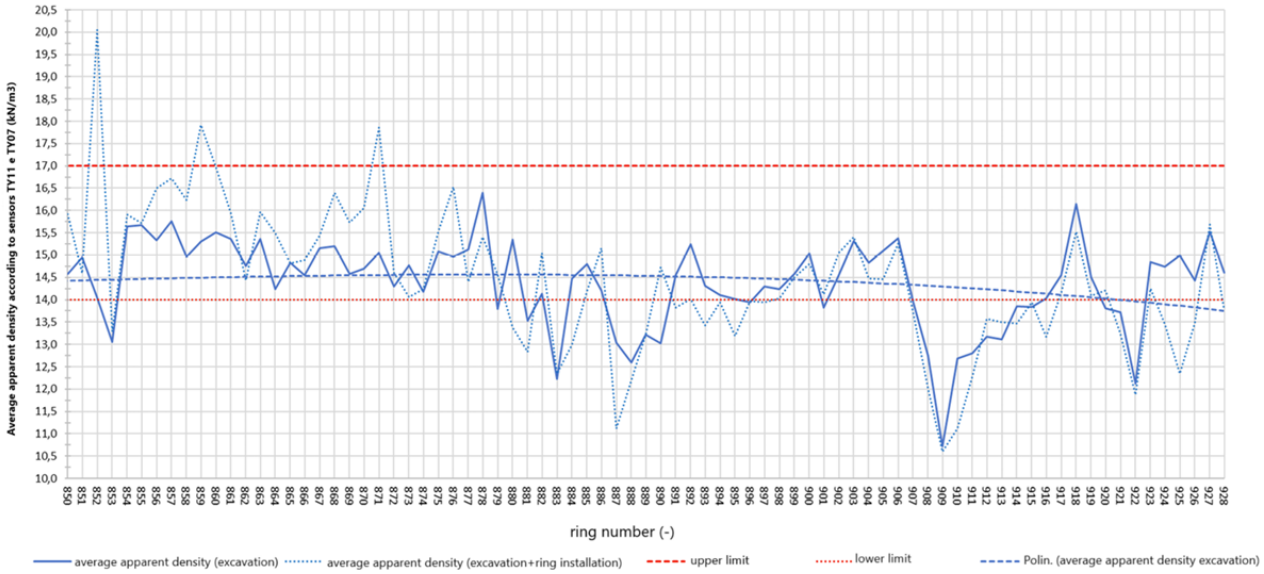


Figure 5.59 Average apparent density in the excavation chamber, TY06 and TY11 sensors (Report, 2024)

| Omog. Segments Geom. | segment number | day | n° of ring installed | Lenght L (m) | starting pk (m) | final pk (m) | L total (m) | pressure sensors TY11-TY07 | | | | |
|---|---|---|---|---|---|---|---|---|---|---|---|---|
| | | | | | | | | | | | average $\gamma_{app}$ over 24h | |
| | | | | | | | | $\gamma_{app, exc.}$ (kN/m$^3$) | lower limit | upper limit | $\gamma_{app, excavation}$ (kN/m$^3$) | $\gamma_{app, excavation+ring installation}$ (kN/m$^3$) |
| FYRmar+ FYRar | 11 | 21/06/2024 | 10 | 6.52 | 4243.48 | 4250.00 | 104.0 | 15 | 14 | 17 | 14.9 | 16.3 |
| | | | | 11.54 | 4250.00 | 4261.54 | | 15 | 14 | 17 | | |
| | | 22/06/2024 | 11 | 13.46 | 4261.54 | 4275.00 | | 15 | 14 | 17 | 14.9 | 15.6 |
| | | | | 6.26 | 4275.00 | 4281.26 | | 15 | 14 | 17 | | |
| | | 24/06/2024 | 10 | 15.68 | 4281.26 | 4296.94 | | 15 | 14 | 17 | 14.9 | 15.1 |
| | | | | 2.33 | 4296.94 | 4299.27 | | 15 | 14 | 17 | | |
| | | 25/06/2024 | 1 | 1.79 | 4299.27 | 4301.07 | | 15 | 14 | 17 | 13.5 | 12.8 |
| | | 01/07/2024 | 10 | 17.96 | 4301.07 | 4319.03 | | 15 | 14 | 17 | 13.6 | 13.5 |
| | | 02/07/2024 | 12 | 17.91 | 4319.03 | 4336.94 | | 15 | 14 | 17 | 14.5 | 14.2 |
| | 12 | | | 3.65 | 4336.94 | 4340.59 | | 15 | 14 | 17 | | |
| | | 03/07/2024 | 15 | 26.99 | 4340.59 | 4367.58 | | 15 | 14 | 17 | 13.8 | 13.4 |
| | | 04/07/2024 | 10 | 17.99 | 4367.58 | 4385.57 | | 15 | 14 | 17 | 14.3 | 13.6 |

Table 43 Average apparent density in the excavation chamber, TY06 and TY11 sensors (Report, 2024)

## 5.7 From July 5th to July 15th (rings installed 924-972)

The excavation progress reported falls within the section covered by P.A.T. n°5 (Table 7). Excavation operations were halted on July 7th due to the saturation of the temporary spoil disposal tanks, and excavation resumed on the morning of July 12th. Excavation was again interrupted from July 14th to 20th; during this downtime, maintenance was carried out on the cutterhead under normal pressure conditions, replacing the worn peripheral disc cutters. It is noted that the reconfiguration of the cutterhead, with the introduction of disc cutters in place of rippers, was completed at pk 3+918, and the downtime for replacing the worn cutters is the first after the reconfiguration. Excavation then resumed regularly on 21/07/2024.

In the graph in Figure 5.60, the pressure $\mathbf{p_{f,c}}$ is shown as a function of the ring number, while Table 45 presents the average value of $\mathbf{p_{f,c}}$ for each section, based on the progress.

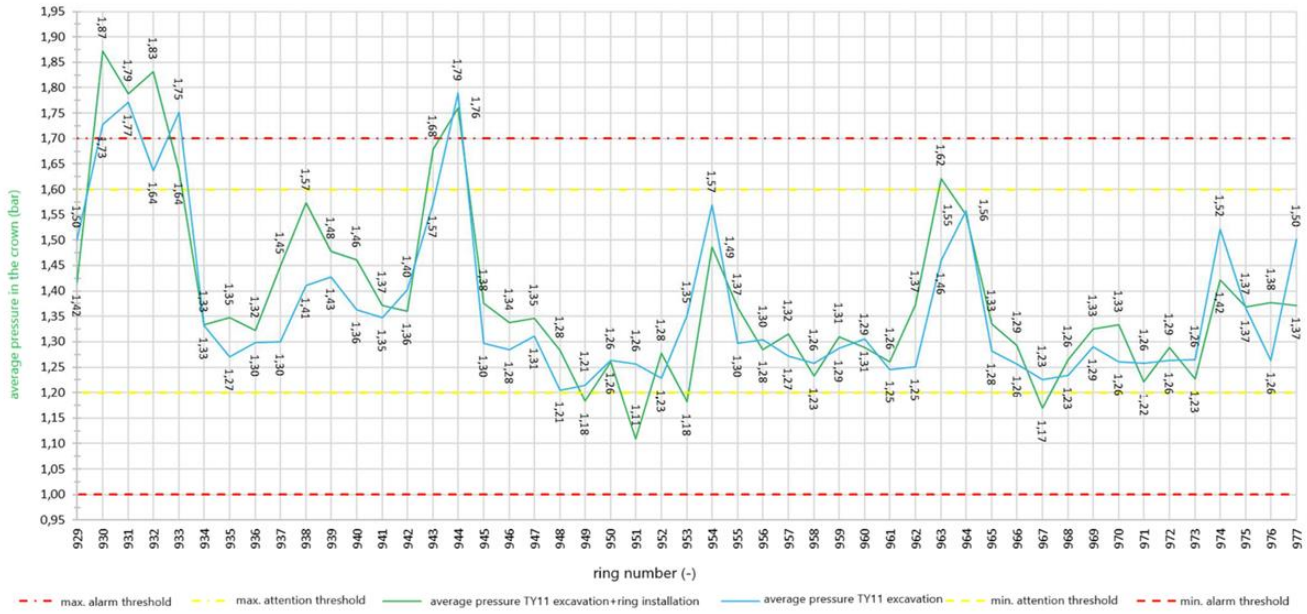


Figure 5.60 Average pressure in the crown during excavation and at the completion of the ring installation (TY11 sensor) (Report, 2024)

| Omog. Segments Geom. | segment number | day | n° of ring installed | Lenght L (m) | starting pk (m) | final pk (m) | L total (m) | $p_f$ (bar) | $p_{f,c}$ (bar) | ATTENTION (bar) | | ALARM (bar) | | average $p_{f,c}$ value (bar) | |
|---|---|---|---|---|---|---|---|---|---|---|---|---|---|---|---|
| | | | | | | | | | | MIN | MAX | MIN | MAX | excavation | excavation + ring installation |
| FYRmar+FYRar | 12 | 05/06/2024 | 4 | 7.19 | 4385.57 | 4392.77 | 88.2 | 2.0 | 1.3 | 1.2 | 1.6 | 1.0 | 1.7 | 1.66 | 1.73 |
| | | 06/06/2024 | 11 | 19.80 | 4392.77 | 4412.57 | | 2.0 | 1.3 | 1.2 | 1.6 | 1.0 | 1.7 | 1.41 | 1.46 |
| | | 12/06/2024 | 12 | 21.59 | 4412.57 | 4434.16 | | 2.0 | 1.3 | 1.2 | 1.6 | 1.0 | 1.7 | 1.34 | 1.33 |
| | | 13/06/2024 | 8 | 14.41 | 4434.16 | 4448.57 | | 2.0 | 1.3 | 1.2 | 1.6 | 1.0 | 1.7 | 1.30 | 1.34 |
| | | 14/06/2024 | 14 | 25.25 | 4448.57 | 4473.82 | | 2.0 | 1.3 | 1.2 | 1.6 | 1.0 | 1.7 | 1.32 | 1.32 |

Table 44 Average pressure in the crown during excavation and at the completion of the ring installation (TY11 sensor) (Report, 2024)

The $\mathbf{p_{f,c}}$ pressure is predominantly between the minimum and maximum attention thresholds, respectively 1.2 and 1.6 bar, during excavation and at the completion of the ring installation. In rings 930, 931, 932, 933, and 945, the $\mathbf{p_{f,c}}$ pressure during excavation and at the completion of the ring installation remained close to the maximum alarm threshold of 1.7 bar, exceeding it by a maximum of 0.17 bar at the end of the installation. It is assumed that there was a somewhat more unstable excavation face in this section, although the advancement was not affected by it.

### 5.7.1 Injection volume and pressure

The location of the injection lines is referenced in Figure 5.4, while for the calculation of the volumes of two-component grout to be injected from each individual line, equations (5.1) and (5.2) from section 5.1.1 were used.

The same proportions were applied to calculate the minimum volume of 10.74 m³ in the case of shield tail ground contact.

For the alert and alarm thresholds of the volume corresponding to line #i, to be filled with two-component grout, the procedure followed was the same as for the total mix volume per ring, using the formulas (5.3a)-(5.3.d) already presented in section 5.1.1.

The graph in Figure 5.61 shows the injection volume of the two-component grout, while Table 46 provides the average volume value **V** per section.

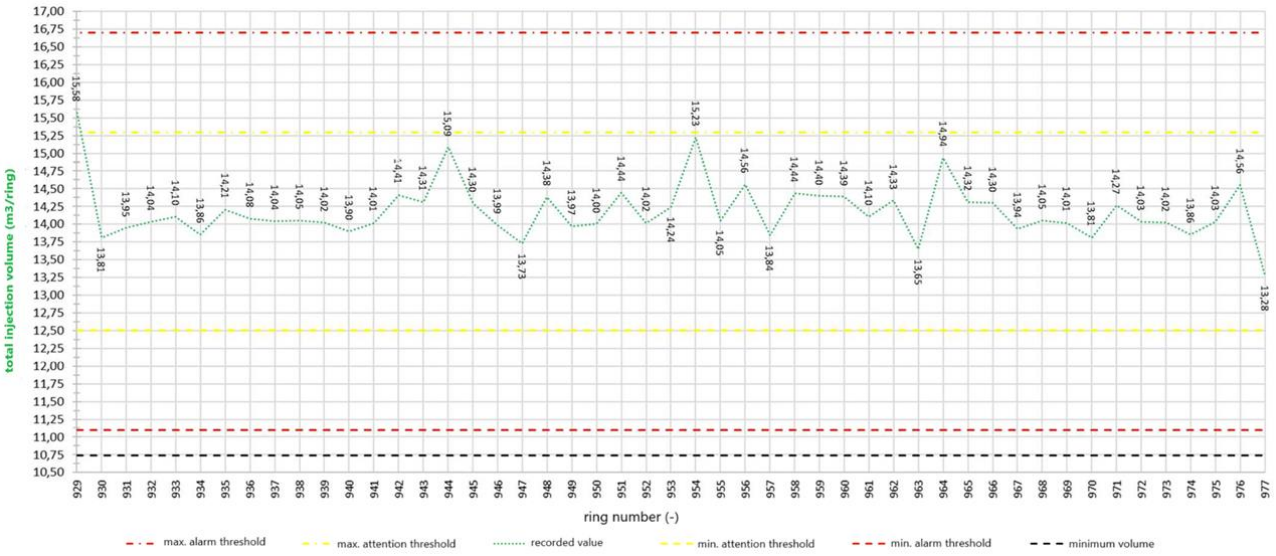


Figure 5.61 Total injection volume of the two-component mixture in m³/ring (Report, 2024)

| Omog. Segments Geom. | segment number | day | n° of ring installed | Lenght L (m) | starting pk (m) | final pk (m) | L total (m) | V (m³/ring) | ATTENTION (m³/ring) | | ALARM (m³/ring) | | minimum V (m³/ring) | average V (m³/ring) |
|---|---|---|---|---|---|---|---|---|---|---|---|---|---|---|
| | | | | | | | | | MIN | MAX | MIN | MAX | | |
| FYRmar+FYRar | 12 | 05/06/2024 | 4 | 7.19 | 4385.57 | 4392.77 | 88.2 | 13.91 | 12.52 | 15.30 | 11.13 | 16.69 | 10.74 | 14.35 |
| | | 06/06/2024 | 11 | 19.80 | 4392.77 | 4412.57 | | 13.91 | 12.52 | 15.30 | 11.13 | 16.69 | 10.74 | 14.09 |
| | | 12/06/2024 | 12 | 21.59 | 4412.57 | 4434.16 | | 13.91 | 12.52 | 15.30 | 11.13 | 16.69 | 10.74 | 14.29 |
| | | 13/06/2024 | 8 | 14.41 | 4434.16 | 4448.57 | | 13.91 | 12.52 | 15.30 | 11.13 | 16.69 | 10.74 | 14.21 |
| | | 14/06/2024 | 14 | 25.25 | 4448.57 | 4473.82 | | 13.91 | 12.52 | 15.30 | 11.13 | 16.69 | 10.74 | 14.10 |

Table 45 Average injection volume of the two-component mixture in m³/ring per section (Report, 2024)

The pressure of the individual injection lines for component A was calculated using formula (5.4) (section 5.1.1).

The alert and alarm thresholds were defined as for the face pressure and the pressure in the crown (equations (5.5a)-(5.5d), section 5.1.1).

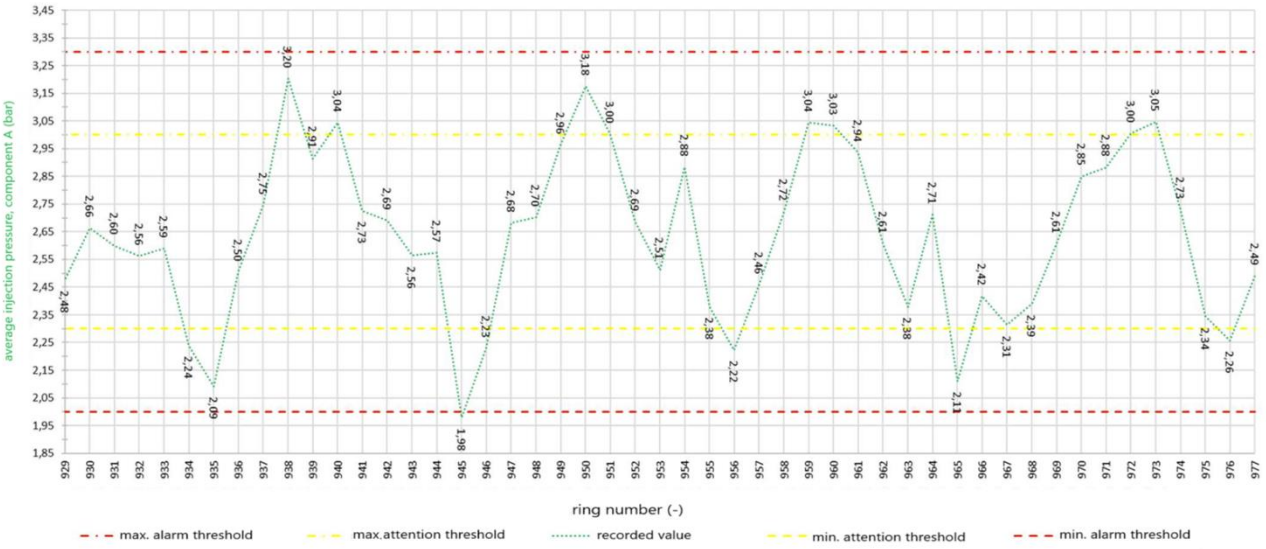


Figure 5.62 Average injection pressure of component A per section (Report, 2024)

| Omog. Segments Geom. | segment number | day | n° of ring installed | Lenght L (m) | starting pk (m) | final pk (m) | L total (m) | $p_m$ (bar) | ATTENTION (bar) | | ALARM (bar) | | average $p_m$ (bar) |
|---|---|---|---|---|---|---|---|---|---|---|---|---|---|
| | | | | | | | | | MIN | MAX | MIN | MAX | |
| FYRmar+FYRar | 12 | 05/06/2024 | 4 | 7.19 | 4385.57 | 4392.77 | 88.2 | 2.5 | 2.3 | 3.0 | 2.0 | 3.3 | 2.58 |
| | | 06/06/2024 | 11 | 19.80 | 4392.77 | 4412.57 | | 2.5 | 2.3 | 3.0 | 2.0 | 3.3 | 2.66 |
| | | 12/06/2024 | 12 | 21.59 | 4412.57 | 4434.16 | | 2.5 | 2.3 | 3.0 | 2.0 | 3.3 | 2.65 |
| | | 13/06/2024 | 8 | 14.41 | 4434.16 | 4448.57 | | 2.5 | 2.3 | 3.0 | 2.0 | 3.3 | 2.68 |
| | | 14/06/2024 | 14 | 25.25 | 4448.57 | 4473.82 | | 2.5 | 2.3 | 3.0 | 2.0 | 3.3 | 2.58 |

Table 46 Average injection pressure of component A per section (Report, 2024)

The pressure $\mathbf{p_m}$ maintained within most of the clogs was between the minimum and maximum attention thresholds of 2.3 and 3.0 bar, respectively. In some sections, the pressure $\mathbf{p_m}$ was found to be lower than 2.3 bar and higher than 3.0 bar, but it remained above the minimum alarm threshold of 2.0 bar and below the maximum alarm threshold of 3.3 bar. It is specified that the two-component material gels within 8 seconds, and during this time, the liquid mixture distributes evenly within the annular void between the outer surface of the ring and the tunnel wall, with the clogging occurring during the TBM's advance with the injection chamber always full.
The reduction is justified by the fact that, as shown in reference to Figure 5.62, a more stable excavation face is assumed (thus, since the backfilling injection pressure is always higher than the face pressure, this confirms what was assumed).

### 5.7.2 Thrust and torque

For the position of the 6 thrust groups (A, B, C, D, E, F), refer to Figure 5.7 in paragraph 5.1.2.

The thrusts in the individual thrust groups A, B, C, D, E, and F generated by the expected maximum thrust, both lower and upper, between pk 4+385.573 and 4+473.819, they were determined taking into account that the center of gravity of the pistons is located on the axis of the tunnel. The eccentricity between the thrust axis and the center of gravity of the pistons $\mathbf{e_{app}}$ was calculated by assuming a trapezoidal pressure distribution on the excavation face.
Each thrust is considered on type 2 segments, i.e., segments reinforced with a denser reinforcement starting from 300 m from the tunnel entrance. The maximum excavation thrusts in groups A, B, C, D, E, and F satisfy the SLE, so the maximum thrust during excavation was always lower than the "maximum thrust for type 2 segments" (red line, section, and point).
The thrust exerted by the generic piston i is obtained as seen in section 5.1.2 (equations (5.6)-(5.8)). $\mathbf{S_i}$ and $\mathbf{z_i}$ represent the total thrust exerted by the pistons on the lining ring and the distance from the horizontal axis to the center of gravity of the generic piston **i**, respectively, while **S** is the total thrust exerted by the pistons.

The average and maximum thrusts of only the thrust groups F and C are reported below (Figures 5.63 and Figures 5.64):

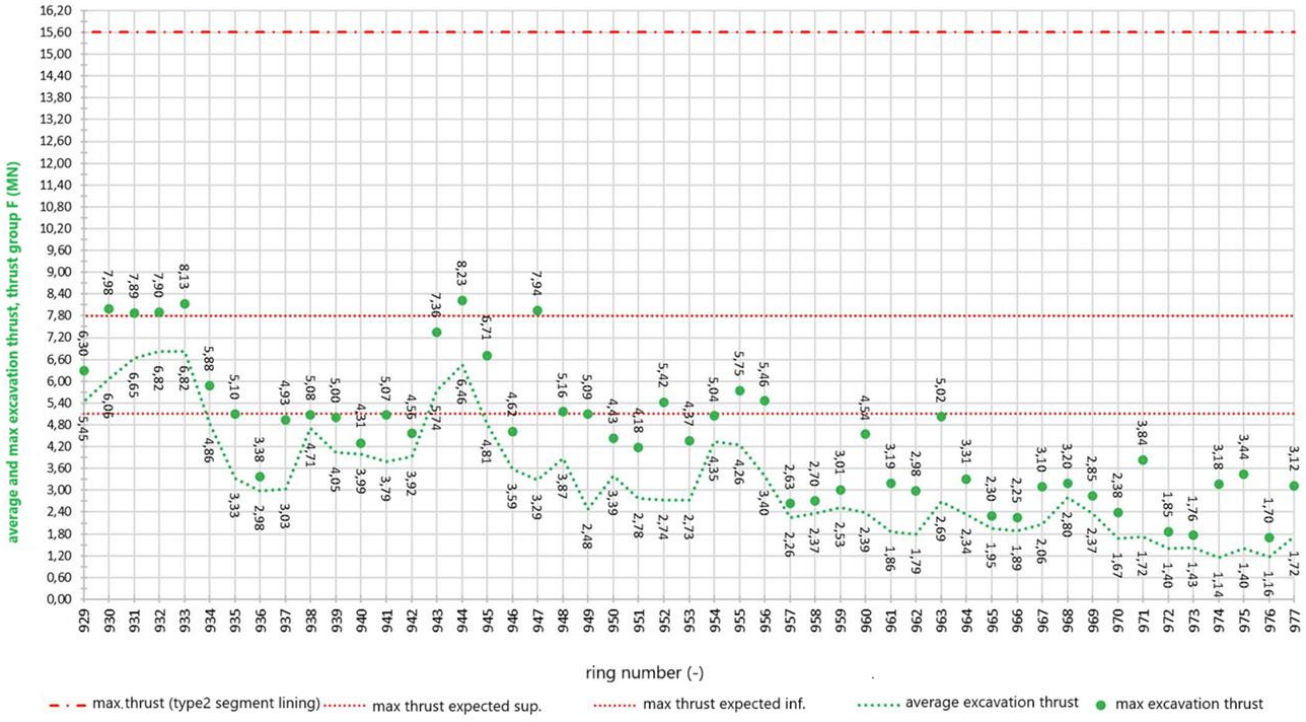


Figure 5.63 Average thrust and maximum thrust during the excavation phase exerted by the thrust group F (Report, 2024)

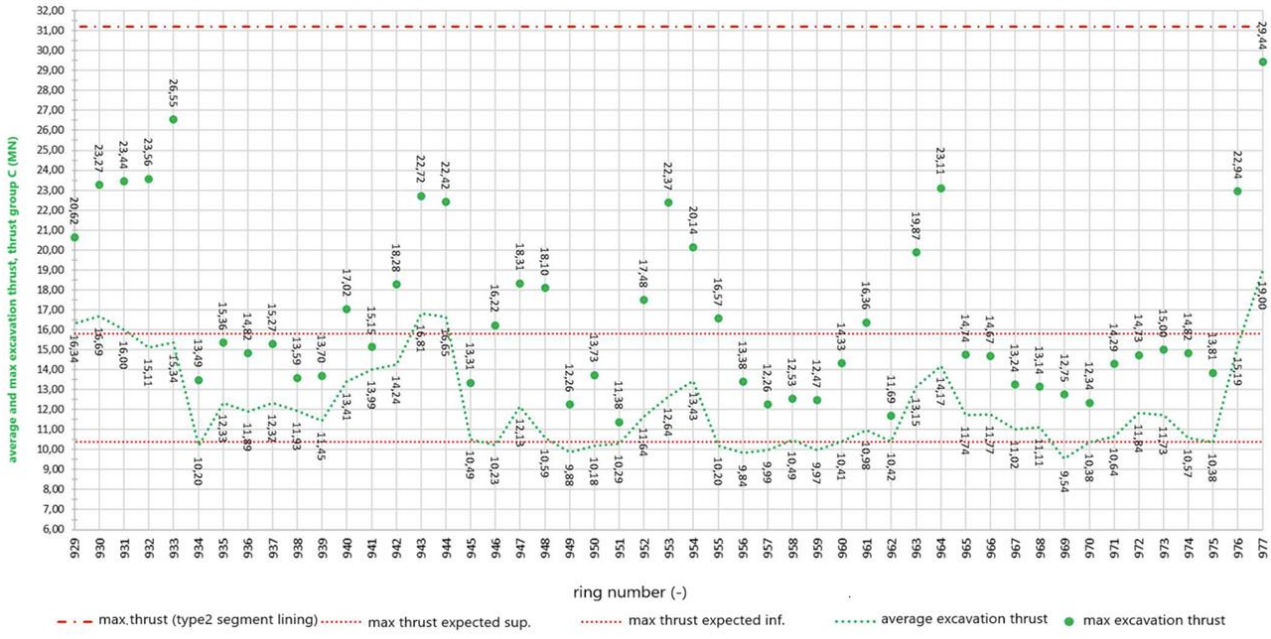


Figure 5.64 Average thrust and maximum thrust during the excavation phase exerted by the thrust group C (Report, 2024)

As expected from the trapezoidal pressure distribution on the excavation face, the thrust pistons of group C show higher values compared to those of group F, as the former are positioned lower than the latter.

A sudden increase in the maximum excavation thrust was observed in thrust group C, with 29.44 MN at ring 977, still below the SLE value of 31.2 MN. Subsequently, it became necessary to interrupt the excavation operations for the replacement of the peripheral cutters located along the periphery of the cutting head. Before the machine was stopped, additional excavation was carried out corresponding to ring 978.

In general, values below the minimum threshold indicate a softer face than expected, which therefore requires less thrust to be applied. It could also be related to a more stable face, which requires less thrust. This decision did not result in any negative consequences for the ongoing excavation.

Regarding the torque, Figure 5.10 (paragraph 5.1.2) also shows the maximum torque values. It is important to note that the torque on the cutterhead, due to friction, is strictly related to the thrust force and penetration.

In the graph in Figure 5.65, the average torque is shown as a function of the ring number, while Table 48 presents the average values for each section according to the progressive.

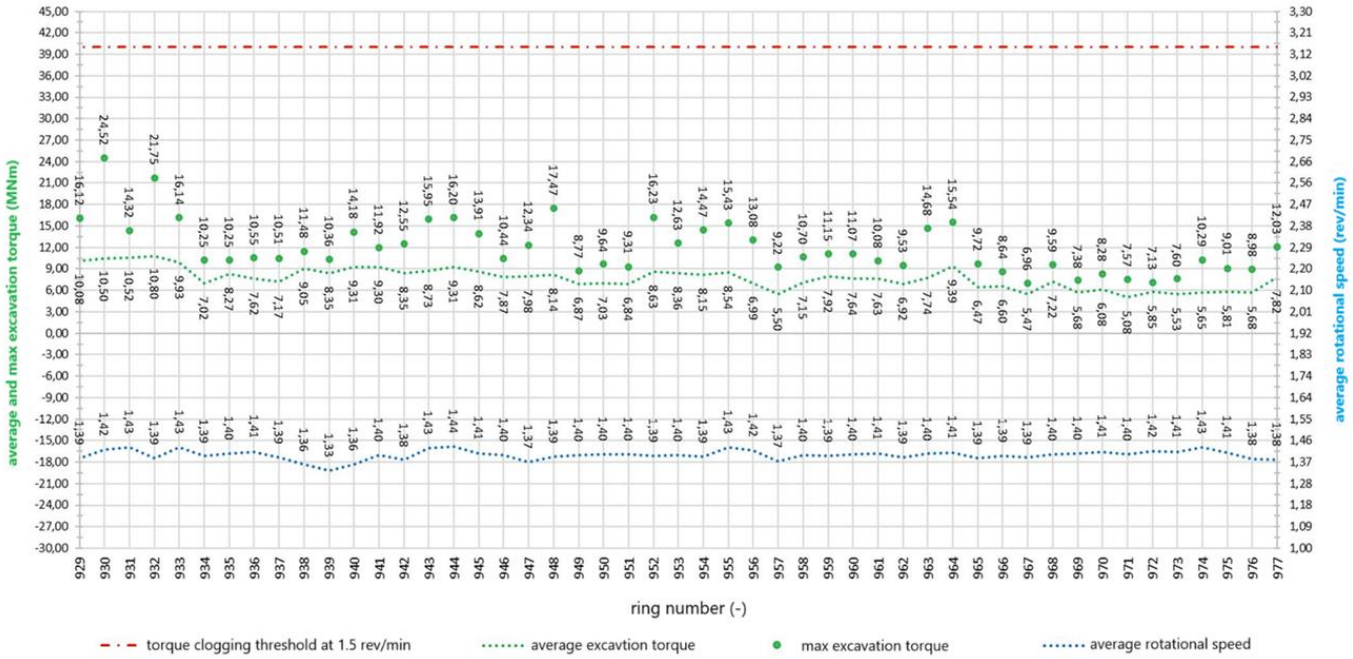


Figure 5.65 Average torque and maximum torque during excavation and average rotational speed (Report, 2024)

In the graph above, a roughly constant trend of torque can be observed, as well as the average rotation speed. Both torque and average rotation speed are within the normal range. It is noted that the rotation speed typically remains around 1.4 rpm, and the maximum torque that can be applied at this rotation speed is approximately twice the maximum torques recorded..

| Omog. Segments Geom. | segment number | day | n° of ring installed | Lenght L (m) | starting pk (m) | final pk (m) | L total (m) | AVERAGE TORQUE (MNm) | MAX. TORQUE (MNm) | TORQUE FOR A CLOGGING THRESHOLD OF 1.5 rev/min (MNm) | average rotation speed ω (rev/min) |
|---|---|---|---|---|---|---|---|---|---|---|---|
| FYRmar+FYRar | 12 | 05/06/2024 | 4 | 7.19 | 4385.57 | 4392.77 | 88.2 | 10.48 | 19.18 | 40 | 1.41 |
| | | 06/06/2024 | 11 | 19.80 | 4392.77 | 4412.57 | | 8.46 | 12.19 | 40 | 1.39 |
| | | 12/06/2024 | 12 | 21.59 | 4412.57 | 4434.16 | | 7.98 | 13.07 | 40 | 1.40 |
| | | 13/06/2024 | 8 | 14.41 | 4434.16 | 4448.57 | | 7.19 | 11.19 | 40 | 1.40 |
| | | 14/06/2024 | 14 | 25.25 | 4448.57 | 4473.82 | | 6.31 | 9.19 | 40 | 1.40 |

Table 47 Average torque and maximum torque during excavation and average rotational speed (Report, 2024)

As can be seen from the graph, each value falls within the limits.

### 5.7.3 Excavated material

The cover on the crown of the final tunnel lining in the section covered by the report ranges between 38.7 and 40.4 m, as shown in the operational geomechanical profile. The unit weight of the FYRmar+FYRar between pk 4+385.573 and 4+473.819 is 21.5 kN/m³.

The diagram of the average weight of the excavated soil for each installed ring, excluding the conditioning (see Chapter 6 for more details on soil conditioning), is compared with its gross average weight in Figure 5.66. In Table 49, following the graph, the net average values per section are provided.

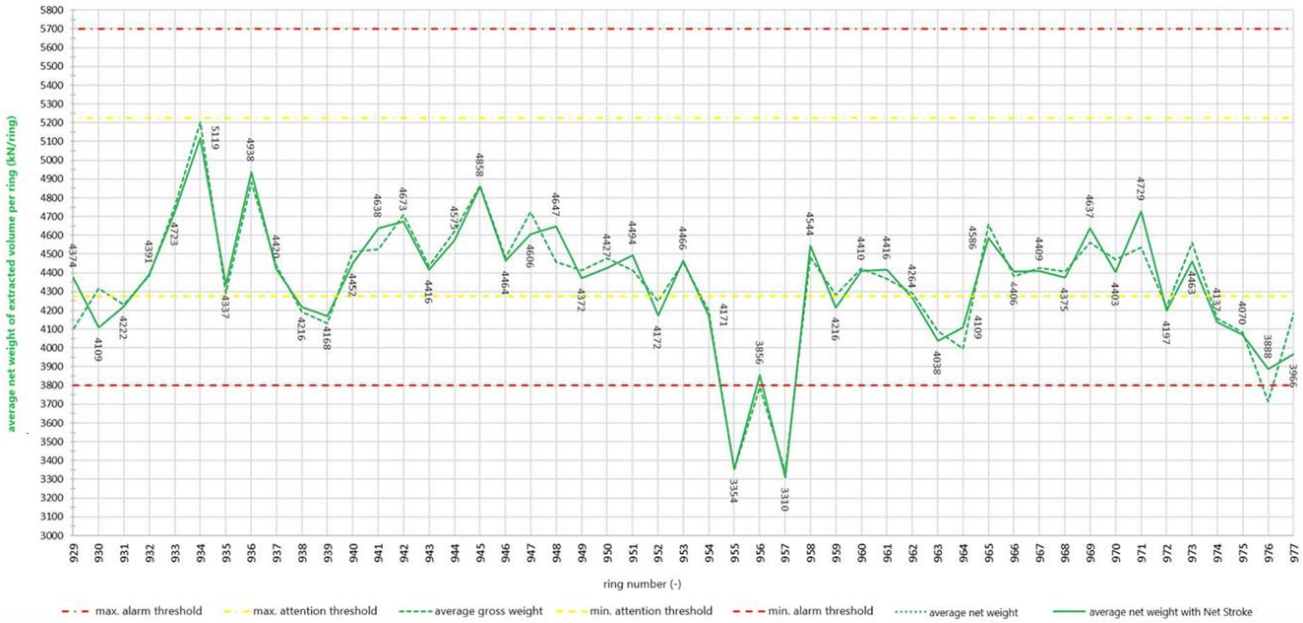


Figure 5.66 Comparison between the net weight and the gross weight of the material extracted per ring (Report, 2024)

| Omog. Segments Geom. | segment number | day | n° of ring installed | Lenght L (m) | starting pk (m) | final pk (m) | L total (m) | REFERENCE WEIGHT $P_t$ (kN) | ATTENTION MIN. (kN) | ATTENTION MAX. (kN) | ALARM MIN. (kN) | ALARM MAX. (kN) | AVERAGE GROSS WEIGHT (kN) | AVERAGE GROSS WEIGHT with NET STROKE (kN) |
|---|---|---|---|---|---|---|---|---|---|---|---|---|---|---|
| FYRmar+FYRar | 12 | 05/06/2024 | 4 | 7.19 | 4385.57 | 4392.77 | 88.2 | 4749 | 4274 | 5224 | 3799 | 5699 | 4257 | 4274 |
| | | 06/06/2024 | 11 | 19.80 | 4392.77 | 4412.57 | | 4749 | 4274 | 5224 | 3799 | 5699 | 4552 | 4555 |
| | | 12/06/2024 | 12 | 21.59 | 4412.57 | 4434.16 | | 4749 | 4274 | 5224 | 3799 | 5699 | 4393 | 4384 |
| | | 13/06/2024 | 8 | 14.41 | 4434.16 | 4448.57 | | 4749 | 4274 | 5224 | 3799 | 5699 | 4134 | 4132 |
| | | 14/06/2024 | 14 | 25.25 | 4448.57 | 4473.82 | | 4749 | 4274 | 5224 | 3799 | 5699 | 4311 | 4313 |

Table 48 The weight of the net excavated material extracted per ring (Report, 2024)

In Figure 5.66, we can observe a significant minimum at rings 955 and 957. In general, an increase in the average extracted weight indicates optimal conditioning, while a minimum value may indicate either overly compact or excessively loose ground. These, although exceeding the alarm threshold values, did not cause any problems during extraction from the screw conveyor, as the conditioning was sufficient to keep the machine operating at optimal levels.

In the diagram in Figure 5.67, the average pressures on sensors TY11 and TY07 are shown (for their positions, refer to Figure 5.1). The average values are calculated during the advancement

phase of the shield or considering both the shield advancement and the installation of the precast ring.The TY11 sensor is located at the top compared to TY07, which justifies the fact that the pressures from the former are higher than those from the latter, given the trapezoidal distribution of thrusts in the excavation chambre.
At ring 994, we observe a significant maximum, consistent with what was seen in the previous figure, and we can therefore hypothesize a less stable face (in contrast to the minimum observed at ring 975).
In Figure 5.68, the average apparent density is shown, calculated using the pressures reported in Figure 5.67, taking into account that the elevation difference between the two sensors is 8 m. Knowing the average apparent density in the excavation chamber allows us to adjust the TBM for more efficient auger extraction, reducing the risk of clogging. Density affects the pressure needed to support the excavation face: if it is too high, it could indicate compact soils, which may require more force or a special support system; a low density might suggest less stable soils. In particular, for soils with low density, water infiltration could become a problem, so monitoring the density helps predict and mitigate this risk.

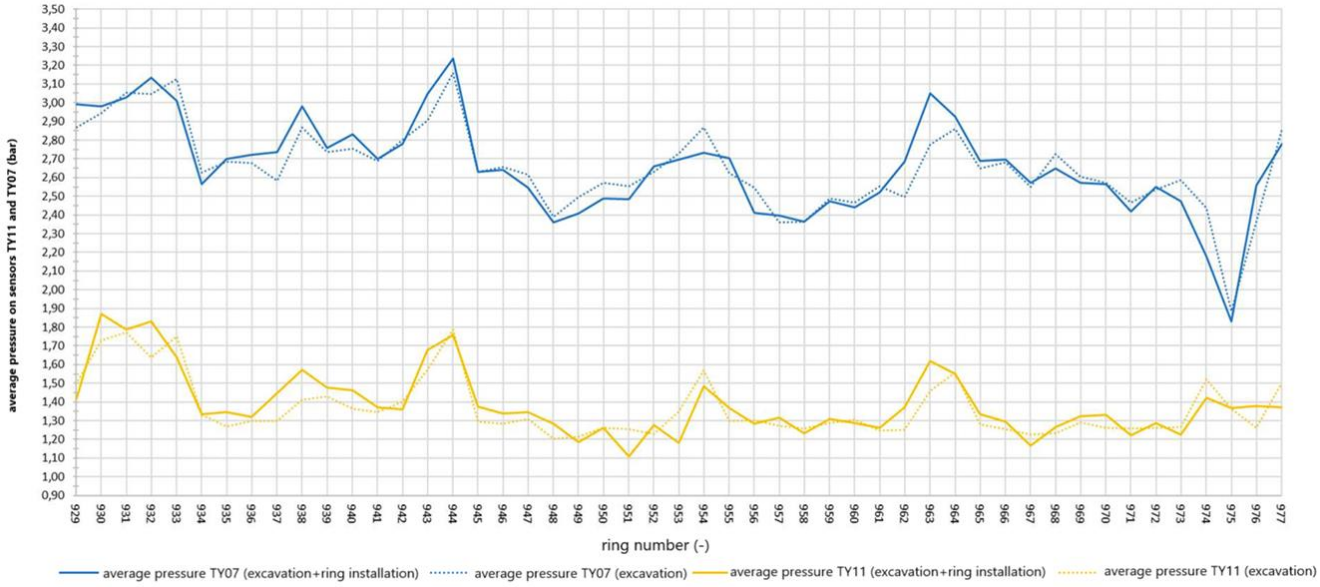


Figure 5.67 Face pressure: comparison between TY06 and TY11 sensors (Report, 2024)

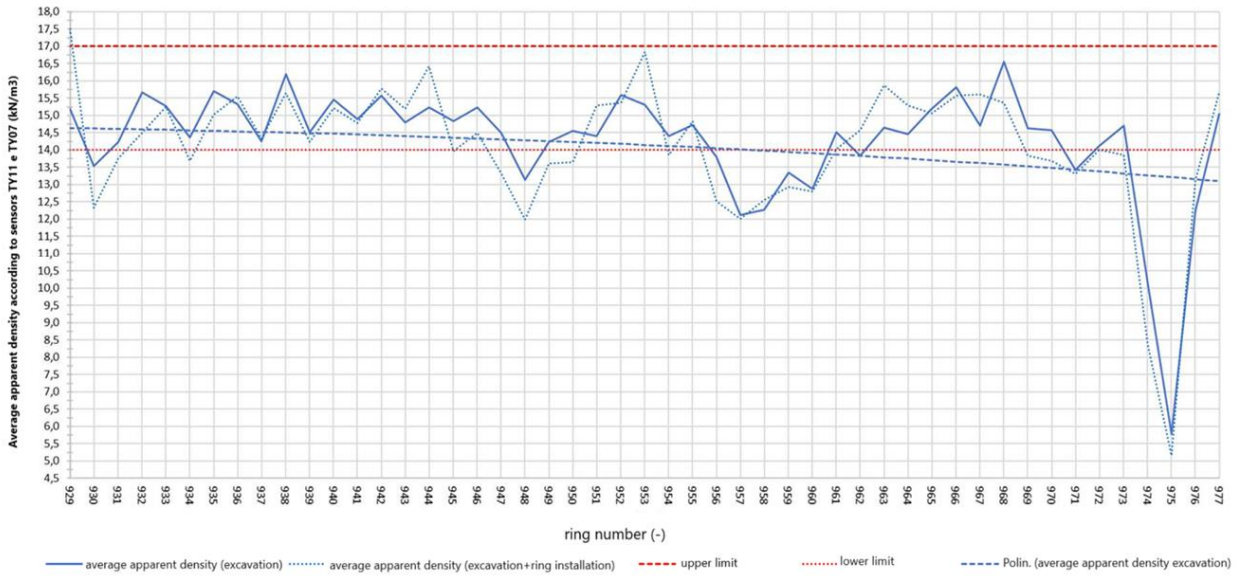


Figure 5.68 Average apparent density in the excavation chamber, TY06 and TY11 sensors (Report, 2024)

| Omog. Segments Geom. | segment number | day | n° of ring installed | Lenght L (m) | starting pk (m) | final pk (m) | L total (m) | pressure sensors TY11-TY07 | | | | |
|---|---|---|---|---|---|---|---|---|---|---|---|---|
| | | | | | | | | | | | average $\gamma_{app}$ over 24h | |
| | | | | | | | | $\gamma_{app,\ exc.}$ (kN/m$^3$) | lower limit | upper limit | $\gamma_{app,\ excavation}$ (kN/m$^3$) | $\gamma_{app,\ excavation+ring\ installation}$ (kN/m$^3$) |
| FYRmar+FYRar | 12 | 05/06/2024 | 4 | 7.19 | 4385.57 | 4392.77 | 88.2 | 15 | 14 | 17 | 14.66 | 14.52 |
| | | 06/06/2024 | 11 | 19.80 | 4392.77 | 4412.57 | | 15 | 14 | 17 | 15.12 | 14.97 |
| | | 12/06/2024 | 12 | 21.59 | 4412.57 | 4434.16 | | 15 | 14 | 17 | 14.68 | 14.47 |
| | | 13/06/2024 | 8 | 14.41 | 4434.16 | 4448.57 | | 15 | 14 | 17 | 13.43 | 13.41 |
| | | 14/06/2024 | 14 | 25.25 | 4448.57 | 4473.82 | | 15 | 14 | 17 | 13.67 | 13.42 |

Table 49 Average apparent density in the excavation chamber, TY06 and TY11 sensors (Report, 2024)

## 5.8 From July 15th to July 24th (rings installed 973-1009)

The excavation progress reported falls within the section covered by P.A.T. No. 5 (Table 7). As mentioned in the previous paragraph, from July 14th to July 21st, there was a stoppage for the replacement of worn cutters. From the 21st onward, excavation resumed regularly.

In the graph in Figure 5.69, the pressure $\mathbf{p_{f,c}}$ is shown as a function of the ring number, while Table 51 presents the average value of $\mathbf{p_{f,c}}$ for each section, based on the progress.

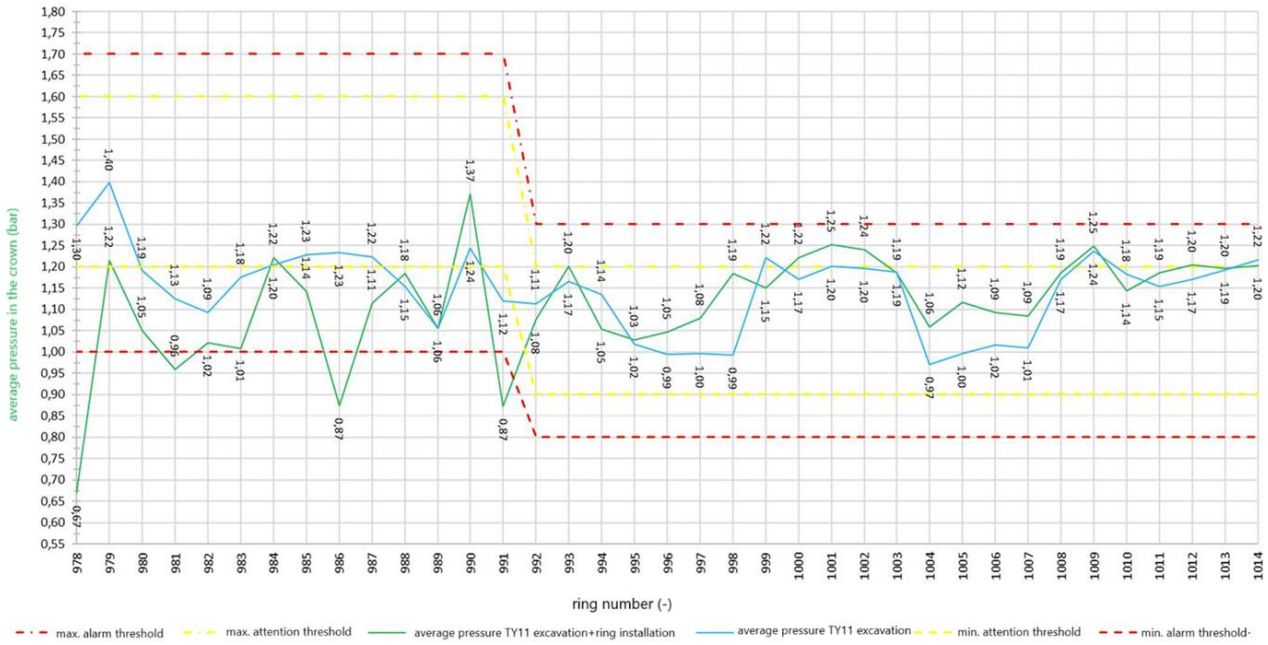


Figure 5.69 Average pressure in the crown during excavation and at the completion of the ring installation (TY11 sensor) (Report, 2024)

| Omog. Segments Geom. | segment number | day | n° of ring installed | Lenght L (m) | starting pk (m) | final pk (m) | L total (m) | $p_f$ (bar) | $p_{f,c}$ (bar) | ATTENTION (bar) | | ALARM (bar) | | average $p_{f,c}$ value (bar) | |
|---|---|---|---|---|---|---|---|---|---|---|---|---|---|---|---|
| | | | | | | | | | | MIN | MAX | MIN | MAX | excavation | excavation + ring installation |
| FYRmar+FYRar | 12 | 21/072024 | 6 | 10.87 | 4473.82 | 4484.69 | | 2.0 | 1.3 | 1.2 | 1.6 | 1.0 | 1.7 | 1.21 | 0.99 |
| | | 22/07/2024 | 11 | 14.42 | 4484.69 | 4499.11 | | 2.0 | 1.3 | 1.2 | 1.6 | 1.0 | 1.7 | 1.17 | 1.11 |
| FYR2c | 11 | | | 5.37 | 4499.11 | 4504.48 | 66.6 | 1.7 | 1 | 0.9 | 1.2 | 0.8 | 1.3 | | |
| | | 23/07/2024 | 8 | 14.36 | 4504.48 | 4518.84 | | 1.7 | 1 | 0.9 | 1.2 | 0.8 | 1.3 | 1.10 | 1.15 |
| | | 24/07/2024 | 12 | 21.55 | 4518.84 | 4540.39 | | 1.7 | 1 | 0.9 | 1.2 | 0.8 | 1.3 | 1.13 | 1.16 |

Table 50 Average pressure in the crown during excavation and at the completion of the ring installation (TY11 sensor) (Report, 2024)

The $\mathbf{p_{f,c}}$ during excavation and at the end of the ring installation is primarily between the minimum attention and alarm thresholds, 1.0 and 1.2 bar, respectively, between pk 4+448.57 and 4+499.11, and between the minimum and maximum attention thresholds, 0.9 and 1.2 bar, respectively, between pk 4+499.11 and 4+540.39. During the installation phase of the ring with prefabricated segments in the section between pk 4+448.57 and 4+499.11, decompressions occurred in the excavation chamber. The decompressions had no effect on the stability of the face and the tunnel, as evidenced by the fact that the maximum excavation thrust was always between the expected lower and upper maximum thrusts, and these two thrusts were calculated assuming no contact between the shield and the ground.

Additionally, it should be noted that the installation of the ring takes place over a short period, and that at ring 978, the operation was performed under normal atmospheric pressure conditions, with $\mathbf{p_{f,c}}$ pressure at the crown on the excavation face equal to 0.

### 5.8.1 Injection volume and pressure

The location of the injection lines is referenced in Figure 5.4, while for the calculation of the volumes of two-component grout to be injected from each individual line, equations (5.1) and (5.2) from section 5.1.1 were used.

The same proportions were applied to calculate the minimum volume of 10.74 m³ in the case of shield tail ground contact.

For the alert and alarm thresholds of the volume corresponding to line #i, to be filled with two-component grout, the procedure followed was the same as for the total mix volume per ring, using the formulas (5.3a)-(5.3.d) already presented in section 5.1.1.

The graph in Figure 5.70 shows the injection volume of the two-component grout, while Table 52 provides the average volume value **V** per section.


Figure 5.70 Total injection volume of the two-component mixture in m³/ring (Report, 2024)

| Omog. Segments Geom. | segment number | day | n° of ring installed | Lenght L (m) | starting pk (m) | final pk (m) | L total (m) | V (m³/ring) | ATTENTION (m³/ring) | | ALARM (m³/ring) | | minimum V (m³/ring) | average V (m³/ring) |
|---|---|---|---|---|---|---|---|---|---|---|---|---|---|---|
| | | | | | | | | | MIN | MAX | MIN | MAX | | |
| FYRmar+FYRar | 12 | 21/072024 | 6 | 10.87 | 4473.82 | 4484.69 | 66.6 | 13.91 | 12.52 | 15.30 | 11.13 | 16.69 | 10.74 | 14.23 |
| | | 22/07/2024 | 11 | 14.42 | 4484.69 | 4499.11 | | 13.91 | 12.52 | 15.30 | 11.13 | 16.69 | 10.74 | 14.29 |
| FYR2c | 11 | | | 5.37 | 4499.11 | 4504.48 | | 13.91 | 12.52 | 15.30 | 11.13 | 16.69 | 10.74 | 14.02 |
| | | 23/07/2024 | 8 | 14.36 | 4504.48 | 4518.84 | | 13.91 | 12.52 | 15.30 | 11.13 | 16.69 | 10.74 | 14.02 |
| | | 24/07/2024 | 12 | 21.55 | 4518.84 | 4540.39 | | 13.91 | 12.52 | 15.30 | 11.13 | 16.69 | 10.74 | 13.96 |

Table 51 Average injection volume of the two-component mixture in m³/ring per section (Report, 2024)

The pressure of the individual injection lines for component A was calculated using formula (5.4) (section 5.1.1).

The alert and alarm thresholds were defined as for the face pressure and the pressure in the crown (equations (5.5a)-(5.5d), section 5.1.1).

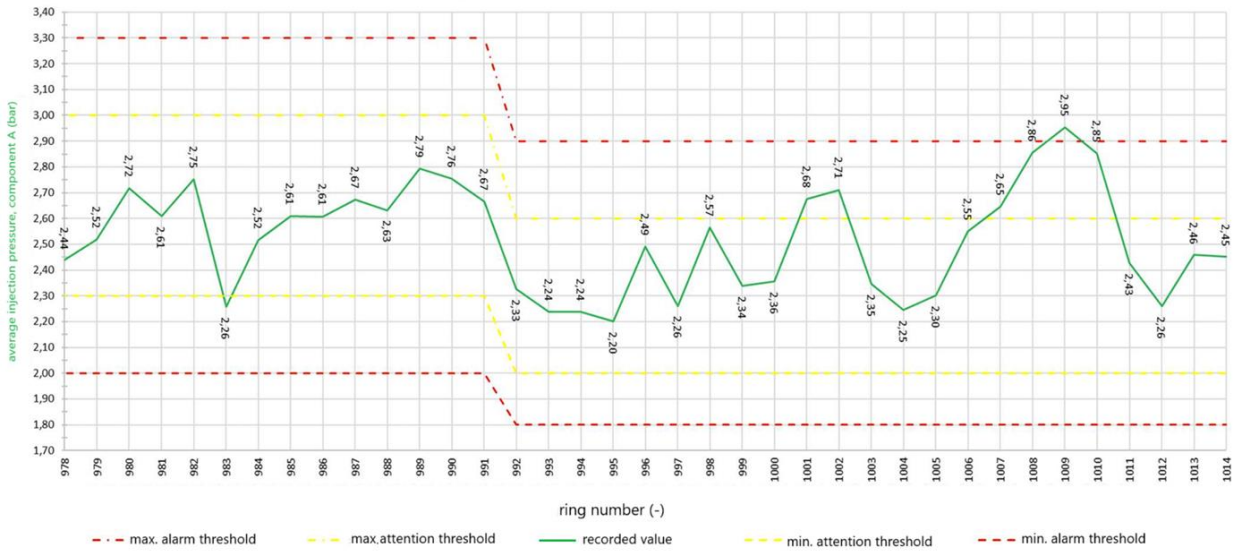


Figure 5.71 Average injection pressure of component A per section (Report, 2024)

| Omog. Segments Geom. | segment number | day | n° of ring installed | Lenght L (m) | starting pk (m) | final pk (m) | L total (m) | $p_m$ (bar) | ATTENTION (bar) | | ALARM (bar) | | average $p_m$ (bar) |
|---|---|---|---|---|---|---|---|---|---|---|---|---|---|
| | | | | | | | | | MIN | MAX | MIN | MAX | |
| FYRmar+FYRar | 12 | 21/072024 | 6 | 10.87 | 4473.82 | 4484.69 | 66.6 | 2.5 | 2.3 | 3.0 | 2.0 | 3.3 | 2.55 |
| | | 22/07/2024 | 11 | 14.42 | 4484.69 | 4499.11 | | 2.5 | 2.3 | 3.0 | 2.0 | 3.3 | 2.55 |
| FYR2c | 11 | | | 5.37 | 4499.11 | 4504.48 | | 2.2 | 2.0 | 2.6 | 1.8 | 2.9 | |
| | | 23/07/2024 | 8 | 14.36 | 4504.48 | 4518.84 | | 2.2 | 2.0 | 2.6 | 1.8 | 2.9 | 2.45 |
| | | 24/07/2024 | 12 | 21.55 | 4518.84 | 4540.39 | | 2.2 | 2.0 | 2.6 | 1.8 | 2.9 | 2.53 |

Table 52 Average injection pressure of component A per section (Report, 2024)

The pressure $\mathbf{p_m}$ maintained within most of the clogs was between the minimum and maximum attention thresholds of 2.3 and 3.0 bar, respectively, between the progressions 4+473.82 and 4+499.11, and between 2.0 and 2.6 bar, between progressions 4+499.11 and 4+540.39.

It is specified that the two-component material gels within 8 seconds, and during this time, the A+B liquid mixture distributes evenly within the annular void between the outer surface of the ring and the tunnel wall. The clogging occurs during the advance of the TBM, with the injection chamber always full. It is clear from the data in Table 4 that, during the 24 hours of production, the injection pressure $\mathbf{p_m}$ conforms to the values reported in P.A.T. No. 5.

The reduction is justified by the fact that, as explained in reference to Figure ?, a more stable excavation face is assumed (therefore, since the backfilling injection pressure is always higher than the face pressure, this confirms the assumption). Conversely, where the value is higher, as for ring 1009.

### 5.8.2 Thrust and torque

For the position of the 6 thrust groups (A, B, C, D, E, F), refer to Figure 5.7 in paragraph 5.1.2.

The thrusts in the individual thrust groups A, B, C, D, E, and F generated by the expected lower and upper maximum thrusts, respectively 40 and 60 MN between pk 4+473.819 and 4+499.110, and 37 and 56 MN between pk 4+499.110 and 4+540.392, they were determined taking into account that the center of gravity of the pistons is located on the axis of the tunnel. The eccentricity between the thrust axis and the center of gravity of the pistons $\mathbf{e_{app}}$ was calculated by assuming a trapezoidal pressure distribution on the excavation face.
Each thrust is considered on type 2 segments, i.e., segments reinforced with a denser reinforcement starting from 300 m from the tunnel entrance. The maximum excavation thrusts in groups A, B, C, D, E, and F satisfy the SLE, so the maximum thrust during excavation was always lower than the "maximum thrust for type 2 segments" (red line, section, and point).
The thrust exerted by the generic piston i is obtained as seen in section 5.1.2 (equations (5.6)-(5.8)). $\mathbf{S_i}$ and $\mathbf{z_i}$ represent the total thrust exerted by the pistons on the lining ring and the distance from the horizontal axis to the center of gravity of the generic piston **i**, respectively, while **S** is the total thrust exerted by the pistons.

The average and maximum thrusts of only the thrust groups F and C are reported below (Figures 5.72 and Figures 5.73):

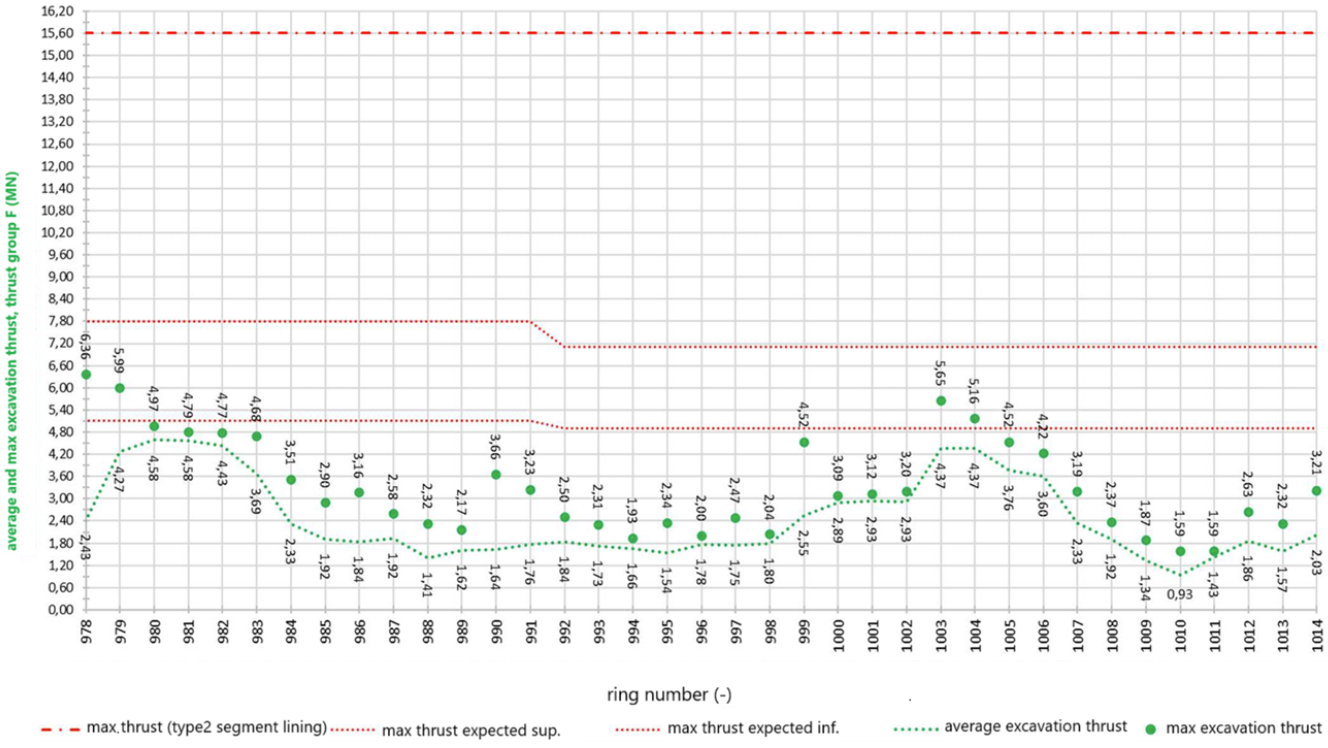


Figure 5.72 Average thrust and maximum thrust during the excavation phase exerted by the thrust group F (Report, 2024)

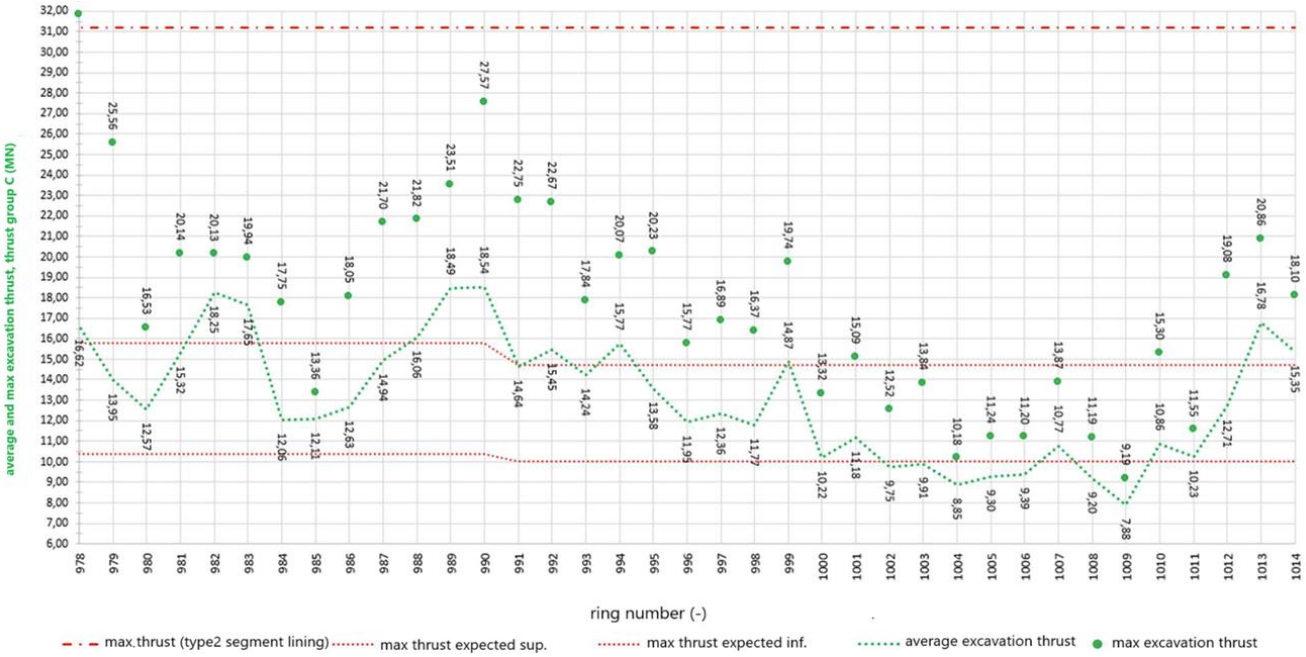


Figure 5.73 Average thrust and maximum thrust during the excavation phase exerted by the thrust group C (Report, 2024)

As expected from the trapezoidal pressure distribution on the excavation face, the thrust pistons of group C show higher values compared to those of group F, as the former are positioned lower than the latter.
In general, values below the minimum threshold indicate a softer face than expected, which therefore requires less thrust to be applied. It could also be related to a more stable face, which requires less thrust. This decision did not result in any negative consequences for the ongoing excavation.

Regarding the torque, Figure 5.10 (paragraph 5.1.2) also shows the maximum torque values. It is important to note that the torque on the cutterhead, due to friction, is strictly related to the thrust force and penetration.

In the graph in Figure 5.74, the average torque is shown as a function of the ring number, while Table 54 presents the average values for each section according to the progressive.

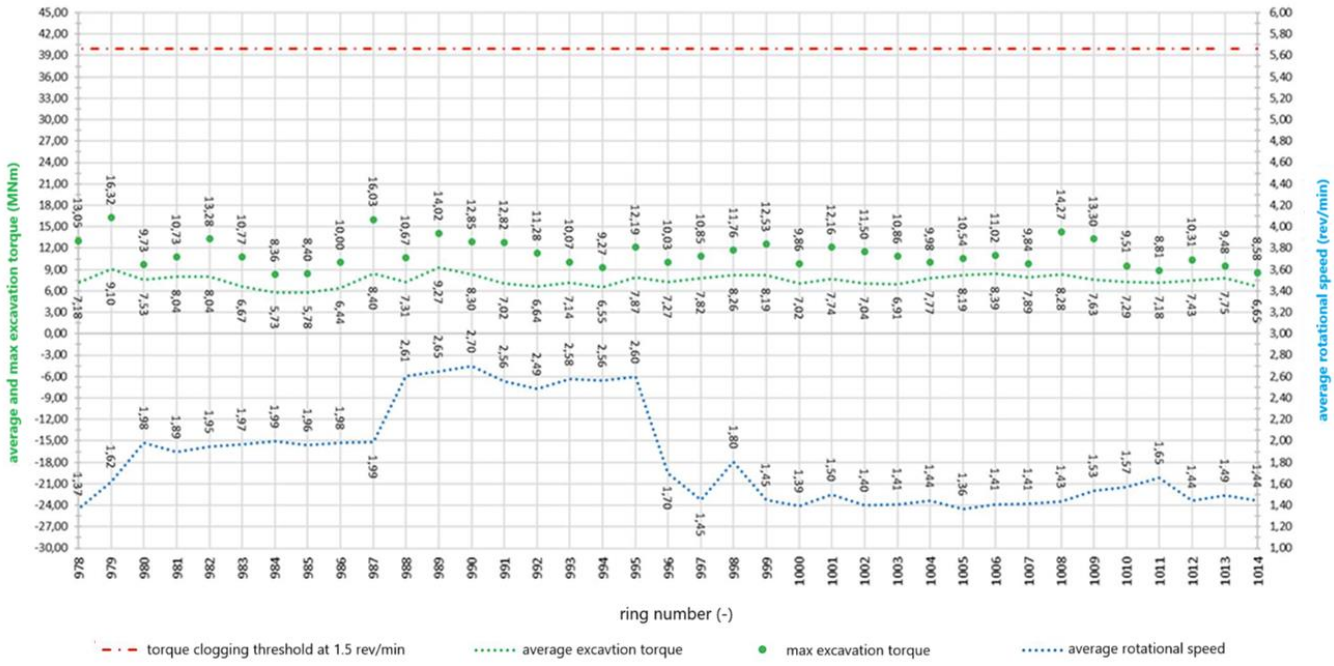


Figure 5.74 Average torque and maximum torque during excavation and average rotational speed (Report, 2024)

An increase in the rotation speed of the cutterhead is noted from ring 978 to ring 995, with a more pronounced increase between rings 988 and 995. The rotation speed of the cutterhead was increased due to the reduction in penetration per revolution **p**, which was caused by the ground face competence. By increasing **ω**, it was possible to maintain the advance speed **v** around 26.7 mm/min between rings 978 and 995. The following relationship exists between the kinematic variables **v**, **p**, and **ω**:

$$\boldsymbol{v}\left[\frac{mm}{min}\right] = \boldsymbol{p}\left[\frac{mm}{giri}\right] \cdot \boldsymbol{\omega}\left[\frac{giri}{min}\right] \qquad (5.9)$$

Additionally, it is noted that between rings 978 and 995, all machine parameters are within the normal range.

| Omog. Segments Geom. | segment number | day | n° of ring installed | Lenght L (m) | starting pk (m) | final pk (m) | L total (m) | AVERAGE TORQUE (MNm) | MAX. TORQUE (MNm) | TORQUE FOR A CLOGGING THRESHOLD OF 1.5 rev/min (MNm) | average rotation speed ω (rev/min) |
|---|---|---|---|---|---|---|---|---|---|---|---|
| FYRmar+FYRar | 12 | 21/072024 | 6 | 10.87 | 4473.82 | 4484.69 | 66.6 | 7.76 | 12.31 | 40 | 1.80 |
| | | 22/07/2024 | 11 | 14.42 | 4484.69 | 4499.11 | | 7.14 | 11.25 | 40 | 2.37 |
| FYR2c | 11 | | | 5.37 | 4499.11 | 4504.48 | | | | | |
| | | 23/07/2024 | 8 | 14.36 | 4504.48 | 4518.84 | | 7.65 | 11.36 | 40 | 1.66 |
| | | 24/07/2024 | 12 | 21.55 | 4518.84 | 4540.39 | | 7.61 | 10.54 | 40 | 1.47 |

Table 53 Average torque and maximum torque during excavation and average rotational speed (Report, 2024)

As can be seen from the graph, each value falls within the limits.

### 5.8.3 Excavated material

The cover on the crown of the final tunnel lining in the section covered by the report ranges between 37.3 and 40.1 meters, as shown in the Geomechanical profile. The unit weight of

FYRmar+FYRar between pk 4+373.819 and 4+500, and of FYR2c between pk 4+500 and 4+540.392, is 21.5 kN/m³.

The diagram of the average weight of the excavated soil for each installed ring, excluding the conditioning (see Chapter 6 for more details on soil conditioning), is compared with its gross average weight in Figure 5.75. In Table 55, following the graph, the net average values per section are provided.

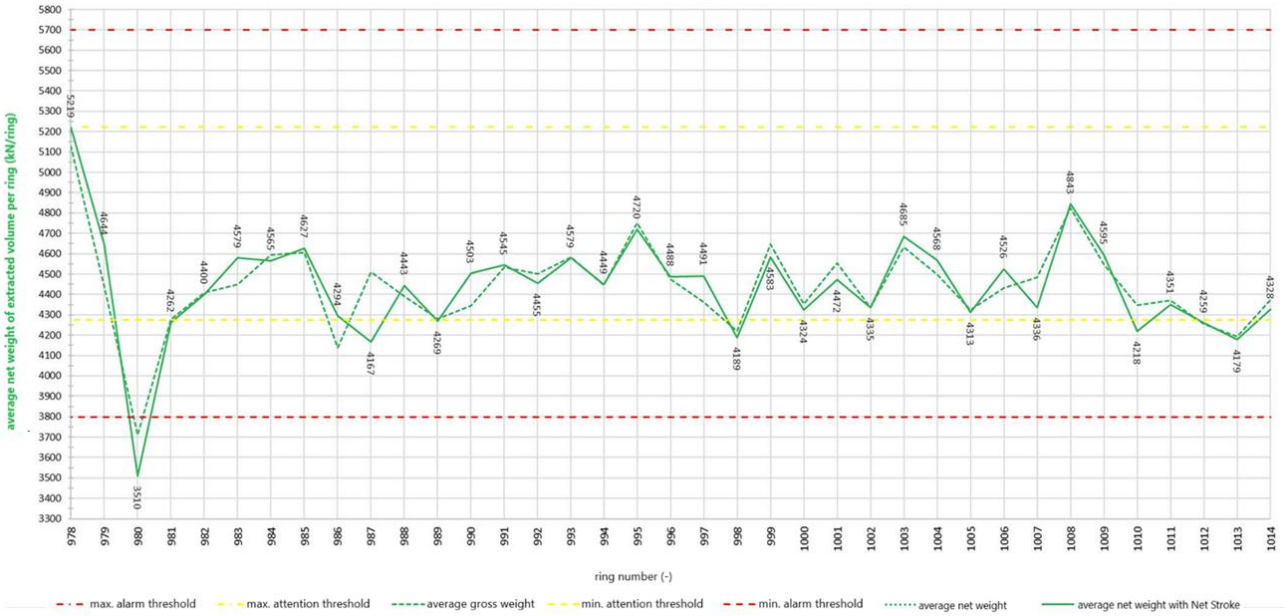


Figure 5.75 Comparison between the net weight and the gross weight of the material extracted per ring (Report, 2024)

| Omog. Segments Geom. | segment number | day | n° of ring installed | Lenght L (m) | starting pk (m) | final pk (m) | L total (m) | REFERENCE WEIGHT $P_t$ (kN) | ATTENTION MIN. (kN) | ATTENTION MAX. (kN) | ALARM MIN. (kN) | ALARM MAX. (kN) | AVERAGE GROSS WEIGHT (kN) | AVERAGE GROSS WEIGHT with NET STROKE (kN) |
|---|---|---|---|---|---|---|---|---|---|---|---|---|---|---|
| FYRmar+FYRar | 12 | 21/072024 | 6 | 10.87 | 4473.82 | 4484.69 | 66.6 | 4749 | 4274 | 5224 | 3799 | 5699 | 4401 | 4436 |
| FYR2c | 11 | 22/07/2024 | 11 | 14.42 | 4484.69 | 4499.11 | | 4749 | 4274 | 5224 | 3799 | 5699 | 4448 | 4445 |
| | | | | 5.37 | 4499.11 | 4504.48 | | | | | | | | |
| | | 23/07/2024 | 8 | 14.36 | 4504.48 | 4518.84 | | 4749 | 4274 | 5224 | 3799 | 5699 | 4462 | 4450 |
| | | 24/07/2024 | 12 | 21.55 | 4518.84 | 4540.39 | | 4749 | 4274 | 5224 | 3799 | 5699 | 4440 | 4433 |

Table 54 The weight of the net excavated material extracted per ring (Report, 2024)

In Figure 5.75, we can observe a significant minimum at ring 980. In general, an increase in the average extracted weight indicates optimal conditioning, while a minimum value may indicate either overly compact or excessively loose ground. Although it exceeded the alarm threshold value, it did not cause any issues during extraction from the screw conveyor, as the conditioning was sufficient to keep the machine operating at optimal levels.

In the diagram in Figure 5.76, the average pressures on sensors TY11 and TY07 are shown (for their positions, refer to Figure 5.1). The average values are calculated during the advancement

phase of the shield or considering both the shield advancement and the installation of the precast ring.The TY11 sensor is located at the top compared to TY07, which justifies the fact that the pressures from the former are higher than those from the latter, given the trapezoidal distribution of thrusts in the excavation chambre.

In Figure 5.77, the average apparent density is shown, calculated using the pressures reported in Figure 5.76, taking into account that the elevation difference between the two sensors is 8 m. Knowing the average apparent density in the excavation chamber allows us to adjust the TBM for more efficient auger extraction, reducing the risk of clogging. Density affects the pressure needed to support the excavation face: if it is too high, it could indicate compact soils, which may require more force or a special support system; a low density might suggest less stable soils. In particular, for soils with low density, water infiltration could become a problem, so monitoring the density helps predict and mitigate this risk.

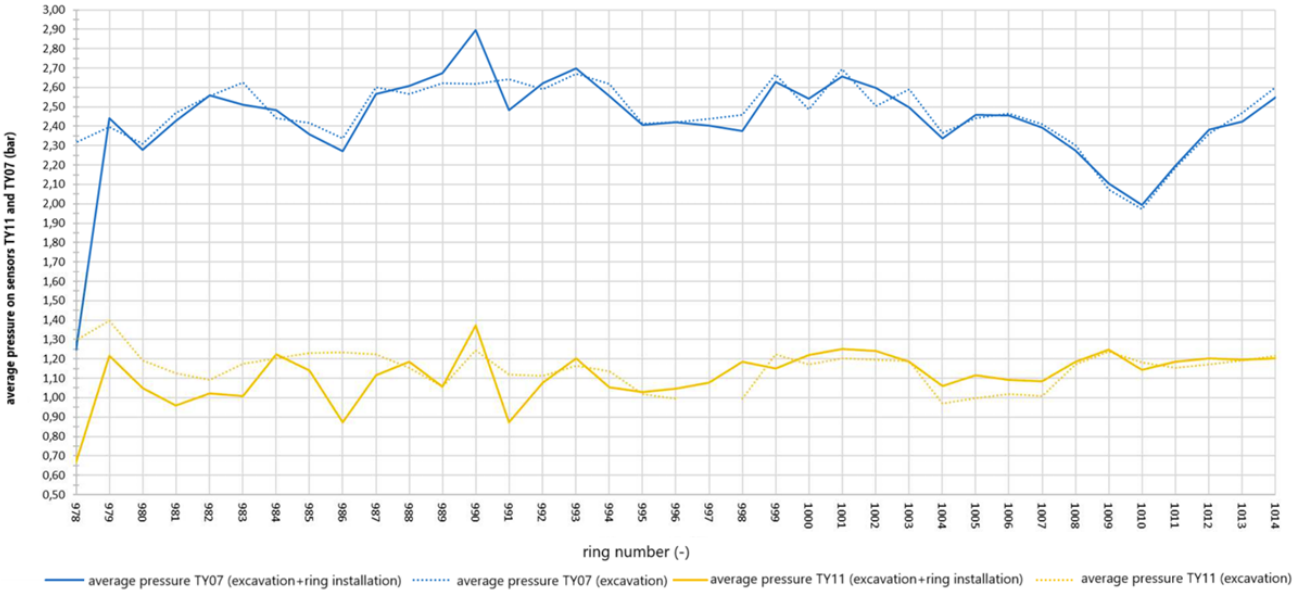


Figure 5.76 Face pressure: comparison between TY06 and TY11 sensors (Report, 2024)

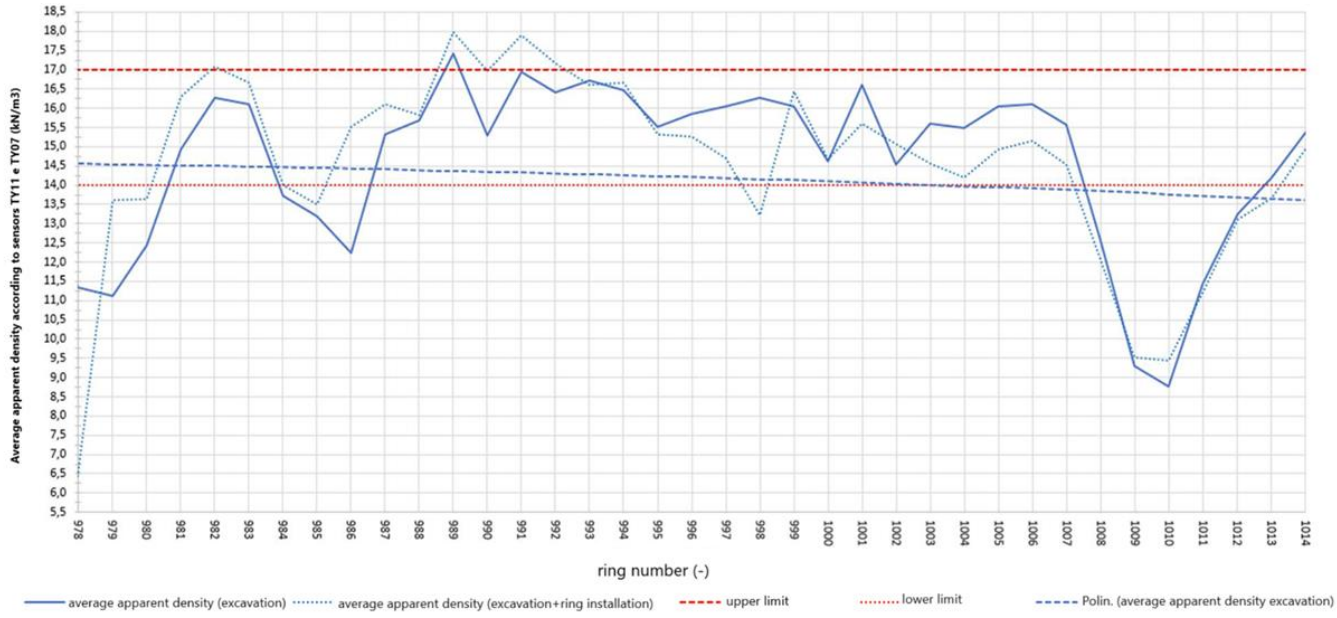


Figure 5.77 Average apparent density in the excavation chamber, TY06 and TY11 sensors (Report, 2024)

| Omog. Segments Geom. | segment number | day | n° of ring installed | Lenght L (m) | starting pk (m) | final pk (m) | L total (m) | pressure sensors TY11-TY07 | | | | |
|---|---|---|---|---|---|---|---|---|---|---|---|---|
| | | | | | | | | $\gamma_{app,\ exc.}$ (kN/m$^3$) | lower limit | upper limit | average $\gamma_{app}$ over 24h | |
| | | | | | | | | | | | $\gamma_{app,\ excavation}$ (kN/m$^3$) | $\gamma_{app,\ excavation+ring\ installation}$ (kN/m$^3$) |
| FYRmar+FYRar | 12 | 21/072024 | 6 | 10.87 | 4473.82 | 4484.69 | 66.6 | 15 | 14 | 17 | 13.70 | 13.96 |
| | | 22/07/2024 | 11 | 14.42 | 4484.69 | 4499.11 | | 15 | 14 | 17 | 15.40 | 16.21 |
| FYR2c | 11 | | | 5.37 | 4499.11 | 4504.48 | | 15 | 14 | 17 | | |
| | | 23/07/2024 | 8 | 14.36 | 4504.48 | 4518.84 | | 15 | 14 | 17 | 15.69 | 15.03 |
| | | 24/07/2024 | 12 | 21.55 | 4518.84 | 4540.39 | | 15 | 14 | 17 | 13.64 | 13.11 |

Table 55 Average apparent density in the excavation chamber, TY06 and TY11 sensors (Report, 2024)

## 5.9 From July 24th to August 2nd (rings installed 1010-1052)

The reported excavation progress falls within the section covered by P.A.T. No. 5 (Table 7). Excavation was stopped on the morning of August 2nd, with the excavation face at pk 4+619, in order to perform maintenance on the cutterhead and replace the worn cutting tools. The intervention in the excavation chamber will be carried out under normal atmospheric pressure conditions.

In the graph in Figure 5.78, the pressure $\mathbf{p_{f,c}}$ is shown as a function of the ring number, while Table 57 presents the average value of $\mathbf{p_{f,c}}$ for each section, based on the progress.

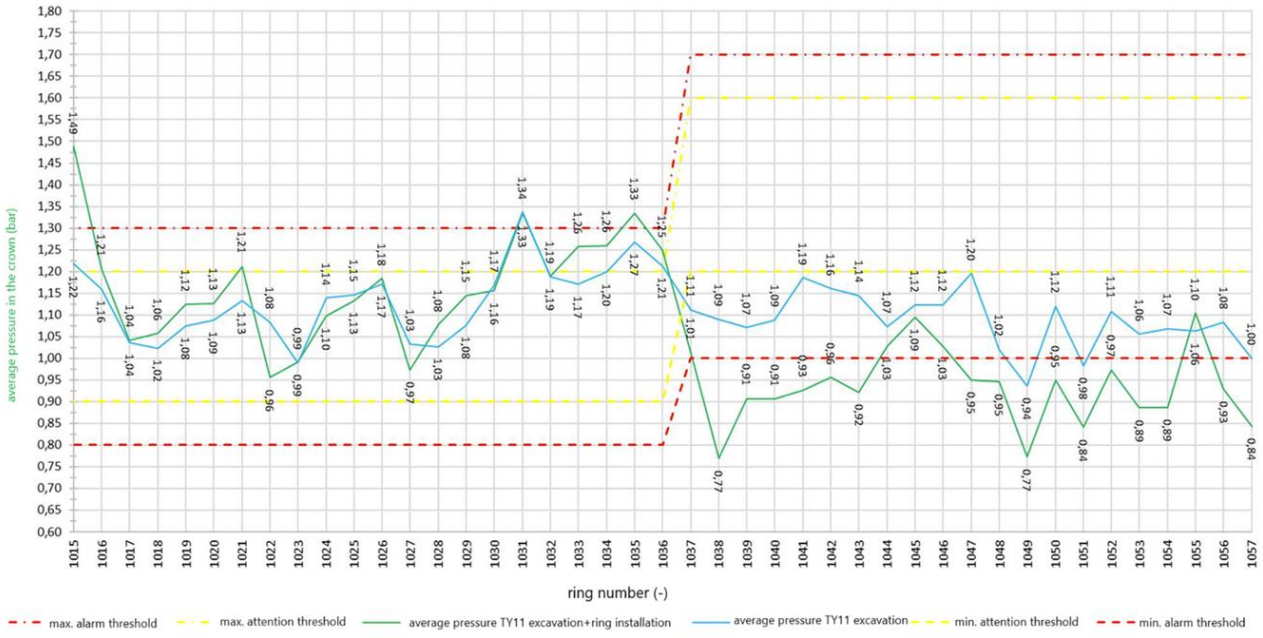


Figure 5.78 Average pressure in the crown during excavation and at the completion of the ring installation (TY11 sensor) (Report, 2024)

| Omog. Segments Geom. | segment number | day | n° of ring installed | Lenght L (m) | starting pk (m) | final pk (m) | L total (m) | $p_f$ (bar) | $p_{f,c}$ (bar) | ATTENTION (bar) | | ALARM (bar) | | average $p_{f,c}$ value (bar) | |
|---|---|---|---|---|---|---|---|---|---|---|---|---|---|---|---|
| | | | | | | | | | | MIN | MAX | MIN | MAX | excavation | excavation + ring installation |
| FYR2c | 13 | 29/07/2024 | 12 | 21.72 | 4540.39 | 4562.11 | 77.4 | 1.7 | 1.0 | 0.9 | 1.2 | 0.8 | 1.3 | 1.11 | 1.13 |
| | | 30/07/2024 | 13 | 17.99 | 4562.11 | 4580.10 | | 1.7 | 1.0 | 0.9 | 1.2 | 0.8 | 1.3 | 1.5 | 1.13 |
| | | | | 5.35 | 4580.10 | 4585.45 | | 2.0 | 1.3 | 1.2 | 1.6 | 1.0 | 1.7 | | |
| | | 31/07/2024 | 9 | 16.15 | 4585.45 | 4601.60 | | 2.0 | 1.3 | 1.2 | 1.6 | 1.0 | 1.7 | 1.12 | 0.97 |
| | | 01/08/2024 | 9 | 16.14 | 4601.60 | 4617.75 | | 2.0 | 1.3 | 1.2 | 1.6 | 1.0 | 1.7 | 1.05 | 0.91 |

Table 56 Average pressure in the crown during excavation and at the completion of the ring installation (TY11 sensor) (Report, 2024)

The $\mathbf{p_{f,c}}$ in the excavation chamber remained predominantly between the minimum and maximum attention thresholds, respectively 0.9 and 1.2 bar between pk 4+540.39 and pk 4+580.10, and between the minimum attention and alarm thresholds, respectively 1.0 and 1.2 bar between pk 4+580.10 and pk 4+617.75.
The decompressions in the excavation chamber during the installation phase of the ring between pk 4+583.70 and pk 4+617.75 had no effect on the stability of the face and/or the tunnel. To confirm this, it is noted that the maximum excavation thrust in the aforementioned section remained predominantly below the expected lower maximum thrust of 40 MN, which was calculated assuming no contact between the shield and the ground. Additionally, it should be noted that the installation of the ring occurs over a short period (the average installation time is approximately 37 minutes).

### 5.9.1 Injection volume and pressure

The location of the injection lines is referenced in Figure 5.4, while for the calculation of the volumes of two-component grout to be injected from each individual line, equations (5.1) and (5.2) from section 5.1.1 were used.

The same proportions were applied to calculate the minimum volume of 10.74 m³ in the case of shield tail ground contact.

For the alert and alarm thresholds of the volume corresponding to line #i, to be filled with two-component grout, the procedure followed was the same as for the total mix volume per ring, using the formulas (5.3a)-(5.3.d) already presented in section 5.1.1.

The graph in Figure 5.79 shows the injection volume of the two-component grout, while Table 58 provides the average volume value **V** per section.

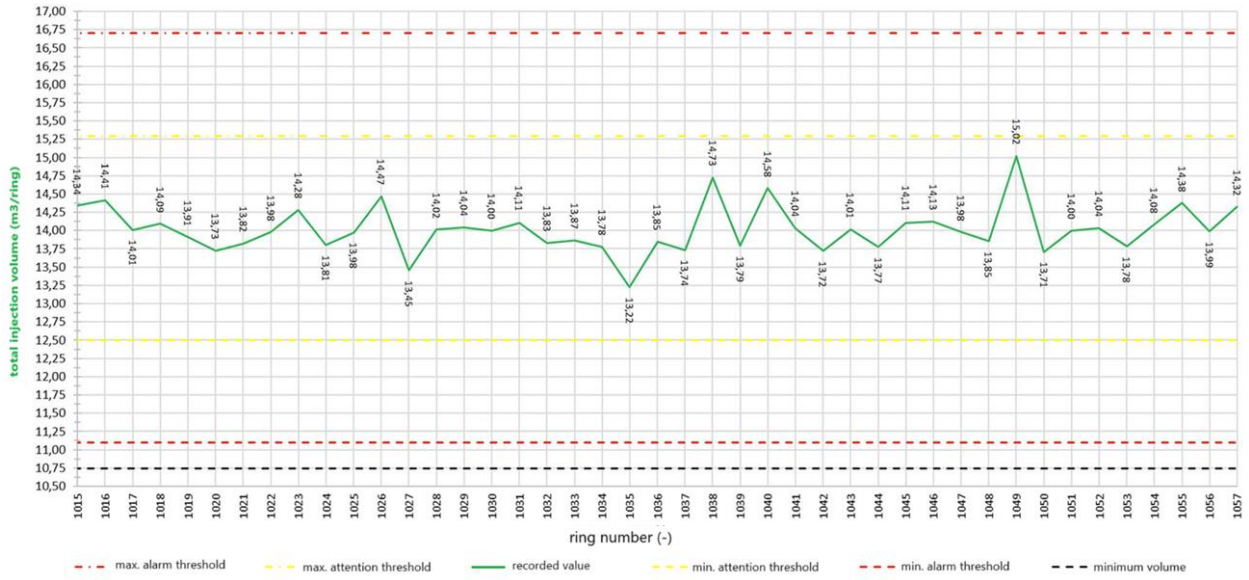


Figure 5.79 Total injection volume of the two-component mixture in m³/ring (Report, 2024)

| Omog. Segments Geom. | segment number | day | n° of ring installed | Lenght L (m) | starting pk (m) | final pk (m) | L total (m) | V (m³/ring) | ATTENTION (m³/ring) | | ALARM (m³/ring) | | minimum V (m³/ring) | average V (m³/ring) |
|---|---|---|---|---|---|---|---|---|---|---|---|---|---|---|
| | | | | | | | | | MIN | MAX | MIN | MAX | | |
| FYR2c | 13 | 29/07/2024 | 12 | 21.72 | 4540.39 | 4562.11 | 77.4 | 13.91 | 12.52 | 15.30 | 11.13 | 16.69 | 10.74 | 14.07 |
| | | 30/07/2024 | 13 | 17.99 | 4562.11 | 4580.10 | | 13.91 | 12.52 | 15.30 | 11.13 | 16.69 | 10.74 | 13.88 |
| | | | | 5.35 | 4580.10 | 4585.45 | | 13.91 | 12.52 | 15.30 | 11.13 | 16.69 | 10.74 | |
| | | 31/07/2024 | 9 | 16.15 | 4585.45 | 4601.60 | | 13.91 | 12.52 | 15.30 | 11.13 | 16.69 | 10.74 | 14.02 |
| | | 01/08/2024 | 9 | 16.14 | 4601.60 | 4617.75 | | 13.91 | 12.52 | 15.30 | 11.13 | 16.69 | 10.74 | 14.15 |

Table 57 Average injection volume of the two-component mixture in m³/ring per section (Report, 2024)

The pressure of the individual injection lines for component A was calculated using formula (5.4) (section 5.1.1).

The alert and alarm thresholds were defined as for the face pressure and the pressure in the crown (equations (5.5a)-(5.5d), section 5.1.1).

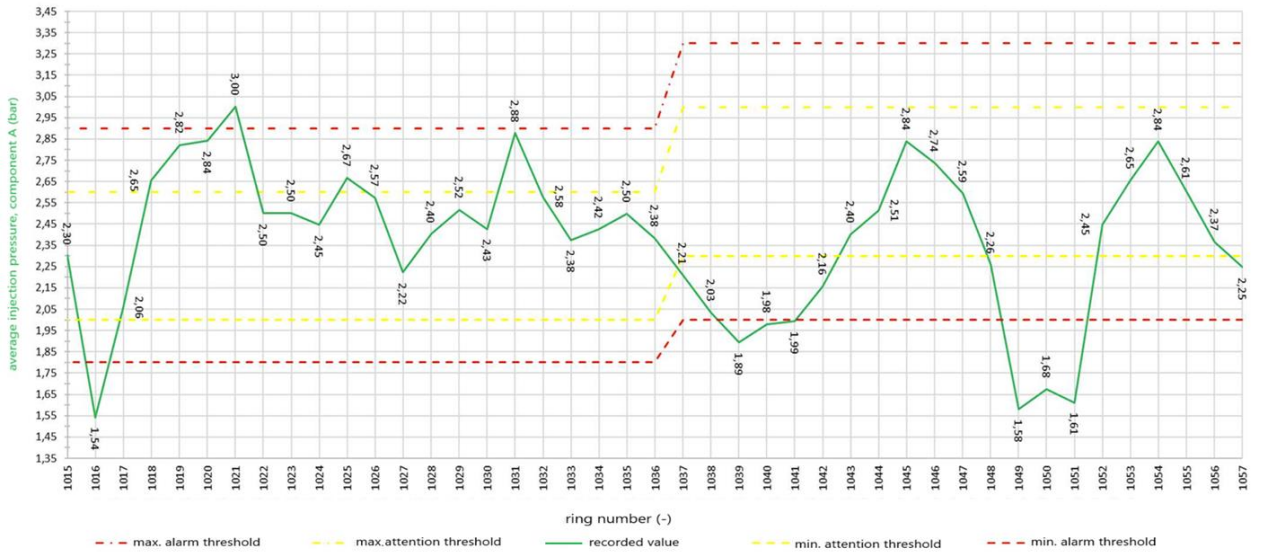


Figure 5.80 Average injection pressure of component A per section (Report, 2024)

| Omog. Segments Geom. | segment number | day | n° of ring installed | Lenght L (m) | starting pk (m) | final pk (m) | L total (m) | $p_m$ (bar) | ATTENTION (bar) | | ALARM (bar) | | average $p_m$ (bar) |
|---|---|---|---|---|---|---|---|---|---|---|---|---|---|
| | | | | | | | | | MIN | MAX | MIN | MAX | |
| FYR2c | 13 | 29/07/2024 | 12 | 21.72 | 4540.39 | 4562.11 | 77.4 | 2.2 | 2.0 | 2.6 | 1.8 | 2.9 | 2.49 |
| | | 30/07/2024 | 13 | 17.99 | 4562.11 | 4580.10 | | 2.2 | 2.0 | 2.6 | 1.8 | 2.9 | 2.37 |
| | | | | 5.35 | 4580.10 | 4585.45 | | 2.5 | 2.3 | 3.0 | 2.0 | 3.3 | |
| | | 31/07/2024 | 9 | 16.15 | 4585.45 | 4601.60 | | 2.5 | 2.3 | 3.0 | 2.0 | 3.3 | 2.39 |
| | | 01/08/2024 | 9 | 16.14 | 4601.60 | 4617.75 | | 2.5 | 2.3 | 3.0 | 2.0 | 3.3 | 2.23 |

Table 58 Average injection pressure of component A per section (Report, 2024)

The pressure $\mathbf{p_m}$ maintained for many clogs was between the minimum and maximum attention thresholds, respectively 2.0 and 2.6 bar between pk 4+540.39 and pk 4+580.10, and 2.3 and 3.0 bar between pk 4+580.10 and pk 4+617.75.

The reduction is justified by the fact that, as explained in reference to Figure 5.80, a more stable excavation face is assumed (therefore, since the backfilling injection pressure is always higher than the face pressure, this confirms the assumption). An example is demonstrated by rings 1049 and 1051.

### 5.9.2 Thrust and torque

For the position of the 6 thrust groups (A, B, C, D, E, F), refer to Figure 5.7 in paragraph 5.1.2.

The thrusts in the individual thrust groups A, B, C, D, E, and F generated by the expected lower and upper maximum thrusts, respectively 37 and 56 MN between pk 4+540.39 and pk 4+580.10, and 40 and 60 MN between pk 4+580.10 and pk 4+617.75., they were determined taking into account that the center of gravity of the pistons is located on the axis of the tunnel. The eccentricity between the thrust axis and the center of gravity of the pistons $\mathbf{e_{app}}$ was calculated by assuming a trapezoidal pressure distribution on the excavation face.
Each thrust is considered on type 2 segments, i.e., segments reinforced with a denser reinforcement starting from 300 m from the tunnel entrance. The maximum excavation thrusts in groups A, B, C, D, E, and F satisfy the SLE, so the maximum thrust during excavation was always lower than the "maximum thrust for type 2 segments" (red line, section, and point).
The thrust exerted by the generic piston i is obtained as seen in section 5.1.2 (equations (5.6)-(5.8)). $\mathbf{S_i}$ and $\mathbf{z_i}$ represent the total thrust exerted by the pistons on the lining ring and the distance from the horizontal axis to the center of gravity of the generic piston **i**, respectively, while **S** is the total thrust exerted by the pistons.

The average and maximum thrusts of only the thrust groups F and C are reported below (Figures 5.81 and Figures 5.82):

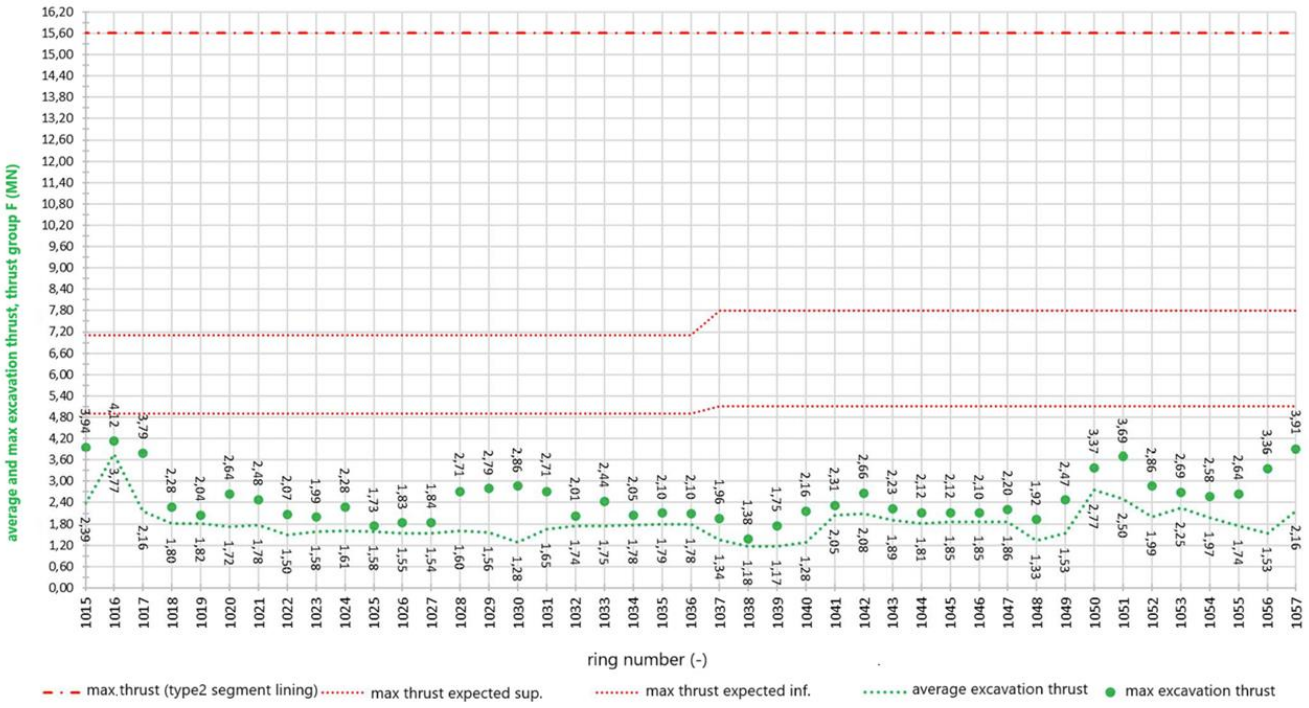


Figure 5.81 Average thrust and maximum thrust during the excavation phase exerted by the thrust group F (Report, 2024)

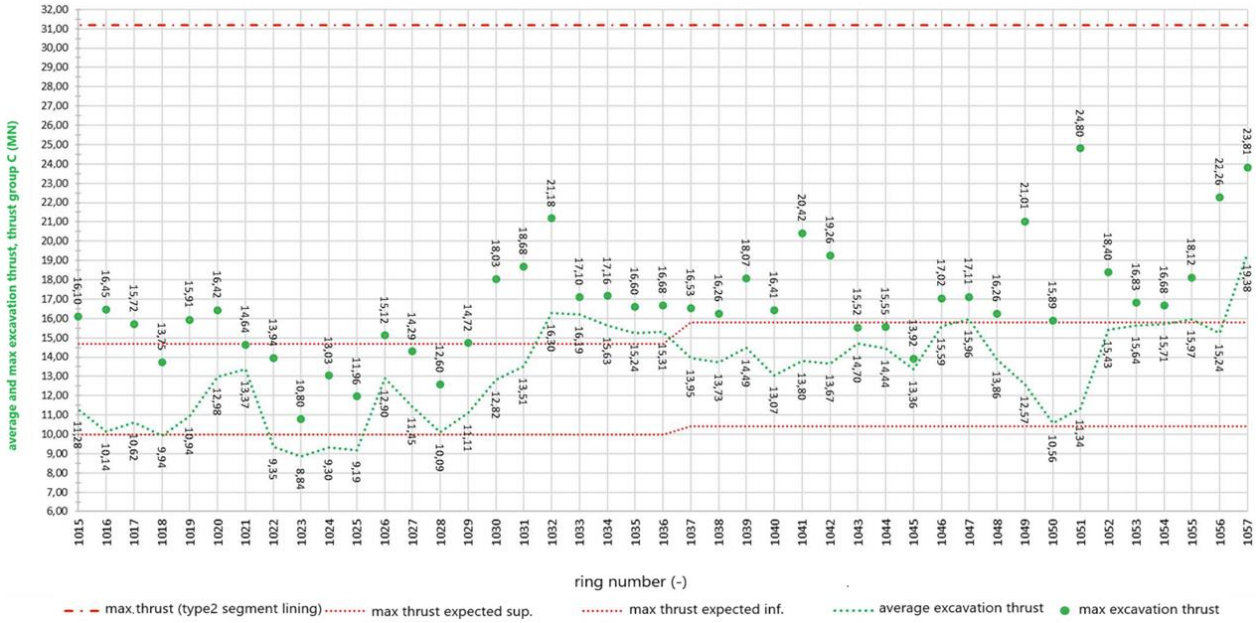


Figure 5.82 Average thrust and maximum thrust during the excavation phase exerted by the thrust group C (Report, 2024)

As expected from the trapezoidal pressure distribution on the excavation face, the thrust pistons of group C show higher values compared to those of group F, as the former are positioned lower than the latter.

In general, values below the minimum threshold indicate a softer face than expected, which therefore requires less thrust to be applied. It could also be related to a more stable face, which requires less thrust. This decision did not result in any negative consequences for the ongoing excavation.

Regarding the torque, Figure 5.10 (paragraph 5.1.2) also shows the maximum torque values. It is important to note that the torque on the cutterhead, due to friction, is strictly related to the thrust force and penetration.

In the graph in Figure 5.83, the average torque is shown as a function of the ring number, while Table 60 presents the average values for each section according to the progressive.

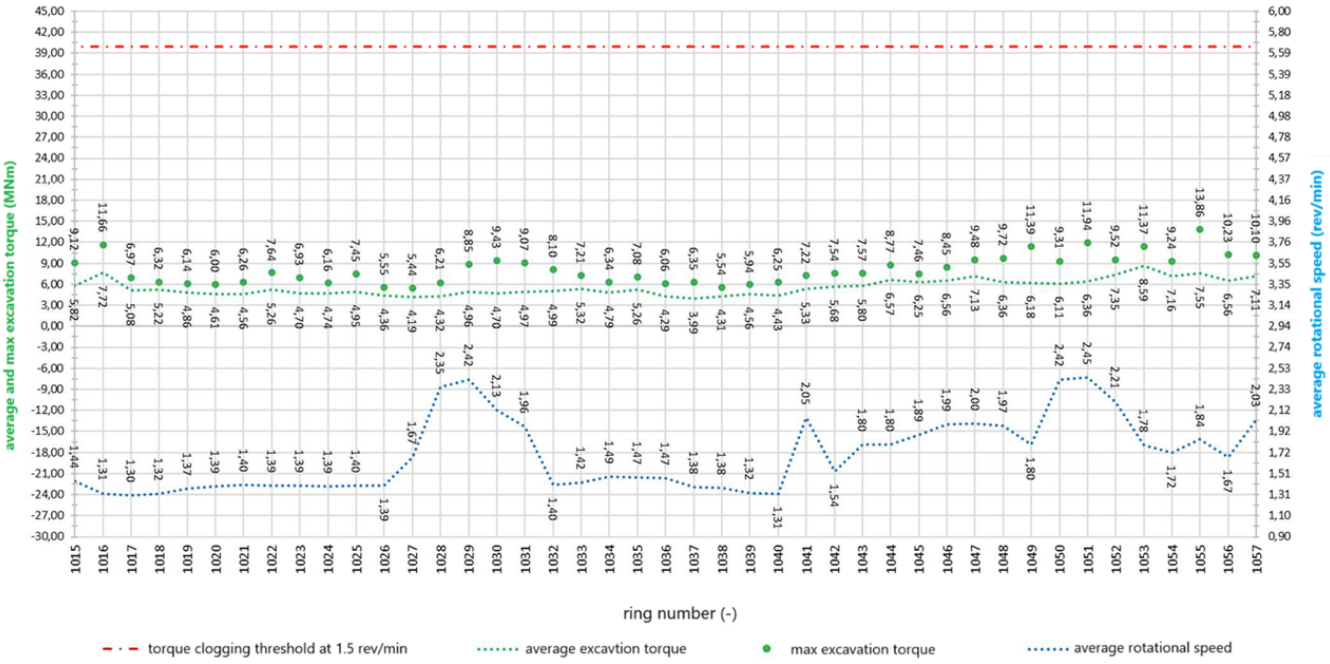


Figure 5.83 Average torque and maximum torque during excavation and average rotational speed (Report, 2024)

In the graph above, a roughly constant trend of torque can be observed, as well as for the average rotation speed. The latter varies more between rings 657 and 660: this can be justified by the fact that a section of harder ground increases friction between the excavation face and the cutterhead, thus requiring a decrease in the average rotation speed (and vice versa, as for ring 624). Another explanation is that the rotation speed of the cutterhead was increased due to the reduction in penetration per revolution **p**, which is caused by the competence of the excavation face. By increasing **ω**, it was possible to maintain the advance speed **v** between rings 1026 and 1032. The relationship between the kinematic variables **v**, **p**, and **ω** is given by equation (5.9) in paragraph 5.1.2.

| Omog. Segments Geom. | segment number | day | n° of ring installed | Lenght L (m) | starting pk (m) | final pk (m) | L total (m) | AVERAGE TORQUE (MNm) | MAX. TORQUE (MNm) | TORQUE FOR A CLOGGING THRESHOLD OF 1.5 rev/min (MNm) | average rotation speed ω (rev/min) |
|---|---|---|---|---|---|---|---|---|---|---|---|
| FYR2c | 13 | 29/07/2024 | 12 | 21.72 | 4540.39 | 4562.11 | 77.4 | 5.16 | 7.18 | 40 | 1.38 |
| | | 30/07/2024 | 13 | 17.99 | 4562.11 | 4580.10 | | 4.66 | 7.05 | 40 | 1.68 |
| | | | | 5.35 | 4580.10 | 4585.45 | | | | | |
| | | 31/07/2024 | 9 | 16.15 | 4585.45 | 4601.60 | | 6.01 | 8.05 | 40 | 1.82 |
| | | 01/08/2024 | 9 | 16.14 | 4601.60 | 4617.75 | | 7.00 | 10.77 | 40 | 1.99 |

Table 59 Average torque and maximum torque during excavation and average rotational speed (Report, 2024)

As can be seen from the graph, each value falls within the limits.

### 5.9.3 Excavated material

The cover on the crown of the final tunnel lining in the section covered by the report ranges from 25.0 to 37.5 meters, as shown in the Geomechanical profile. The unit weight of FYR2c between pk 4+540.39 and pk 4+617.75 is 21.5 kN/m³.

The diagram of the average weight of the excavated soil for each installed ring, excluding the conditioning (see Chapter 6 for more details on soil conditioning), is compared with its gross average weight in Figure 5.84. In Table 61, following the graph, the net average values per section are provided.

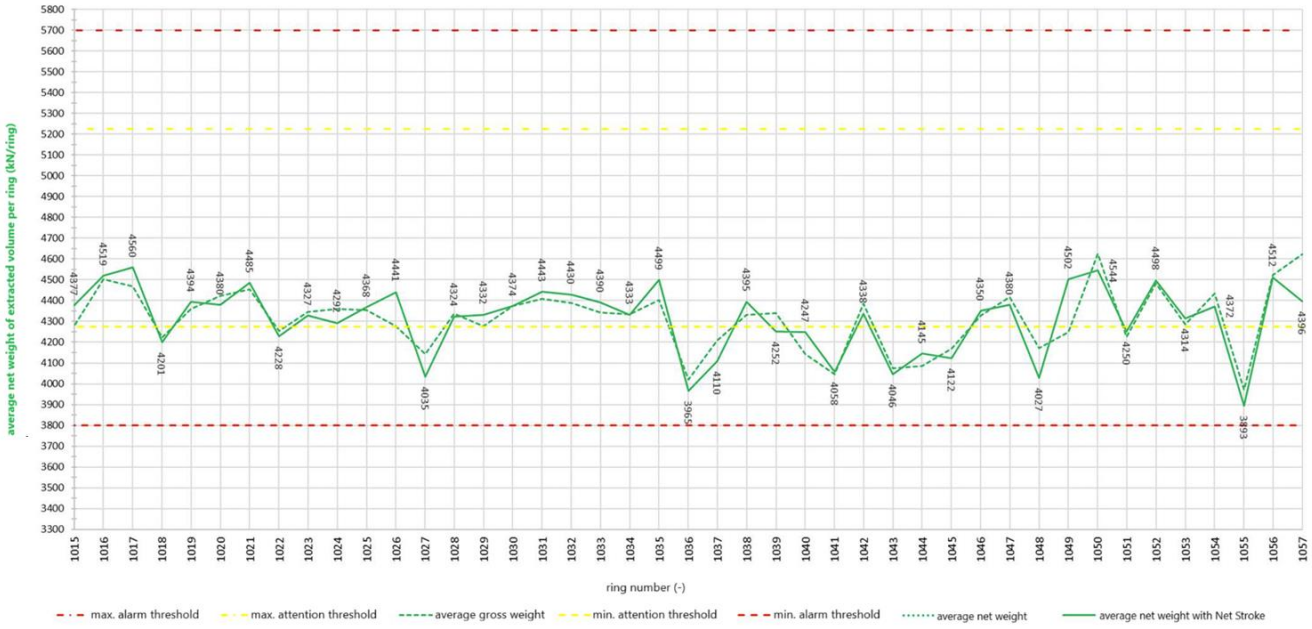


Figure 5.84 Comparison between the net weight and the gross weight of the material extracted per ring (Report, 2024)

| Omog. Segments Geom. | segment number | day | n° of ring installed | Lenght L (m) | starting pk (m) | final pk (m) | L total (m) | REFERENCE WEIGHT $P_t$ (kN) | ATTENTION MIN. (kN) | ATTENTION MAX. (kN) | ALARM MIN. (kN) | ALARM MAX. (kN) | AVERAGE GROSS WEIGHT (kN) | AVERAGE GROSS WEIGHT with NET STROKE (kN) |
|---|---|---|---|---|---|---|---|---|---|---|---|---|---|---|
| FYR2c | 13 | 29/07/2024 | 12 | 21.72 | 4540.39 | 4562.11 | 77.4 | 4749 | 4274 | 5224 | 3799 | 5699 | 4358 | 4381 |
| | | 30/07/2024 | 13 | 17.99 | 4562.11 | 4580.10 | | 4749 | 4274 | 5224 | 3799 | 5699 | 4301 | 4299 |
| | | | | 5.35 | 4580.10 | 4585.45 | | | | | | | | |
| | | 31/07/2024 | 9 | 16.15 | 4585.45 | 4601.60 | | 4749 | 4274 | 5224 | 3799 | 5699 | 4202 | 4190 |
| | | 01/08/2024 | 9 | 16.14 | 4601.60 | 4617.75 | | 4749 | 4274 | 5224 | 3799 | 5699 | 4380 | 4365 |

Table 60 The weight of the net excavated material extracted per ring (Report, 2024)

In Figure 5.84, we can observe a fluctuating trend of the average extracted weight, but still within the alarm threshold limits. In general, an increase in the average extracted weight indicates optimal conditioning, while a minimum value may indicate either overly compact or excessively loose ground.

In the diagram in Figure 5.85, the average pressures on sensors TY11 and TY07 are shown (for their positions, refer to Figure 5.1). The average values are calculated during the advancement phase of the shield or considering both the shield advancement and the installation of the precast ring.The TY11 sensor is located at the top compared to TY07, which justifies the fact that the pressures from the former are higher than those from the latter, given the trapezoidal distribution of thrusts in the excavation chambre.
At ring 1038, we observe a significant minimum, consistent with what was seen in the previous figure, and we can therefore hypothesize a rather stable face.

In Figure 5.86, the average apparent density is shown, calculated using the pressures reported in Figure 5.85, taking into account that the elevation difference between the two sensors is 8 m. Knowing the average apparent density in the excavation chamber allows us to adjust the TBM for more efficient auger extraction, reducing the risk of clogging. Density affects the pressure needed to support the excavation face: if it is too high, it could indicate compact soils, which may require more force or a special support system; a low density might suggest less stable soils. In particular, for soils with low density, water infiltration could become a problem, so monitoring the density helps predict and mitigate this risk.

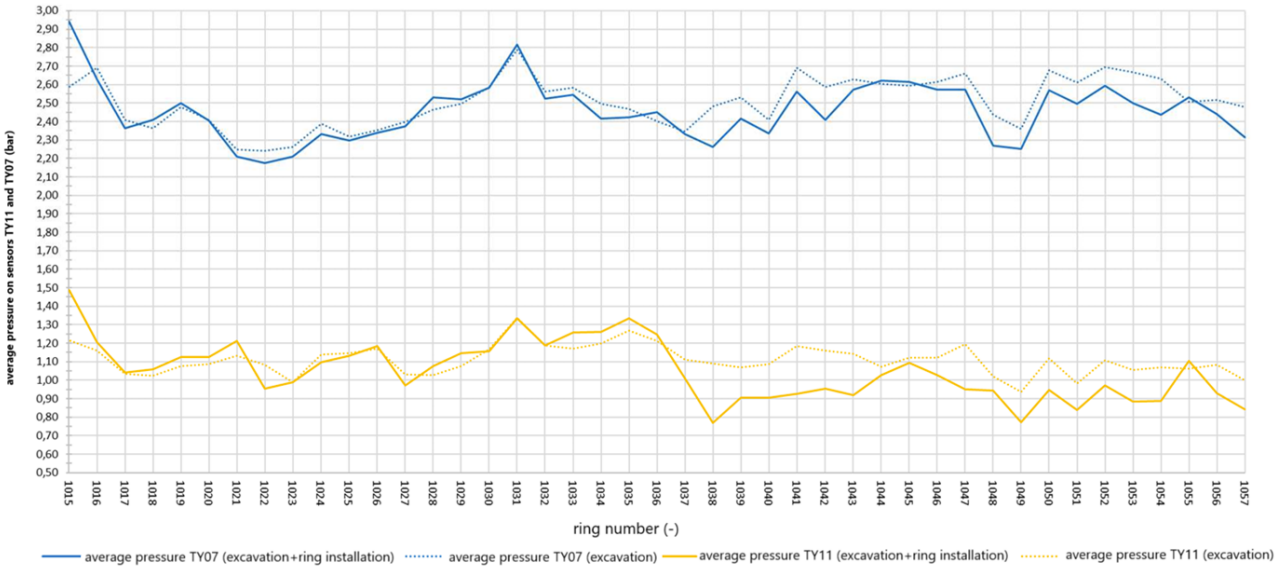


Figure 5.85 Face pressure: comparison between TY06 and TY11 sensors (Report, 2024)

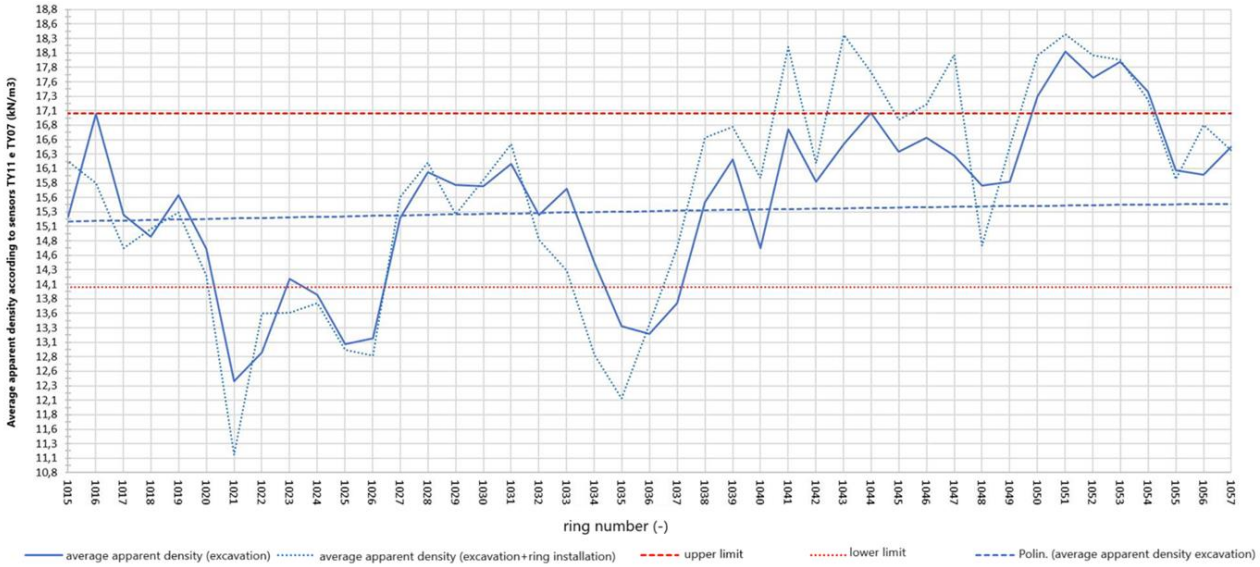


Figure 5.86 Average apparent density in the excavation chamber, TY06 and TY11 sensors (Report, 2024)

| Omog. Segments Geom. | segment number | day | n° of ring installed | Lenght L (m) | starting pk (m) | final pk (m) | L total (m) | pressure sensors TY11-TY07 | | | | |
|---|---|---|---|---|---|---|---|---|---|---|---|---|
| | | | | | | | | $\gamma_{app,\ exc.}$ (kN/m$^3$) | lower limit | upper limit | average $\gamma_{app}$ over 24h | |
| | | | | | | | | | | | $\gamma_{app,\ excavation}$ (kN/m$^3$) | $\gamma_{app,\ excavation+ring\ installation}$ (kN/m$^3$) |
| FYR2c | 13 | 29/07/2024 | 12 | 21.72 | 4540.39 | 4562.11 | 77.4 | 15 | 14 | 17 | 14.33 | 14.07 |
| | | 30/07/2024 | 13 | 17.99 | 4562.11 | 4580.10 | | 15 | 14 | 17 | 15.09 | 14.98 |
| | | | | 5.35 | 4580.10 | 4585.45 | | 15 | 14 | 17 | | |
| | | 31/07/2024 | 9 | 16.15 | 4585.45 | 4601.60 | | 15 | 14 | 17 | 16.19 | 17.00 |
| | | 01/08/2024 | 9 | 16.14 | 4601.60 | 4617.75 | | 15 | 14 | 17 | 16.94 | 17.23 |

Table 61 Average apparent density in the excavation chamber, TY06 and TY11 sensors (Report, 2024)

# 6. Data comparison

This chapter provides an overview of the entire progress, for a time range that spans from March 19, 2024, to August 2, 2024, i.e., from pk 3+716.09 to pk 4+616.04 (covering a tunnel length from 1001.93m to 1902.20m). To this end, excavation reports, machine data, and excavation analysis are presented through graphs generated by the TPC (Tunnelsoft) software, which was previously discussed in paragraph 4.2.5. These pieces of information make up the excavation data archive, which is also useful for a back analysis by the designers and the contracting company.

## 6.1 Excavation report and machine data

In Figure 6.1 shows the daily progress graph to define the actual productivity of the TBM and the team. The advancement phase encountered greater difficulties during the period from the end of May to early June, while the best performances were observed in the first half of July, linked to a ground quality that was more favorable for excavation (confirmed by the fact that in the preceding days, maintenance interventions were possible on the brushes and disc cutters under normal atmospheric conditions, see paragraphs 5.6 and 5.7).

Where there are no values, it is because the progress was halted due to routine maintenance on the machine or in the mucking tanks.As observed in the graph, the average performance is around 6.65 meters of daily progress.

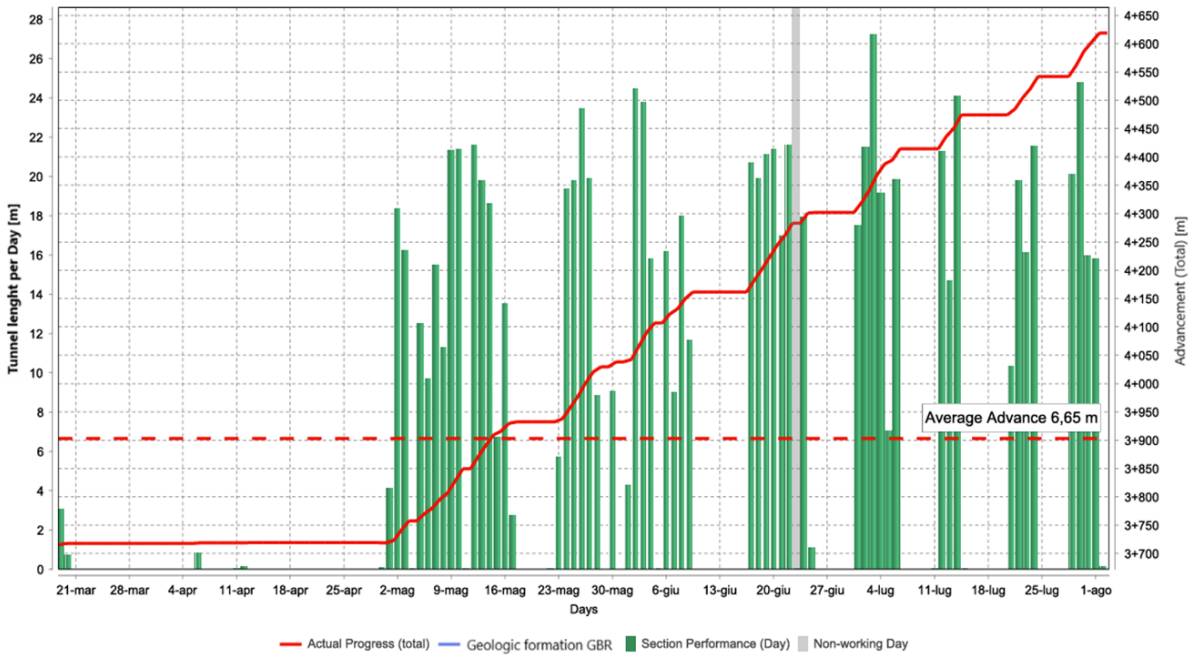


Figure 6.1 advancement (Tunnelsoft)

Figure 6.2 shows the penetration **p** [mm/rev] and the Cutterhead advance rate [mm/min] (also known as the penetration speed v in paragraph 5.1.2). Figure 6.3, on the other hand, shows the rotation speed **ω** [rev/min], which is related to **p** and **v** according to the equation presented in paragraph 5.1.2.

$$\boldsymbol{v}\left[\frac{mm}{min}\right] = \boldsymbol{p}\left[\frac{mm}{rev}\right] \cdot \boldsymbol{\omega}\left[\frac{rev}{min}\right] \qquad (5.9)$$

To maintain a constant value of **v**, the values of **p** and **ω** had to be balanced. Therefore, an increase in **p** corresponds to a decrease in **ω**, and vice versa. The variable is mainly influenced by the encountered ground; thus, when facing harder ground, a decrease in p is balanced by an increase in ω, as observed in the section from 1700m to 1800m of the tunnel length.
The average values for v are 30.2 mm/min, while for **p**, they are 21.5 mm/rev.

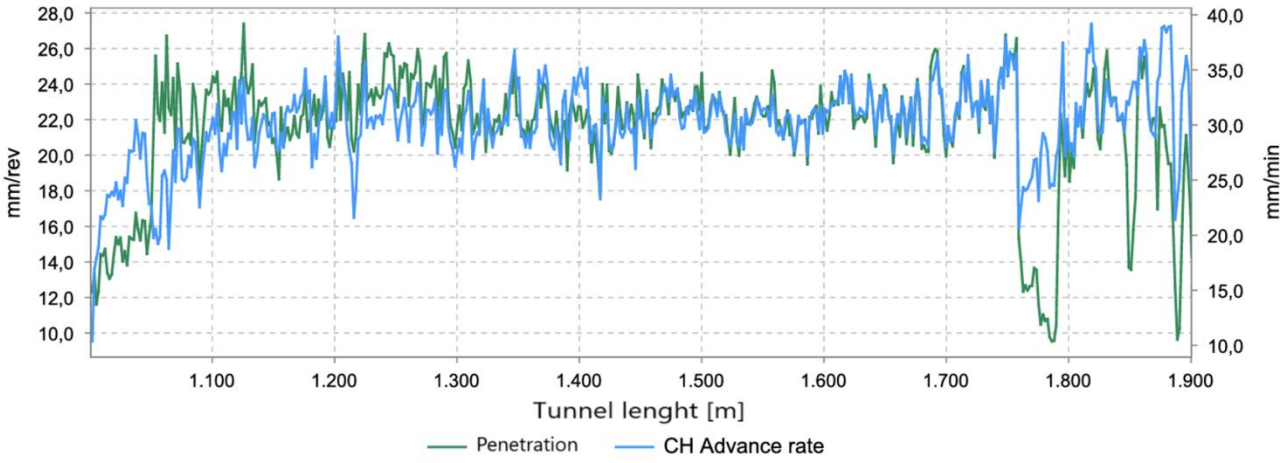


Figure 6.2 Advancement and Penetration Speed (Tunnelsoft)

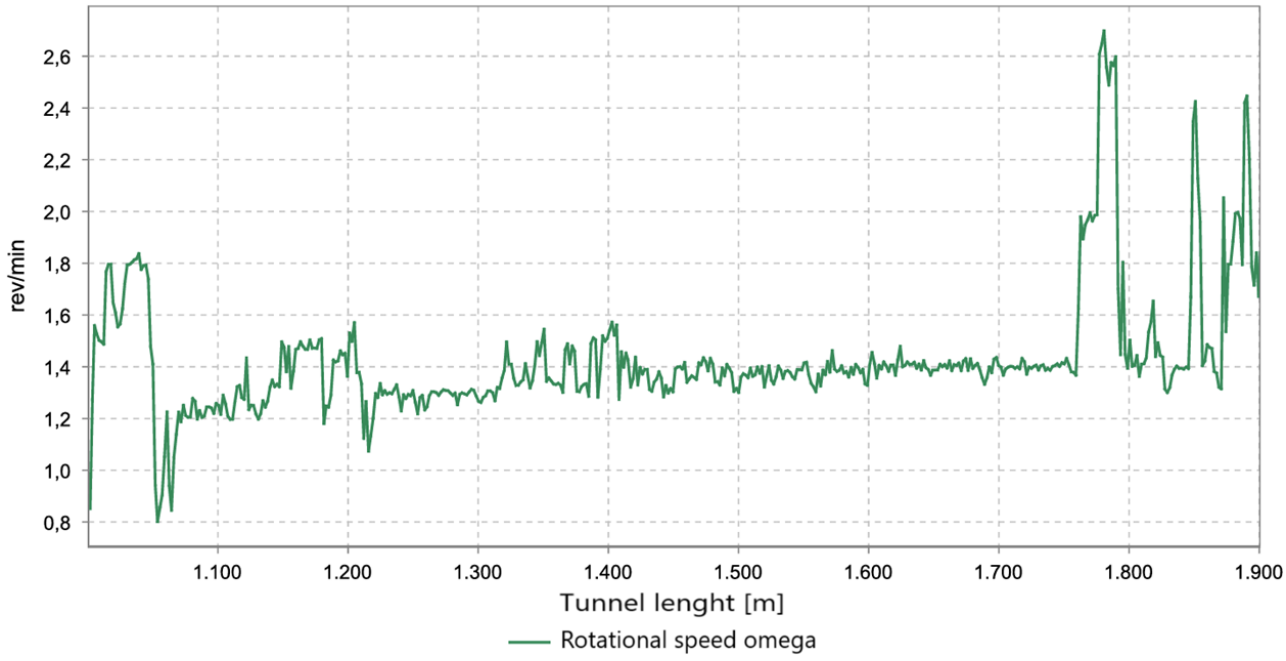


Figure 6.3 Rotational speed (Tunnelsoft)

Figure 6.4 shows the torque per meter of advancement. This graph is, for mechanical reasons, closely related to the graph in Figure 6.3, as a higher rotation speed requires a higher torque, and vice versa. The average value is 6597.4 kNm. Figure 6.4 shows the torque per meter of advancement. This graph is, for mechanical reasons, closely related to the graph in Figure 6.3, as a higher rotation speed requires a higher torque, and vice versa. The average value is 6597.4 kNm.

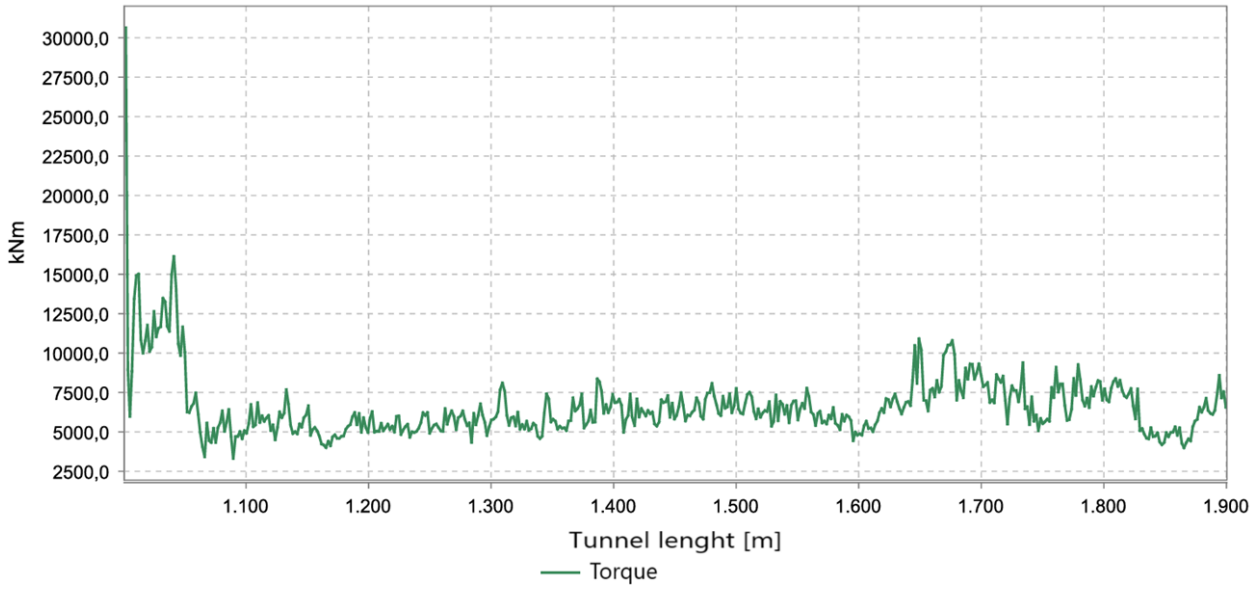


Figure 6.4 Torque (Tunnelsoft)

In the graphs in Figure 6.5 and Figure 6.6, we have respectively the thrust force and the ground pressure at the crown measured by the TY11 sensor (the latter with an average of 1.7 bar). The values fluctuate in both graphs: in particular, both for the thrust and the crown pressure, maximum values are reached between 1200m and 1600m. This highlights the unstable nature of the encountered ground, which consequently requires an increase in thrust from the pistons.

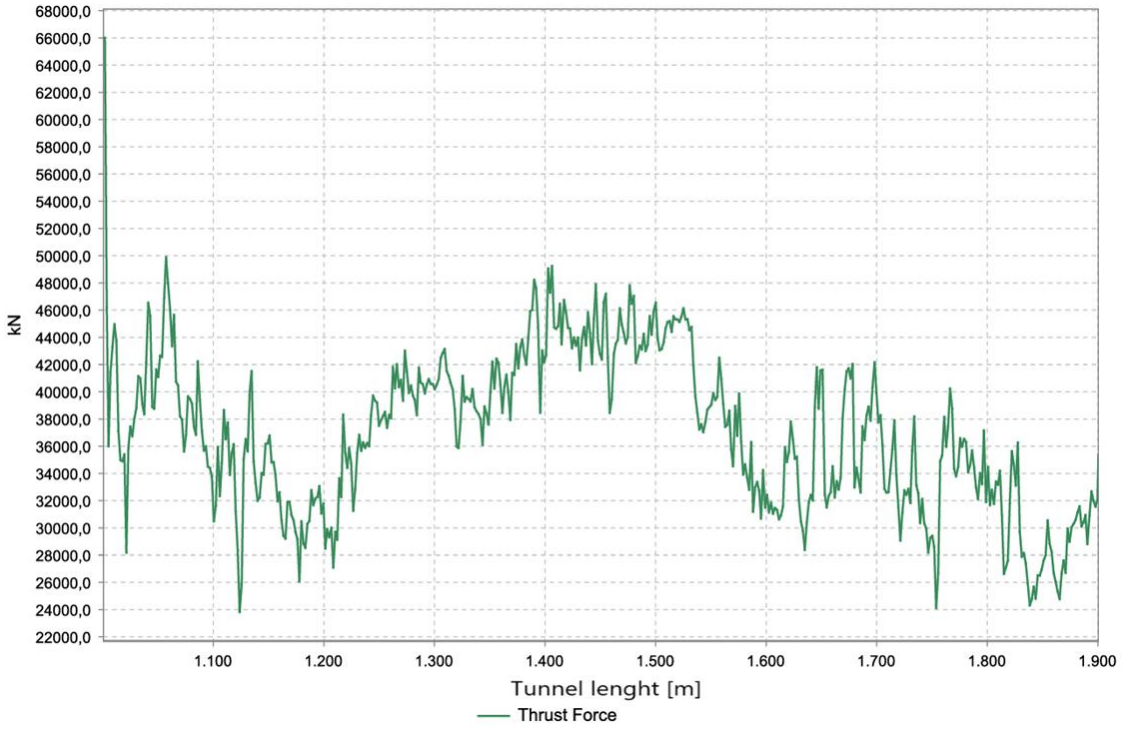


Figure 6.5 Thrust Force (Tunnelsoft)

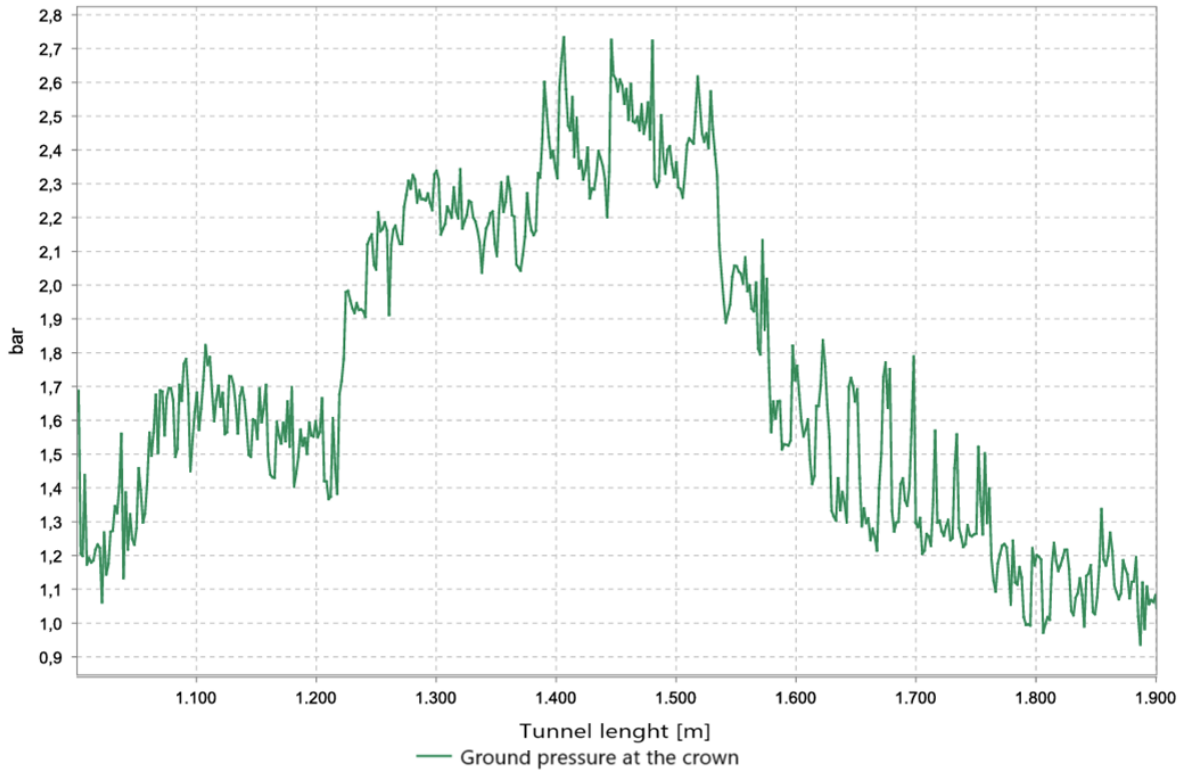


Figure 6.6 Ground pressure on the crown, sensor TY11 (Tunnelsoft)

What was shown in Figure 6.4 and Figure 6.5 is repeated in Figure 6.7 but with respect to the number of rings installed. An average torque value of 1.4 rev/min is observed, with peaks mainly between the installation of segments 970 and 1000. As seen in paragraph 5.8.2, this is due to the fact that the rotation speed of the cutterhead was increased due to the reduction in penetration per revolution **p**: by increasing **ω**, it was possible to maintain the advance speed **v** around 26.7 mm/min.

For the thrust force, an average excavation value of 42,900.5 kN is observed.

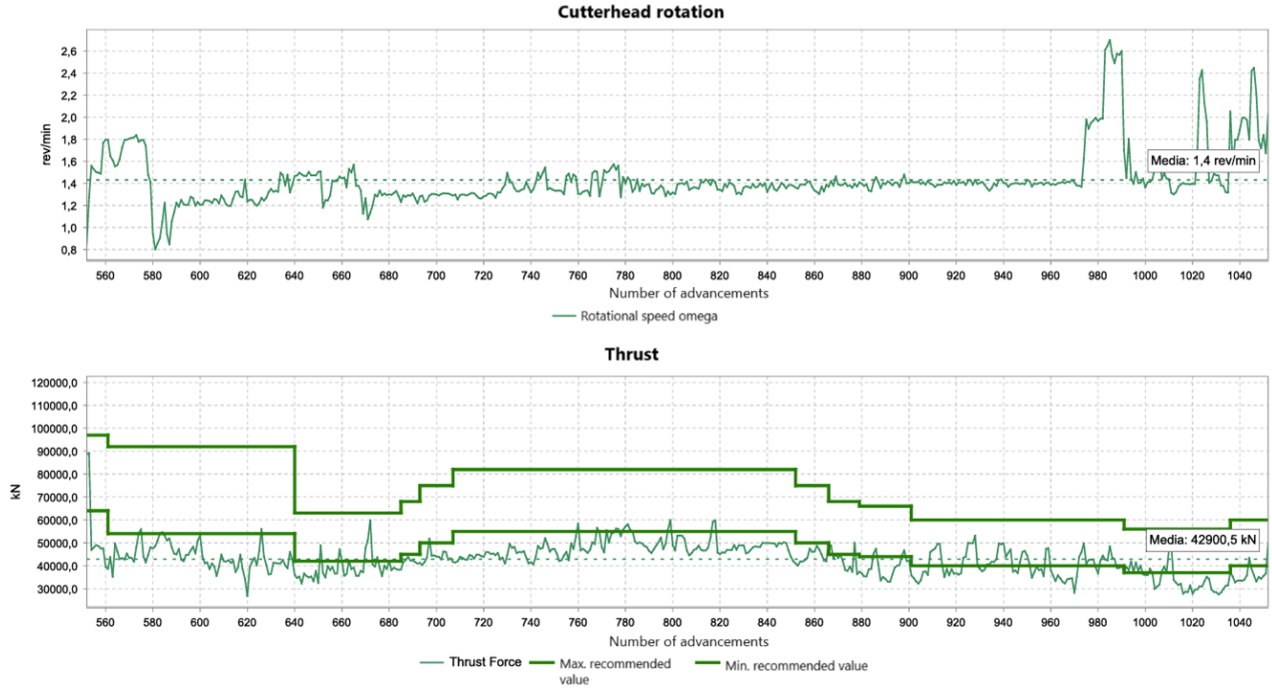


Figure 6.7 Torque and thrust force per segment (Tunnelsoft)

Figure 6.8 presents the screw conveyor data for installed rings. The pressure in the screw conveyor is essential to ensure that the excavated material is effectively moved from the cutting head to the transport section. If the pressure is too low, the material may not be extracted correctly, slowing down the advance process. If the pressure is too high, there could be a risk of damaging the system or blocking the conveyor. Monitoring the screw conveyor pressure also helps keep the machine in optimal conditions during drilling.In general, the screw conveyor extraction speed also determines the pressure applied in the excavation chamber: higher extraction speeds reduce the pressure in the excavation chamber, while a slowdown in extraction tends to maintain or increase the pressure in the chamber. This concept applies as long as a constant advance speed is maintained.

It can therefore be concluded that on less stable excavation fronts, the screw conveyor extraction speed is reduced in an attempt to keep the pressures high both below and above the conveyor, minimizing pressure losses between different points.

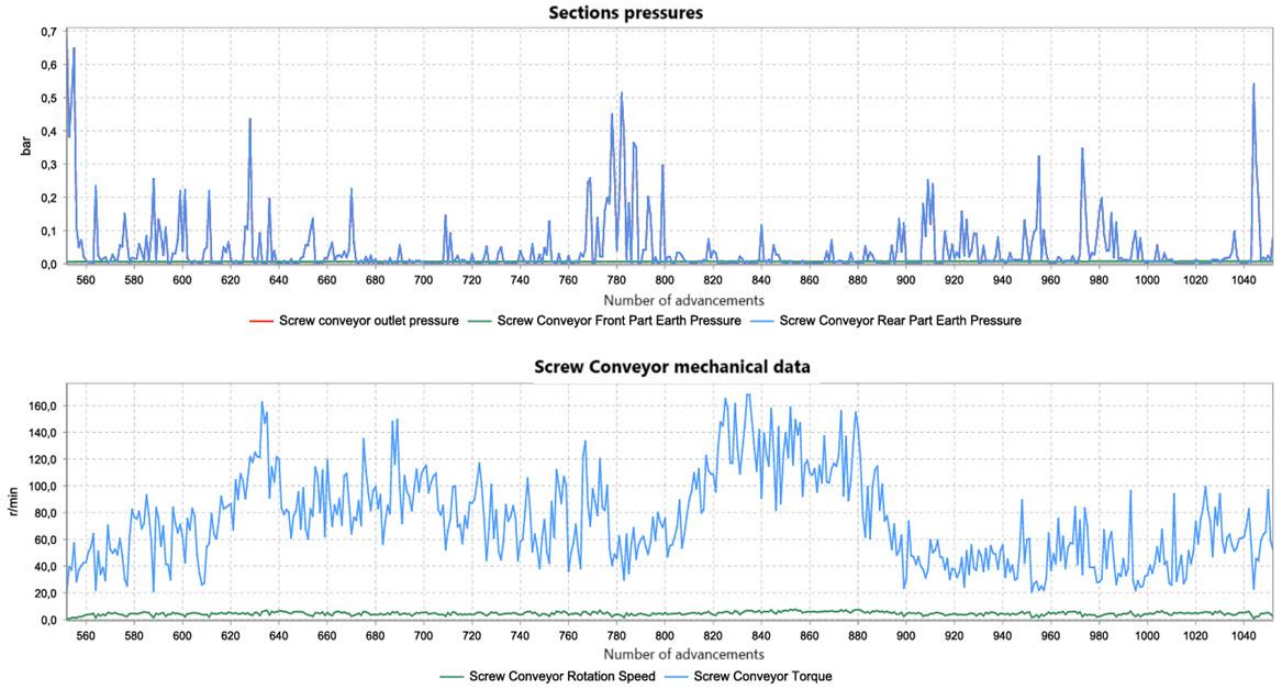


Figure 6.8 Screw conveyor preassures, rotation speed and torque (Tunnelsoft)

In Figures 6.9 and 6.10, respectively, the volume of the two-component mixture and its injection pressure are shown. From the graph in Figure 6.8, it is evident that there is a close relationship between the injection pressure and the earth pressure in the crown, as seen in Figure 6.6. Therefore, the evaluations made earlier regarding the excavation face also apply here.
Regarding the quantity of injected volume, the values in Figure 6.9 remain almost always within the alarm threshold limits, except near the 1500m mark of the excavated tunnel, where a peak is evident during the period described in paragraph 5.6 (June 21st to July 4th, rings installed 845-923). It is worth noting that only during the installation of rings 915 and 918 was the crown pressure higher than the maximum alarm threshold of 1.7 bar, suggesting a less stable excavation face than expected. Despite this, no problems were encountered during the advancement.

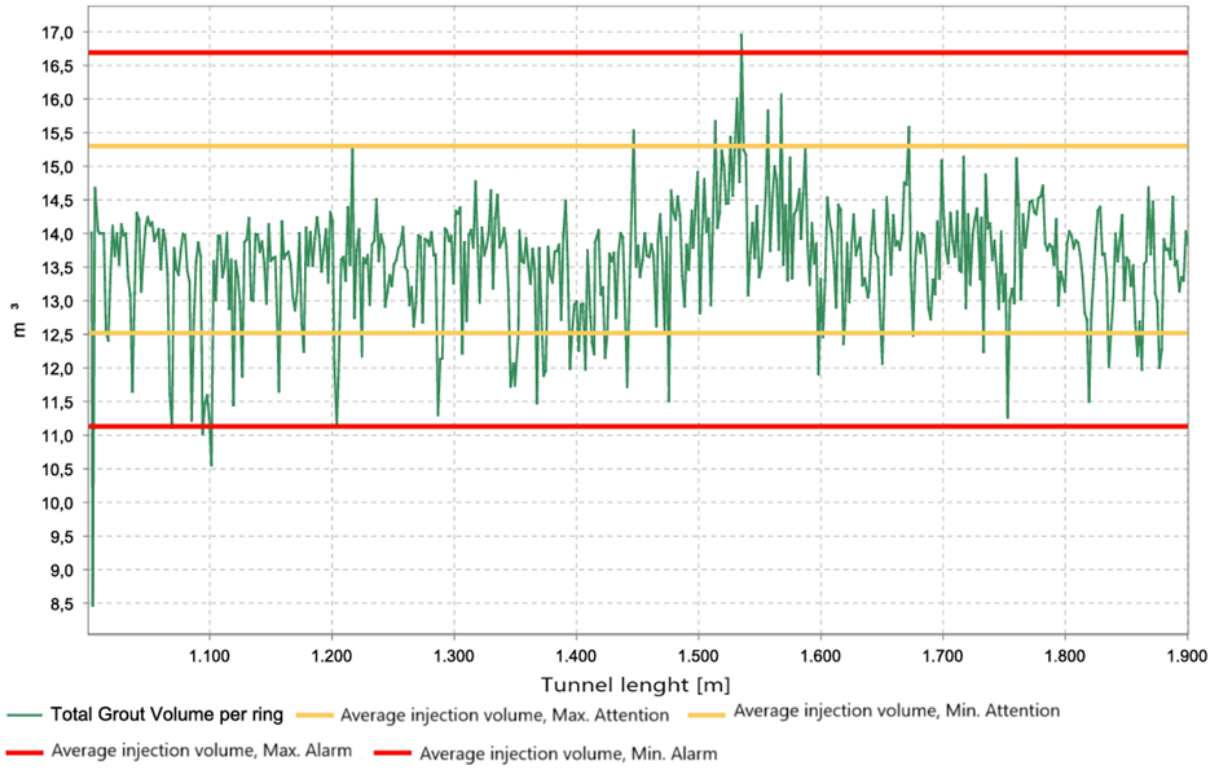


Figure 6.9 Grout volume (Tunnelsoft)

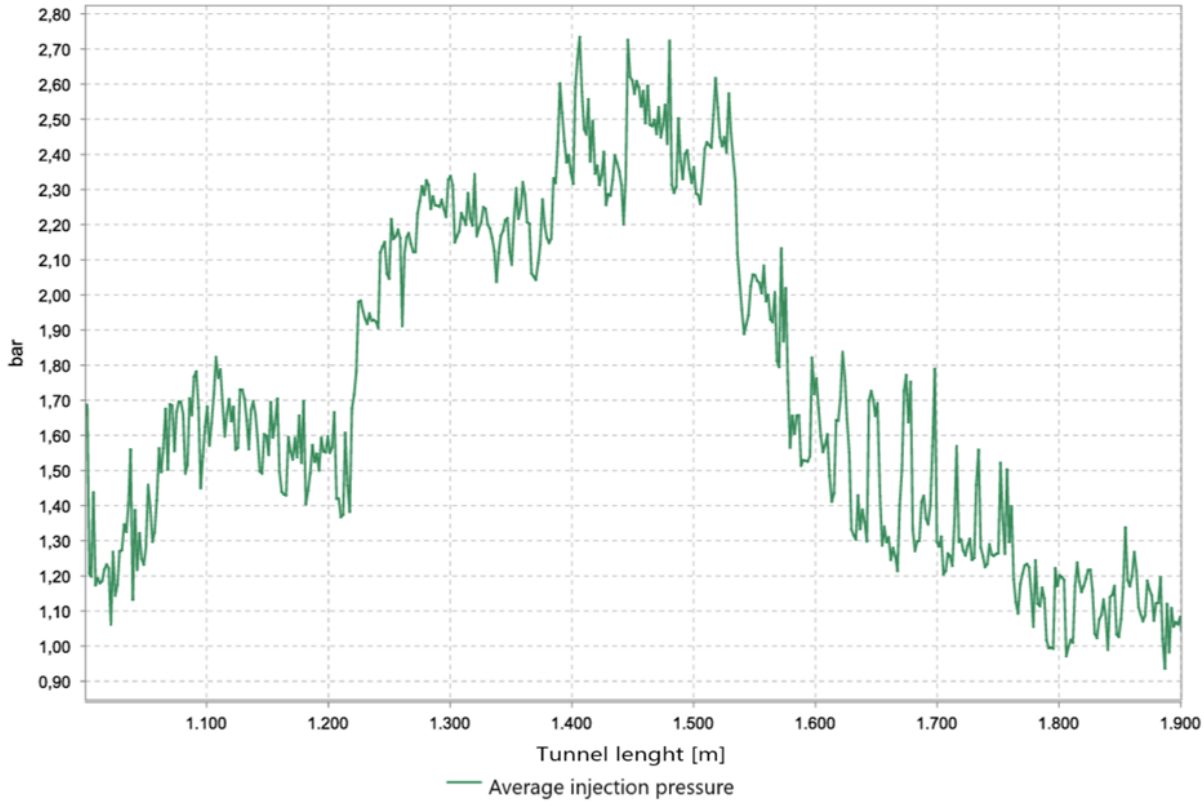


Figure 6.10 Injection pressure (Tunnelsoft)

For further details, the volumes and pressures of component A (composed of water, cement, bentonite, and retarding/fluidifying agent) and component B (accelerator), which together make up the backfilling, are presented separately. In Figure 6.11, quite constant values of injected volumes per ring can be observed, with approximately 1000 liters/ring for component B and 13,000 liters/ring for component A.

Figure 6.12 instead shows the pressures of component A and B for each of the ten injection lines (for the position of the injection lines, refer to Figure 5.4 in paragraph 5.1.1).

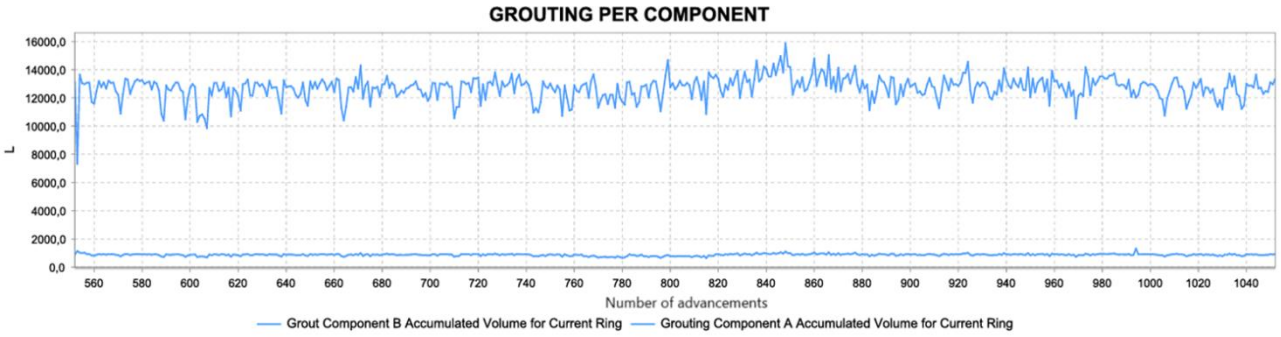


Figure 6.11 Grouting volume for component A and B (Tunnelsoft)

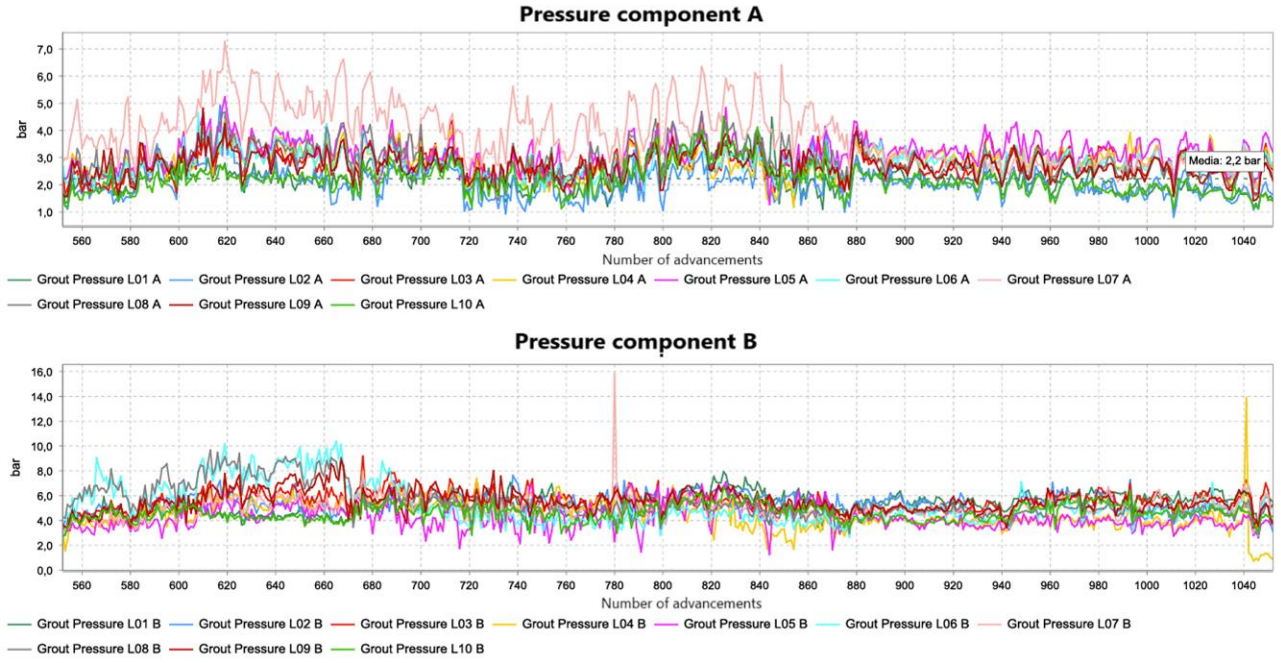


Figure 6.12 Pressure of component A and B for injection line (Tunnelsoft)

Figure 6.13

## 6.2 Excavation analysis

This chapter concludes with a more detailed analysis of the ground conditioning that was carried out throughout the excavation.

Soil conditioning is a fundamental component of the excavation process in EPB-TBMs, entailing the modification of soil properties to optimize tunneling operations. The incorporation of soil conditioning agents provides a range of advantages, including the reduction of wear on mechanical components in contact with the soil, enhancement of pressure distribution uniformity within the excavation chamber, reduction of frictional forces, and lowering of soil permeability, among others. Consequently, a comprehensive assessment of the conditioned soil is imperative to ensure the efficient operation of the EPB-TBM. The selection of the type and quantity of conditioning agents is determined by the specific characteristics of the soil and the requirements of the project. Additives can be injected at multiple points within the machine, such as ahead of the cutting head, within the excavation chamber, and along the screw conveyor. The variability of soil characteristics across different geological formations presents a challenge, complicating the selection of appropriate conditioning agents.

Commonly employed additives for soil conditioning include water, foam, long-chain polymers, anti-clogging agents (specifically for cohesive soils), lubricating agents, dispersing agents, abrasion inhibitors, bentonite slurry, and fillers.
Water is among the most widely used agents for soil conditioning in EPB-TBMs and is essential for maintaining the required pressure within the excavation chamber. It serves to control the consistency and flow characteristics of the excavated soil.
Foam is a primary conditioning additive in EPB-TBM tunneling, typically composed of a significant volume of air encapsulated within surfactant bubbles. To produce foam, water and a foaming agent are combined in specific ratios to create a foaming solution. This solution is then introduced, along with a stream of compressed air, into a foam generator.

Average composition for a normally used foam:

- Foaming agent 0.5-3%
- Water 5-10%
- Air 90-95%
- Polymer (eventual) <0.1%

Foaming agent can have inside a small amount of polymer to stabilize the foam bubbles.

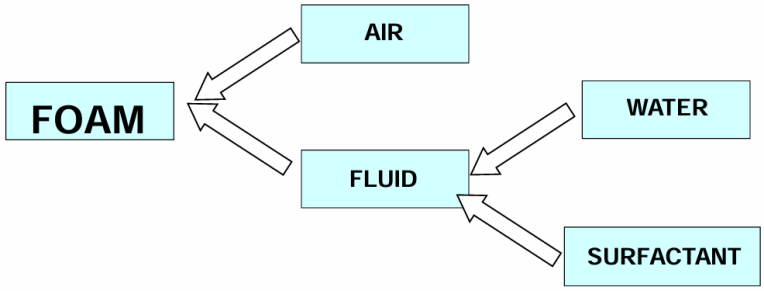


Figure 6.14 Foam composition (Peila, 2022-2023)

A **surfactant** is a chemical substance that reduces the surface tension between two liquids or between a liquid and a solid. Surfactants are molecular compounds with a hydrophilic (water-attracting) part and a hydrophobic (water-repelling). This structure allows surfactants to stabilize mixtures of different liquids, to generate the foam.

In tunnels, among the main design parameters are those related to foam and soil conditioning in general. These are respectively the FER (Foam Expansion Ratio), the FIR (Foam Injection Ratio) and the TR (Treatment Ratio) defined according to the following equations:

$$FER = \frac{V_{foam}}{V_{generation\ liquid}} \quad [-] \quad (6.1)$$

$$FIR = \frac{V_{foam}}{V_{excavated\ soil}} * 100 \quad [\%] \quad (6.2)$$

$$TR = \frac{V_{surfactant}}{V_{excavated\ soil}} \quad [-] \quad (6.3)$$

- The FER provides information regarding the ratio between the foam volume and the volume of the liquid generator from which it was produced. Specifically, its values range from 8 (wet foam) to 20 (dry foam).
- The FIR, on the other hand, is a percentage ratio of the foam volume used to the volume of the soil to be conditioned.
- The TR The ratio between the volume of surfactant used to condition the soil volume and the soil volume itself. It is a conditioning parameter that primarily concerns the environmental aspect; in fact, in practice, it must remain below a threshold value, defined for each type of soil based on ecotoxicological tests.

Although the values of the P.A.T. define the thresholds within which to operate, the decision regarding the variation of the quantities of each parameter is made during operations by the TBM operator/pilot. The latter, using the machine's main parameters (cutterhead and screw conveyor torque, pressures in the excavation chamber and in the shield, penetration, advance rate, weight difference on the scales), selects the optimal modulation of the quantities of water, foam, and bentonite (where necessary).

In Figure 6.15, the components of the FER and FIR described in Figure 6.16 are listed. The foam liquid volume, the surfactant, and the free bentonite water show a generally constant value, with isolated and sporadic peaks. In particular, peaks in the foam liquid volume indicate that the operator needed to reduce the FER. Evidence supporting this hypothesis can be found in the fact that the cubic meters of surfactant injected tend to remain constant even when there are peaks in the foam liquid volume. There could be several reasons for this: one possibility is that the operator encountered a section of soil with water presence, making it unnecessary to further waste water from the tanks.
Another explanation might be that a more wear-intensive section than expected was encountered, which required an increase in the free water at the face to lower the temperature at the cutterhead while still maintaining a constant advance rate and penetration. This hypothesis seems to be

confirmed by the fact that, in the third diagram of Figure 6.15, starting from ring 550, there is a sharp increase in the quantity of free water injected.
Lastly, it is also possible that one of the foam lines simply became blocked.
Whatever the reason, the FER graph in Figure 6.16 shows that this decision allowed the operator to maintain a constant FER in the excavation chamber (red line), likely to ensure a more even distribution of pressures in the chamber and to reduce or maintain constant torque values on the screw. Evidence for this can be seen in the FIR of the same graph, which remains virtually unchanged in the chamber.

The weight of the natural soil shows a decrease starting from the installation of ring 950, coinciding with the decrease in volumes in the excavation chamber. Observing that both the FER and the FIR remain constant, it can be deduced that the foam volume has increased, in accordance with formula (6.2). All of this could mean that the excavation was done through more compact clays, while at the same time encountering a more stable face, which required a reduced volume in the excavation chamber to counteract the pressures coming from it. To support this, let's compare the graphs in Figures 6.2 and 6.3, where, in correspondence with this section, we observe a decrease in the penetration rate and the need for an increase in the cutterhead rotation speed, respectively.

It is reasonable to think that the foam optimized the excavation performance in terms of penetration.

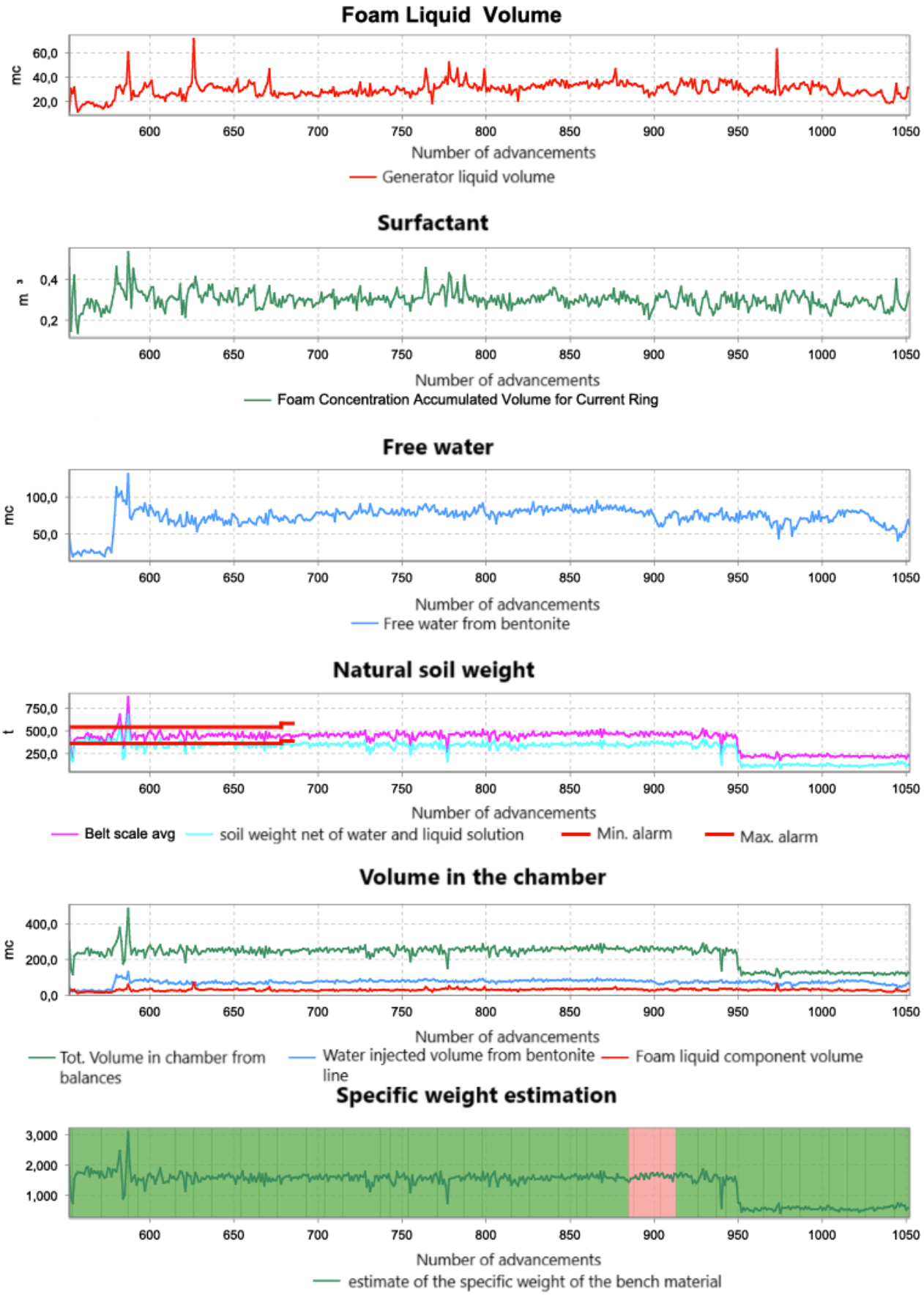


Figure 6.15 Foam liquid volume, surfactant, water, natural soil weight, volume in the chambre, specific weight estimate (Tunnelsoft)

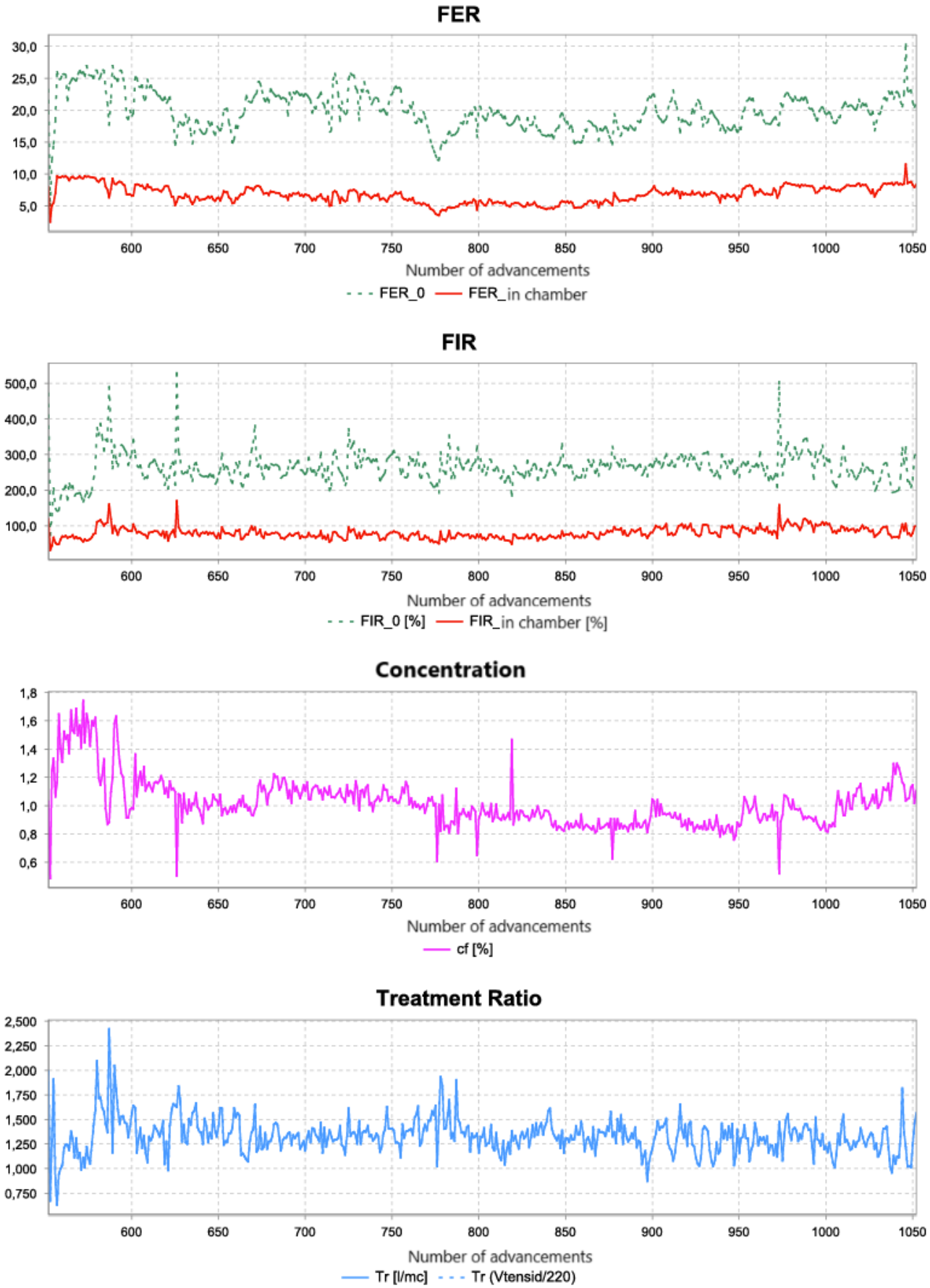


Figure 6.16 FER, FIR, foam concentration, treatment ratio (Tunnelsoft)

# Conclusions

The graphic representation of the data provided by the TPC (Tunnelsoft) software allowed for a detailed analysis of each progressive stage and each installed ring, thus creating an important archive of information that defines the 'identikit' of the excavation carried out.

The excavation proceeded without significant problems, maintaining an average progress of 6.65m per day, almost always under hyperbaric conditions, except for some more stable sections where it was possible to operate under normobaric conditions. The thrust and torque were almost always within the limits.
The conditioning of the soil using foam proved to be optimal, managing to maintain both FIR and FER values constant throughout the entire section.

It is highlighted the predominant role and importance of the monitoring carried out by the various work teams, who are constantly supported by the P.A.T. (TBM Progress Protocol) for each section. Staying within the limits of this protocol is the main objective of the entire production, in order to ensure a progress that reflects the mechanical capabilities for which the TBM was designed in accordance with the terrain to be faced.
It is also found that often the predictions made during the design phase did not exactly match the reality during the advancement phase. In fact, in the first part of the section, it was possible to often stay below the values set by the P.A.T., highlighting better terrain characteristics than expected. In the middle phase of the analyzed section, however, there were the highest peaks or minima beyond the respective alarm thresholds, thus suggesting the presence of terrain with more heterogeneous characteristics and a tendency to face less stable fronts. This was indeed demonstrated by the need for maintenance on the various machine tools.
Supporting the team was the crucial use of the BEAM-Scan monitoring system (Bore-tunnelling Electrical Ahead Monitoring), a geophysical forecasting technology to enable real-time monitoring of the ground conditions and the presence of water ahead of the face, simultaneously with the excavation. This system allowed for the adjustment of machine parameters to optimize the ongoing excavation.

Having access to this amount of real-time data allows designers to compare their predictions with the actual status of the project, thus creating a true back analysis. This is functional to the improvement of the forecasting models used, possibly leading to the establishment of new correlations (also and especially empirical ones) that make the art of tunneling even more accurate.

# Annexes

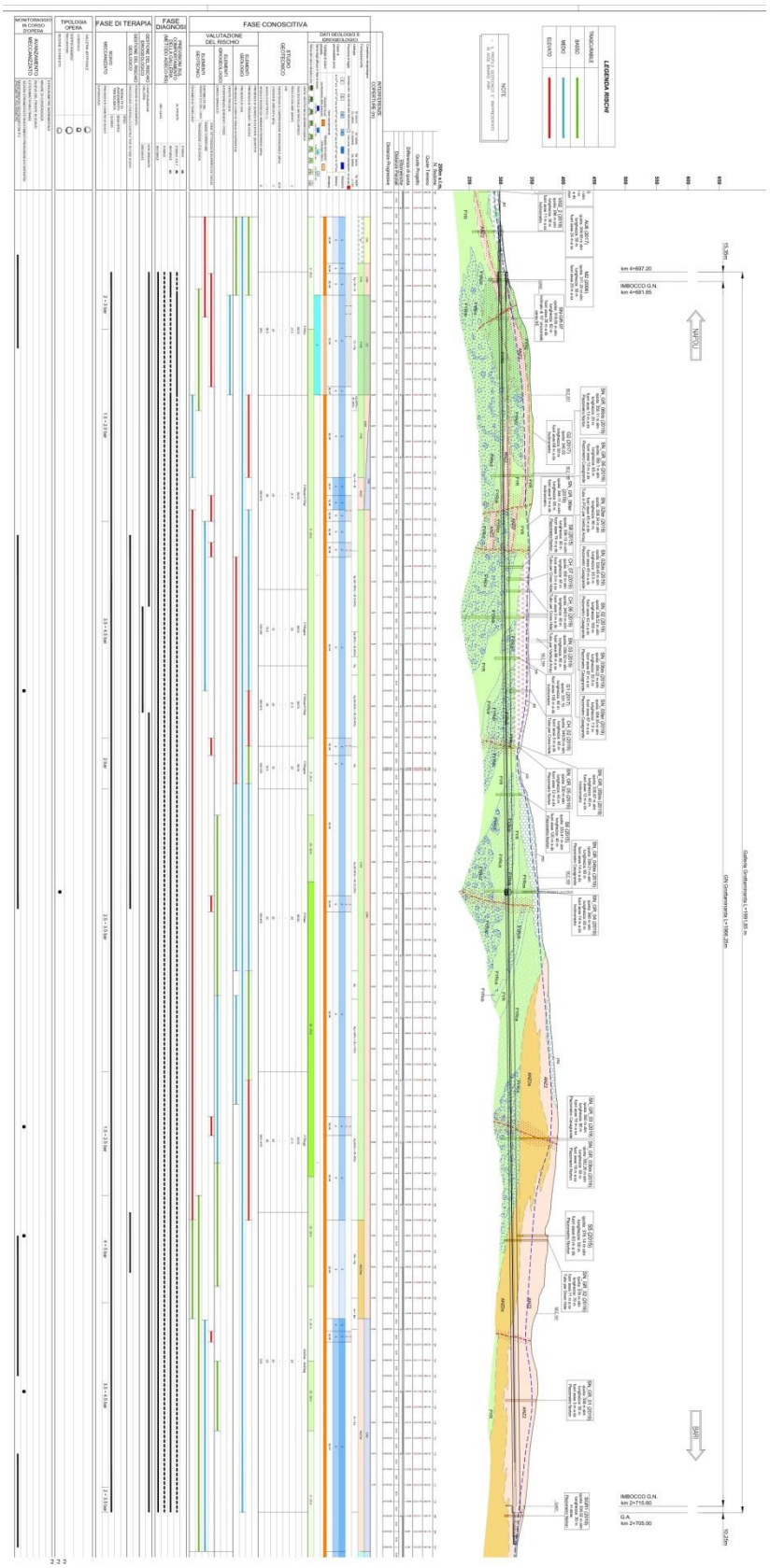

Annex 1 Geotechnical/Geomechanical profile – Grottaminarda Tunnel (Relazione, 2021)

# References


Britta Schößer, A. A. (2023). Face Support, Soil Conditioning and Material Transport in Earth-Pressure-Balance and Hydro Shield Machines. *Interaction Modeling in Mechanized Tunneling* . G. Meschke et al. (Eds.).

Bruland, A. (1998). Hard rock tunnel boring. Doctoral Thesis. *Norwegian University of Science and Technology (NTNU)* . Trondheim.

Cigla, M., & Ozdemir, L. (2000). Computer modelling for improved production of mechanical excavators. Salt Lake City UT, USA: SME Annual Meeting.

Elaborati, G. (2021, December 22). Elaborati Generali, GN01 Galleria naturale Grottaminarda da km 2+705 a km 4+695. *PROGETTO ESECUTIVO DI DETTAGLIO: tratta NAPOLI - BARI, RADDOPPIO TRATTA APICE-ORSARA, I LOTTO FUNZIONALE APICE HIRPINIA* .

GEEG. (2020, May). Geotechnical & Evironmental Engineering Group, SAPIENZA - Università di Roma. *IRPINIA-ORSARO: VALUTAZIONE PRELIMINARE DELLA FRESABILITÀ DEI LITOTIPI INTERESSATI DALLO SCAVO MECCANIZZATO* .

Herrenknecht. (2025). *Herrenknecht AG*. Tratto da https://www.herrenknecht.com/en/products/productdetail/epb-shield/

Hollmann FS, T. M. (2013). Assessment method for clay clogging and disintegration of fines in mechanised tunneling. *Tunnelling and Underground Space Technology , Volume 37*, Pages 96-106.

M. Herrenknecht, B. M. (1996). *Mechanised Shield Tunneling.* Berlin: Ernst&Sohn.

Monitoraggio. (2020, June 10). Relazione di monitoraggio, GN01 Galleria naturale Grottaminarda da km 2+705 a km 4+695. *PROGETTO ESECUTIVO DI DETTAGLIO: tratta NAPOLI - BARI, RADDOPPIO TRATTA APICE-ORSARA, I LOTTO FUNZIONALE APICE HIRPINIA* .

Ozdemir, L. (1977). Development of Theoretical Equations for Predicting Tunnel Boreability. Golden, Colorado, U.S.A.: Colorado school of mines, Ph.D. Thesis.

Peila, D. (2022-2023). Slides from the Tunneling course.

Plinninger R.J., K. H. (2004). Wear Prediction in Hardrock Excavation using the CERCHAR Abrasiveness Index (CAI). *EUROCK 2004 & 53rd Geomechanics Colloquium. Schubert (ed.)* .

R. Bono, G. Pini, B. Giurgola. (2018). *TBM Shift Engineer Handbook – Volume I* . Milan.

Relazione, t.-i. (2021, September 3). Relazione tecnico-illustrativa. *PROGETTO ESECUTIVO DI DETTAGLIO: tratta NAPOLI - BARI, RADDOPPIO TRATTA APICE-ORSARA, I LOTTO FUNZIONALE APICE HIRPINIA* .

Report. (2024, From March 19th to August 2nd). REPORT SETTIMANLE DI SCAVO, GN01-GALLERIA NATURALE Grottaminarda. *PROGETTO ESECUTIVO DI DETTAGLIO: tratta NAPOLI - BARI, RADDOPPIO TRATTA APICE-ORSARA, I LOTTO FUNZIONALE APICE HIRPINIA* .

Rostami J., O. L. (1996). Comparison between CSM and NTH Hard Rock TBM Performance Prediction Models. *Proceedings of the Annual Technical Meeting of the Institute of Shaft Drilling Technology (ISDT)* . Las Vegas.

Rostami, J. O. (1993). A new model for performance prediction of hard rock TBMs. *Proceedings of the Rapid Excavation and Tunneling Conference (RETC)*, (p. Pages 793-809). Boston, U.S.A.

Sisgeo, p. (s.d.). *SISGEO, inclined to improvement*. Tratto da https://sisgeo.com/it/prodotti/

Tamez. (s.d.). Tamez E. (1984) “Estabilidad de tuneles excavados en suelos” - Mexican Engineering Academy.

Tj., S. M. (1982). The Cerchar Abrasivity Index and Its Relation to Rock Mineralogy and Petrography. *Rock Mechanics 15, 1-7* .

TOTO. (2013, February 22). *TOTO Holding S.p.A.* Tratto da https://www.youtube.com/watch?v=dvqEuZWbAw4

TunnelPro. (s.d.). *TunnelPro S.p.A. website*. Tratto da https://tunnelpro.it/en/epb

Tunnelsoft. (s.d.). *TPC (Tunnel Processing Controller)*. Tratto da tunnelsoft.com: https://www.tunnelsoft.com/

Webuild. (s.d.). *Webuild S.p.A. website*. Tratto da https://www.webuildgroup.com/en/media/press-notes/webuild-new-leap-forward-high-speed-high-capacity-naples-bari-railway-line/

**liberatoria**

**Paolo Cartasegna** <p.cartasegna@hirpinia-av.it> 7 maggio 2025 alle ore 16:03
A: "kessj90@gmail.com" <kessj90@gmail.com>

Jad, come confermato per le brevi ti rilasciamo nulla osta ad utilizzo e pubblicazione in tesi dei dati tecnici inerenti lo scavo meccanizzato raccolti durante il tuo tirocinio presso Hirpinia AV.


**Paolo Cartasegna**

HR manager

***+39 333 2029226***

p.cartasegna@hirpinia-av.it

Consorzio Hirpinia AV

Via G. V. Bona, 65 – 00156 Roma

## Prohibition of Publication of Thesis Data

The data, information, and contents included in this thesis are to be considered confidential and are protected by confidentiality agreements. Any dissemination, reproduction, or publication – even partial – on any medium or platform is strictly prohibited without prior written authorization from the author and/or any third parties involved.

Unauthorized use, communication, or disclosure of the contents of this thesis may constitute a violation of applicable laws regarding intellectual property protection and trade secrets.